NH$_3$ condensation within plate heat exchangers
Flow patterns, heat transfer and frictional pressure drop

Tao, Xuan

DOI

Publication date
2021

Document Version
Final published version

Citation (APA)

Important note
To cite this publication, please use the final published version (if applicable).
Please check the document version above.

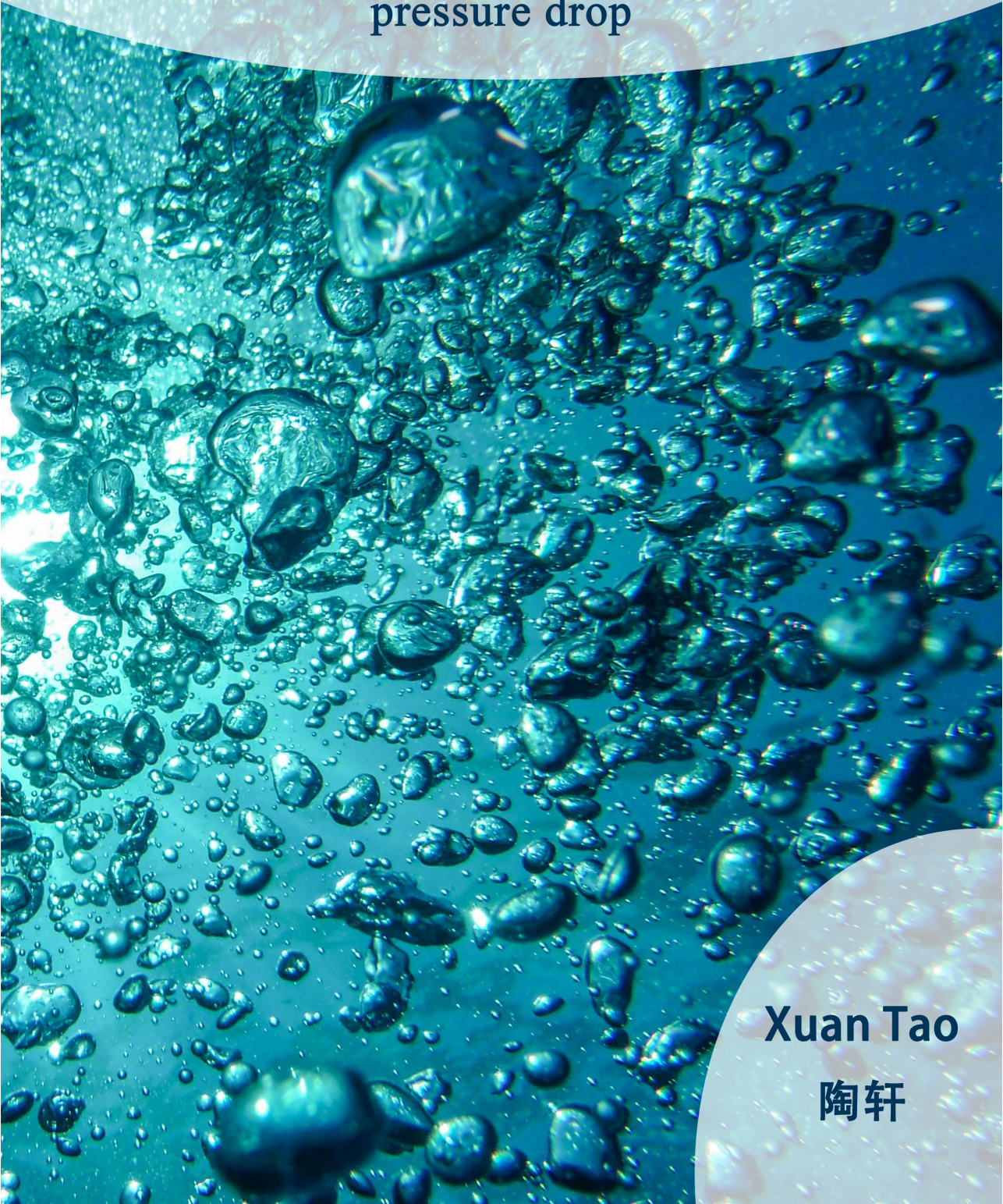# NH₃ Condensation within Plate Heat Exchangers:

Flow patterns, Heat Transfer & Frictional pressure drop

Xuan Tao

陶轩

NH$_3$ CONDENSATION WITHIN PLATE HEAT EXCHANGERS

FLOW PATTERNS, HEAT TRANSFER AND FRICTIONAL PRESSURE DROP

NH_3 CONDENSATION WITHIN PLATE HEAT EXCHANGERS

FLOW PATTERNS, HEAT TRANSFER AND FRICTIONAL PRESSURE DROP

Proefschrift

ter verkrijging van de graad van doctor
aan de Technische Universiteit Delft,
op gezag van de Rector Magnificus Prof. dr.ir. T.J.H van der Hagen
voorzitter van het College voor Promoties,
in het openbaar te verdedigen op dinsdag januari 12 2021 om 10:00 uur

door

Xuan TAO

Bachelor of Science in Energy, Power System & Automation,
Xi'an Jiaotong University, China
Master of Science in Power Engineering & Engineering Thermophysics,
Zhejiang University, China
geboren te Ningshan, Shaanxi Province, China.

Keywords:	Condensation mechanism; heat transfer; two-phase frictional pressure drop; flow pattern; experimental database; plate heat exchanger; NH_3
Printed by:	Ridderprint

An electronic version of this dissertation is available at
http://repository.tudelft.nl/.

独立之精神，自由之思想：
在孤独中求是，因果毅而坦然，为卓越而专注，知伟大而敬畏

Stay Hungry. Stay Foolish

CONTENTS

SUMMARY

Energy shortage and energy related environmental problems are urgent issues to be addressed in the coming years. Low-grade heat is utilized to drive energy conversion cycle and to produce electricity, which is a renewable and sustainable approach to energy supply. These thermodynamic cycles for energy conversion require eco-friendly working fluids and highly efficient heat transfer processes. NH_3 is a natural refrigerant with superior thermal properties such as large latent heat and high thermal conductivity. However, the application of NH_3 is restrained due to safety issues. Plate heat exchangers have the potential to be used in the thermal facility of NH_3 for the recovery of low-grade heat. These compact structures are able to transfer large heat loads with reduced charge of working fluid, thereby mitigating the safety risk. For instance, the Organic Rankine Cycles of NH_3 equipped with plate heat exchangers have smaller sizes compared with the plants filled with other refrigerants. Furthermore, plate heat exchangers have the advantage of design flexibility and easy maintenance for highly efficient heat transfer, bringing about wide utilization in refrigeration, pharmacy and chemical engineering.

In this thesis, NH_3 condensation is experimentally and theoretically investigated in plate heat exchangers. The main aim is to provide design methods of compact plate condensers used in the thermal facility of NH_3, which are not available in open literature. The experiments of NH_3 condensation have been reported, but no design method is provided. The heat transfer and frictional pressure drop correlations of hydrofluorocarbons (HFCs), hydrocarbons (HCs) and hydrofluoroolefins (HFOs) are assessed making use of an experimental database. Most suitable correlations are recommended.

In Chapter 1, the geometric characteristics of plate heat exchangers are specified. The channel parameters mainly include chevron angles, area enlargement factors and hydraulic diameters. The corrugated channels of plate heat exchangers bring new research challenges. This thesis approaches scientific problems using experimental and theoretical methodology. Experiments of NH_3 condensation are conducted including flow patterns, heat transfer and frictional pressure drop. The results for other working fluids are referred to for the analysis of NH_3. The flow patterns of air/water show that film flow covers large ranges of mass fluxes and vapor qualities. The heat transfer and frictional pressure drop correlations of HFCs, HCs and HFOs are mainly divided into homogeneous flow

correlations and separated flow correlations. The condensation of NH_3 takes place as separated flow. The heat transfer and frictional pressure drop correlations of NH_3 are derived from the experimental data. These mechanistic models identify the transition of flow patterns.

The non-dimensional numbers quantifying two-phase flow and condensation are listed in Chapter 2. The condensation mechanisms are divided into gravity-controlled condensation and convective condensation. The transition is primarily determined by mass fluxes and vapor qualities, as well as fluid properties. Condensation pressures, inlet superheating, plate geometries and temperature driving forces have relatively small influences on the transition. The sensitivity of heat transfer coefficients to mass fluxes depends on condensation mechanisms, while frictional pressure drops are almost independent of condensation mechanisms. The flow patterns of air-water are characterized and are integrated into maps using non-dimensional numbers. The flow pattern map based on the liquid Reynolds number, Re_L, versus the non-dimensional gas velocity, $J_G/\Lambda^{0.5}$, well describes the transition of flow patterns.

In Chapter 3, heat transfer and frictional pressure drop correlations are summarized for condensation in PHEs. An experimental database is built including HFCs, HCs, HFOs and CO_2. The mass fluxes are in the range of 2-150 $kgm^{-2}s^{-1}$. The chevron angles and hydraulic diameters have values of 25.7°-70° and 3.23-8.08 mm, respectively. The saturated temperatures are within the scope of -34.4 to 72.1 °C, while the reduced pressures are from 0.03 to 0.49. Eight heat transfer correlations are assessed with this experimental database. Applicable correlations are selected. Six frictional pressure drop correlations are compared with the database, and the prediction is relatively poor. A new correlation is developed using multi-variable regression analysis with non-dimensional numbers. This new correlation predicts 87.5% of the experimental data within ±50%.

The experimental setup and the methods of data reduction are described in Chapter 4. The thermodynamic cycles, measurement instrumentations and test section are specified. The calculations of the heat transfer coefficients and frictional pressure drop are presented.

In Chapter 5, the experimental results of NH_3 condensation are presented, including flow patterns, heat transfer coefficients and frictional pressure drop. Visualization experiments were conducted between 20 and 100 $kgm^{-2}s^{-1}$, observing full film flow and partial film flow. The flow patterns are the phenomenological reasons of the condensation mechanisms. The heat transfer and frictional pressure drop experiments range the mass fluxes of 21-78 $kgm^{-2}s^{-1}$, the averaged vapor qualities of 0.05-0.65 and the saturated pressure of 630 to 930 kPa. Higher vapor qualities remarkably increase the heat transfer coefficients and frictional pressure drop. Larger mass fluxes significantly contribute to fric-

tional pressure drop and moderately enhance heat transfer. The effect of saturated pressure on frictional pressure drop is minor. The experimental data are compared with the correlations recommended in Chapter 3, but the agreement is poor. New predictive models need to be developed for NH_3 condensation in PHEs.

In Chapter 6, predictive models for NH_3 condensation are developed including heat transfer and frictional pressure drop. The models make use of the experimental results presented in Chapter 5. The heat transfer model identifies the transition from full film flow to partial film flow, which represents the transition between condensation mechanisms. The physical interpretation of the model is discussed. The transition criterion accounts for the wetting characteristics. A modified Lockhart-Martinelli model is proposed for the frictional pressure drop, which shows separated flow characteristics. The model adds up the liquid pressure drop, vapor pressure drop and interface pressure drop. The proposed heat transfer and frictional pressure drop models show good predictive performances. NH_3 flow has non-negligible two-phase slip because of the large density ratio. Plate heat exchangers have corrugated channels and tend to break up the liquid film. These distinct flow characteristics are shown by flow patterns and are identified by the predictive models.

Conclusions are listed in Chapter 7. The experimental data of NH_3 condensation in plate heat exchangers are collected including flow patterns, heat transfer coefficients and frictional pressure drop. Heat transfer and frictional pressure drop models are consequently developed. Results for HFCs, HCs and HFOs are obtained by comparing several correlations with the experimental database in literature. Because NH_3 has larger two-phase density ratio than most HFCs, HCs and HFOs, separated flow models are proposed for NH_3, while homogeneous flow models are suggested for other working fluids. Recommendations are made to develop widely applicable predictive methods for various working fluids and operating conditions.

SAMENVATTING

De uitdagingen die energie-gerelateerde milieuproblemen met zich meebrengen worden steeds groter. Restwarmte is een herbruikbare energiebron en biedt een duurzame oplossing voor de energievraag. In de thermodynamische cyclus, die gebruikt wordt voor het omzetten van restwarmte in bruikbare energie, vereist milieuvriendelijke werkmedia en efficiënte warmteoverdrachtsprocessen. Ammoniak (NH_3) is een natuurlijk koelmiddel met uitstekende thermische eigenschappen, zoals hoge thermische geleidbaarheid. De toepasbaarheid van NH_3 is echter beperkt vanwege veiligheidsrisico's. Platenwarmtewisselaars kunnen in de thermische faciliteit van NH_3 worden gebruikt voor het omzetten van restwarmte naar elektriciteit. Deze compacte apparaten zijn met een kleine hoeveelheid van het werkmedium in staat om veel warmte over te brengen. Zo wordt het veiligheidsrisico verminderd. De Organic Rankine Cycles van NH_3, die zijn uitgerust met platenwarmtewisselaars, zijn kleiner van formaat in vergelijking met de installaties waarin andere koelmiddelen worden gebruikt. Bovendien hebben platenwarmtewisselaars het voordeel dat ze veel ontwerpflexibiliteit hebben en dat ze eenvoudig te onderhouden zijn om de warmteoverdracht zo efficiënte mogelijk te houden. Door deze voordelen worden platenwarmtewisselaars veel gebruikt voor koeling, en in de chemische en farmaceutische industrie.

In dit proefschrift wordt de condensatie van NH_3 in platenwarmtewisselaars onderzocht, zowel experimenteel als theoretisch. Het belangrijkste doel is om ontwerpmethoden aan te dragen voor compacte plaatcondensatoren die kunnen worden gebruikt in de thermische faciliteit van NH_3 en die niet beschikbaar zijn in openbare literatuur. Correlaties van warmteoverdracht en drukverlies door wrijving van HFCs, HCs en HFOs worden beoordeeld aan de hand van een experimentele database.

In Hoofdstuk 1 worden de kenmerken van platenwarmtewisselaars gespecificeerd. De belangrijkste parameters zijn de 'chevron' hoeken, oppervlakte vergroting en hydraulische diameters. De gegolfde vorm van de kanalen in platenwarmtewisselaars brengt nieuwe uitdagingen met zich mee. In dit proefschrift worden deze uitdagingen zowel theoretisch als experimenteel aangepakt. Met experimenten worden stromingspatronen, warmteoverdracht en drukverlies door wrijving geanalyseerd van NH_3-condensatie. Voor de analyse van NH_3 wordt verwezen naar de resultaten van andere werkvloeistoffen. De stromingspatronen van luchtwatermengsels laten zien dat filmstroming een groot gebied

dekt van de massafluxen en dampkwaliteiten. De warmteoverdracht en de drukverlies door wrijving correlaties van HFCs, HCs en HFOs kunnen worden verdeeld in correlaties voor homogene stromingen en gescheiden stromingen. Tijdens de condensatie van NH_3 is er een gescheiden stroming. De correlaties tussen warmteoverdracht en drukverlies door wrijving van NH_3 worden bepaald aan de hand van experimentele data. Deze modellen beschrijven de overgang tussen de stromingspatronen.

In Hoofdstuk 2 wordt een overzicht gemaakt van de dimensieloze getallen waarmee twee-fase stromingen en condensatie beschreven kunnen worden. De manier waarop condensatie plaatsvindt, is onderverdeeld in de door zwaartekracht gestuurde condensatie en condensatie door convectie. De overgang hiertussen wordt voornamelijk bepaald door de massaflux, de dampfractie, en de eigenschappen van het vloeistof. De condensatiedruk, inlaatoververhitting, plaatgeometrie en temperatuurverschillen hebben een relatief kleine invloed op de overgang. De overgang heeft voornamelijk invloed op de warmteoverdrachtscoëfficiënten, maar heeft weinig invloed op de drukverliezen door wrijving. De stromingspatronen van luchtwatermengsels wordt gekarakteriseerd door dimensieloze getallen. Het spectrum van stromingsvormen gebaseerd op de Reynolds nummer van vloeistof, Re_L, versus de dimensie-loos damp snelheid, $J_G/\Lambda^{0.5}$, reproduceert de resultaten van de verschillend onderzoeken beter dan de andere spectra.

In Hoofdstuk 3 worden de correlaties van de warmteoverdracht en wrijvingsdrukval voor condensatie in platenwarmtewisselaars samengevat. Er wordt een experimentele database opgebouwd met data voor HFCs, HCs, HFOs en CO_2. De massaflux ligt tussen 2 en 150 $kgm^{-2}s^{-1}$. De 'chevron' hoeken en hydraulische diameters liggen respectievelijk tussen 25.7° en 70° en 3.23 en 8.08 mm. De verzadigde temperatuur ligt tussen -34.4 en 72.1 °C, en de gereduceerde druk tussen 0.03 en 0.49. Acht warmteoverdracht correlaties worden vergeleken aan de hand van de database en de meest geschikte worden geselecteerd. Zes correlaties van wrijvingsdrukverlies worden vergeleken met de database en de voorspelling is relatief slecht. Er wordt een nieuwe correlatie ontwikkeld met behulp van een multivariabele regressieanalyse met dimensieloze getallen. Deze nieuwe correlatie voorspelt 87.5% van de experimentele gegevens binnen een marge van ±50%.

De experimentele opzet en de methoden van datareductie worden beschreven in hoofdstuk 4. De thermodynamische cycli, de meetinstrumenten en het testgedeelte worden gespecificeerd. De berekeningen van de warmteoverdrachtscoëfficiënten en de wrijvingsdrukval worden gepresenteerd.

In hoofdstuk 5 worden de experimentele resultaten van NH_3 condensatie gepresenteerd, inclusief stromingspatronen, warmteoverdrachtscoëfficiënten en w-

rijvingsdrukval. Visualisatie-experimenten werden uitgevoerd tussen 20 en 100 $kgm^{-2}s^{-1}$, met het observeren van volledige filmstroom en gedeeltelijke filmstroom. De stromingspatronen zijn de fenomenologische gevolgen van de condensatiemechanismen. De warmteoverdracht en wrijvingsdrukexperimenten variëren van de massastromen van 21-78 $kgm^{-2}s^{-1}$, met de gemiddelde dampkwaliteit van 0.05-0.65 en de verzadigde druk van 630 tot 930 kPa. Hogere dampkwaliteiten verhogen opmerkelijk de warmteoverdrachtscoëfficiënten en de wrijvingsdrukval. Grotere massafluxen dragen aanzienlijk bij aan de wrijvingsdrukval en verbeteren de warmteoverdracht matig. Daarbij is het effect van verzadigde druk op de wrijvingsdrukval is gering. De experimentele gegevens worden vergeleken met de correlaties die worden aanbevolen in hoofdstuk 3, maar, de overeenkomsten zijn slecht. Er moeten nieuwe voorspellende modellen worden ontwikkeld voor de NH_3 condensatie in PHE's.

In hoofdstuk 6 worden voorspellende modellen ontwikkeld voor de condensatie in PHE's, inclusief warmteoverdracht en wrijvingsdrukverlies. De modellen maken gebruik van de experimentele resultaten in hoofdstuk 5. Het warmteoverdrachtmodel identificeert de overgang van volledige filmstroom naar gedeeltelijke filmstroom, die de overgang tussen condensatiemechanismen weergeeft. De fysieke interpretatie van het model wordt behandeld. Het overgangscriterium is verantwoordelijk voor de bevochtigingseigenschappen. Voor de wrijvingsdrukval wordt een aangepast Lockhart-Martinelli-model voorgesteld en dat gescheiden stromingskarakteristieken vertoont. Het model telt de vloeistofdrukval, de dampdrukval en de interfacedrukval op. De voorgestelde modellen voor warmteoverdracht en wrijvingsdrukverlies vertonen goede voorspellende prestaties. NH_3 flow heeft een niet te verwaarlozen twee-fasen slip vanwege de grote dichtheidsverhouding. Platenwarmtewisselaars hebben golfkanalen en hebben de neiging om de vloeistoffilm te breken. Deze verschillende stromingskarakteristieken worden getoond door stromingspatronen en worden geïdentificeerd door de voorspellende modellen.

De conclusies staan vermeld in hoofdstuk 7. De experimentele gegevens van NH_3 condensatie in platenwarmtewisselaars worden verzameld inclusief stromingspatronen, warmteoverdrachtscoëfficiënten en wrijvingsdrukverlies. De modellen voor warmteoverdracht en wrijvingsdrukverlies zijn dan hierbij ook ontwikkeld. De resultaten voor HFCs, HCs en HFOs worden verkregen door verschillende correlaties te vergelijken met de experimentele database in de literatuur. Omdat NH_3 een grotere tweefasige dichtheidsverhouding heeft dan de meeste HFCs, HCs en HFOs, en worden deze gescheiden stromingsmodellen voorgesteld voor NH_3, terwijl homogene stromingsmodellen worden gesuggereerd voor andere werkende vloeistoffen. Aanbevelingen worden gedaan om breed toepasbare voorspellende methoden te ontwikkelen voor verschillende werkvloeistof-

fen en bedrijfsomstandigheden.

NOMENCLATURE

Symbols

A	Actual heat transfer area	[m^2]
A_f	Flow passage area	[m^2]
$\hat{a}$	Corrugation amplitute	[m]
c_p	Specific heat capacity	[Jkg^{-1}K^{-1}]
d	Diameter	[m]
d_e	Equivalent diameter	[m]
d_g	Channel gap	[m]
d_h	Hydraulic diameter	[m]
d_p	Plate thickness	[m]
f	Fanning friction factor	[-]
f_D	Darcy friction factor	[-]
g	Gravitational constant	[ms^{-2}]
G	Mass flux	[kgm^{-2}s^{-1}]
h	Enthalpy	[Jkg^{-1}]
k_i	Parameters defined in Eq. 3.60	[-]
KE/V	Kinetic energy per unit of volume	[Jm^{-3}]
L	Overall plate length	[m]
L_p	Port-to-port plate length	[m]
$\dot{m}$	Mass flow rate	[kgs^{-1}]
m_i	Parameters defined in Eq. 3.60	[-]

n_i	Parameters defined in Eq. 3.60	[-]
p	Corrugation pitch	[m]
p_{cp}	Compressed plate pitch	[m]
P	Pressure	[Pa]
$\dot{Q}$	Heat flow rate	[W]
$\dot{q}$	Heat flux	[Wm^{-2}]
T	Temperature	[K]
U	Overall heat transfer coefficient	[Wm^{-2}K^{-1}]
u	Superficial velocity	[ms^{-1}]
$\dot{V}$	Volume flow rate	[m^{3}s^{-1}]
v	Specific volume	[m^{3}kg^{-1}]
W	Overall plate width	[m]
W_{p}	In gasket plate width	[m]
x	Vapor quality	[-]

Dimensionless Numbers

Bd	Bond number	[-]
Bo	Boiling number	[-]
Co	Convection number	[-]
Con	Confinement number	[-]
$E\ddot{o}$	Eötvös number	[-]
Fr	Froude number	[-]
Ga	Galileo number	[-]
Ja	Jakob number	[-]
J_G	Non-dimensional gas velocity	[-]

Nu	Nusselt number	[-]
Pr	Prandtl number	[-]
Re	Reynolds number	[-]
R_v	Gas to liquid volume ratio	[-]
We	Weber number	[-]
X	Lockhart-Martinelli parameter	[-]

Greek letters

α	Heat transfer coefficient	$[\mathrm{Wm^{-2}K^{-1}}]$
β	Chevron angle to flow direction	[°]
β_{flow}	Chevron angle perpendicular to flow direction	[°]
γ	Corrugation aspect ratio	[-]
Δ	Difference	[-]
δ	Surface roughness	[m]
ε	Void fraction	[-]
Θ	Fraction of convective condensation	[-]
Θ_i	Parameters defined in Eqs. 3.60 and 4.1	[-]
ϕ	Surface enlargement factor	[-]
ϕ_L	Two-phase friction multiplier	[-]
ζ	Parameter defined in Eq. 3.58	[-]
κ_i	Parameters defined in Eqs. 2.32 and 2.36	[-]
λ	Thermal conductivity	$[\mathrm{Wm^{-1}K^{-1}}]$
Λ	Property modifying factor	[-]
Λ_{wave}	Corrugation wavelength	[m]
Ω	Wave number	[-]

μ	Dynamic viscosity	[Pas]
ξ	Parameter defined in Eq. 4.19	[-]
ρ	Density	[kgm^{-3}]
σ	Surface tension	[Nm^{-1}]

Subscripts

0	Basic
a	Ammonia
after	After cooler
air	Air
av	Averaged
c	Combined or transitional condensation
cc	Convective condensation
com	Combined value
cr	Critical conditions
cw	Cold water
de	Deceleration
ele	Elevation
eq	Equivalent
exp	Experimental data
fri	Frictional pressure drop
G	Gas or vapor
GO	Gas or vapor only
gc	Gravity-controlled condensation
high	High limit

homo	Homogeneous flow
hw	Hot water
in	Inlet of test section
int	At two-phase interface
L	Liquid
LG	Latent liquid to vapor
ll	Laminar-laminar flow
LO	Liquid only
LTi	Limits in Eqs. 6.4-6.5
low	Low limit
max	The maximum value
mea	Measurement
mix	Mixture or mixing process
mod	Modified
ori	Orifice
out	Outlet of test section
p	Plate or effective plate area
port	Port of test section
pre	Predicted data
pure	Pure fluid
sat	At saturation conditions
sup	Superheating
test	Test section
TP	Two-phase
T	Transition value

tt   Turbulent-turbulent flow

tube   Connection tube

w   Water

wall   At wall conditions

Abbreviations

BPHE   Brazed plate heat exchanger

EPDM   Ethylene Propylene Diene Monomer

GPHE   Gasketed plate heat exchanger

HC   Hydrocarbon

HFC   Hydrofluorocarbons

HFO   Hydrofluoroolefins

HTC   Heat transfer coefficient

L&M   Lockhart and Martinelli model

LNG   Liquefied Natural Gas

MAE   Mean absolute error

ME   Mean error

M-S&H   Müller-Steinhagen and Heck model

ORC   Organic Rankine Cycle

PHE   Plate heat exchanger

SPHE   Shell and plate heat exchanger

PC   Polycarbonate

PETG   Terephthalate glycol

PMMA   Polymethylmethacrylaat

PS   Polystyrene

PVC   Polyvinylchloride

RMSE   Root mean squared error

1

INTRODUCTION

In the recent decades, the utilization of low grade heat attracts increasing interest given its enormous amount and easy availability [1, 2]. The main resources include solar energy, geothermal energy, the cold energy of LNG, waste heat of industry and the thermal energy of seawater (temperature difference between warm surface seawater and cold deep seawater). The conversion of low grade heat to shaft power can be realized by Organic Rankine Cycles (ORCs) or Kalina Cycles, and is usually implemented in large plants to improve the financial return [3–7]. Limited by the small driving temperature difference, large amount of heat needs to be transferred, which requires highly efficient heat exchangers and large charge of working fluid. The heat exchanger effectiveness dominates the overall cycle efficiency. Compact heat exchangers are needed in the cycle [8]. Kirkenier [9] investigated the application of plate heat exchangers in ORC plants and confirmed the promising performance.

Parts of this Chapter are adapted from: Tao, X., Nuijten, M. P., Infante Ferreira, C. A., 2018. Two-phase vertical downward flow in plate heat exchangers: Flow patterns and condensation mechanisms. Int. J. Refrig. 85, 489-510 [10] and Tao, X., Kirkenier, J. A., Infante Ferreira, C. A., 2019. Condensation of NH_3 within a plate heat exchanger of small diameter channel. The 6th ASME International Conference on Micro/Nanoscale Heat and Mass Transfer. Dalian, China, paper 3920 [11].

1

1.1. BACKGROUND

Since plate heat exchangers (PHEs) were invented about one century ago, their application has covered industry and laboratories because of the superior performance such as favorable heat transfer coefficients (HTCs), reduced liquid holdup and compactness [12]. PHEs have gained increasing applications with single-phase and two-phase in recent decades [13–17].

PHEs are promising candidates for condensation processes since their corrugated channels tend to break up the condensate and enhance the heat transfer. During condensation, heat transfer and frictional pressure drop are sensitive to mass flux, vapor quality, heat flux, condensation pressure, superheating, fluid properties and plate geometries [10]. Condensation has been widely investigated by experiments, which have resulted in heat transfer and frictional pressure drop correlations. Experimental results show promising performance, but the mechanisms of energy and momentum transport are not fully understood [18].

1.2. GEOMETRIC CHARACTERISTICS

As shown in Figure 1.1, PHEs are composed of outside frame plates and inside stacked plates. The frame plates form the architecture of PHEs, while the stacked plates provide the effective heat transfer areas. The stacked plates have approximately sinusoidal corrugations. A flow channel is formed by two adjacent plates. These plates are corrugated and form periodic flow channels. The corrugated plates provide larger heat transfer areas. The flow is disturbed and secondary flow is introduced, which enhances the thermal performance. PHEs have large heat transfer areas per volume unit and small hydraulic diameters. The small flow passage area reduces the charge of working fluid. The heat transfer areas are adjusted by changing the number of plates. Hot and cold fluids flow alternately and counter-currently in the channels. PHEs are mostly installed vertically. During condensation and evaporation, the condensing fluid and evaporating fluid flow downward and upward, respectively.

Figures 1.2-1.4 summarize the general geometry of PHEs. The overall geometric parameters are the overall plate width, W, the in gasket plate width, W_p, the overall plate length, L, and the port-to-port length, L_p, as given in Figure 1.2. The basic heat transfer area of the plate, A_0, is the product of W_p and L_p. The effective heat transfer area, A_p, is obtained by multiplying A_0 with an area enlargement factor, ϕ, which is the ratio of the wavy plate surface to its plane projection. This factor depends on the corrugation characteristics and is defined in Eq. 1.2.

The area enclosed by the dash line of Figure 1.2 is further described in Figure 1.3. The plate contains sinusoidal corrugations. The chevron angle, β, is the angle between the corrugation and main flow direction, while β_{flow} is the chevron
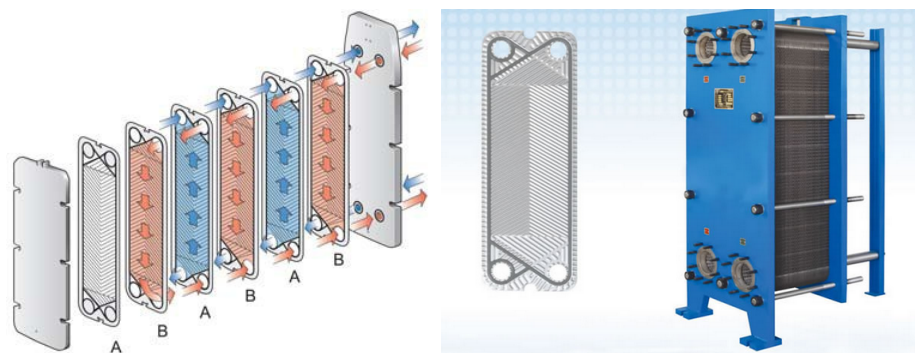
Figure 1.1: The configuration of PHEs with outside frame plates and inside stacked plates. Hot and cold fluids flow alternately and counter-currently between the stacked plates. (Online information)
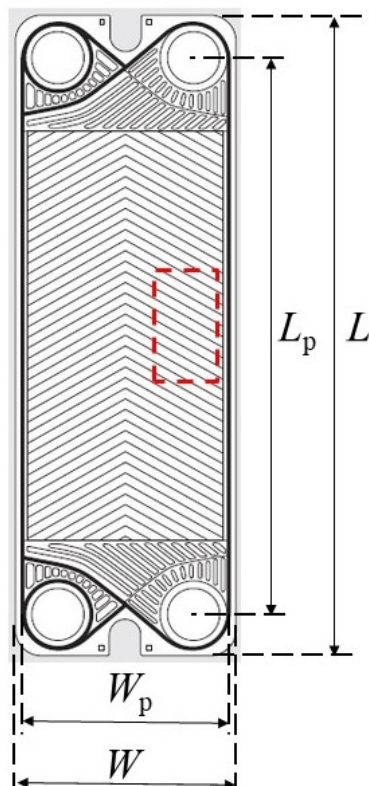
Figure 1.2: Representation of a plate with corrugation pattern indicating the overall plate width, W, the in gasket plate width, W_p, the overall plate length, L, and the port-to-port length, L_p.
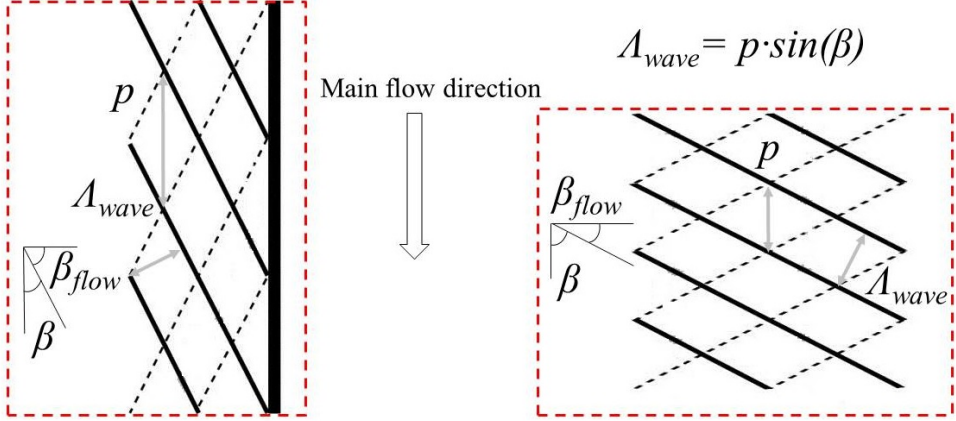
Figure 1.3: Representation of the corrugation profile including the corrugation pitch, p, the corrugation wavelength, Λ_{wave}, and the chevron angle, β; β_{flow} is the angle of the corrugation perpendicular to the flow direction; (left) small chevron angle and (right) large chevron angle. Based on Winkelmann [19].
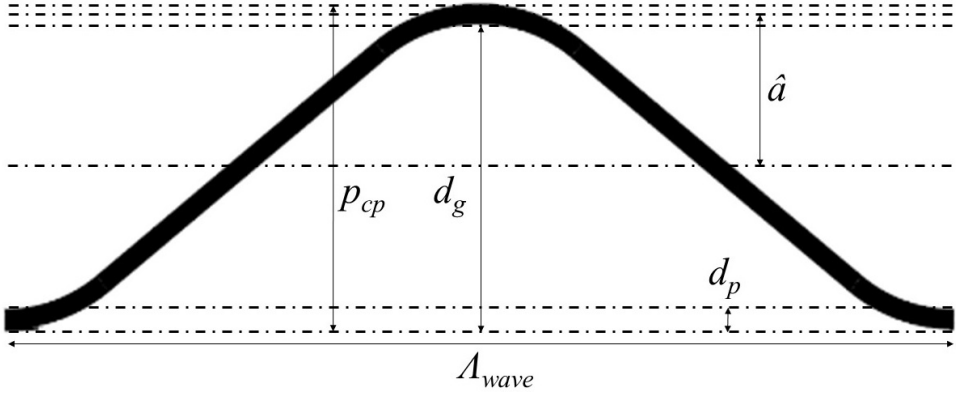
Figure 1.4: The relation between the compressed plate pitch, p_{cp}, the plate thickness, d_{p}, the channel gap, d_{g}, the corrugation amplitude, $\hat{a}$ and the corrugation wavelength, Λ_{wave}. Based on Winkelmann [19].

angle perpendicular to the flow direction. In this thesis, β is referred to as the chevron angle. The corrugation pitch, p, is the corrugation length in the main flow direction, and the wavelength, Λ_{wave}, is the corrugation length in the direction of the corrugation pattern. Both are related through the chevron angle, β. The corrugations are mirrored in the center plane of the plate, making the pattern symmetrical. Two plates are placed with opposite pattern directions and contact at the top of the corrugations.

$$\Omega = \frac{\pi(p_{\text{cp}} - d_{\text{p}})}{\Lambda_{\text{wave}}} = \frac{\pi d_{\text{g}}}{\Lambda_{\text{wave}}} = \frac{2\pi \hat{a}}{\Lambda_{\text{wave}}} \tag{1.1}$$

$$\phi(\Omega) \approx \frac{1}{6}(1 + \sqrt{1 + \Omega^2} + 4\sqrt{1 + \frac{\Omega^2}{2}}) \tag{1.2}$$

Figure 1.4 presents a sinusoidal corrugation and is the detail of Figure 1.3. The average spacing between the plates is the channel gap, d_{g}, and is defined as twice the amplitude, $\hat{a}$. d_{g} is also referred to as pressing depth. The compressed plate pitch, p_{cp}, is the sum of the channel gap and the plate thickness, d_{p}. p_{cp} is the effective depth added to a PHE. The algebraic relationships are indicated in Eq. 1.1, which is the definition of the wave number, Ω. In Eq. 1.2, the area enlargement factor, ϕ, is approximately a function of the wave number, Ω, for a sinusoidal corrugation [20].

The corrugation aspect ratio, γ, is twice the ratio of the channel gap to the wavelength, which indicates the degree of surface corrugation [21, 22]. γ is sometimes regarded as four times the ratio [23]. This study adopts the former definition:

$$\gamma = \frac{2d_{\text{g}}}{\Lambda_{\text{wave}}} = \frac{4\hat{a}}{\Lambda_{\text{wave}}} \tag{1.3}$$

The hydraulic diameter, d_{h}, and the equivalent diameter, d_{e}, are given in Eqs. 1.4-1.5 [20, 21]:

$$d_{\text{h}} = \frac{2d_{\text{g}}}{\phi} = \frac{4\hat{a}}{\phi} \tag{1.4}$$

$$d_{\text{e}} = 2d_{\text{g}} = 4\hat{a} \tag{1.5}$$

1.3. MAIN RESEARCH CHALLENGES

Several research challenges about the condensation in PHEs are identified in open literature [19, 24–34], which are listed below:

1

1. The condensation mechanisms are classified into gravity-controlled condensation and convective condensation. The transition happens when interfacial shear prevails over gravity. The HTCs are determined by the condensation mechanisms. The transition criterion has been in-depth studied in regular channels such as smooth tubes. The geometry of PHEs changes the criterion, and the transition needs to be investigated by analysing the physical process.

2. Flow patterns indicate the vapor-liquid distribution of two-phase flow, and change with varying vapor qualities during condensation. Flow pattern maps describe the condensation process and are the basis of mechanistic models. The condensing flow patterns are the phenomenological reasons of the condensation mechanisms and can be observed by visualization experiments. The corrugated structure of plates needs to be mirrored to a transparent plate for observation. The manufacturing process is challenging. Moreover, the transparent plate is required to be both machinable and compatible with the working fluid.

3. PHEs have large heat loads, and the vapor quality changes significantly along the flow direction. The overall measurements of complete condensation identify the performance of the units, but cannot capture the details of vapor quality distribution, which is important to exploit the potential of PHEs. Local heat transfer experiments can be implemented by measuring the temperature of the secondary fluid and thus the vapor quality distribution. However, the measurement of small temperature changes has large relative uncertainty for a given sensor accuracy.

4. The condensation within PHEs involves several factors including mass fluxes, vapor qualities, reduced pressures, refrigerant properties and geometric structures. Most heat transfer and frictional pressure drop correlations are derived from experimental data collected for specific operating ranges, so that their predictive accuracy is unknown outside these ranges. A comprehensive experimental database is needed to assess the correlations and to develop predictive methods applicable for wide ranges.

5. During the condensation of refrigerant mixtures, heat and mass are transferred simultaneously from vapor to liquid. The correlations for pure refrigerants can be modified to predict the HTCs of azeotropic mixtures and near-azeotropic mixtures. The modification involves the mass transfer by including an extra heat transfer resistance to the condensation HTC of pure refrigerants. However, zeotropic mixtures of high temperature glide, such

as NH_3/H_2O, have more complex condensation processes. The temperature glide changes significantly with concentrations. The mass transfer resistance hinders heat transfer, while the concentration difference drives the phase change.

6. Numerical models are powerful tools to design PHEs and to optimize geometric structures. The calculation of PHEs can be integrated into the design of plants to predict the performance under various operating conditions. Numerical models are used to choose the plate number to balance the heat transfer performance and frictional pressure drop.

7. Two-phase flow is generally modelled as homogeneous flow or separated flow. The homogeneous model assumes the two-phase velocities are the same, and the flow can be considered as a single equivalent fluid. According to the separated model, the vapor velocity is larger than the liquid velocity because of the density difference. Void fraction is the ratio of the vapor-occupied area to the total area in a cross-section, which is the basis to develop mechanistic models of heat transfer and frictional pressure drop. Void fraction relies on the two-phase slip ratio. It is needed to quantify the liquid film thickness during condensation. It also helps to determine the area of dry zones when the wall is not completely wetted because the liquid mass flux is small. The void fraction in PHEs has not been investigated up to now. Predictive methods for other channel types can be a departing point.

8. The flow distribution within PHEs affects the thermal and hydraulic performance. The mass fluxes are different among channels under the condition of flow maldistribution, which reduces the effective heat transfer areas and increases the frictional pressure drop. The flow is interrupted by the corrugated surface in a single channel, and more than one flow pattern is likely to take place simultaneously. The flow is represented by the dominant flow pattern. Distributors or manifolds play important roles.

9. Heat transfer is enhanced in different ways. During the condensation of pure refrigerants such as NH_3, liquid film is the main heat transfer resistance. When the film is broken, vapor is in contact with the cold wall directly, which enhances the heat transfer. Sharp plate structures break up the liquid film and are beneficial. The condensation of mixtures is hindered by mass transfer resistance. For NH_3/H_2O condensation, the concentration difference between vapor and liquid drives the phase change. To promote the mass transfer, the plate structure should be designed to maintain thin and continuous liquid film.

Table 1.1: Critical diameters (mm) according to different transition criteria (P_{sat}=690 kPa)[a]

Fluids	Eö=100	Con=0.5	Bd=0.09
NH_3	1.37	4.35	0.65
NH_3/H_2O (90%)	1.66	5.28	0.79
CO_2	0.74	2.36	0.35
R134a	0.52	1.66	0.25
R410A	0.58	1.86	0.28

[a] The fluid properties are calculated using Refprop 9.1 [39]

1.4. Methodology

1.4.1. Problem description

NH_3 has favorable transport properties and large latent heat [35–37]. PHEs can handle large flow rates and have large heat transfer areas per unit volume. The combination of PHEs and NH_3 is promising for large and intermediate heat loads. The compact structures reduce the charge of working fluid and other equipment investments. The corrugation channels of PHEs enhance the heat transfer and complicate the prediction of HTCs and frictional pressure drop.

PHEs mostly have hydraulic diameters of 2-5 mm [18], which are close to the critical diameters of micro or mini channels [38]. The transition from macro-channels to micro-channels happens when surface tension dominates over gravity. It is determined by channel sizes and fluid properties. Several criteria have been proposed to predict the transition such as Eötvös number, Eö, confinement number, Con, and Bond number, Bd, which will be presented in Eqs. 2.22-2.24. All of these non-dimensional numbers indicate the relative importance of surface tension and gravity depending on size effects. The critical values of these non-dimensional numbers have been determined, and are shown in Table 1.1. These criteria are compared for different fluids, and the discrepancy is noticeable. The critical diameter of NH_3 is relatively large because of the large surface tension. In fact, both surface tension and gravity need to be identified near the critical diameter. The large surface tension of NH_3 enhances the micro-channel characteristics during the condensation in PHEs [11].

The flow characteristics are determined by the balance of gravity, shear force, inertial force and surface tension. The relative magnitudes of these forces in the confined channels differ from those in large smooth tubes. Surface tension affects heat transfer and frictional pressure drop because of two-phase interface and wetting characteristics. The heat transfer is enhanced when the vapor is in direct contact with the cold wall. In small diameter channels, larger surface tension increases the contact angle, and tends to reduce the flow resistance [40]. Ungar and Cornwell [41] tested the adiabatic two-phase flow of NH_3 in small

tubes. The correlations developed for large tubes over-predicted the pressure drop. Surface tension tends to smooth the two-phase interface and reduce the shear force.

Heat transfer and frictional pressure drop are functions of the occurring flow patterns. NH_3 has distinct fluid properties from HFCs and HCs. NH_3 is characterized by large two-phase density ratio, thermal conductivity, surface tension and latent heat. To the best of the author's knowledge, no correlation has been specially proposed for NH_3 condensation in PHEs. In tubes, the correlations derived from HFCs or HCs mismatch the experimental data of NH_3 [37, 42]. In PHEs, it is unknown whether the correlations of HFCs or HCs are accurate for NH_3. This work investigates NH_3 condensation in PHEs.

1.4.2. EXPERIMENTAL AND THEORETICAL APPROACHES

Despite the promising performance of PHEs in NH_3 systems, research on NH_3 condensation is limited. The condensation of HFCs, HCs and HFOs in PHEs has been widely investigated by experiments, but reports on NH_3 data are scarce. Details of the experiments are missing in old papers [43, 44].

Experiments of NH_3 pose strict requirements on the experimental setup. Because NH_3 is corrosive, experimental setups are required to be fabricated from stainless steel and to exclude copper components and Teflon sealings. Gear pumps are suitable for laboratories since they can handle small mass flow rates without sharp fluctuations. Stainless steel gear pumps are required for NH_3 systems [37]. Diaphragm pumps are robust for corrosive fluids, but introduce fluctuations for small mass flow rates. To reduce the fluctuations, dampers need to be installed at the outlet of diaphragm pumps [45]. Reliable ventilation is needed, and experimental system must be installed in fume hoods so that no NH_3 escapes to the environment. As will be shown in Table 6.1, NH_3 has large latent heat, whose value is more than 5 times larger than R134a and R410A. To achieve the same operating conditions of mass fluxes and vapor qualities, the cooling and heating capacities of NH_3 systems are much larger, increasing the facility cost. Otherwise, experimental data are limited to small mass fluxes or low vapor qualities [46–49].

The condensation HTCs of NH_3 are large because of the high thermal conductivity. The corresponding heat transfer resistances are relatively small compared with the secondary fluid, which brings about large measurement uncertainty. To improve the accuracy, high-precision sensors are required. The mass flux of secondary fluid should be kept large to reduce the heat transfer resistance [45].

Thonon et al. [50] discussed the design of PHEs used for single-phase heat transfer, evaporation and condensation. Single-phase heat transfer is deterio-

1

rated in the downstream areas of the corrugation edges because of recirculation. During evaporation, the critical vapor quality of dryout is lower for PHEs than for smooth geometries, which is attributed to the fact that the corrugation washes the liquid film out from the wall. This structure seems to promote condensate drainage and to enhance heat transfer.

García-Cascales et al. [51] summarized the heat transfer correlations of single-phase, evaporation and condensation in PHEs. The Akers et al. [52] correlation is widely adopted by adding non-dimensional fluid properties or geometric parameters. The correlations of evaporation and condensation include heat fluxes and vapor qualities, and are compared with experimental data. In general, the evaporation correlations predict the experimental data better than the condensation correlations.

Amalfi et al. [21, 53] collected the predictive methods and experimental data of flow boiling in PHEs, including 1903 heat transfer and 1513 frictional pressure drop data points. The flow direction is mostly vertically upward. The predictive methods cannot accurately calculate the experimental data of large ranges. The database was used to develop new heat transfer and frictional pressure drop correlations by dimensional analysis coupled with multi-variable regression analysis, whose predictive performance is satisfactory. A similar analysis was carried out on the condensation within PHEs, and eight heat transfer correlations were compared with 325 experimental data points [54]. The selected correlations did not perform well, but no new correlation was proposed.

Eldeeb et al. [55] surveyed the heat transfer and frictional pressure drop correlations of evaporation and condensation, and calculated the HTCs of several refrigerants. In PHEs, condensation has been reported less than evaporation. The predictions of these correlations are considerably different, and need to be validated with experimental data. Despite the growing need for accurate prediction, the available simulation tools of PHEs are limited.

Most correlations have limited applicable ranges. Widely applicable and accurate correlations are needed. To survey the state of art, the condensation mechanisms in PHEs are firstly reviewed in this thesis. The transition from gravity-controlled condensation to convective condensation is mainly determined by mass fluxes and vapor qualities. The fluid properties also play important roles [10].

The flow patterns of air/water in PHEs have been experimentally investigated without phase change. This thesis presents a detailed overview of two-phase vertically downward flow, which is the common flow direction of condensers and absorbers [10]. The flow patterns of condensing NH_3 are different because of the distinct two-phase density ratio and surface tension in comparison to air/water. Additionally, the vapor qualities decrease from the inlet to the outlet during dia-

batic flow, gradually changing the flow patterns.

In this thesis, the heat transfer and frictional pressure drop correlations for condensation in PHEs are summarized [18]. An experimental database is developed including HFCs, HCs, HFOs and CO_2, but NH_3 is not included. Most correlations have been derived from experimental data, and are applicable in the original and similar operating ranges. To be assessed in larger ranges, these correlations are compared with the experimental database. Suitable methods are recommended to calculate the heat transfer and frictional pressure drop. These correlations are mainly classified into homogeneous flow correlations and separated flow correlations. Heat transfer and frictional pressure drop correlations of homogeneous flow are characterized by an equivalent Reynolds number and are more suitable for fluids of small two-phase density ratio [18, 52]. Heat transfer correlations of separated flow adopt a two-phase multiplier approach and involve the effect of interfacial shear force using empirical constants [18, 56]. Frictional pressure drop correlations of separated flow are mostly based on Lockhart-Martinelli model [57, 58]. Generally, two-phase Fanning friction factor approach over-predicts the experimental data of seperated flow, while Lockhart-Martinelli model under-predicts the experimental data of homogeneous flow [18, 59].

To develop predictive methods for NH_3 condensation, the flow patterns, HTCs and frictional pressure drop are experimentally investigated [45]. An uncertainty analysis is used to evaluate the reliability of experimental results. The flow patterns are full film flow and partial film flow. Experimental HTCs and frictional pressure drop show sharp sensitivity to the vapor qualities, and are compared with the correlations recommended for HFCs, HCs and HFOs [18, 60, 61]. The disagreement between the correlations and NH_3 experimental data indicates that NH_3 condensing flow is a separated flow.

The flow patterns are analyzed by comparing with the results of air/water. The flow patterns allow for the phenomenological analysis of condensation mechanisms and friction characteristics. The theories of condensing flow in tubes serve as the starting points for the predictive models of PHEs. Derived from experimental data, heat transfer and frictional pressure drop models are developed based on flow patterns. The heat transfer model distinguishes convective condensation and combined condensation. A two-phase multiplier heat transfer correlation is developed for convective condensation, which corresponds to full film flow. Full film flow in PHEs is equivalent to annular flow in tubes. All the heat is transferred through the condensate film. Combined condensation applies to partial film flow, and is composed of convective condensation and gravity-controlled condensation. Partial film flow in PHEs is comparable to stratified flow in tubes. Vapor condenses directly at dry zones, and the condensation is gravity-controlled. The gravity-controlled condensation deviates from

1

Nusselt's theory because of the two-phase shear force and liquid convection. A modified Lockhart-Martinelli model is proposed to predict the frictional pressure drop. The heat transfer and frictional pressure drop models are developed by describing the primary physical processes, while the flow details cannot be quantified and are considered by involving empirical constants. The developed model is compared with other experimental data, and the applicable range is analyzed [59].

1.5. OUTLINE OF THIS THESIS

In this thesis, NH_3 condensation in PHEs is investigated using experimental and theoretical approaches. The research challenges 1-4 introduced in Section 1.3 are addressed. Condensation mechanisms are identified to predict the HTCs of NH_3 condensation. Flow patterns are observed by visualization experiments, which determine the forms of heat transfer and frictional pressure drop correlations. Since NH_3 has large latent heat, the change of vapor qualities is small for given heat transfer rates, and partial condensation is measured. The sensitivity to vapor quality is investigated by controlling the inlet/outlet vapor quality. The dominant influencing factors of NH_3 condensation are recognized as mass fluxes, vapor qualities and saturated pressures, which are taken as the control variables during the experiments.

Figure 1.5 illustrates the outline of this thesis by highlighting the topics of chapters. The relation between chapters is shown. This thesis is mainly focoused on NH_3 condensation in PHEs. The condensation of HFCs, HCs and HFOs in PHEs is widely reported in literature, which is summarized for comparison. The theories of condensation in tubes are used as the starting points to develop predictive models. The key outputs are also presented.

A literature review is presented in Chapter 2, including the condensation mechanisms and flow patterns for vertically downward flow in PHEs. The transition from gravity-controlled condensation to convective condensation is affected by several factors, among which mass flux and vapor quality are dominant. Flow pattern maps of the previous studies are integrated and translated into non-dimensional forms.

The heat transfer and frictional pressure drop correlations for condensation in PHEs are summarized in Chapter 3. These correlations are classified into basic forms. An experimental database is built including the data of HFCs, HCs, HFOs and CO_2. This database is composed of 2376 heat transfer data points and 1590 frictional pressure drop data points. Eight heat transfer correlations are assessed with the database, and the best correlations are recognized. Six frictional pressure drop correlations are compared with the database. The prediction of frictional pressure drop is relatively poor, and a new correlation is developed.

1
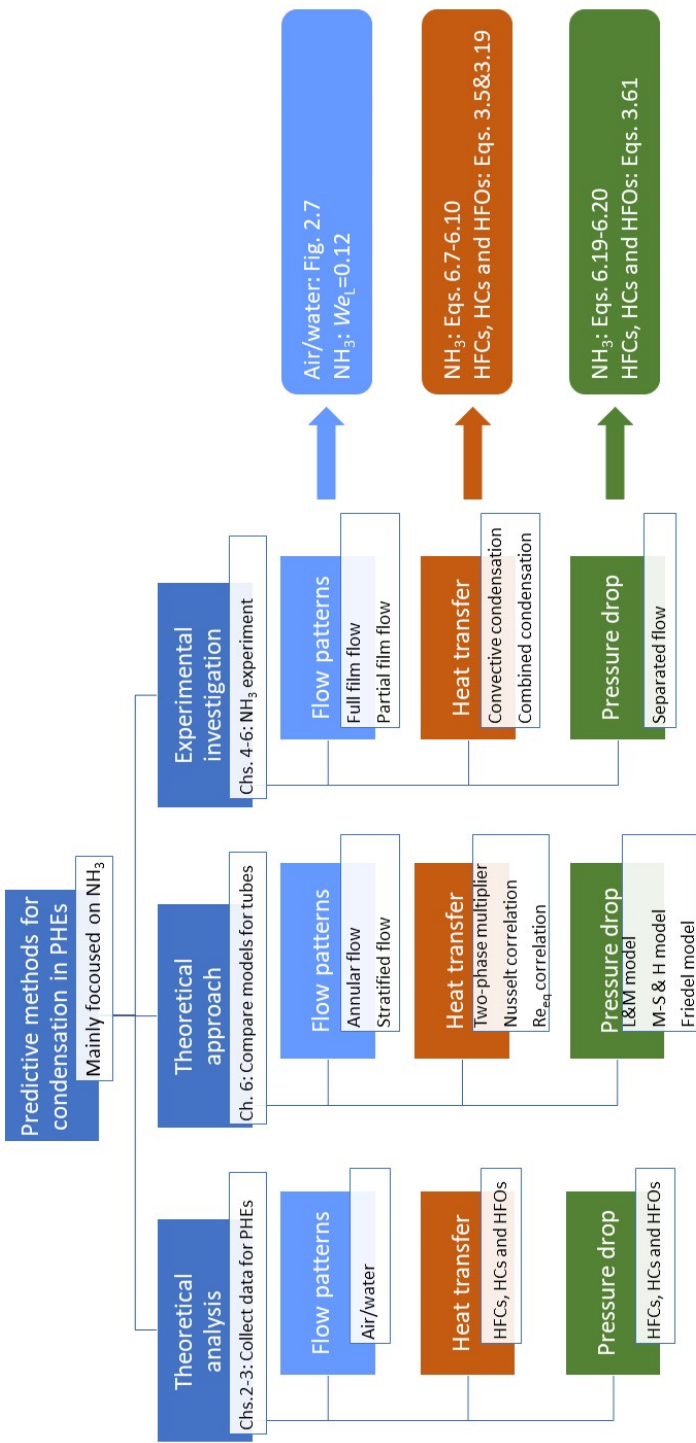
Figure 1.5: Outline of this thesis. Flow patterns, heat transfer and frictional pressure drop are experimentally investigated for NH$_3$ condensation in PHEs. Flow patterns of air/water, heat transfer and frictional pressure drop of HFCs, HCs and HFOs are analyzed by collecting experimental data from literature. The theories of condensation and two-phase pressure drop for tubes are referred to. Suitable predictive methods are recommended for these fluids.

1

The experimental setup is described in Chapter 4. The uncertainty of measurement instrumentations is specified. The methods of data reduction are explained. The HTCs and frictional pressure drop of single-phase H_2O are obtained. The results are used for the data reduction of NH_3 condensation, and for the validation of single-phase correlations in VDI [20]. Single-phase correlations are needed to predict condensing flow.

In Chapter 5, the experimental results of NH_3 condensation are presented including flow patterns, heat transfer and frictional pressure drop. The flow patterns are full film flow and partial film flow. The transition line in the flow pattern map mainly depends on the liquid mass flux. The HTCs and frictional pressure drop show conspicuous characteristics of separated flow, and cannot be predicted by the correlations suitable for other refrigerants. Another approach is needed for NH_3 condensation.

In Chapter 6, a heat transfer model is developed based on flow patterns, which represents the transition from convective condensation to gravity- controlled condensation. The physical interpretation of the two-phase multiplier approach and the deviation from Nusselt's theory are discussed. A transition criterion of condensation mechanisms is proposed according to the wetting characteristics. Since the flow patterns indicate separated flow, the Lockhart-Martinelli model is selected and is modified to predict the frictional pressure drop.

Conclusions and recommendations are presented in Chapter 7.

2

LITERATURE REVIEW OF CONDENSATION MECHANISMS AND FLOW PATTERNS

In this Chapter, the non-dimensional numbers used for two-phase flow and condensation are listed. Condensation mechanisms and the influencing factors of transition are discussed. The flow patterns are characterized, and the original data are summarized in flow pattern maps using u_G versus u_L and x versus G. Integrated flow pattern maps are developed using non-dimensional numbers.

.

2.1. NON-DIMENSIONAL NUMBERS FOR CONDENSATION

Several non-dimensional numbers are used to quantify the two-phase flow and condensation. These non-dimensional numbers indicate the flow characteristics as the functions of fluid properties, operating conditions and channel sizes. For the convenience of discussion, this Section lists these numbers and distinguishes between similar definitions.

2.1.1. FLUID PROPERTIES OF TWO-PHASE FLOW

The Lockhart-Martinelli parameter, X, describes the separated two-phase flow of four combinations: turbulent liquid and turbulent vapor, laminar liquid and turbulent vapor, turbulent liquid and laminar vapor, as well as laminar liquid and laminar vapor [57]. In the cases of turbulent-turbulent flow and laminar-laminar flow, X_{tt} and X_{ll} are calculated with Eqs. 2.1-2.2 based on the single-phase pressure drop correlations in tubes [62].

$$X_{tt} = \left(\frac{1-x}{x}\right)^{0.875} \left(\frac{\rho_G}{\rho_L}\right)^{0.5} \left(\frac{\mu_L}{\mu_G}\right)^{0.125} \tag{2.1}$$

$$X_{ll} = \left(\frac{1-x}{x}\right)^{0.5} \left(\frac{\rho_G}{\rho_L}\right)^{0.5} \left(\frac{\mu_L}{\mu_G}\right)^{0.5} \tag{2.2}$$

Eq. 2.3 defines the Convection number, which mainly indicates the influence of vapor quality [19, 63]. Kuo et al. [61] calculated the Convection number differently as given in Eq. 2.4.

$$Co = \left(\frac{\rho_G}{\rho_L}\right)^{0.5} \left(\frac{1-x}{x}\right)^{0.8} \tag{2.3}$$

$$Co_2 = \left(\frac{\rho_G}{\rho_L}\right) \left(\frac{1-x}{x}\right)^{0.8} \tag{2.4}$$

In Eq. 2.5, the averaged density is calculated by assuming homogeneous flow at the averaged vapor quality. The two-phase flow is treated as a single fluid. For homogeneous flow, the density of two-phase flow only depends on the vapor quality and the saturated liquid/vapor densities. Eq. 2.5 is widely used to represent the averaged two-phase density, and is adopted in this thesis without special explanation. Eq. 2.6 is the universal form with ε being the void fraction. Eq. 2.5 is a special case of Eq. 2.6 for homogeneous void fraction.

$$\frac{1}{\rho_{av}} = \frac{1-x_{av}}{\rho_L} + \frac{x_{av}}{\rho_G} \tag{2.5}$$

$$\rho_{av} = (1-\varepsilon)\rho_L + \varepsilon\rho_G \tag{2.6}$$

The Nusselt number is the non-dimensional HTC. When applied for condensation, the thermal conductivity uses the value of liquid phase.

$$Nu = \frac{\alpha d_{\mathrm{h}}}{\lambda} \qquad (2.7)$$

The Prandtl number is used to predict the HTC during convective condensation. The value of liquid phase is usually taken since the heat passes through the condensate film:

$$Pr_{\mathrm{L}} = \frac{c_{p,\mathrm{L}} \mu_{\mathrm{L}}}{\lambda_{\mathrm{L}}} \qquad (2.8)$$

In Eq. 2.9, Oshinowo and Charles [64] proposed to use a property modifying parameter. It is a function of the liquid properties relative to those of water under the same conditions.

$$\Lambda = \frac{\mu_{\mathrm{L}}/\mu_{\mathrm{w}}}{\left(\frac{\rho_{\mathrm{L}}}{\rho_{\mathrm{w}}}\left(\frac{\sigma_{\mathrm{L}}}{\sigma_{\mathrm{w}}}\right)^{3}\right)^{0.25}} \qquad (2.9)$$

2.1.2. FORCES IN CONDENSING FLOW

The Reynolds number is the ratio of inertia to viscous forces and has different forms including Re_{eq}, Re_{LO}, Re_{L} and Re_{G}. Eq. 2.10 gives the equivalent Reynolds number of two-phase flow, Re_{eq}, which is more relevant for homogeneous flow. G is the mass flux and d_{h} is the hydraulic diameter. The liquid only Reynolds number, Re_{LO}, in Eq. 2.11 is defined by assuming all the fluid is liquid. Re_{LO} is used to calculate the liquid only HTC. Eq. 2.12 defines the liquid Reynolds number, Re_{L}, which is also known as the condensate Reynolds number. Re_{L} only considers the mass flux of liquid phase. Similarly, the vapor Reynolds number, Re_{G}, in Eq. 2.13 focuses on the mass flux of the vapor phase. Eqs. 2.10-2.13 use the dynamic viscosities of liquid or vapor. In Eq. 2.14, the modified Reynolds number, Re_{mod}, includes the averaged dynamic viscosity instead [65].

$$Re_{\mathrm{eq}} = \frac{G\left((1-x) + x(\rho_{\mathrm{L}}/\rho_{\mathrm{G}})^{0.5}\right) d_{\mathrm{h}}}{\mu_{\mathrm{L}}} \qquad (2.10)$$

$$Re_{\mathrm{LO}} = \frac{G d_{\mathrm{h}}}{\mu_{\mathrm{L}}} \qquad (2.11)$$

$$Re_{\mathrm{L}} = \frac{G_{\mathrm{L}} d_{\mathrm{h}}}{\mu_{\mathrm{L}}} = \frac{G(1-x) d_{\mathrm{h}}}{\mu_{\mathrm{L}}} \qquad (2.12)$$

$$Re_{\mathrm{G}} = \frac{G_{\mathrm{G}} d_{\mathrm{h}}}{\mu_{\mathrm{G}}} = \frac{G x d_{\mathrm{h}}}{\mu_{\mathrm{G}}} \qquad (2.13)$$

$$Re_{\text{mod}} = Gd_{\text{h}} \left(\frac{1 - x_{\text{av}}}{\mu_{\text{L}}} + \frac{x_{\text{av}}}{\mu_{\text{G}}} \right) \tag{2.14}$$

The Weber number is the ratio of inertia to surface tension. Eqs. 2.15-2.16 apply for the liquid phase and vapor phase, respectively. In Eq. 2.17, the homogeneous Weber number, We_{homo}, is calculated from the averaged density [53, 66].

$$We_{\text{L}} = \frac{\rho_{\text{L}} u_{\text{L}}^2 d_{\text{h}}}{\sigma} = \frac{G^2 (1 - x)^2 d_{\text{h}}}{\rho_{\text{L}} \sigma} \tag{2.15}$$

$$We_{\text{G}} = \frac{\rho_{\text{G}} u_{\text{G}}^2 d_{\text{h}}}{\sigma} = \frac{G^2 x^2 d_{\text{h}}}{\rho_{\text{G}} \sigma} \tag{2.16}$$

$$We_{\text{homo}} = \frac{\rho_{\text{av}} u_{\text{av}}^2 d_{\text{h}}}{\sigma} = \frac{G^2 d_{\text{h}}}{\rho_{av} \sigma} \tag{2.17}$$

The Froude number is the ratio of inertia to gravity. Kuo et al. [61] included the liquid Froude number, Fr_{L}, in the heat transfer correlation, which has the form of Eq. 2.18. The two-phase Froude number has several forms. In Eq. 2.19, Oshinowo and Charles [64] and Bergles et al. [67] used Fr_{TP} to represent flow pattern maps. In Eq. 2.20, the non-dimensional gas velocity, J_{G}, is the ratio of inertia to gravity. It is widely used to distinguish condensation mechanisms [68, 69].

$$Fr_{\text{L}} = \frac{G^2}{\rho_{\text{L}}^2 g d_{\text{h}}} \tag{2.18}$$

$$Fr_{\text{TP}} = \frac{(u_{\text{G}} + u_{\text{L}})^2}{g d_{\text{h}}} \tag{2.19}$$

$$J_{\text{G}} = \frac{x G}{\left(g d_{\text{h}} \rho_{\text{G}} (\rho_{\text{L}} - \rho_{\text{G}}) \right)^{0.5}} \tag{2.20}$$

The Galileo number, Ga, represents the ratio of gravity to viscous force and is defined in Eq. 2.21 [70].

$$Ga = \frac{\rho_{\text{L}} (\rho_{\text{L}} - \rho_{\text{G}}) g d_{\text{h}}^3}{\mu_{\text{L}}^2} \tag{2.21}$$

The Bond number, Bd, indicates the ratio of buoyancy to surface tension and distinguishes macroscale and microscale during two-phase flow [53].

$$Bd = \frac{(\rho_{\text{L}} - \rho_{\text{G}}) g d_{\text{h}}^2}{\sigma} \tag{2.22}$$

Eötvös number, $E\ddot{o}$, and confinement number, Con, also quantify channel size effects and distinguish the transition between macroscale and microscale [38].

$$E\ddot{o} = \frac{(2\pi)^2 \sigma}{(\rho_L - \rho_G) g d_h^2} \tag{2.23}$$

$$Con = \left(\frac{\sigma}{(\rho_L - \rho_G) g d_h^2} \right)^{0.5} \tag{2.24}$$

In Eq. 2.25, R_v is the ratio of gas to liquid superficial velocities, with the superficial gas and liquid velocities, u_G and u_L, calculated in Eqs. 2.26-2.27 [64].

$$R_v = \frac{\dot{V}_G}{\dot{V}_L} = \frac{u_G}{u_L} \tag{2.25}$$

$$u_G = \frac{\dot{V}_G}{W_p d_g} \tag{2.26}$$

$$u_L = \frac{\dot{V}_L}{W_p d_g} \tag{2.27}$$

2.1.3. HEAT FLUX, SENSIBLE HEAT AND LATENT HEAT

The Boiling number, Bo, is the non-dimensional heat flux and is defined in Eq. 2.28, where Δh_{LG} is the latent heat [61, 71]. The equivalent Boiling number is given in Eq. 2.29 [72, 73].

$$Bo = \frac{\dot{q}}{G \Delta h_{LG}} \tag{2.28}$$

$$Bo_{eq} = \frac{\dot{q}}{G\left((1-x) + x(\rho_L/\rho_G)^{0.5}\right) \Delta h_{LG}} \tag{2.29}$$

Eq. 2.30 indicates the influence of condensate film on heat transfer [74]. Δh_{LG} is added with the sensible heat of the liquid film because the condensate is subcooled. This parameter is referred to as the Jakob number, Ja [65, 75].

$$Ja = \frac{c_{p,L}(T_{sat} - T_{wall})}{\Delta h_{LG} + 0.68 c_{p,L}(T_{sat} - T_{wall})} \tag{2.30}$$

2.2. CONDENSATION MECHANISMS

This Section presents the transition of condensation mechanisms, which is affected by a series of factors. Condensation mechanisms have significant influences on heat transfer performance, but minor effects on frictional pressure drop. Condensation within PHEs can be classified as gravity-controlled condensation or convection-controlled condensation. Different concepts are utilized to describe the two regimes. Gravity-controlled condensation is also known as laminar falling film or laminar film condensation. Convective condensation or forced convection condensation is referred to as turbulent, shear dominated condensation. Interfacial shear is dominant in this regime. There can be a transition regime where both gravity and shear are non-negligible. In gravity-controlled regime, HTCs decrease with increasing mass flux, or stay almost constant if turbulence plays a role. HTCs generally increase with mass flux in convective condensation. Mancin et al. [76] distinguished condensation into a temperature driving force dependent regime and a temperature driving force independent regime, which are equivalent to gravity-controlled condensation and convective condensation.

2.2.1. MASS FLUX, G

Mass flux is the main contributor to the transition from gravity-controlled condensation to convective condensation. The exact transition mass fluxes depend on refrigerant properties and PHE geometries. Longo [77, 78] experimentally studied the effects of mass flux for HFCs (R236fa, R134a and R410A) and HCs (R600a, R290 and R1270). The HTCs are mass flux independent at small mass flux, and increase with mass flux at larger values. The transition takes place at about 20 $\text{kgm}^{-2}\text{s}^{-1}$ for HFCs and 16.5 $\text{kgm}^{-2}\text{s}^{-1}$ for HCs. When the flow is classified by Re_{eq}, the transition value is 1650 for HFCs and HCs [77, 78]. At small mass fluxes, condensation is mainly governed by gravity, and is less affected by interfacial shear. In this regime, Nusselt's [79] derivation for laminar film condensation on a vertical wall gives a good approximation, predicting decreasing HTCs for larger mass fluxes. However, during Longo's experiments, the HTCs remained constant with increasing mass flux [77, 78]. The author attributed this to the measurement uncertainty and the existence of turbulence at small mass flux. Convective condensation takes place at larger mass fluxes and is governed by interfacial shear. The HTCs increase with larger mass fluxes. For most refrigerants, the interfacial shear reduces the thickness of the condensate film and promotes turbulence in the condensate film.

Sarraf et al. [27] investigated R601 condensation in a PHE with the mass fluxes of 9 to 30 $\text{kgm}^{-2}\text{s}^{-1}$. Infrared thermography was utilized for local measurements of the thermo-hydraulic characteristics. The HTCs increase with higher

vapor qualities. The HTCs decrease with increasing mass fluxes at first, and then keep almost constant for larger mass fluxes.

Mancin et al. [80, 81] analyzed the condensation of R407C and R410A in a PHE. The transition mass flux is approximately 20 $\mathrm{kgm^{-2}s^{-1}}$. Thonon and Bontemps [82] investigated the condensation of HCs including R601, R600, R290 and R600/R290 mixture. In the gravity-controlled regime, the HTC decreases with larger mass fluxes. Turbulence arises at larger mass fluxes and improves the HTCs.

Yan et al. [71] and Kuo et al. [61] investigated the condensation HTC and frictional pressure drop of R134a and R410A in a vertical PHE. The experiments were carried out at the mass fluxes of 60 to 120 $\mathrm{kgm^{-2}s^{-1}}$ for R134a and 50 to 150 $\mathrm{kgm^{-2}s^{-1}}$ for R410A. The HTCs increase with mass flux, indicating convective condensation. Grabenstein and Kabelac [83] measured the condensation of R134a in a PHE. Temperatures of the wall and secondary fluid were measured at seven locations to obtain local HTCs. The HTCs increase with mass fluxes for 38-62 $\mathrm{kgm^{-2}s^{-1}}$, which shows convective condensation.

The factors enhancing heat transfer also increase frictional pressure drop. Independent of the condensation regime, frictional pressure drop increases with mass fluxes and vapor qualities [61, 71, 77, 78].

2.2.2. Vapor quality, x

HTCs increase with vapor qualities since higher vapor qualities reduce the thickness of condensate film and heat transfer resistance. Mancin et al. [81] demonstrated that the HTCs of R407C and R410A increase with outlet vapor quality when mass flux is maintained constant. The increase is specifically noticeable at larger mass fluxes.

Yan et al. [71] and Kuo et al. [61] reported that the HTCs increase with the vapor quality. According to Grabenstein and Kabelac [83], the local HTCs of R134a increase with mass flux at high vapor quality and stay nearly constant at lower vapor quality.

2.2.3. Condensation pressure, P

Condensation pressure plays a role by changing the fluid properties. The two-phase density ratio and liquid thermal conductivity are smaller at higher condensation pressures. Yan et al. [71] and Kuo et al. [61] concluded that higher condensation pressure slightly reduces the HTC. Grabenstein and Kabelac [83] had similar conclusion and stated that the influence is larger at high vapor qualities. Condensation pressure is considered to have minor influences by others. According to Longo [77, 78, 84–86], the condensation pressure does not affect the transition mass flux and HTCs. Winkelmann [19] also reported that the conden-

sation pressure has no effect on the HTCs. Thonon and Bontemps [82] reached different conclusions. Higher condensation pressures increase the HTCs in the gravity-controlled regime and improve the transition mass fluxes.

Higher condensation pressures increase vapor density and reduce liquid dynamic viscosity. So the frictional pressure drop decreases. Winkelmann [19], Wang and Zhao [74] and Han et al. [87] confirmed the influence of condensation pressure on frictional pressure drop. Grabenstein and Kabelac [83] indicated that the influence is more significant at larger mass fluxes. On the other hand, the experiments of Longo [77, 78], Yan et al. [71] and Kuo et al. [61] showed small influences.

2.2.4. TEMPERATURE DRIVING FORCE, $\Delta T = T_{\text{sat}} - T_{\text{wall}}$ AND HEAT FLUX, $\dot{q}$
The heat flux is proportional to the temperature difference between the wall and refrigerant. Generally, both temperature driving force and heat flux are the functions of other operating conditions imposed on the system.

Mancin et al. [81] found that HTCs decrease with larger temperature difference. Jokar et al. [88] studied R134a condensation. As temperature difference increases, HTCs decrease sharply at gravity-controlled regime, and decrease slightly at convective regime. Mancin et al. [76] distinguished condensation regimes according to their dependence on temperature driving force. The dependent regime is gravity-controlled, while the independent regime corresponds to convective condensation. The HTC in the transition regime is a combination of both regimes.

Yan et al. [71] and Kuo et al. [61] investigated the effect of mean heat flux. HTCs increase with mean heat flux, but the effect is limited compared with mass fluxes and vapor qualities. The local measurements of Sarraf et al. [27] showed that the local heat flux is not constant, and the variation can reach 4 times along the condenser.

According to Yan et al. [71] and Kuo et al. [61], frictional pressure drop increases slightly with mean heat flux. Djordjević et al. [89] and Shi et al. [72] arrived at similar conclusions.

2.2.5. INLET SUPERHEATING, T_{sup}
Condensation of superheated vapor starts directly at the inlet of condensers or a distance from the inlet. Hrnjak and Kondou [90] claimed that condensation starts where the wall temperature is below the saturation temperature.

Longo [84–86] concluded that superheating in the inlet does not affect the transition mass flux. The superheated vapor is assumed to condense directly without de-superheating region near the inlet characterized as vapor single-phase heat transfer. Similarly, the condensate film along the channel is subcooled

without subcooling region near the outlet operating as liquid single-phase heat transfer. The saturation temperature is used to calculate the mean HTCs. Superheated vapor increases condensation kinetics and reduces condensate thickness, enhancing heat transfer. Mancin et al. [80, 81] assumed that the wall temperature is lower than the local dew temperature at the inlet, and superheated vapor condenses directly.

The infrared thermography of Sarraf et al. [91] indicated that the condensation region starts a distance from the inlet and ends apart from the outlet. De-superheating and subcooling regions are demonstrated. The superheating zone improves flow distribution and enhances the interfacial shear. Superheating does not affect the transition mass flux of condensation mechanisms. The heat transfer enhancement is stronger at gravity-controlled regime than at convective regime. Moreover, condensation droplets appear to form at superheating zone, and drag and evaporate along the flow path by interfacial shear and gravity [91]. Jokar et al. [65, 88] determined de-superheating and subcooling regions using single-phase HTCs.

Additionally, Sarraf et al. [91] reported that the superheating increases frictional pressure drop slightly at gravity-controlled regime and noticeably at convective regime. On the other hand, Longo [86] denied the effect of superheating on frictional pressure drop.

2.2.6. MIXTURES

Thonon and Bontemps [82] measured the condensation of R600/R290 mixtures at different concentrations. The HTC of mixtures is lower than that of both pure components. Larger mass fluxes improve the mixture HTCs independent of condensation mechanisms, and the improvement is significant at small mass fluxes. The mass transfer resistance deteriorates the heat transfer. The mixing in the gas phase is limited for small mass fluxes, and the deterioration is noticeable. Larger mass fluxes contribute to the mixing of the gas phase. According to Mancin et al. [80, 81], the condensation of zeotropic mixture R407C and near-azeotropic mixture R410A is similar to pure fluids.

2.2.7. REFRIGERANT PROPERTIES

Condensation of refrigerants including HFCs, HCs and their mixtures in PHEs has been widely investigated. Longo [77, 78] considered the thermal conductivity of liquid to be the dominant fluid properties for heat transfer. The two-phase density ratio determines the transition between homogeneous flow and separated flow. Novelty refrigerants such as R365mfc, R1234yf, R1234ze(E), R1234ze(Z) and R1233zd(E) were also investigated [66, 73, 83, 92–94].

Wang and Zhao [74] studied steam condensation in a PHE. The Nusselt num-

ber increases with larger mass flux, but decreases with higher outlet vapor quality and larger temperature differences. Complete condensation has better heat transfer performance than partial condensation.

Frictional pressure drop mainly depends on density ratio and liquid viscosity. Longo [77, 78] concluded that R410A has smaller frictional pressure drop relative to R236fa and R134a, while the frictional pressure drop of R1270 is smaller than of R600a and R290. According to Yan et al. [71] and Kuo et al. [61], R410A has smaller frictional pressure drop than R134a at high vapor quality but has larger frictional pressure drop at low vapor quality.

2.2.8. Plate geometry
Han et al. [87] measured the condensation HTC and the frictional pressure drop in brazed PHEs with chevron angles of 45°, 55°, and 70°. R410A and R22 were tested with varying mass flux, condensation temperature and vapor quality. The HTCs increase with mass flux and vapor quality, which indicates convective condensation. Larger chevron angles contribute to higher HTCs. Chevron angles have stronger influences at large mass fluxes and high vapor qualities.

Mancin et al. [81] measured PHEs of different plate number, length and width. None of the tested PHEs shows superior heat transfer performance, but less channels reduce maldistribution. Jin and Hrnjak [95] showed that the end plates of PHEs function as fins. This effect becomes noticeable when the plate number is small.

Han et al. [87] reported that larger chevron angles increase frictional pressure drop. Larger chevron angles intensify the effect of mass flux, vapor quality and condensation temperature on frictional pressure drop.

Würfel and Ostrowski [96] tested PHEs with neighbouring plates of 30°/30°, 30°/60° and 60°/60°. The frictional pressure drop increases with chevron angles, and the frictional pressure drop of 30°/60° is between 30°/30° and 60°/60°.

2.3. Flow patterns

2.3.1. Description of flow patterns
Flow patterns interpret the gas-liquid configuration and the interface characteristics. Table 2.1 lists the flow patterns in PHEs and allocates reference numbers to each study. Flow patterns are described similarly with different separating lines. Chevron angles and working fluids may affect separating lines and are treated as specific characteristics. Grabenstein et al. [97] tested two chevron angles but observed negligible effect on transitions, so chevron angles are not specific characteristics in this case. Four main flow patterns are identified in this study, while the other flow patterns are considered to be the transition between main flow

patterns or the synonym of main flow patterns. The main flow patterns are bubbly, slug, churn and film flow.

The flow patterns of Buscher [101] are not included in the development of the integrated flow pattern maps, but are used for validation. Table 2.1 also presents the flow patterns in round mini tubes as References 11 and 12 [102, 103], which will be discussed in Section 2.3.3. Jiang and Bai [104] visualized air/water flow in a capsule-type PHE, and found that the main flow patterns are film flow, plug flow and churn flow. They proposed transition criteria of the flow patterns. Film flow changes into plug or churn flow when the waves grow large enough to block the gas core. It happens when the liquid flow rate increases and occupies larger flow area. The gas has smaller flow area and accelerates. Consequently, the gas pressure decreases. The pressure at the bottom of the waves is larger than that at the top, enlarging the waves. Plug flow changes into churn flow when the breaking forces dominate over coalescence forces, which are determined by turbulence and surface tension, respectively. The flow in capsule-type PHEs shows different characteristics from chevron-type PHEs.

Figure 2.1 presents the four main flow patterns. The sequence generally follows the occurrence of flow patterns with increasing gas mass flux. For simplification, the corrugated channel is replaced with smooth tubes.

Bubbly flow consists of continuous liquid phase and dispersed bubbles smaller than the main channel dimensions. This is the first main flow pattern and is divided into regular and irregular bubbly flow. The bubbles are sized with spherical shape for regular bubbly flow. With increasing gas mass flux, the flow transforms to irregular bubbly flow, and the bubbles vary in size and shape.

Slug flow have several large bubbles which are regularly shaped but have similar dimensions to the main channel. It is the second main type. The Taylor bubbles are formed by merging small bubbles and make the flow intermittent. The characteristic shape of the Taylor bubble resembles a bullet with a hemispherical nose and a blunt tail. Liquid slug is between the Taylor bubbles and may contain small bubbles.

Churn flow is generally accepted as the chaotic version of slug flow and is intermittent flow. Because the amount of liquid between the large bubbles is too little to form stable liquid zones, the liquid zones break up and stir the flow. The two-phase interface is disordered. In some cases, the fluid oscillates but retains a net velocity in the flow direction. Churn flow may include small bubbles in the liquid film apart from the gas bulk. In fact, churn flow is difficult to be distinguished from slug flow quantitatively. Slug flow has smooth bubble boundaries and can be regarded as the transition between bubbly flow and churn flow.

Finally, *film flow* is equivalent to annular flow in tubes, since thin liquid film flows on the channel walls and continuous gas bulk flows in the middle. Film flow

2

Table 2.1: List of flow patterns reported in visualization experiments

Reference number	Study	Specific characteristics[a]	Flow patterns
1	Tribbe & Müller-Steinhagen [98]	β=30°/30° β=30°/60°	Regular bubbly, irregular bubbly, transition between bubbly and churn[b], churn, film, partial film
2	Tribbe & Müller-Steinhagen [98]	β=60°/60°	Regular bubbly, irregular bubbly, transition between bubbly and churn[b], churn, film, partial film
3	Vlasogiannis et al. [99]	-	Bubbly, transition between bubbly and rivulet[c], slug, rivulet
4	Winkelman [19]	-	Churn, wavy, film, partial film
5	Nilpueng & Wongwises [100]	-	Slug, annular liquid bridge, annular liquid bridge/air alone
6	Grabenstein & Kabelac [83]	Air /Water	Bubbly, slug, film
7	Grabenstein & Kabelac [83]	R365mfc	Bubbly, slug, film
8	Grabenstein et al. [97]	Air /Water	Bubbly, irregular bubbly, slug, film
9	Grabenstein et al. [97]	R365mfc	Bubbly, irregular bubbly, slug, film
10	Buscher [101]	β=75°/75°, Air /Water	Roundish bubble, irregular blob-like bubble, stagnant gas phase, bigger gas unit, heterogeneous, partial film, full film
11	Fukano & Kariyasaki [102]	Round mini tube, d=4.9 mm	Dispersed bubbly, intermittent (elongated bubbly, slug, churn), annular
12	Mehta & Banerjee [103]	Round mini tube, d=2.1 mm	Bubbly, slug -bubbly, slug, churn, slug-annular, annular
13	Jiang & Bai [104]	Capsule-type PHE, β=23.5°/66.5°[d], Air /Water	Film, plug, churn

[a] Chevron angles or working fluids.
[b] The transition between bubbly and churn is abbreviated as transition 1 in the following flow pattern maps.
[c] The transition between bubbly and rivulet is abbreviated as transition 2 in the following flow pattern maps.
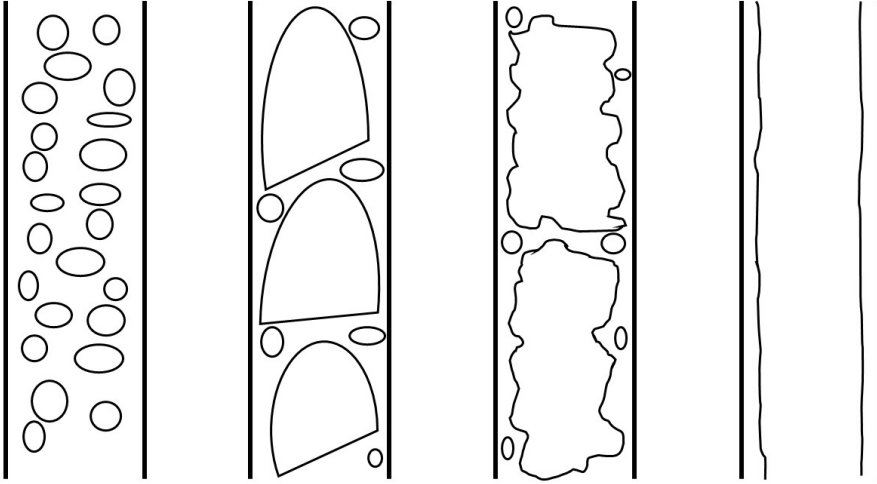[d] These are the angles between capsules and the vertical direction.

Figure 2.1: Representations of the four main flow patterns for vertically downward flow in PHEs. From left to right: bubbly flow, slug flow, churn flow and film flow.

is separated flow, and vapor phase has larger velocity than liquid phase. When rivulets or waves appear on the film surface, the flow is termed as rivulet or wavy flow. Annular-liquid bridge flow occurs as the disturbances are strong enough to span from one side of the film to the other side, whose presence needs more liquid. Annular-liquid bridge flow is different from slug or churn flow since the liquid bridge is unstable and cannot intermit the gas core. Film flow is classified into full film flow and partial film flow. Full film flow has enough liquid so that the wall surface is completely wetted. Partial film flow happens as the amount of liquid decreases. The limited liquid film cannot wet the entire surface so part of the surface dries up.

Bubbly flow is a combination of large liquid mass flux and small gas mass flux, while film flow is composed of less liquid and more gas. When the mass fluxes of both phases are limited and no Taylor bubble appears, the flow is regarded as transition between bubbly flow and film flow.

2.3.2. PREVIOUS STUDIES ON FLOW PATTERNS
OPERATING CONDITIONS OF VISUALIZATION EXPERIMENTS
The studies listed in Table 2.1 mostly used air/water under adiabatic conditions without phase change. Table 2.2 summarizes the PHE geometries and the operating conditions used to develop integrated flow pattern maps. Some operating pressures were not clearly reported. Only Vlasogiannis et al. [99] reported clearly

Table 2.2: Overview of the visualization experiments for two-phase vertical downward flow in PHEs[a].

Study	Model/type	P [kPa]	T [°C]	Gas	Liquid	Transparent plate[b]
Tribbe et al. [98, 105][c]	Alfa-Laval	250	25	Air	Water	Polyester
Vlasogiannis et al. [99]	Alfa-Laval P-01	130	25	Air	Water	Plexiglas
Winkelman [19]	Commercial[f]	130	25	Air	Water	PMMA
Nilpueng & Wongwises [100][d]	Commercial[f]	130	25	Air	Water	Polyurethane
Grabenstein et al. [83, 97][e]	Industrial[f]	100	39.8	R365mfc	R365mfc	Polyurethane

Study	L_p [mm]	W_p [mm]	d_h [mm]	d_g [mm]	d_p [mm]	A_{wave} [mm]	ϕ
Tribbe et al. [98, 105]	640	210	3	0.5	12	5.26	1.14
Vlasogiannis et al. [99]	352	100	2.4	0.6	10	4.24	1.13
Winkelman [19]	400	160	3	0.6	9.3	4.90	1.22
Nilpueng & Wongwises [100]	635	100	2.5	0.5	8.5	4.20	1.19
Grabenstein et al. [83, 97]	408	388	3	0.5	11.4	5.19	1.16

Study	Plate type	Profile	A_f [cm²]	β [°][g]	Mixing distributor	Inlet area
Tribbe et al. [98, 105]	Chevron	Sinusoidal	6.3	30/30,60/60,30/60	Single section	Triangular
Vlasogiannis et al. [99]	Chevron	Sinusoidal	2.4	60/60	Single section	Triangular
Winkelman [19]	Chevron	Sinusoidal	4.8	25.7/25.7	Single section	Triangular
Nilpueng & Wongwises [100]	Chevron	Sinusoidal	2.5	35/80	Single section	Triangular
Grabenstein et al. [83, 97]	Double chevron	Sinusoidal	11.6	63/63/63/63,27/27/27/27[h]	Eight sections	Rectangular

a All the visualization experiments had no phase change. Some of the geometric details are not reported and are determined by assumption.
b All the metal plates are stainless steel.
c Tribbe and Müller-Steinhagen [105] only visualized air-water and also tested the frictional pressure drop of air and aqueous solution.
d In these experiments, air-water were heated by hot water but without phase change.
e Grabenstein and Kabelac [83] and Grabenstein et al. [97] visualized R365mfc, and the visualization experiments were adiabatic.
f Commercial / Industrial refers to the width of the plates, the industrial plates being wider.
g The structure is symmetrical for combination of the same chevron angles, and unsymmetrical for combination of different chevron angles.
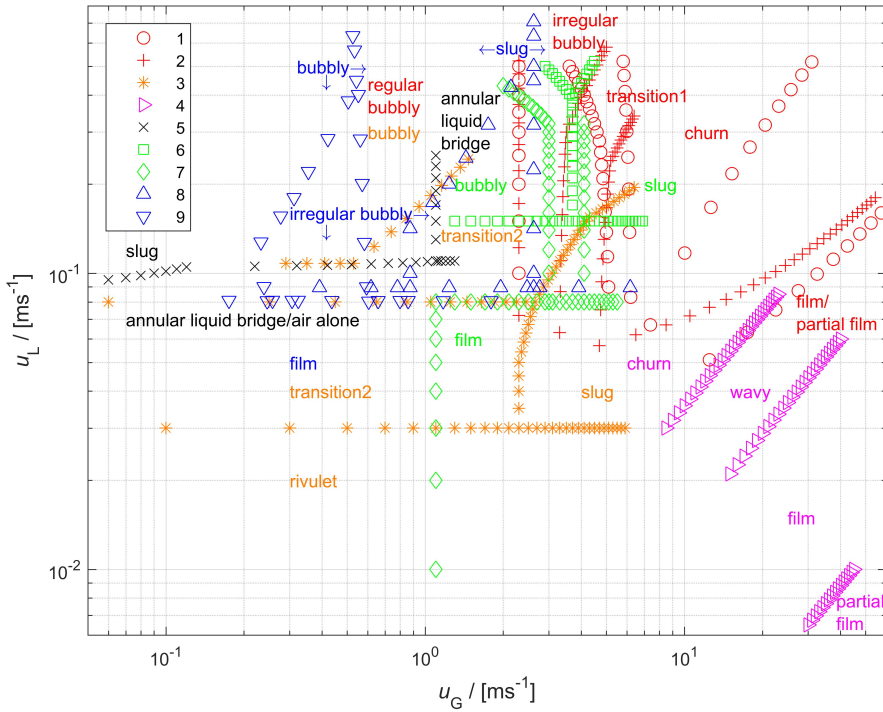h Double chevron structure is composed of four chevron angles.

Figure 2.2: Flow pattern map of vertical downward flow in PHEs using logarithmic scales [19, 83, 97–100]. The superficial velocities of the vapor and liquid phases are used in the axes. Separating lines are presented and the flow pattern descriptions are located in the zone. The reference numbers in the legend indicate these studies and are listed in Table 2.1.

that the air flow was converted to atmospheric pressure. The outlets of the PHEs were mostly connected to atmospheric vessels. When not reported, the operating pressure is taken as the atmospheric pressure added with 50% of the frictional pressure drop. The operating pressures mainly affect the vapor density but have limited effects on other fluid properties. The geometric details of the PHEs and the flow distributors are also presented.

PRESENTATION OF ORIGINAL FLOW PATTERN MAPS

Flow pattern maps are composed of separating lines between flow patterns. In order to build integrated flow pattern maps, the separating lines of the original studies are firstly analyzed. Winkelmann [19] presented the data points of flow patterns but without separating lines, which are assumed to be straight lines in the original map.
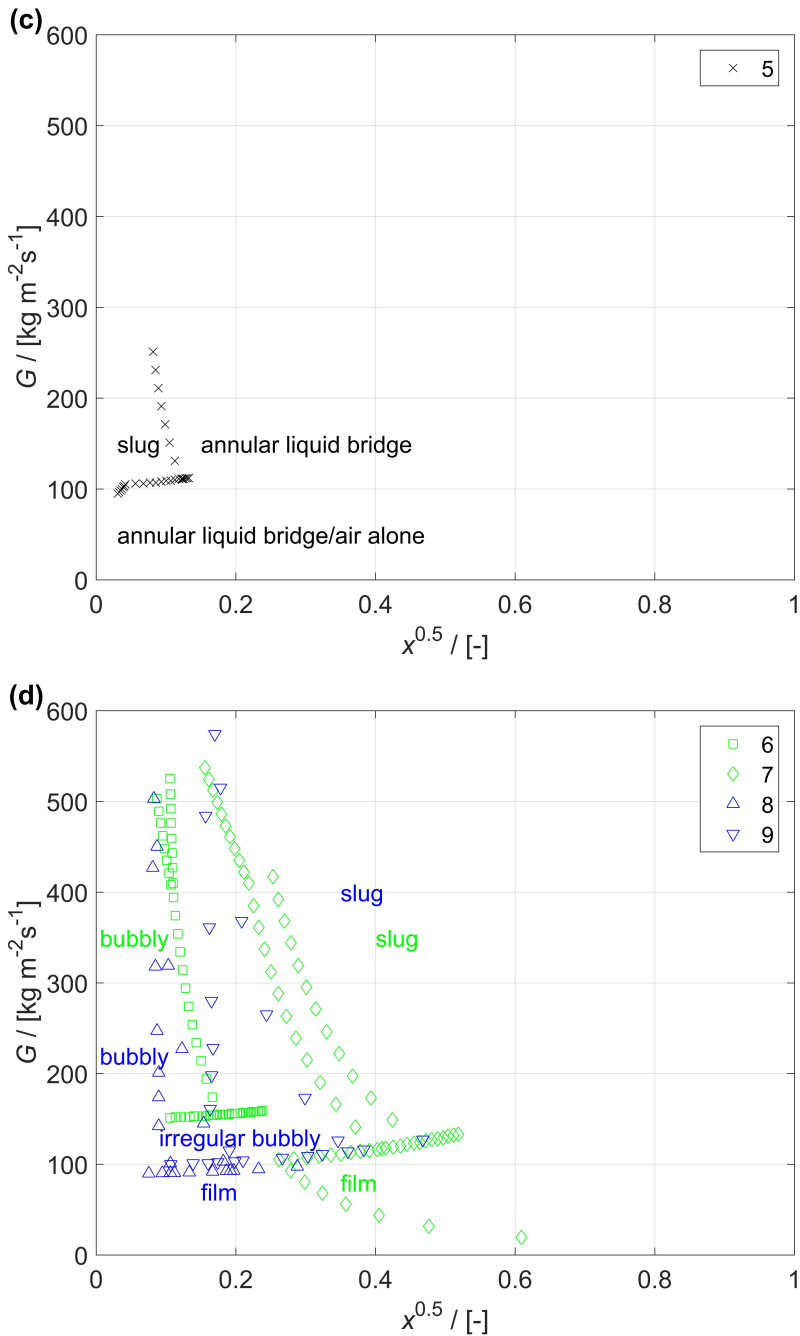
2
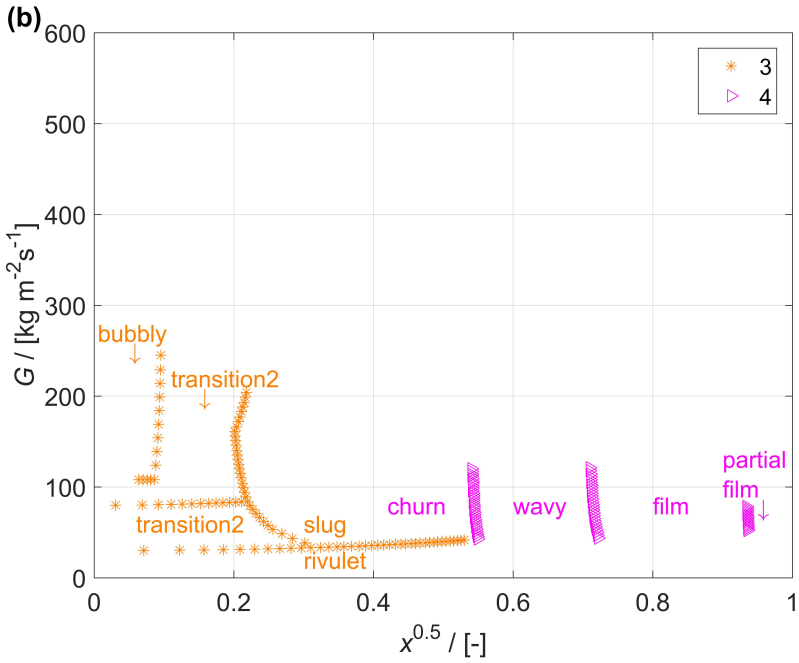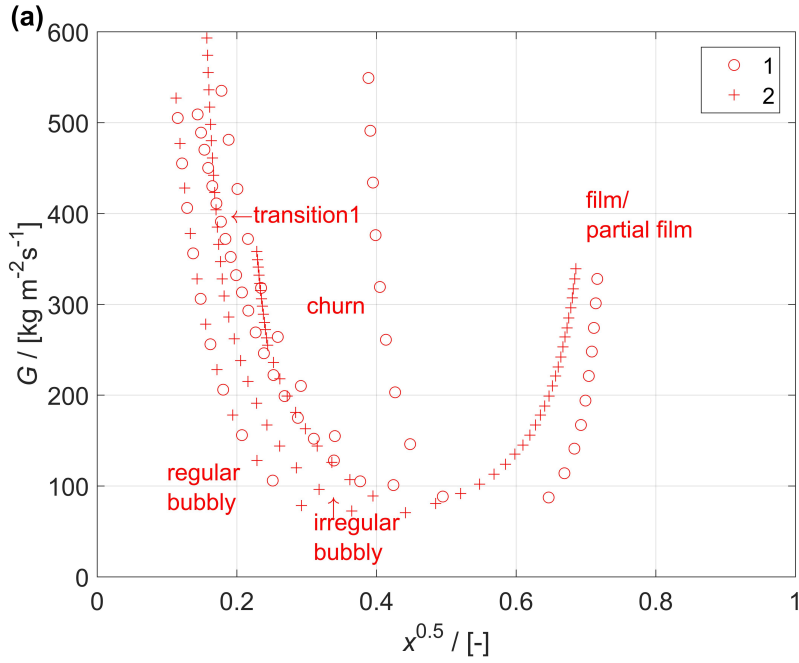
Figure 2.3: The separating lines between flow patterns reported in the different studies as the function of mass flux and the square root of vapor quality. The regions of film flow have better agreement than other flow patterns. The reference numbers listed in the legend are given in Table 2.1.

2

Except for Grabenstein et al. [97], all the studies presented the maps in the form of two-phase superficial velocities (u_G versus u_L), which are combined in Figure 2.2. In order to identify fluid properties and geometries, the two-phase velocities should be nondimensionalized.

Dobson and Chato [106] investigated condensation in horizontal smooth tubes and presented a flow pattern map in mass flux - vapor quality ($G - x$) axes. This map has been widely adopted in tube studies [107]. Figure 2.3 presents separating lines using $G - x$. The square root of vapor quality is used to expand the regions of flow patterns at low vapor quality and to improve the readability.

2.3.3. DEVELOPMENT OF INTEGRATED FLOW PATTERN MAPS

This Section translates the original flow pattern maps to new maps by comparing a series of axes combinations. $\rho_G u_G^2$ versus $\rho_L u_L^2$ and $(We_G Re_G (R_\nu / (R_\nu + 1)))^{0.5}$ versus $(We_L Re_L (1/(R_\nu + 1)))^{0.5}$ have been recommended [97, 108], but show poor performance in the present analysis. The map of $Re_{eq} / \Lambda^{0.5}$ versus $R_\nu^{0.5}$ also performs poorly. $Fr_{TP} / \Lambda^{0.5}$ versus $R_\nu^{0.5}$ and Re_L versus $J_G / \Lambda^{0.5}$ show better performance, and will be further discussed.

FLOW PATTERN MAP BASED ON $Fr_{TP} / \Lambda^{0.5}$ VERSUS $R_\nu^{0.5}$

$Fr_{TP} / \Lambda^{0.5}$ versus $R_\nu^{0.5}$ include superficial velocities, PHE geometries and fluid properties [64]. Most fluid properties are computed using Refprop 9.1 [39], while the surface tension of air/water is taken from Vargaftik et al. [109].

Figure 2.4 plots the separating lines and marks the zones of flow patterns. The y-axis is limited to $R_\nu^{0.5} \leq 20$ to improve the readability. Thus some separating lines from Winkelmann [19] are left out.

Figure 2.5 presents a simplified flow pattern map derived from Figure 2.4, which identifies the main flow patterns. The flow is full film/partial film at large volume ratio of gas to liquid. At small ratio, the flow changes from regular bubbly, irregular bubbly to slug flow with increasing Froude numbers. Transition between bubbly and film flow appears at small Froude numbers, while churn flow is between slug and full film/partial film flow at large Froude numbers. The full film/partial film flow also includes the annular, annular-liquid bridge, wavy and rivulet flow. However, different flow patterns overlap in this map.

FLOW PATTERN MAP BASED ON Re_L VERSUS $J_G / \Lambda^{0.5}$

Figure 2.6 involves Re_L versus $J_G / \Lambda^{0.5}$, which identify inertia, viscous force and gravity. Re_L accounts for the non-dimensional liquid mass flux, while $J_G / \Lambda^{0.5}$ interprets the non-dimensional gas mass flux. This combination also identifies mass flux and vapor quality. The map is simplified in Figure 2.7 to show the main information. Dashed lines instead of solid lines are used between similar flow
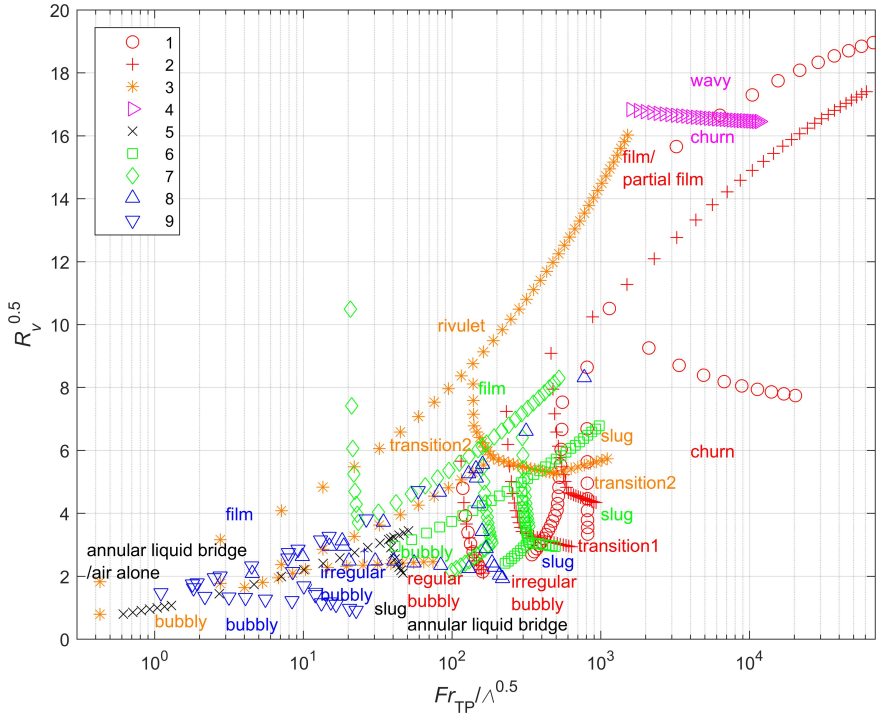
Figure 2.4: Flow pattern map of two-phase flow in PHEs, with non-dimensional quantities on the x-axis ($Fr_{TP}/\Lambda^{0.5}$) and y-axis ($R_v^{0.5}$) [19, 83, 97–100]. Definitions of the non-dimensional quantities are explained in Eqs. 2.9, 2.19 and 2.25. Separating lines are presented and the flow patterns are indicated. The reference numbers in the legend indicate these studies and are listed in Table 2.1.

patterns. Full film flow happens at small liquid mass fluxes even if the gas mass fluxes are small. At larger liquid mass fluxes, the flow becomes regular bubbly, irregular bubbly, slug, churn and full film flow with increasing gas mass fluxes. Additionally, transition between bubbly flow and film flow takes place at intermediate liquid mass fluxes. Partial film flow happens at small liquid mass fluxes and large gas mass fluxes.

Constant vapor quality lines are constructed in this map. Eq. 2.31 is the ratio of the axes and is the function of vapor quality, with κ_1 and x calculated in Eqs. 2.32-2.33.

$$\frac{J_G/\Lambda^{0.5}}{Re_L} = \frac{G_G}{(g d_h \rho_G (\rho_L - \rho_G))^{0.5} \Lambda^{0.5}} \frac{\mu_L}{G_L d_h} = \kappa_1 \frac{G_G}{G_L} = \kappa_1 \frac{x}{1-x} \tag{2.31}$$
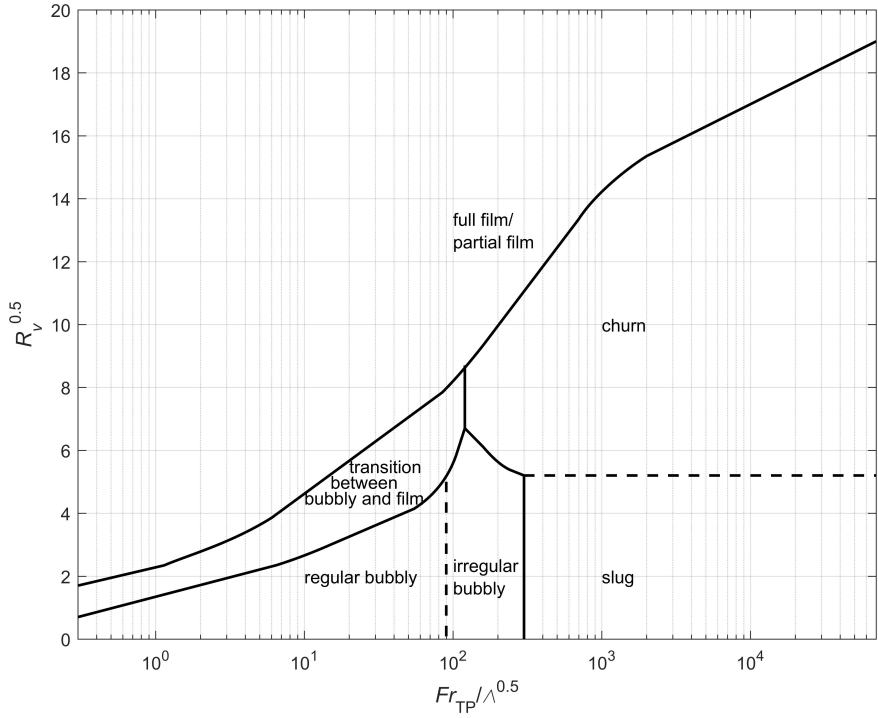
2

Figure 2.5: Simplified flow pattern map in PHEs, which uses non-dimensional quantities on the x-axis ($Fr_{TP}/\Lambda^{0.5}$) and y-axis ($R_v^{0.5}$). The characteristic fluid properties are these of air and water at 25 °C and 150 kPa. Separating lines differentiate regular bubbly flow, irregular bubbly flow, slug flow, churn flow, full film/partial film flow and transition between bubbly and film flow.

$$\kappa_1 = \frac{\mu_L}{(gd_h\rho_G(\rho_L - \rho_G))^{0.5}\Lambda^{0.5}d_h} \tag{2.32}$$

$$x = \frac{G_G}{G_G + G_L} \tag{2.33}$$

Constant overall mass flux lines are constructed by adding both axes as illustrated in Eqs. 2.34 and 2.35, with κ_2 and G calculated in Eqs. 2.36-2.37.

$$\frac{J_G}{\Lambda^{0.5}} + Re_L = \frac{G_G}{(gd_h\rho_G(\rho_L - \rho_G))^{0.5}\Lambda^{0.5}} + \frac{G_L d_h}{\mu_L} = \frac{1}{\kappa_2}\left(G_G + G_L + \left(\kappa_2\frac{d_h}{\mu_L} - 1\right)G_L\right) \tag{2.34}$$

$$\frac{J_G}{\Lambda^{0.5}} = \frac{1}{\kappa_2}\left(G + \left(\kappa_2\frac{d_h}{\mu_L} - 1\right)\frac{\mu_L}{d_h}Re_L\right) - Re_L = \frac{G}{\kappa_2} - \frac{\mu_L}{\kappa_2 d_h}Re_L \tag{2.35}$$
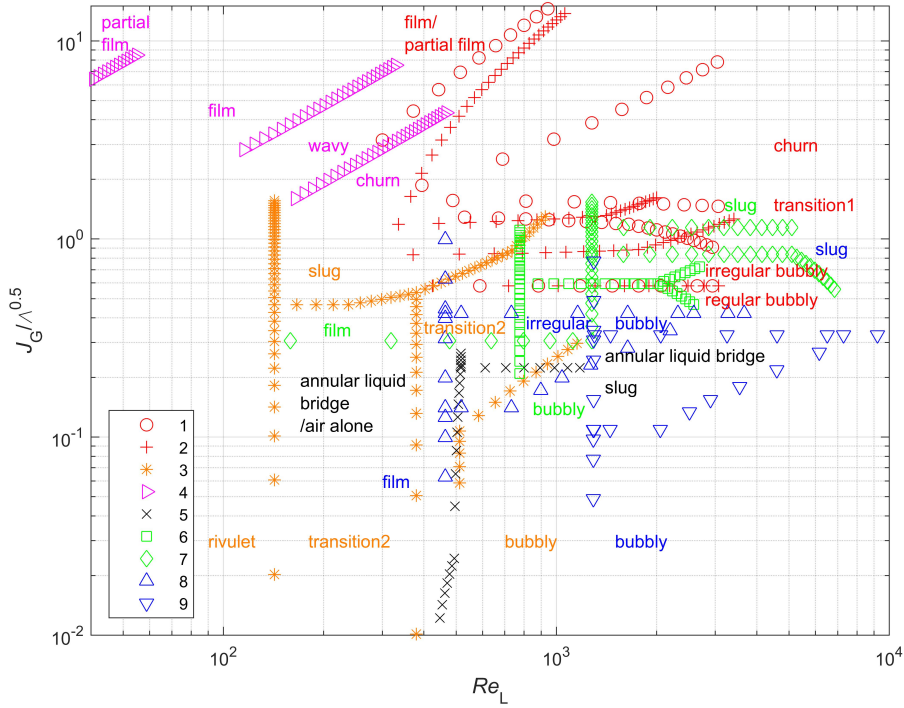
Figure 2.6: Flow pattern map of two-phase flow in PHEs, with non-dimensional quantities on the x-axis (Re_L) and y-axis ($J_G/\Lambda^{0.5}$) [19, 83, 97–100]. The non-dimensional quantities are introduced in Eqs. 2.12, 2.20 and 2.9. Separating lines are presented and the flow patterns are indicated. The reference numbers in the legend indicate these studies and are listed in Table 2.1.

$$\kappa_2 = (g\,d_{\mathrm{h}}\rho_G(\rho_L - \rho_G))^{0.5}\,\Lambda^{0.5} \tag{2.36}$$

$$G = G_G + G_L \tag{2.37}$$

The condensation process is depicted in this flow pattern map by identifying a constant overall mass flux line with decreasing vapor quality. Figure 2.8 depicts the condensation of NH_3. Full film flow and partial film flow cover a large range for the vapor qualities above 0.5. Other flow patterns take place at low vapor qualities. The flow pattern map is developed from air/water, and is used for NH_3. According to Dobson and Chato [106], the difference of fluid properties can be identified by multiplying the superficial velocities of the refrigerant with the square root of the density ratios. In this way the two-phase kinetic energies are
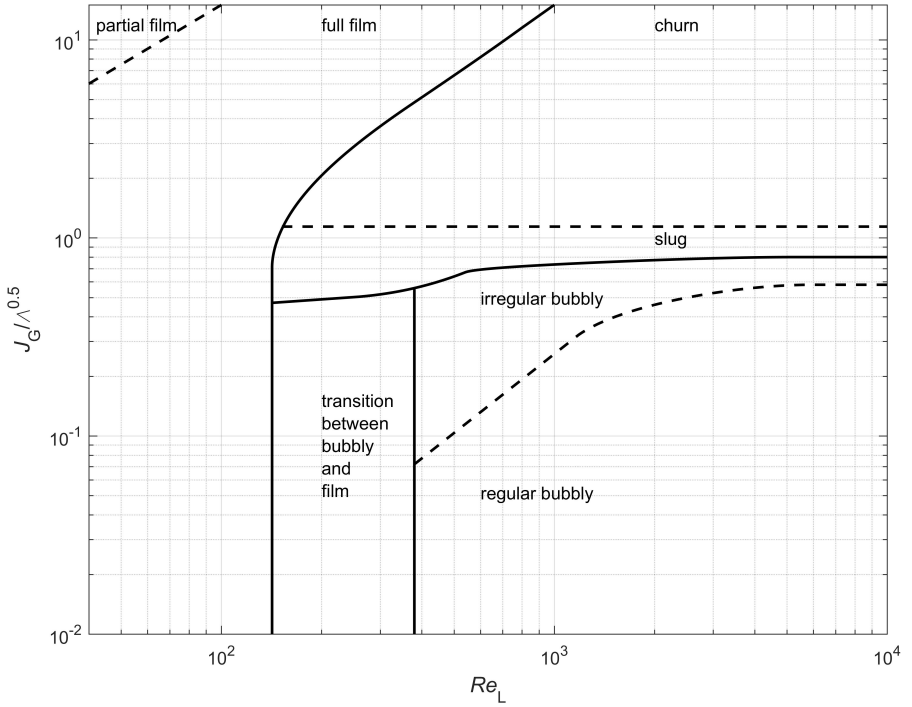
Figure 2.7: Simplified flow pattern map in PHEs using non-dimensional quantities on the x-axis (Re_L) and y-axis ($J_G/\Lambda^{0.5}$). The characteristic fluid properties are these of air and water at 25 °C and 150 kPa. Separating lines differentiate regular bubbly flow, irregular bubbly flow, slug flow, churn flow, full film/partial film flow and transition between bubbly and film flow.

accounted for. The axes of this map are non-dimensional two-phase velocities. The modifications are presented in Eqs. 2.38-2.39. Figure 2.8 shows the original and modified condensation lines. The condensation lines move to film flow after modification. The vapor density of NH_3 is larger than of air, while the liquid density of NH_3 is smaller than of water.

$$J_{G,mod} = \sqrt{\rho_{a,G}/\rho_{air}} J_G \qquad (2.38)$$

$$Re_{L,mod} = \sqrt{\rho_{a,L}/\rho_w} Re_L \qquad (2.39)$$

COMPARISON WITH OTHER FLOW PATTERN MAPS

Buscher [101] carried out visualization experiments on air/water flowing in a PHE horizontally, vertically upward and downward. The flow direction makes
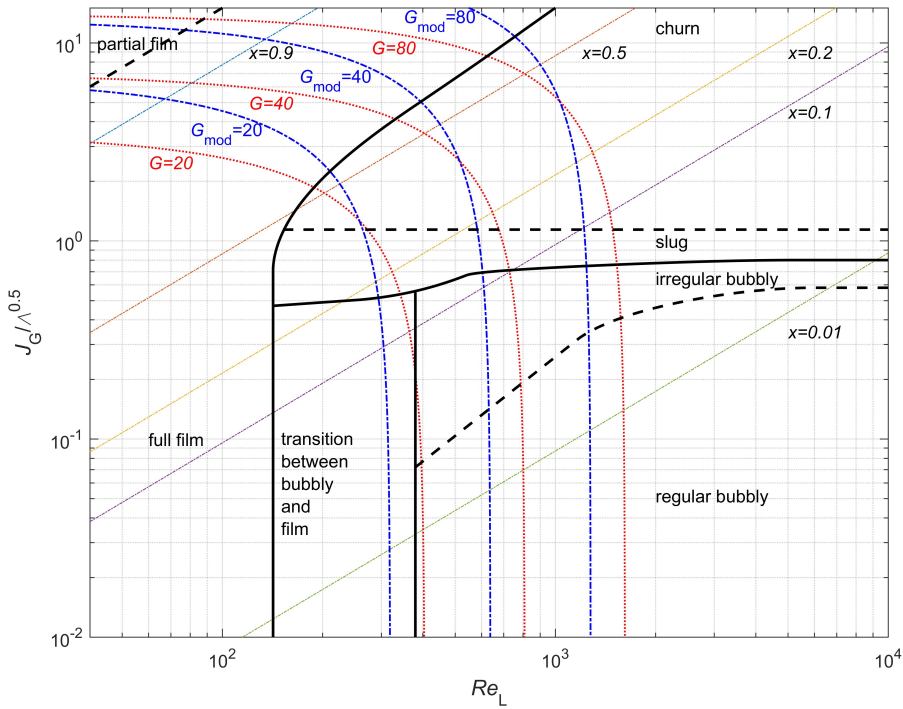
Figure 2.8: Simplified flow pattern map includes lines for constant overall mass flux and constant vapor quality of NH_3. The fluid properties of NH_3 are determined at the saturated pressure of 690 kPa. The original and modified condensation lines are presented.

a difference only at small mass flow rates. This discussion is limited to vertically downward flow. Injection nozzles were specially designed to promote uniform two-phase distribution across the channel width. The homogeneous void fraction model is chosen to predict the transition among primary flow patterns. Buscher's flow pattern model excludes phase change and mass transfer [101].

As shown in Table 2.1, Buscher [101] described and classified the flow patterns in detail. For the convenience of comparison in Figure 2.9, similar flow patterns are combined. *Regular and irregular bubbly flow* includes roundish bubbles, irregular blob-like bubbles and stagnant gas phase, whose transition is determined by the bubble breakage. The bubble breakage is modelled according to turbulent kinetic energy. Stagnant gas phase only happens for vertical downward flow. Big bubbles stagnate behind the contact points when the mass flow rates of liquid and vapor are very low. *Intermittent flow* is divided into bigger gas unit and heterogeneous flow. The large bubbles are formed by the mergence of
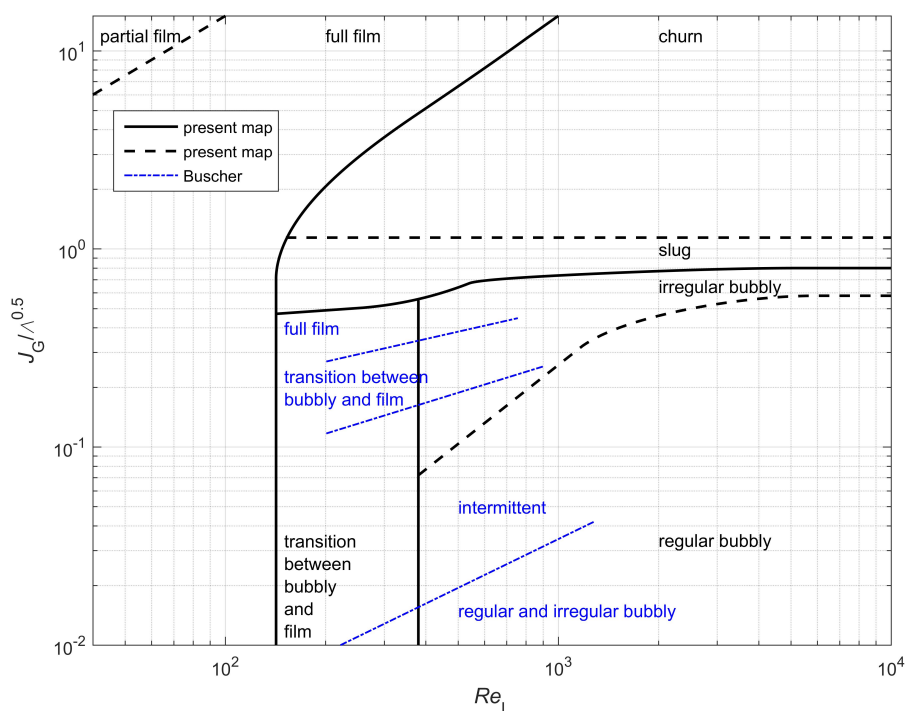
Figure 2.9: Comparison of flow pattern maps. The integrated map of PHEs is compared with the map of Buscher [101], which shows the separating lines among the primary flow patterns. This map applies for the vertically downward flow of air-water.

small bubbles. Buscher [101] differentiated intermittent flow from slug flow or churn flow. Slug flow and churn flow are considered to have periodical changing of gas-liquid across the whole channel width, which are not observed. The partial film flow termed by Buscher [101] is a combination of film flow and bubbly flow, which is referred to as *transition between bubbly and film* in the integrated map. *Full film flow* is also observed.

In Figure 2.9, the map of Buscher [101] covers the range of small and intermediate gas mass fluxes. The transition mainly depends on the gas mass flux. Regular and irregular bubbly flow takes place at small gas mass fluxes. It changes into intermittent flow with more gas. The flow is full film when gas is dominant. Two flow patterns happen simultaneously for the transition region between bubbly and film flow. The present map and Buscher's map have similar transition trends, but the separating lines diverge. The main reason for the divergence is the assumption of operating pressures, which determine the vapor density and
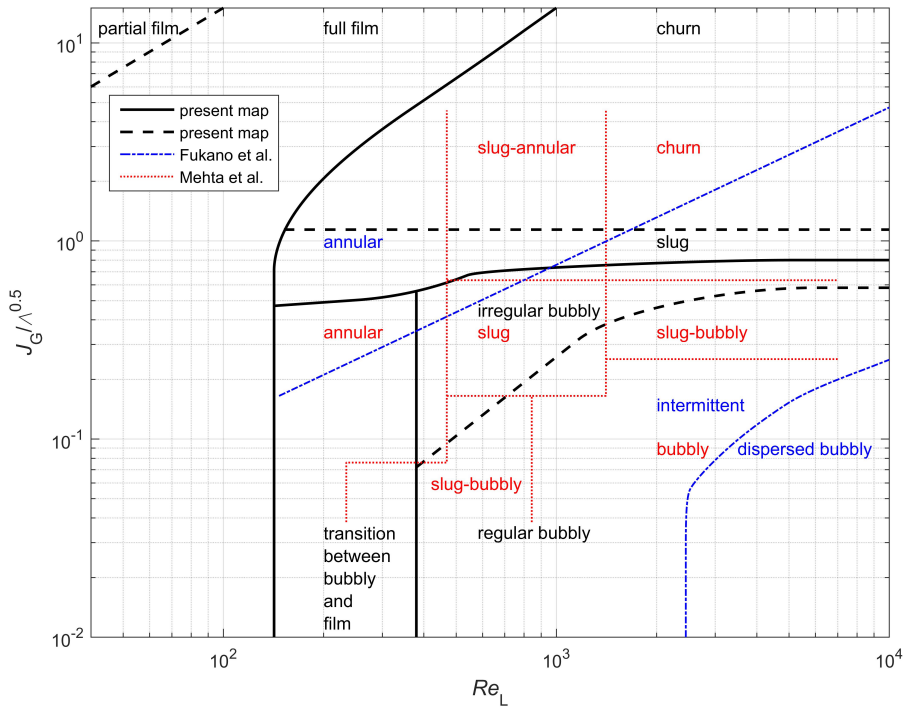
Figure 2.10: Comparison of flow pattern maps. The map of PHEs is compared with that of round mini tubes, which are applicable for the vertically downward flow of air-water [102, 103].

gas mass fluxes.

The present flow pattern map is also compared with round mini tubes whose diameters are close to the hydraulic diameters of PHEs. Flow patterns are the functions of geometric structure, flow direction and working fluid [38, 102, 103]. The maps of air/water downward flow within mini tubes have been chosen for comparison. Table 2.1 lists the reported flow patterns. Fukano and Kariyasaki [102] treated elongated bubbly, slug and churn flow as intermittent flow [110]. Mehta and Banerjee [103] introduced the transition flow patterns of slug-bubbly and slug-annular.

In Figure 2.10 presents the comparison. According to Fukano and Kariyasaki [102], the flow is annular at small liquid mass fluxes and large gas mass fluxes. It becomes dispersed bubbly with more liquid and less gas. Annular flow and dispersed bubbly flow are separated by a large region of intermittent flow.

In Figure 2.10, the separating lines from Mehta and Banerjee [103] are vertical and horizontal, which indicates that the transition happens at constant mass

fluxes of liquid or gas. The flow is annular at small liquid mass flux. Slug appears at intermediate two-phase mass fluxes, and changes into churn with increasing liquid and gas. Bubbly flow occurs at large amount of liquid and small amount of gas. Slug-bubbly and slug-annular describe the gradual transition of flow patterns.

The present flow pattern map agrees with the maps of tubes regarding the position of flow patterns and transition trends. It is film flow when gas phase is dominant, while bubbly flow appears when liquid dominates. When both phases are of equivalent amount, the flow is slug or churn. Churn is the chaotic version of slug. Nevertheless, the separating lines show poor agreement. This is partly attributed to the determination of flow patterns. For instance, Fukano and Kariyasaki [102] classified elongated bubbly flow as intermittent flow, which is similar to irregular bubbly flow in the present map. Moreover, the separating lines show a general shift. In the map of PHEs, the bubbly flow occupies a larger region. Corrugation structure breaks up gas volume and suppresses the coalescence of bubbles. For PHEs, the separating line of film flow shifts to the left, which corresponds to smaller liquid mass flux. Film flow is transformed into slug or churn flow when the waves on the film surface are large enough to connect to the film on the other side and to separate the gas in the center. Thus certain amount of liquid is required. The corrugation of PHEs promotes the development of waves and makes the transition happen with less liquid. PHEs enhance the stir and mix of two-phase flow.

UNCERTAINTY OF INTEGRATED FLOW PATTERN MAPS

In the integrated flow pattern maps, the separating lines diverge. In other words, different flow patterns overlap. The reasons are below:

Subjectivity of flow pattern determination: Flow patterns are determined by subjective observation. The description of flow patterns is not standard. For example, some researchers neglect the distinction between full film flow and partial film flow. Additionally, the separating lines between flow patterns divide the map sharply. In fact, flow patterns change gradually. Moreover, more than one flow pattern can take place simultaneously, and the flow is described using the dominant flow pattern.

Different structure of distributor: The distributors of PHEs affect the two-phase distribution at the inlet. The liquid and vapor can be homogeneous or separated depending on the mixing at the inlet area. The effect of distributor is more prominent at the inlet and weakens along the flow direction. Table 2.2 lists the structures of distributor used in the visualization experiments.

Unknown experimental conditions: Some geometric parameters of the plate are not clearly defined, such as the wavelength, Λ_{wave}. The pressure, P, and tem-
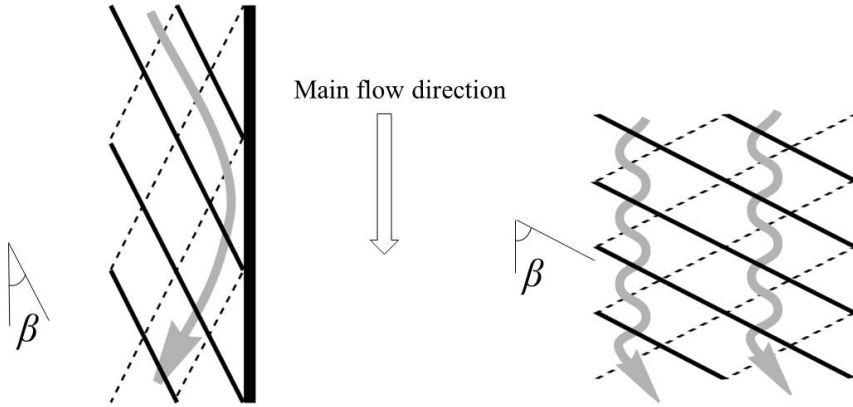
Figure 2.11: Flow paths in PHEs: (left) crossing flow at small chevron angle and (right) wavy longitudinal flow at large chevron angle. Referring to Winkelmann [19].

perature, T, are not reported in every study and are assumed in these cases.

2.4. FLOW PATHS

Flow paths define the flow direction in a channel. Figure 2.11 represents the two flow paths within the channel. The flow path is divided into crossing flow and wavy longitudinal flow. For crossing flow, the fluid is from one side of the plate to the other side. The fluid changes direction at the edge and moves along the adjacent plate. For wavy longitudinal flow, the fluid changes direction at each crossing point of two adjacent plates.

Flow paths depend on the PHE geometry. Crossing flow tends to occur in PHEs with small chevron angles, while wavy longitudinal flow arises with larger chevron angles [111]. Both paths usually exist simultaneously. The central spine of the plate acts as a boundary to flow, directing approaching flow along the furrows of the adjacent plate. The ratio of channel gap to corrugation wavelength, $d_{\mathrm{g}}/\Lambda_{\mathrm{wave}}$, also affects flow paths. A large ratio indicates deep grooves and intensifies crossing flow [112]. Martin [20] presented the detailed description of flow paths. Sarraf et al. [113] and Focke and Knibbe [111] confirmed that the two flow paths coexist.

Flow paths are the functions of mass fluxes. According to the numerical sim-

ulation of Sarraf et al. [113], crossing flow is dominant at small mass flux, and gradually changes into wavy longitudinal flow with increasing mass flux. On the contrary, Dović et al. [112] carried out visualization experiments and observed stronger crossing flow for small mass flux.

2.5. CONCLUSIONS

In this Chapter, a literature review of condensation mechanisms and flow patterns is presented for two-phase vertically downward flow in PHEs.

- The transition from gravity-controlled condensation to convective condensation is determined by mass flux and vapor quality. Fluid properties affect the transition mass flux. The influences of other factors are relatively small.

- Two integrated flow pattern maps are constructed making use of $Fr_{\text{TP}}/\Lambda^{0.5}$ versus $R_\nu^{0.5}$ and Re_{L} versus $J_{\text{G}}/\Lambda^{0.5}$. The second map better predicts the transition of flow patterns in PHEs, and agrees qualitatively with the maps for two-phase downward flow in mini-tubes.

3

ASSESSMENT OF CORRELATIONS FOR HFCS, HCS AND HFOS

In this Chapter, condensation correlations in PHEs are summarized. An experimental database are built. The correlations are assessed by comparison with the database. Heat transfer correlations are classified according to the basic forms, which are based on flow assumption and the determination of dominant influencing factors. Among the correlations selected for assessment, Longo et al. [60] and Kuo et al. [61] show the best predictive performance. Frictional pressure drop correlations are classified into homogeneous flow and separated flow. The selected correlations are assessed with the database, and the predictive performance is poor. A new frictional pressure drop correlation is developed and is cross validated.

3

3.1. SUMMARY OF EXPERIMENTAL DATABASE

To assess the correlations of heat transfer and frictional pressure drop in available literature, this Section develops an experimental database and gives a summary in Table 3.1. Only condensation experiments are involved, and the flow is always vertically downward. There are 2376 heat transfer data points and 1590 frictional pressure drop data points. The test sections are brazed plate heat exchangers (BPHEs) or gasketed plate heat exchangers (GPHEs). For circular shell and plate heat exchangers (SPHEs), the heat transfer and flow characteristics are different due to the circular plates [114]. Most data were determined by overall measurements, while local HTCs were also measured [19, 27, 72, 83, 89, 115]. The composition of the heat transfer database is further presented in Figure 3.1. The working fluids are pure refrigerants (HFCs, HCs, HFOs and CO_2), near-azeotropic mixtures (R410A and R404A) and one zeotropic mixture (R407C). R134a and R410A account for approximately half of the database. Data for NH_3 are not available. The classifications of chevron angles and hydraulic diameters are discrete, spanning the ranges of 25.7°-70° and 3.2-8.1 mm, respectively. The mass fluxes are from 0 to 150 kgm^{-2}s^{-1}, and mostly have small and intermediate values. The saturated temperatures are mostly concentrated in 20-40 °C. All the data below 0 °C are from the condensation of CO_2 [75]. The reduced pressures are nearly evenly distributed from 0 to 0.5.

Most inlet conditions are saturated two-phase or superheated vapor, while the outlets are saturated two-phase or subcooled liquid. Some of the inlets and outlets are controlled to be saturated vapor and saturated liquid, respectively [82, 83]. In terms of superheating and subcooling, some research assumed that single-phase regions for de-superheating or subcooling do not appear, and used the saturated temperature for data reduction [76, 80, 81, 84–86]. However, Hayes et al. [75, 116] predicted the areas of de-superheating and subcooling regions using single-phase HTCs, and calculated the HTCs and frictional pressure drop for two-phase region. Local measurements determined the starting and ending points of condensation directly, allowing the calculation of the local HTCs [19, 27, 72, 89, 115].

Table 3.1: Experimental database of heat transfer and frictional pressure drop for condensation in plate heat exchangers.

Study	PHE type &channel[a]	Refrigerants	$d_h/d_e/\beta/\Lambda_{wave}$[b] [mm/mm/-/mm]	L_p/W_p [mm/mm]	T_{sat} [°C]	P_{sat} [bar]	G [kgm^{-2}s^{-1}]	x [-]	Inlet/outlet[c]	$\dot{q}$ [kWm^{-2}]	N_{HT}/N_{PD}[d]
Sarraf [27, 91]	BPHE &1/1	R601	3.44/4.4/55°/6	476/111.4	36.5	1.0	9-29.8	0-1	SHV/SCL	20-66.5	144/24
Winkelmann [19]	GPHE &1/2[e]	R134a	4.65/6/25.7°/9.32 3.68/4.3/45°/7	400/160	28.2-39.9	7.3-10.1	63	0-1	SHV/TP	6.9-51	111/41
Han [87]	BPHE &2/3	R410A	3.68/4.3/55°/5.2 3.68/4.3/70°/4.9	478/115	20-30	14.4-18.9	13-34	0.15-0.9	TP/TP	4.7-5.3	58/58
Longo [77, 78, 84–86, 92–94, 117, 118]	BPHE &4/5	R236fa,R134a, R410A,R152a, R404A,R290, R600a,R1270, R1234ze(E), R1234ze(Z), R1234yf	3.23/4/65°/8	278/72	25-40	2.1-24.2	5-45	0-1	SHV/SCL TP/TP	5-25	823/528
Grabenstein [83]	GPHE&-	R134a	5.19/6/63°/11.4	368/408	11.1-23.7	4.3-6.4	30-74	0-1	SV/SL	8.5-17.6	42/19
Kabelac [115] Djordjevic [89] Shi [72]	GPHE &4/5	R134a	5.52/6.4/63.3°/12	1092/486	16.2-29	5.1-7.5	22-65	0-1	SHV/SCL	11.5-35	200/184
Hayes [75, 116]	BPHE &1/2	CO_2	3.33/4/30°/- 3.33/4/30°-63°/- 3.33/4/63°/-	444.5/127	-34.4-17.8	1.2-2.1	2-45	0-1	SHV/SCL	2.5-15.7	98/83
Yan [71] Kuo [61]	BPHE &1/1	R134a, R410A	3.38/5.8/60°/10	450/120	19.9-35.5	7-19.5	50-150	0.1-0.9	TP/TP	10-20	228/227
Mancin [76, 80, 81]	BPHE &1/2,3/4,2/3	R407C, R410A, R32	-/-/65°/-	487/247 325/94 526/111	36.5-41.8	16.1-22.7	15-40	0.01-1	SHV/TP	-	194/0
Thonon [82]	BPHE&-	R601, R600, R290	8.08/10/45°/-	300/300	26.9-70.3	1.5-18	2-18.5	0-1	SV/SL	-	52/0

3

3

Table 3.1 Continued: Experimental database of heat transfer and frictional pressure drop for condensation in plate heat exchangers.

Study	PHE type &channel[a]	Refrigerants	$d_h/d_e/\beta/A_{wave}$[b] [mm/mm/-/mm]	L_p/W_p [mm/mm]	T_{sat} [°C]	P_{sat} [bar]	G [kgm^{-2}s^{-1}]	x [-]	Inlet/ outlet[c]	$\dot{q}$ [kWm^{-2}]	N_{HT}/N_{PD}[d]
Zhang [66]	BPHE &7/8	R134a,R245fa, R1234ze(E), R1233zd(E)	3.4/4/65°/7	278/76	29.7-71.0	2.9-16.3	16-90	0-1	SHV/SCL	4.0-57.4	208/208
Soontarapiromsook [119]	GPHE[f] &1/1	R134a	-/5/65°/-	360/100	40-50	10.2-13.2	61-89	0.1-0.8	TP/TP	5-15	96/96
Shon [73]	BPHE&-	R1233zd(E)	3.32/3.88/60°/7.5	234/117	38.6-51.5	2-3	13.0-23.8	0.2-0.9	TP/TP	2.5-4.5	122/122
Overall range		HFCs,HCs, HFOs,CO$_2$	3.23-8.08/4-10/ 25.7°-70°/4.9-12	234-1092/ 72-486	-34.4 to 72.1	1.0-24.2	2-150	0-1		2.5-66.5	2376/ 1590

[a] Number at condensation side/ Number at cold water side.
[b] Underlined data are obtained by calculation.
[c] SHV: Superheated vapor; SCL: Subcooled liquid; TP: Two-phase; SV: Saturated vapor; SL: Saturated liquid.
[d] $N_{HT}/$: Number of heat transfer data points; $N_{PD}/$: Number of frictional pressure drop data points.
[e] These cold water channels are curved tubes.
[f] These test sections are composed of three kind of plates with different surface roughness.

In fact, at the superheated inlets, when the wall temperature is below the saturated temperature, the vapor starts to condensate without specific vapor regions [90, 120]. The heat flux is transferred for phase change and de-superheating simultaneously [91]. The appearance of vapor regions is determined by the superheating degree, mass fluxes and heat fluxes. The onset of condensation happens earlier when the mass flux is smaller and the heat flux is larger [121, 122]. When the condensers were connected with compressors, the superheating was significant, and the vapor regions were excluded by local measurements [72, 89, 115]. According to the infrared measurement of Sarraf et al. [91], the areas of de-superheating regions decreased for smaller superheating degrees. Based on calculation, Mancin et al. [76] claimed that the vapor region did not appear for their experimental data since the wall temperature was below the saturated temperature.

The subcooling at the outlet is less investigated. Since the liquid film is subcooled by the wall, vapor phase remains present when the bulk vapor quality becomes 0 [121]. The appearance of liquid regions is expected to depend on the subcooling degree. The experiments of Longo [84–86] had small subcooling degrees, and the author assumed that there was no liquid region. Zhang et al. [66] and Sarraf et al. [91] considered the de-superheating and saturated two-phase regions as a whole, but subtracted the subcooling region.

To compare the correlations with the experimental data in Sections 3.3 and 3.5, assumptions are made if operating parameters are not clearly reported in the original papers. In PHEs, the vapor quality usually changes largely because of the small mass fluxes and large heat transfer areas. The averaged vapor qualities of the inlet and outlet represent the operating conditions. In the papers, both actual heat transfer areas and projected heat transfer areas are used during data reduction. The present database conforms the HTCs to the values based on actual heat transfer areas, so the experimental data can be compared with the correlations. Some of the geometric parameters are missing and are calculated according to the equations in Section 1.2 [10]. Fluid properties are determined using Refprop 9.1 and updated files from NIST [39]. Most of the frictional pressure drop data are collected under the same operating conditions as for heat transfer.

3.2. HEAT TRANSFER CORRELATIONS

Section 2.2 reviews the condensation mechanisms in PHEs [10]. In gravity- controlled regime, according to Nusselt's theory, the thickness of the condensate film increases with mass flux and deteriorates the heat transfer. In fact, the waves at the condensate surface cannot be eliminated, and the HTCs may stay constant. Convective condensation is governed by interfacial shear, where HTCs mostly increase with mass flux. The transition of the condensation mechanisms is primar-

3

(a)

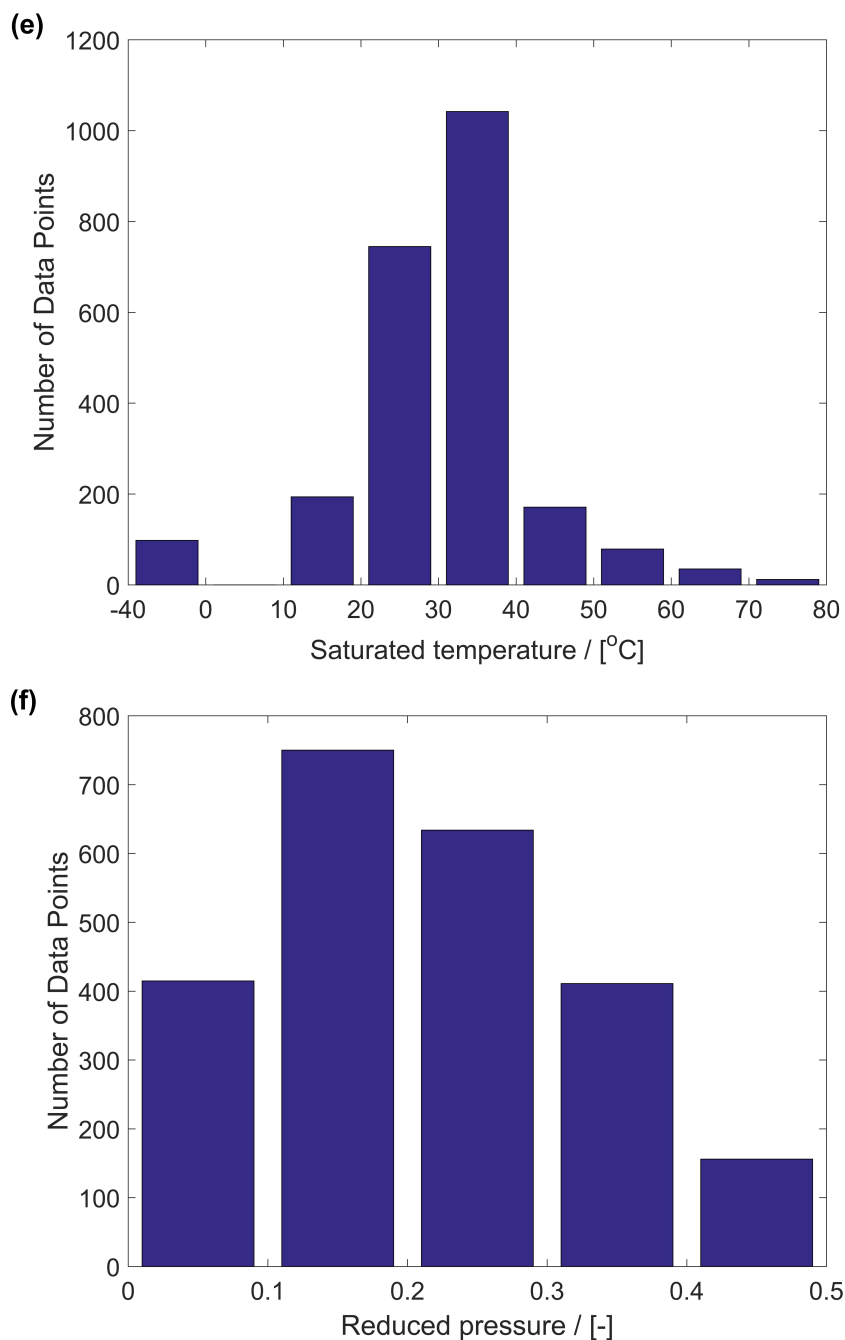
(b)

(c)

(d)

(e)

(f)
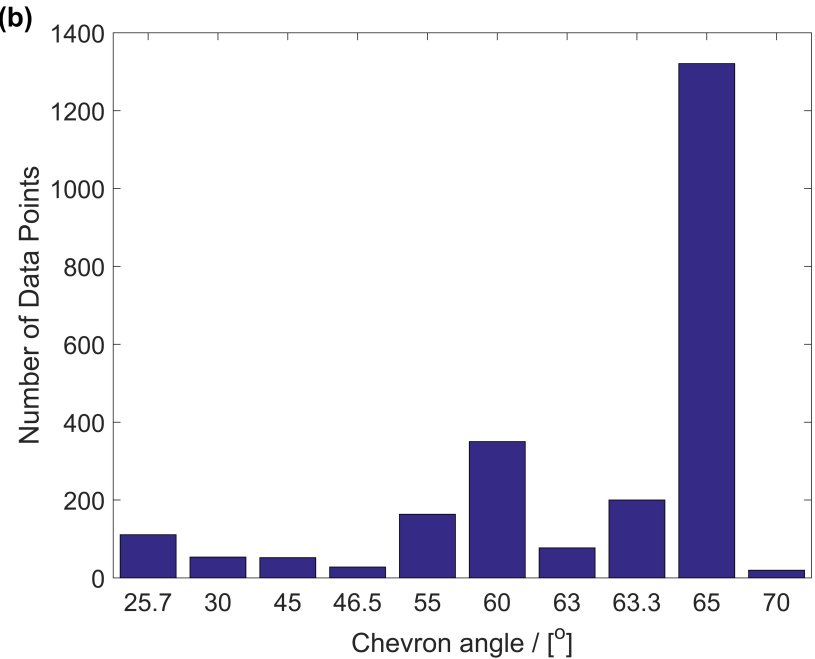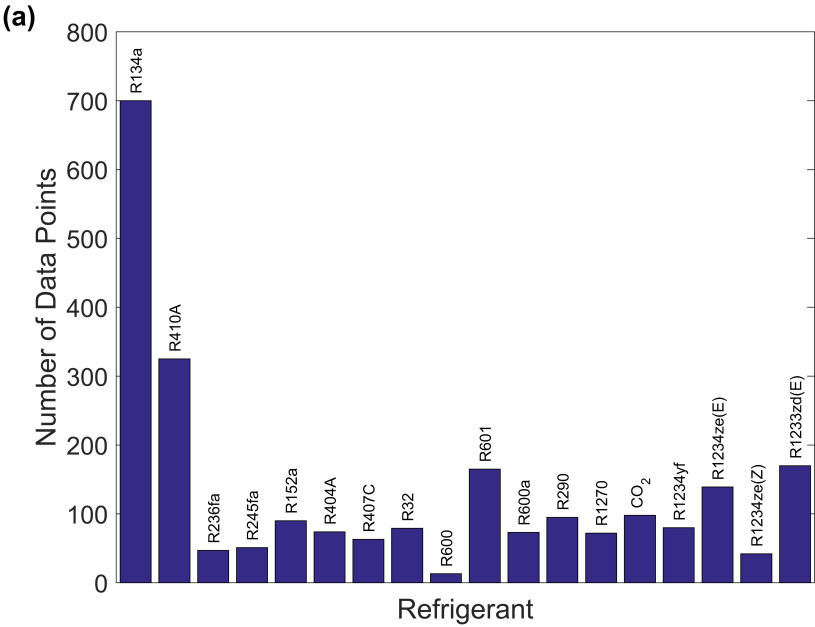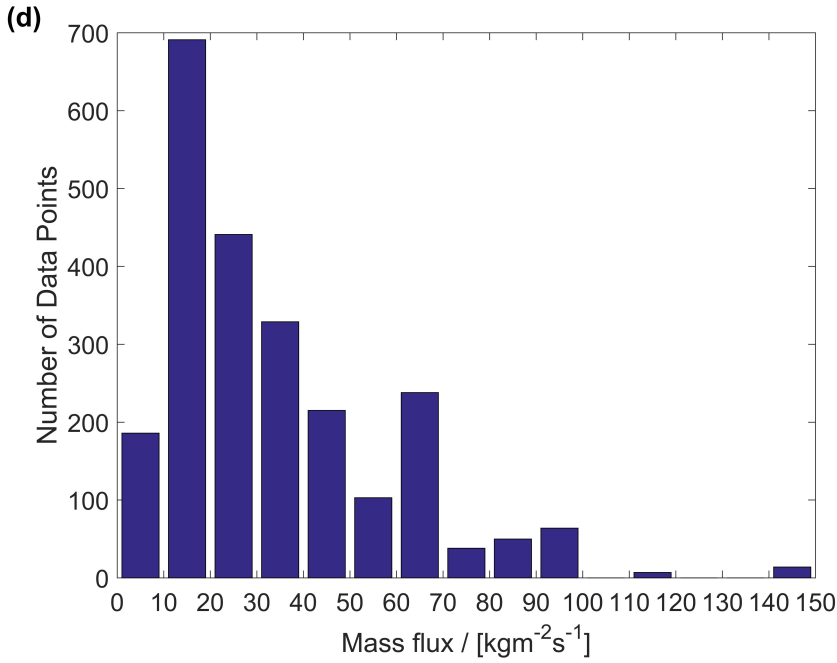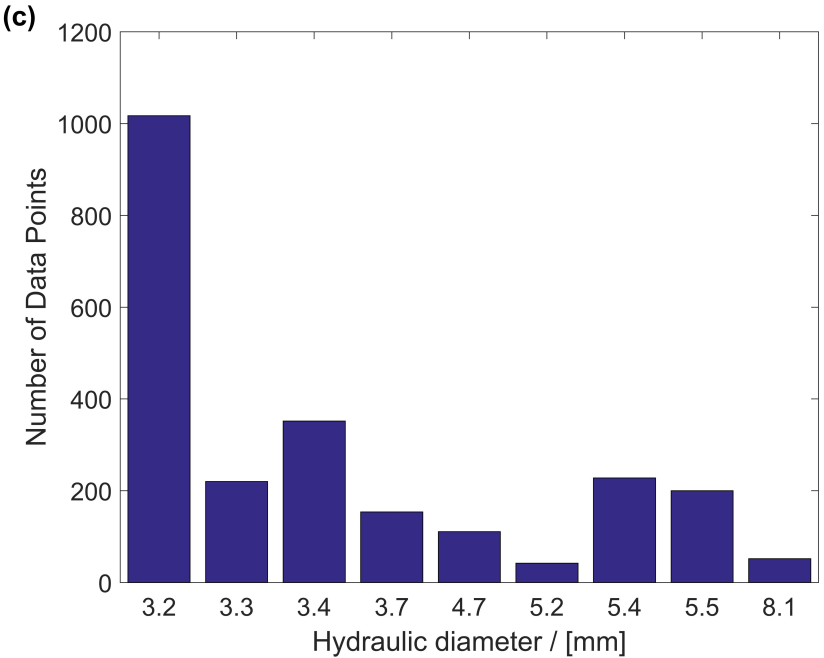
Figure 3.1: Composition of the heat transfer database divided by (a) Refrigerants, (b) Chevron angles, (c) Hydraulic diameters, (d) Mass fluxes, (e) Saturated temperatures, (f) Reduced pressures.

ily contributed by mass flux and vapor quality. Higher vapor quality enhances heat transfer for most refrigerants, except for steam [74].

Condensation heat transfer correlations from different groups are summarized in this Section, which calculate the HTCs based on actual heat transfer areas unless otherwise explained. All the correlations predict the averaged HTCs except for Shi et al. [72]. The correlations are classified by the basic forms that were firstly presented or widely accepted. Some of them are developed by modifying the basic forms.

3.2.1. NUSSELT CORRELATION

The classical Nusselt correlation shown in Eq. 3.1 was originally proposed for laminar film condensation on a vertical plate with saturated vapor [79]. Longo et al. [60] adopted Eq. 3.2 for saturated condensation in the gravity-controlled regime within PHEs. ϕ is the surface enlargement factor of the plates calculated by Eq. 1.2. Moreover, Webb [123] and Longo et al. [60] extended the application to superheated vapor by adding the de-superheating specific enthalpy change to the latent heat, as indicated in Eq. 3.3.

$$Nu_{gc} = \frac{\alpha_{gc} L_p}{\lambda_L} = 0.943 \left(\frac{g \rho_L (\rho_L - \rho_G) L_P^3 \Delta h_{LG}}{\mu_L \lambda_L \Delta T} \right)^{0.25} \tag{3.1}$$

$$Nu_{gc} = \frac{\alpha_{gc} L_p}{\lambda_L} = 0.943 \phi \left(\frac{g \rho_L (\rho_L - \rho_G) L_P^3 \Delta h_{LG}}{\mu_L \lambda_L \Delta T} \right)^{0.25} \tag{3.2}$$

$$\Delta h_{sup} = \Delta h_{LG} + c_{p,G} (T_{sup} - T_{sat}) \tag{3.3}$$

3.2.2. AKERS CORRELATION

Akers et al. [52] presented heat transfer correlations of convective condensation for horizontal tubes by using Re_{eq}, which is shown in Eq. 3.4. In Eq. 3.5, Longo et al. [60] calculated the HTCs of saturated vapor based on projected heat transfer areas, and ϕ is included. Yan et al. [71] chose different parameters as shown in Eq. 3.6. Zhang et al. [66] considered the influence of heat flux by including Bo in Eq. 3.7. Shon et al. [73] proposed Eq. 3.8 for R1233zd(E).

$$Nu_{cc} = \frac{\alpha_{cc} d_h}{\lambda_L} = a Re_{eq}^m Pr_L^n \tag{3.4}$$

$$Nu_{cc} = \frac{\alpha_{cc} d_h}{\lambda_L} = 1.875 \phi Re_{eq}^{0.445} Pr_L^{0.333} \tag{3.5}$$

$$Nu_{cc} = \frac{\alpha_{cc} d_h}{\lambda_L} = 4.118 Re_{eq}^{0.4} Pr_L^{0.333} \tag{3.6}$$

Table 3.2: Constants in Eqs. 3.11-3.12, depending on the plate combination.

Plates	a	m	k
30°/30°	0.325	0.62	0.4
30°/60°	3.2	0.46	0.3
60°/60°	3.77	0.43	0.14

$$Nu_{cc} = \frac{\alpha_{cc} d_h}{\lambda_L} = 4.3375 Re_{eq}^{0.5383} Pr_L^{0.333} Bo^{-0.3872} \tag{3.7}$$

$$Nu_{cc} = \frac{\alpha_{cc} d_h}{\lambda_L} = 2.337 Re_{eq}^{1.024} Re_{LO}^{-0.294} Pr_L^{0.333} Bo^{0.361} \tag{3.8}$$

Han et al. [87] added geometric parameters to the basic Akers correlation as shown in Eq. 3.9, where Λ_{wave} is the corrugation wave length and β is the chevron angle in the unit of radian. In Eq. 3.10, Soontarapiromsook et al. [119] considered the surface roughness of the plates, whose influence is relatively small compared with chevron angles.

$$Nu_{cc} = \frac{\alpha_{cc} d_h}{\lambda_L} = \left(11.22 \left(\frac{\Lambda_{wave}}{d_h}\right)^{-2.83} \beta^{-4.5}\right) Re_{eq}^{0.35 \left(\frac{\Lambda_{wave}}{d_h}\right)^{0.23} \beta^{1.48}} Pr_L^{0.333} \tag{3.9}$$

$$Nu_{cc} = \frac{\alpha_{cc} d_h}{\lambda_L} = 5.095 \times 10^{-6} Re_{eq}^{0.566} Pr_L^{9.753} \left(\frac{\delta}{d_h}\right)^{0.121} \tag{3.10}$$

The correlation of Würfel and Ostrowski [96] also involves geometry as shown in Eq. 3.11, and is based on projected heat transfer areas. This Reynolds number is calculated in Eq. 3.12. Both Nu_{cc} and Re_h depend on the chevron angles of neighbouring plates, which are listed in Table 3.2. The vapor quality in Eq. 3.12 is the averaged value and is 0.5 for complete condensation.

$$Nu_{cc} = \frac{\alpha_{cc} d_h}{\lambda_L} = a Re_h^m Pr_L^{0.333} \tag{3.11}$$

$$Re_h = \frac{G((1 - x_{av}) + x_{av}(\rho_L / \rho_G)^k) d_h}{\mu_L} \tag{3.12}$$

3.2.3. WEBB CORRELATION

In Eq. 3.13, Webb [123] proposed a theoretical model for superheated condensation inside tubes, and applied this model to the inside of enhanced tubes and outside of a bundle of tubes. The driving temperature difference is between saturated temperature and wall temperature. Both latent heat and sensible heat contribute to heat transfer. α_{sat} is the condensation HTC of saturated vapor; α_G is the single-phase HTC between superheated vapor and two-phase interface. $c_{p,G} \dot{q}_{LG}/\Delta h_{LG}$ accounts for the movement of the condensing vapor to the interface, which enhances single-phase heat transfer, where $\dot{q}_{LG}$ is the local heat flux due to phase change only. The temperature ratio term approaches zero as the superheating vanishes. Longo et al. [60] extended this model to PHEs.

$$\alpha_{sup} = \alpha_{sat} + \frac{T_{sup} - T_{sat}}{T_{sat} - T_{wall}}\left(\alpha_G + \frac{c_{p,G}\dot{q}_{LG}}{\Delta h_{LG}}\right) \tag{3.13}$$

3.2.4. SHAH CORRELATION

Shah [56] presented a correlation for condensation in horizontal, vertical, and inclined tubes by modifying the liquid only HTC, which is shown in Eqs. 3.14-3.15. Liquid only HTC, α_{LO}, assumes all the fluid is liquid, and in fact single-phase HTC applies. Vapor quality and reduced pressure were included. This correlation was verified by extensive experimental data, and was widely adopted to PHEs. Since the geometric structures of both condensation side and cooling water side are the same, the same correlation applies to α_{LO} and the HTC of cooling water. Kuo et al. [61] presented the single-phase heat transfer correlations of both refrigerant and cooling water, which are almost the same [71].

$$\alpha_{cc} = \alpha_{LO}\left((1-x)^{0.8} + \frac{3.8x^{0.76}(1-x)^{0.04}}{(P_{sat}/P_{cr})^{0.38}}\right) \tag{3.14}$$

$$\alpha_{LO} = 0.023 Re_{LO}^{0.8} Pr_L^{0.4} \frac{\lambda_L}{d_h} \tag{3.15}$$

Shi et al. [72] determined the parameters in Eq. 3.16 by minimizing the prediction errors, but α_{LO} is not given. Since this correlation is derived from local measurement data, it is considered to predict local HTC. Additionally, Eqs. 3.17-3.18 from Thonon and Bontemps [82] identify gravity-controlled condensation, and indicate the negative influence of mass flux. These correlations calculate the HTCs of projected heat transfer areas. Kuo et al. [61] proposed HTC in Eqs. 3.19-3.20, which is a function of Co_2 in Eq. 2.4, Fr_L in Eq. 2.18 and Bo in Eq. 2.28.

$$\alpha_{cc} = \alpha_{LO}\left((1-x)^{0.8} + \frac{3.00388x^{1.296}}{(1-x)^{0.496}(P_{sat}/P_{cr})^{0.648}}\right) \tag{3.16}$$

$$\alpha_{cc} = 1564 Re_{eq}^{-0.76} \alpha_{LO} \tag{3.17}$$

$$\alpha_{LO} = 0.347 Re_{LO}^{0.653} Pr_L^{0.33} \frac{\lambda_L}{d_h} \tag{3.18}$$

$$\alpha_{cc} = \alpha_{LO} \left(0.25 Co_2^{-0.45} Fr_L^{0.25} + 75 Bo^{0.75} \right) \tag{3.19}$$

$$\alpha_{LO} = 0.2092 Re_{LO}^{0.78} Pr_L^{0.333} \left(\frac{\mu_{av}}{\mu_{wall}} \right)^{0.14} \frac{\lambda_L}{d_h} \tag{3.20}$$

Palmer et al. [70] developed correlations for small mass flux and heat flux. Several refrigerants were tested containing two kinds of lubricants. The experimental data show different trends, which indicates the influence of lubricants. Two correlations were consequently proposed. R22, R290 and R290/R600a were lubricated with mineral oil, and the correlation is presented in Eqs. 3.21-3.22. α_L is liquid HTC and assumes that the liquid phase flows alone; ϕ_L is the two-phase friction multiplier; X_{tt} is the Lockhart-Martinelli parameter; Ga is calculated in Eq. 2.21. R32/R152a was lubricated with polyol ester oil and was calculated by Eq. 3.24.

$$\alpha_{cc} = \alpha_L^{0.387} \phi_L^{0.0824} Ga^{0.346} \left(\frac{P_{sat}}{P_{cr}} \right)^{1.5} \left(-\log_{10} \frac{P_{sat}}{P_{cr}} \right)^{1.5} \left(\frac{\lambda_L}{d_h} \right)^{0.613} \tag{3.21}$$

$$\alpha_L = 0.16 Re_L^{0.89} Pr_L^{0.3} \frac{\lambda_L}{d_h} \tag{3.22}$$

$$\phi_L = \left(1 + \frac{12}{X_{tt}} + \frac{1}{X_{tt}^2} \right)^{0.5} \tag{3.23}$$

$$\alpha_{cc} = \alpha_L^{0.298} Ga^{0.346} \left(\frac{P_{sat}}{P_{cr}} \right)^{1.5} \left(-\log_{10} \frac{P_{sat}}{P_{cr}} \right)^{1.5} \left(\frac{\lambda_L}{d_h} \right)^{0.702} \tag{3.24}$$

3.2.5. Mancin correlation
Mancin et al. [81] proposed to combine gravity-controlled condensation and convective condensation in Eq. 3.25. Nusselt correlation in Eq. 3.1 was used for gravity-controlled condensation. The correlation from Cavallini et al. [68] was chosen for convective condensation in Eq. 3.26, which also includes α_{LO}.

$$\alpha_c = \left(\alpha_{gc}^2 + \alpha_{cc}^2 \right)^{0.5} \tag{3.25}$$

$$\alpha_{cc} = \alpha_{LO} \left(1 + 1.128 x^{0.817} \left(\frac{\rho_L}{\rho_G} \right)^{0.3685} \left(\frac{\mu_L}{\mu_G} \right)^{0.2363} \left(1 - \frac{\mu_G}{\mu_L} \right)^{2.144} Pr_L^{-0.1} \right) \quad (3.26)$$

In a later paper, Mancin et al. [76] improved this correlation by considering the transition between gravity-controlled condensation (temperature driving force dependent regime) and convective condensation (temperature driving force independent regime) proposed by Cavallini et al. [68]. The transition is determined by non-dimensional gas velocity, J_G, in Eq. 2.20.

$$\begin{cases} J_G \leq J_{G,low}, & \text{gravity} - \text{controlled condensation} \\ J_{G,low} < J_G < J_{G,high}, & \text{transition regime} \\ J_G \geq J_{G,high}, & \text{convective condensation} \end{cases} \quad (3.27)$$

$$J_{G,low} = 0.89 - 0.93 e^{-0.087 \left(\left(\frac{1}{x} - 1 \right)^{0.8} \left(\frac{P_{sat}}{P_{cr}} \right)^{0.4} \right)^{-1.17}} \quad (3.28)$$

$$J_{G,high} = \left(\left(\frac{7.5}{4.3 \left(\left(\frac{\mu_L}{\mu_G} \right)^{0.1} \left(\frac{\rho_G}{\rho_L} \right)^{0.5} \left(\frac{1-x}{x} \right)^{0.9} \right)^{1.11} + 1} \right)^{-3} + 2.6^{-3} \right)^{-0.333} \quad (3.29)$$

Eq. 3.30 gives the HTC of gravity-controlled condensation, while Eq. 3.26 calculates convective condensation. Eq. 3.31 is applied in the transition regime.

$$Nu_{gc} = 1.1316 \left(\frac{g \rho_L (\rho_L - \rho_G) L_P^3 \Delta h_{LG}}{\mu_L \lambda_L \Delta T} \right)^{0.25} \quad (3.30)$$

$$\alpha_c = \alpha_{gc} + \frac{J_G - J_{G,low}}{J_{G,high} - J_{G,low}} \left(\alpha_{cc} - \alpha_{gc} \right) \quad (3.31)$$

3.2.6. WANG CORRELATION

In Eq. 3.32, Wang and Zhao [74] identified the subcooling of condensate. During condensation, the liquid film is considered to have lower temperature than the saturated temperature. The density ratio indicates the influence of reduced pressure. Re_L is defined in Eq. 2.12. Instead of the averaged vapor quality, the vapor quality of the PHE outlet is used here, which shows the feature of partial condensation. Ja is calculated in Eq. 2.30. Jokar et al. [65] added more property parameters in Eq. 3.33.

Table 3.3: Constants and application range of Eq. 3.34, depending on the plate combinations.

Plates	C1	C2	C3	C4	C5	C6	C7	Re_{LO}
30°/30°	0.37	0.706	0.35	-0.91	0.16	0.032	1.18	67-1276
30°/63°	0.16	0.727	0.35	-0.90	0.17	0.147	1.00	164-1233
63°/63°	0.11	0.771	0.35	-0.92	0.12	0.0105	2.00	129-1156

$$Nu_{cc} = \frac{\alpha_{cc}d_h}{\lambda_L} = 0.00115 \left(\frac{Re_L}{Ja}\right)^{0.983} Pr_L^{0.333} \left(\frac{\rho_L}{\rho_G}\right)^{0.248} \tag{3.32}$$

$$Nu_{cc} = \frac{\alpha_{cc}d_h}{\lambda_L} =$$
$$3.371 Re_L^{0.55} Pr_L^{0.3} Ja^{-1.05} \left(\frac{G^2}{\rho_L^2 c_{p,L}(T_{sat}-T_{wall})}\right)^{0.25} \left(\frac{\rho_L\sigma}{\mu_L G}\right)^{0.05} \left(\frac{\rho_L}{\rho_L-\rho_G}\right)^2 \tag{3.33}$$

Hayes et al. [75] presented Eq. 3.34 and Table 3.3, which are derived from the complete condensation of CO_2 by excluding the single-phase areas of de-superheating and subcooling. The tested PHEs had three combinations of chevron angles.

$$Nu_{cc} = \frac{\alpha_{cc}d_h}{\lambda_L} = C1 Re_{LO}^{C2} Pr_L^{C3} Ja^{C4} \left(\frac{G^2}{\rho_L^2 c_{p,L}(T_{sat}-T_{wall})}\right)^{C5} \left(\frac{\rho_L\sigma}{\mu_L G}\right)^{C6} \left(\frac{\rho_L}{\rho_L-\rho_G}\right)^{C7} \tag{3.34}$$

3.2.7. WINKELMANN CORRELATION

Winkelmann [19] claimed that vapor quality is more influential than mass flux. According to Eq. 3.35, the Convection number, Co, as shown in Eq. 2.3, is more relevant than Re_{eq}.

$$Nu_{cc} = \frac{\alpha_{cc}d_h}{\lambda_L} = 94 Co^{-0.46} Pr_L^{0.333} \quad 0.07 < Co < 0.28 \tag{3.35}$$

3.2.8. CORRELATION FOR MIXTURES

To predict mixture condensation, Thonon and Bontemps [82] referred to the correlation of Silver [124] and Bell and Ghaly [125] in Eq. 3.36. Molecular diffusion in the vapor phase induces mass transfer resistance, and deteriorates the heat transfer. The mass transfer resistance is assumed to be proportional to the heat transfer resistance of the vapor, α_G^{-1}, and to the derivative of temperature with enthalpy, dT/dh.

$$\alpha_{c,mix} = \left(\alpha_{c,pure}^{-1} + x c_{p,G} \frac{dT}{dh} \alpha_G^{-1} \right)^{-1} \tag{3.36}$$

3.3. ASSESSMENT OF HEAT TRANSFER CORRELATIONS

Generally, the basic forms of heat transfer correlations only include the dominant parameters. To improve the accuracy in certain operating conditions, the modified forms change the indexes and multipliers, or involve the parameters of fluid property and geometry. But the modifications may not be applicable beyond the tested range. In this Section, eight correlations are compared with the experimental database introduced in Section 3.1, and are assessed in wider ranges. These correlations are representative for the different basic forms. The correlations of Longo et al. [60] and Thonon and Bontemps [82] are derived from projected heat transfer areas, and are converted to the HTCs of actual heat transfer areas for comparison. Several assumptions are made to supplement the missing information:

- For the experimental data of superheated inlet and subcooled outlet, some researchers subtracted the single-phase areas for de-superheating and subcooling [19, 27, 72, 75, 89, 115, 116], while others assumed no single-phase region when the superheating degree or subcooling degree is small [76, 80, 81, 84–86]. In these cases, the vapor qualities are taken as 1 or 0. The averaged vapor quality of 0.5 and saturated temperature are inputted to calculate the HTC.

- The surface enlargement factor, ϕ, is calculated from channel gap and corrugation wavelength. The hydraulic diameter, d_h, is the ratio of the equivalent diameter, d_e to ϕ. The details are presented in Section 1.2.

- The heat flux varies with mass flux, and is used to calculate Bo. When not specified, the heat flux is determined by the enthalpy change and heat transfer area.

- The temperature difference between the condensate and wall is reported in Mancin et al. [76, 80, 81] and Hayes et al. [75]. It is calculated from the heat flux and experimental HTC when not specified. This temperature difference is involved in the HTCs for gravity-controlled condensation and Jakob number, Ja.

Figure 3.2(a) assesses the correlation of Longo et al. [60], Eq. 3.5. It predicts 93.0% of the experimental data within ±50%, which is the best prediction among the selected correlations. High HTCs, which correspond to large mass

fluxes and high vapor qualities, are slightly under-predicted. This correlation is derived from the experimental data of complete condensation, and the mass fluxes are less than 45 $kgm^{-2}s^{-1}$. The experimental data of CO_2 [75] are over-predicted since the fluid properties are significantly different from other refrigerants. The thermal conductivity of liquid CO_2 is large, and the reduced pressure is high during condensation. This over-prediction is more significant for small HTCs.

In Figure 3.2(b), the prediction of Yan et al. [71] is similar to Longo et al. [60], but low HTCs, which correspond to small mass fluxes, are over-predicted. This correlation predicts more than half of the experimental data within ±50%. It has been developed from partial condensation in the range of 60-120 $kgm^{-2}s^{-1}$ and for the averaged vapor qualities of 0.1-0.9.

In Figure 3.2(c), the prediction of Han et al. [87] is lower than a large portion of the experimental data, and shows sensitivity to geometric parameters. As shown in Table 3.1, the experimental data of Han et al. [87] were obtained from three geometries, where d_h and Λ_{wave} are smaller than for most other papers. This correlation seems to be only applicable to the tested geometric parameters.

In Figure 3.2(d), the correlation of Kuo et al. [61] slightly under-predicts the experimental data. 88.4% of the experimental data are predicted within ±50%, which is the second best. This correlation involves the influence of heat flux by using Bo, and the heat flux is in the range of 10000-20000 Wm^{-2}. The under-prediction of Thonon and Bontemps [82] and Han et al. [87] is noticeable as these experimental data had smaller heat fluxes.

In Figure 3.2(e), the correlation of Thonon and Bontemps [82] predicts their own data accurately, but the predicted values decrease with the experimental data from other researchers. This correlation is derived from the experimental data of small mass fluxes (around 2-20 $kgm^{-2}s^{-1}$). According to this correlation, the HTCs decrease with larger mass fluxes for gravity-controlled condensation. This sensitivity is over-estimated. It is not suitable for convective condensation, especially at large mass fluxes.

In Figure 3.2(f), the correlation of Palmer et al. [70] over-predicts most of the experimental data. The working fluid of this correlation is the mixture of several refrigerants and oil. Moreover, it is developed for small mass fluxes.

In Figure 3.2(g), the correlation of Mancin et al. [81] combines gravity- controlled condensation and convective condensation using an asymptotic power-law. This correlation was recommended by Sarraf et al. [27]. Sarraf et al. [27] used an infrared camera to measure the end plates temperature of working fluid side and cold water side. The temperature difference between the plate and fluid is assumed to be negligible, and the plate temperature represents the fluid. These local HTCs span a large range and cannot be predicted by other correlations. Sar-

raf et al. [27] argued that the local HTCs based on infrared measurement are higher than the overall HTCs. Constant heat flux is assumed to determine the overall HTCs, but this assumption can hardly be reasonable.
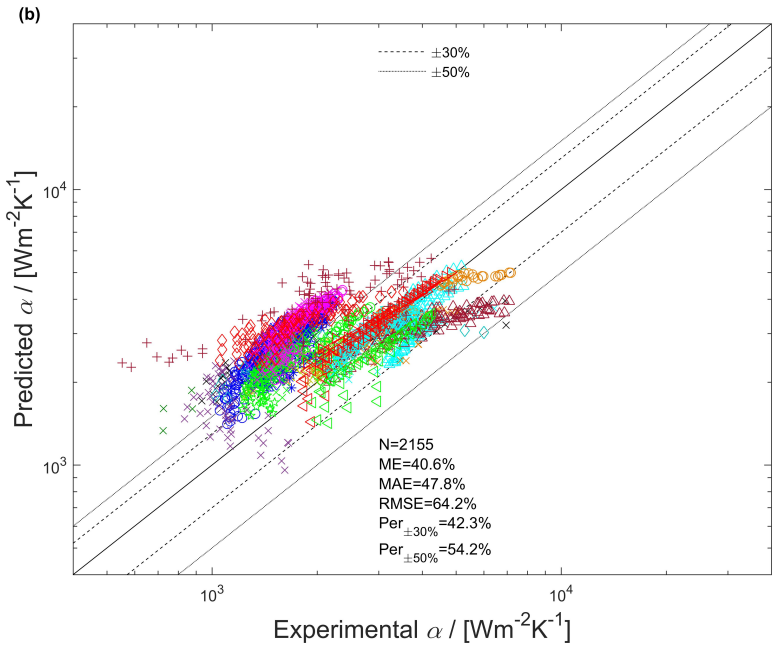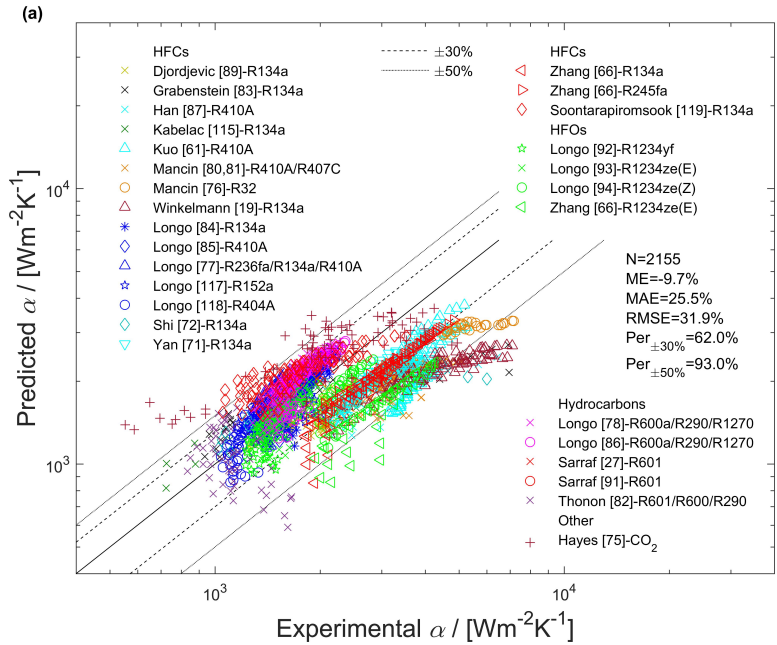
In Figure 3.2(h), the correlation of Hayes et al. [75] is the only one proposed for CO_2, but over-predicts most other refrigerants. This correlation excludes the areas of de-superheating and subcooling regions during data reduction, without quantifying the influence of vapor qualities. It is developed using dimensional analysis. The applicability seems to be limited to the complete condensation of CO_2.
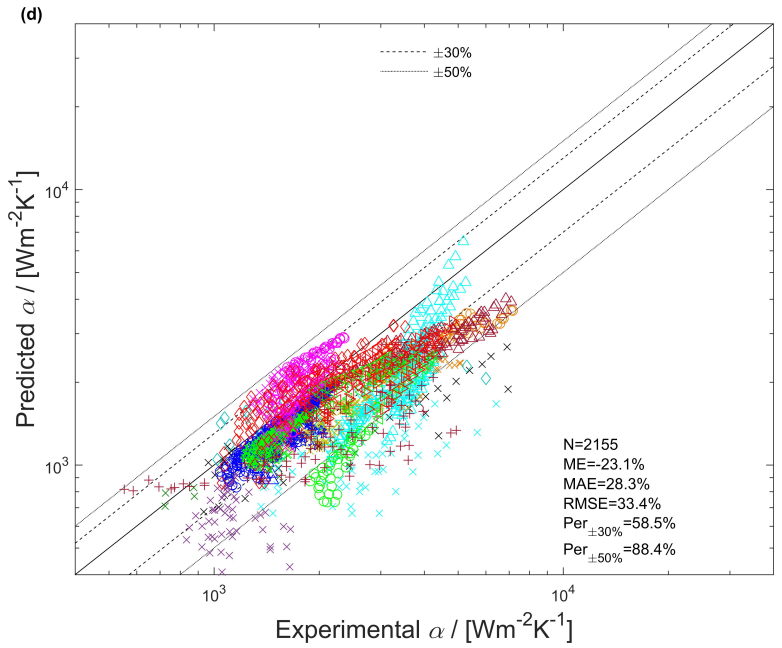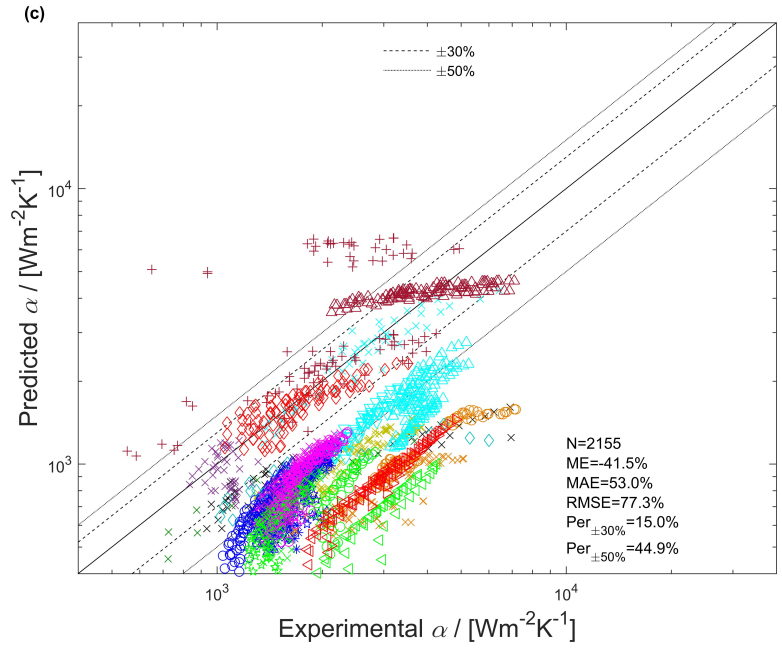
The correlation of Longo et al. [60] is derived from the complete condensation of several refrigerants as shown in Table 3.1. The mass fluxes are 5 - 45 $kgm^{-2}s^{-1}$. This correlation can be expanded to the ranges described in Table 3.1, but is less suitable for CO_2. NH_3 is not included in the experimental database and requires further investigation. During the condensation in PHEs, gravity-controlled condensation takes place at small mass fluxes and low vapor qualities [27, 77, 78, 80–82]. Eq. 3.5 is originally developed for convective condensation, and predicts the HTCs of gravity-controlled condensation within ±50%.
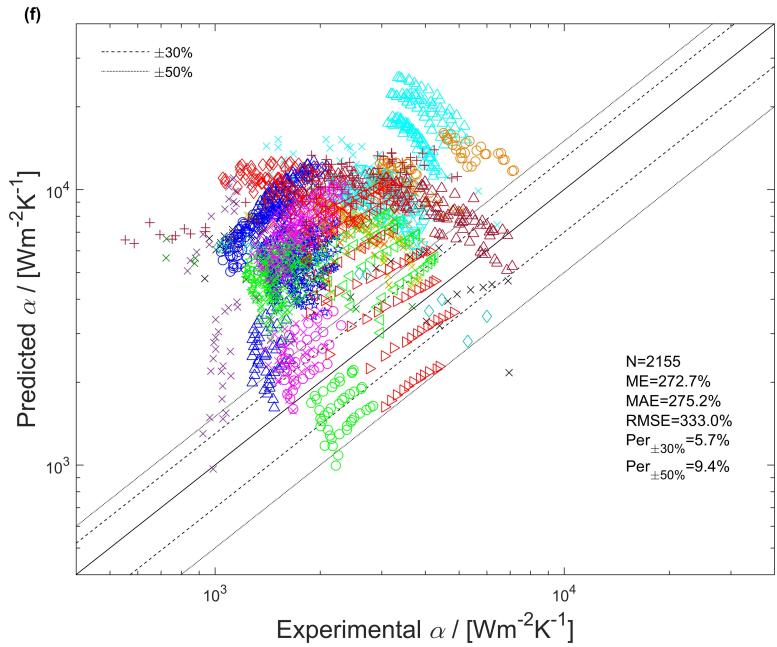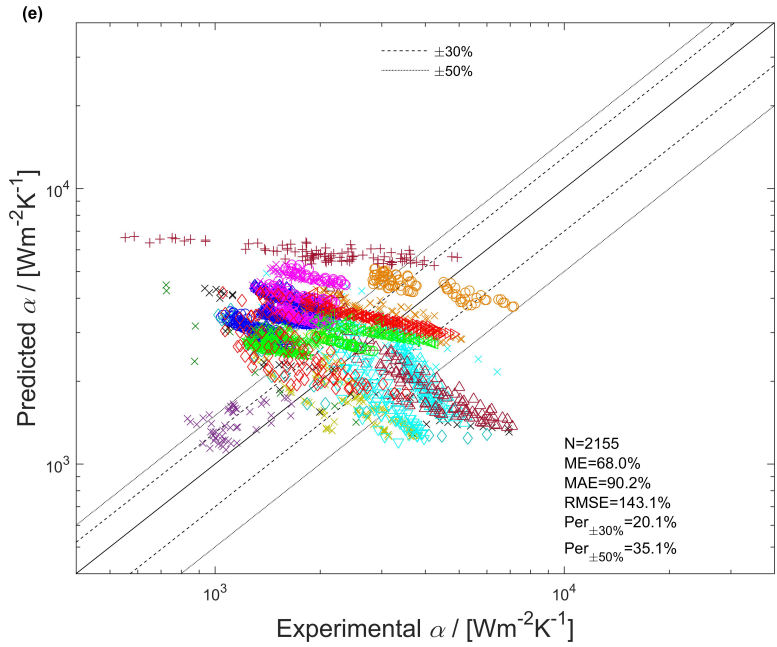
Condensation mechanisms are the function of vapor qualities, whose influence is remarkable during partial condensation. The condensation mechanisms are determined by the two-phase flow distribution and interaction at the interface. The correlation of Longo et al. [60] involves Re_{eq}, and assumes homogeneous two-phase flow. The equivalent fluid properties are considered as a combination of liquid and vapor [52]. The correlation of Kuo et al. [61] assumes separated flow, and also shows satisfactory prediction. This correlation calculates the liquid only HTCs, and considers the heat transfer enhancement contributed by vapor flow and heat flux [56, 63]. The knowledge of flow patterns helps to develop a mechanistic model for condensation within PHEs [68, 106, 126].

3.4. FRICTIONAL PRESSURE DROP CORRELATIONS

Section 2.2 summarized the influencing factors of frictional pressure drop [10]. The contributing factors of heat transfer generally increase frictional pressure drop. Despite the condensation mechanisms, frictional pressure drop increases with mass flux and vapor quality monotonically. The other influencing factors are plate geometry, condensation pressure, superheating and heat flux. This Section presents frictional pressure drop correlations. The two-phase frictional pressure drop correlations are suggested to be classified into three types [21]. Two-phase Fanning friction factors assume homogeneous flow, while Lockhart-Martinelli's model is based on separated flow. Kinetic energy model is originally proposed by modifying the homogeneous void fraction model. Lockhart-Martinelli model and Kinetic energy model were first developed for adiabatic

3

(a)

HFCs
× Djordjevic [89]-R134a
× Grabenstein [83]-R134a
× Han [87]-R410A
× Kabelac [115]-R134a
△ Kuo [61]-R410A
× Mancin [80,81]-R410A/R407C
○ Mancin [76]-R32
△ Winkelmann [19]-R134a
✳ Longo [84]-R134a
◇ Longo [85]-R410A
△ Longo [77]-R236fa/R134a/R410A
☆ Longo [117]-R152a
○ Longo [118]-R404A
◇ Shi [72]-R134a
▽ Yan [71]-R134a

-- - ±30%
···· ±50%

HFCs
◁ Zhang [66]-R134a
▷ Zhang [66]-R245fa
◇ Soontarapiromsook [119]-R134a
HFOs
✩ Longo [92]-R1234yf
× Longo [93]-R1234ze(E)
○ Longo [94]-R1234ze(Z)
◁ Zhang [66]-R1234ze(E)

N=2155
ME=-9.7%
MAE=25.5%
RMSE=31.9%
Per$_{\pm 30\%}$=62.0%
Per$_{\pm 50\%}$=93.0%

Hydrocarbons
× Longo [78]-R600a/R290/R1270
○ Longo [86]-R600a/R290/R1270
× Sarraf [27]-R601
○ Sarraf [91]-R601
× Thonon [82]-R601/R600/R290
Other
+ Hayes [75]-CO_2

(b)

-- - ±30%
···· ±50%

N=2155
ME=40.6%
MAE=47.8%
RMSE=64.2%
Per$_{\pm 30\%}$=42.3%
Per$_{\pm 50\%}$=54.2%

(c)

N=2155
ME=-41.5%
MAE=53.0%
RMSE=77.3%
$Per_{\pm30\%}=15.0\%$
$Per_{\pm50\%}=44.9\%$

(d)

N=2155
ME=-23.1%
MAE=28.3%
RMSE=33.4%
$Per_{\pm30\%}=58.5\%$
$Per_{\pm50\%}=88.4\%$

3

(e)

N=2155
ME=68.0%
MAE=90.2%
RMSE=143.1%
$Per_{\pm 30\%}$=20.1%
$Per_{\pm 50\%}$=35.1%

(f)

N=2155
ME=272.7%
MAE=275.2%
RMSE=333.0%
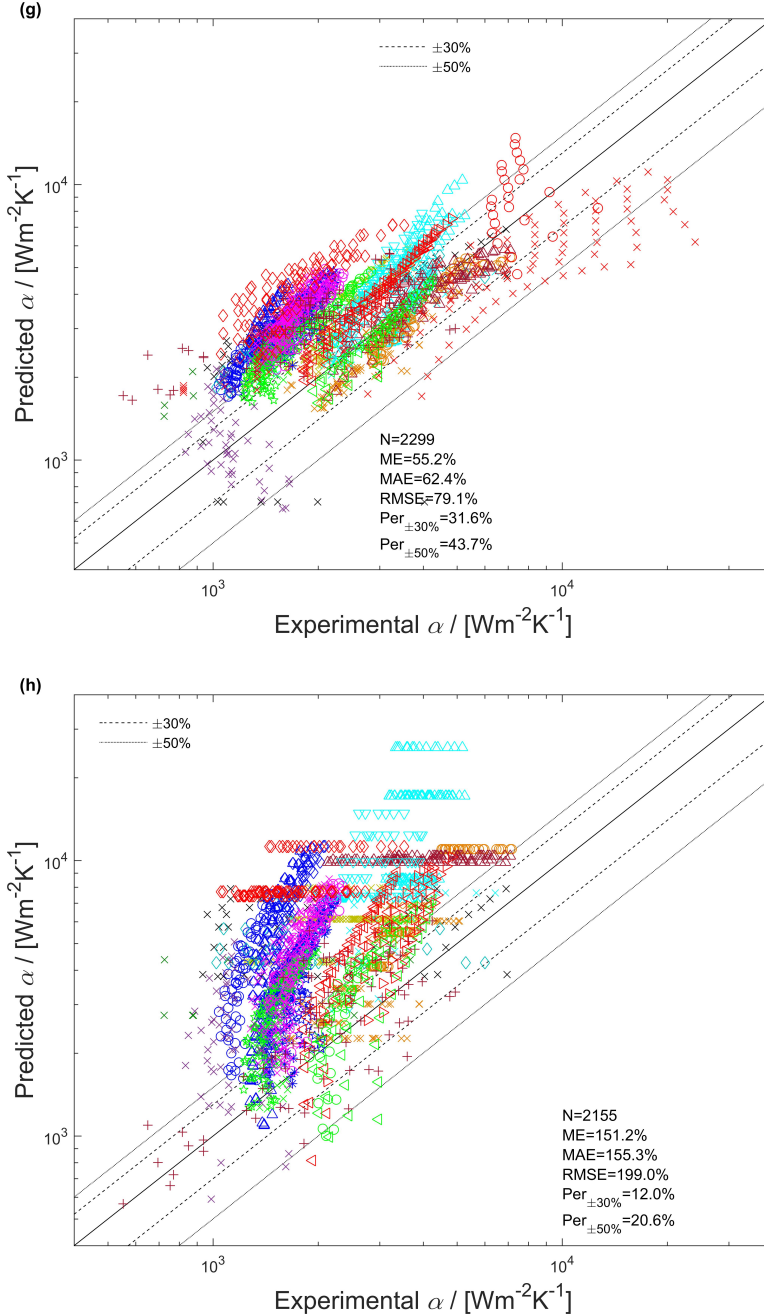$Per_{\pm 30\%}$=5.7%
$Per_{\pm 50\%}$=9.4%

3

Figure 3.2: Comparison of heat transfer correlations with experimental data: (a) Longo et al. [60], (b) Yan et al. [71], (c) Han et al. [87], (d) Kuo et al. [61], (e) Thonon and Bontemps [82], (f) Palmer et al. [70], (g) Mancin et al. [81], (h) Hayes et al. [75]. Number of experimental data (N); Mean error (ME): $\frac{1}{n}\sum_1^n \frac{\alpha_{pre}-\alpha_{exp}}{\alpha_{exp}}$; Mean absolute error (MAE): $\frac{1}{n}\sum_1^n \frac{|\alpha_{pre}-\alpha_{exp}|}{\alpha_{exp}}$; Root mean squared error (RMSE): $\sqrt{\frac{1}{n}\sum_1^n \left(\frac{\alpha_{pre}-\alpha_{exp}}{\alpha_{exp}}\right)^2}$; $Per_{\pm30\%}$: Percentage of experimental data within ±30%; $Per_{\pm50\%}$: Percentage of experimental data within ±50%.

flow and later extended to condensation.

3.4.1. TWO-PHASE FANNING FRICTION FACTOR

Two-phase Fanning friction factors assume homogeneous flow, and the two-phase flow is regarded as single equivalent fluid flow. The frictional pressure drop is calculated similarly to single-phase in Eq. 3.37.

$$\Delta P_{TP} = 2 f_{TP} \frac{G^2}{\rho_{av}} \frac{L_p}{d_h} \tag{3.37}$$

Kuo et al. [61] presented a correlation including Re_{eq} and Bo in Eq. 3.38. The correlation of Yan et al. [71] in Eq. 3.39 is similar, but under-predicts the experimental database significantly. The predictions of Eq. 3.40 from Shi et al. [72] are also lower than the experimental data. In Eq. 3.41, Zhang et al. [66] used We_{homo} to involve surface tension. Shon et al. [73] proposed a correlation as given in Eq. 3.42.

$$f_{TP} = 21500 Re_{eq}^{-1.14} Bo^{-0.085} \tag{3.38}$$

$$f_{TP} = 94.75 Re_{eq}^{-0.0467} Re_{LO}^{-0.4} Bo^{0.5} \left(\frac{P_{sat}}{P_{cr}} \right)^{0.8} \tag{3.39}$$

$$f_{TP} = 350188 Re_{eq}^{-2.19} Bo_{eq}^{-0.23} \tag{3.40}$$

$$f_{TP} = 0.0146 Re_{eq}^{0.9814} We_{homo}^{-1.0064} \tag{3.41}$$

$$f_{TP} = 1261.067 Re_{eq}^{-0.411} Re_{LO}^{-0.57} \tag{3.42}$$

Han et al. [87] considered geometric parameters in Eq. 3.43. Accordingly, frictional pressure drop increases with chevron angles dramatically. Soontarapiromsook et al. [119] investigated the surface roughness of the plates and proposed Eq. 3.44. In Eq. 3.45, Jokar et al. [65] used the modified Reynolds number, Re_{mod}, calculated from the averaged dynamic viscosity in Eq. 2.14.

$$f_{TP} = 3521.1 \left(\frac{\Lambda_{wave}}{d_h} \right)^{4.17} \beta^{-7.75} Re_{eq}^{-1.024 \left(\frac{\Lambda_{wave}}{d_h} \right)^{0.0925}} \beta^{-1.3} \tag{3.43}$$

$$f_{TP} = 2671.743 Re_{eq}^{-0.818} \left(\frac{\delta}{d_h} \right)^{0.065} \tag{3.44}$$

$$f_{TP} = 2.139 \times 10^7 Re_{mod}^{-1.6} \quad 960 < Re_{mod} < 4160 \tag{3.45}$$

Table 3.4: Constants of Eq. 3.46, depending on the plate combinations.

Plates	$C1$	$C2$
30°/30°	1837.4	-0.817
30°/63°	10.65	0
63°/63°	1221.3	-0.815

3

Hayes et al. [116] tested CO_2 condensation in the same PHEs as the experiments leading to Eq. 3.34 and Table 3.3, and proposed Eq. 3.46 and Table 3.4. This correlation depends on the chevron angles of the PHEs.

$$f_{TP} = C1 Re_{LO}^{C2} \tag{3.46}$$

Amalfi et al. [21, 53] developed an experimental database of two-phase frictional pressure drop under evaporative and adiabatic conditions, and proposed Eq. 3.47. This correlation predicts the database well. β/β_{max} is the ratio of chevron angle, where β_{max} is the maximum chevron angle and is 70°.

$$f_{TP} = 15.698 \left(2.125 \left(\frac{\beta}{\beta_{max}} \right)^{9.993} + 0.955 \right) We_{homo}^{-0.475} Bd^{0.255} \left(\frac{\rho_L}{\rho_G} \right)^{-0.571} \tag{3.47}$$

3.4.2. LOCKHART-MARTINELLI MODEL

Lockhart-Martinelli model [57] was originally proposed in a graphical form, and was further developed by Chisholm [58] into correlations in Eqs. 3.48-3.50. This model is derived from the separated, adiabatic flow of air and liquids in tubes. C is determined by the flow regime combinations of liquid and vapor (laminar or turbulent). X is the Lockhart-Martinelli parameter; ϕ_L is the two-phase friction multiplier. In Eqs. 3.51-3.52, the liquid frictional pressure drop, ΔP_L, presumes the liquid flows alone; the vapor frictional pressure drop, ΔP_G, assumes the vapor flows alone; ΔP_{TP} is the two-phase frictional pressure drop.

$$\phi_L^2 = 1 + \frac{C}{X} + \frac{1}{X^2} \tag{3.48}$$

$$X^2 = \frac{\Delta P_L}{\Delta P_G} \tag{3.49}$$

$$\phi_L^2 = \frac{\Delta P_{TP}}{\Delta P_L} \tag{3.50}$$

$$\Delta P_L = 2 f_L \frac{G_L^2}{\rho_L} \frac{L_p}{d_h} = 2 f_L \frac{G^2 (1-x)^2}{\rho_L} \frac{L_p}{d_h} \tag{3.51}$$

Table 3.5: Constants of Eq. 3.57, depending on the plate combinations.

Plates	30°/30°	30°/60°	60°/60°
F	0.1	0.1	0.5

3

$$\Delta P_G = 2 f_G \frac{G_G^2}{\rho_G} \frac{L_p}{d_h} = 2 f_G \frac{G^2 x^2}{\rho_G} \frac{L_p}{d_h} \tag{3.52}$$

In Eq. 3.53, Winkelmann [19] predicted his experimental data of adiabatic air-water and condensing R134a within PHEs. The single-phase Fanning friction factors of liquid and vapor are calculated in Eq. 3.54, where the Reynolds number is Re_L in Eq. 2.12 and Re_G in Eq. 2.13.

$$\phi_L^2 = 1 + \frac{6}{X} + \frac{1}{X^2} \qquad 0.01 \le X \le 1 \tag{3.53}$$

$$f = \begin{cases} 0.3 + 53 Re^{-1}, & 10 < Re < 1700 \\ Re^{-0.135}, & 1700 < Re < 50000 \end{cases} \tag{3.54}$$

In Eq. 3.55, Nilpueng and Wongwises [100] modified the original model to predict their experimental data of upward and downward flow. The single-phase Fanning friction factor is calculated in Eq. 3.56.

$$\phi_L^2 = 1.339 + \frac{4.492}{X} \tag{3.55}$$

$$f = 4.929 Re^{-0.22} \tag{3.56}$$

Wang and Zhao [74] extended this model to steam condensation in a PHE, and proposed a graphical relation between X and ϕ_L.

Würfel and Ostrowski [96] proposed Eq. 3.57 for the condensation of water and n-heptane. F depends on the chevron angles of plates in Table 3.5.

$$\phi_L^2 = \frac{F}{X_{tt}^2} \tag{3.57}$$

3.4.3. KINETIC ENERGY MODEL

In Eqs. 3.58-3.59, Jassim et al. [127] developed a kinetic energy model for adiabatic two-phase flow within PHEs, which was in vertical upward direction. KE/V is the kinetic energy per unit volume. The void fraction, ε, depends on the prevailing flow patterns. The homogeneous void fraction model over-predicts the

kinetic energy, while the selected separated flow models under-predict the kinetic energy. Thus an effective void fraction was recommended by modifying the homogeneous model. The effective void fraction is between the values of homogeneous and separated models, and depends on the PHE structures. The authors concluded that inertial effects, rather than viscous effects, dominate the frictional pressure drop.

$$\Delta P_{\mathrm{TP}} = \zeta \frac{KE}{V} = \zeta \frac{G^2}{2\rho_{\mathrm{av}}} \tag{3.58}$$

$$\rho_{\mathrm{av}} = (1-\varepsilon)\rho_{\mathrm{L}} + \varepsilon\rho_{\mathrm{G}} \tag{3.59}$$

Longo [77, 78] adopted the kinetic energy model for condensation in a PHE, which was vertically downward. The flow is assumed to be homogeneous and is represented by the averaged two-phase density in Eq. 2.5. ζ is 2 for HFCs and 1.9 for HCs.

3.5. ASSESSMENT OF FRICTIONAL PRESSURE DROP CORRELATIONS

In this Section, six representative correlations are compared with the experimental database collected in Section 3.1. ζ of the kinetic energy model depends on the PHE structures. Thus this model is not assessed. The majority of experiments have been carried out to obtain both heat transfer and frictional pressure drop data, and the operating conditions are the same. The assumptions for heat transfer data in Section 3.3 also apply to this Section. The frictional pressure drop is compared in gradient form. Some experimental data have superheated inlet and subcooled outlet. Sarraf et al. [91] and Hayes et al. [116] excluded the single-phase areas and obtained the two-phase pressure drop, but the lengths of two-phase areas were not given. Djordjević et al. [89] and Shi et al. [72] tested the local frictional pressure drop without providing the test length. Thus these experimental data could not be included. Xiao and Hrnjak [121] suggested to predict frictional pressure drop of two-phase from the onset of condensation. When the superheating degree or subcooling degree is small and no single-phase region is assumed, the lengths of two-phase regions are the PHE lengths [76–78, 80, 81, 86].

In Figure 3.3(a), the prediction of Kuo et al. [61] is generally higher than the experimental data. The predicted data are more scattered for small pressure drop, which corresponds to small mass fluxes.

In Figure 3.3(b), the correlation of Han et al. [87] predicts their data well but is not applicable for other experiments. Eq. 3.43 is especially sensitive to chevron angles, which over-predicts the experimental data of large chevron angles, and

under-predicts small chevron angles. The data of Winkelmann [19] are significantly under-predicted because of the small chevron angle. In Figure 3.3(c), the correlation of Hayes et al. [116] over-predicts a large portion of the experimental data.

In Figure 3.3(d), Amalfi et al. [53] predicts 52.7% of the data within ±50%, which is relatively good. This correlation agrees well with the experimental database of evaporation and adiabatic processes. The gradient of vapor quality is opposite during evaporation and condensation.

In Figures 3.3(e) and 3.3(f), the correlations of Winkelmann [19] and Nilpueng and Wongwises [100] generally under-predict the experimental data. Nilpueng and Wongwises [100] modified the original Lockhart-Martinelli model. Some of the predicted values decrease with the increasing experimental data of Yan et al. [71], Kuo et al. [61] and Winkelmann [19].
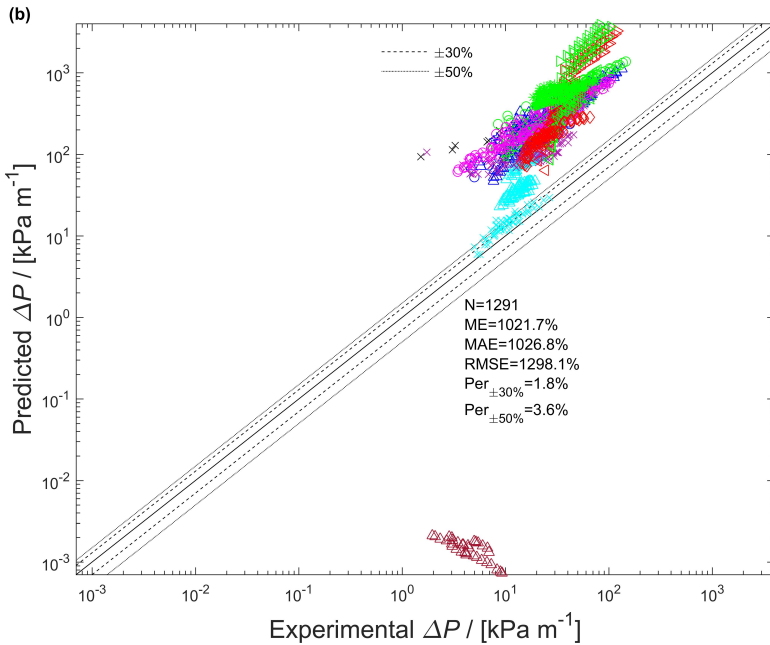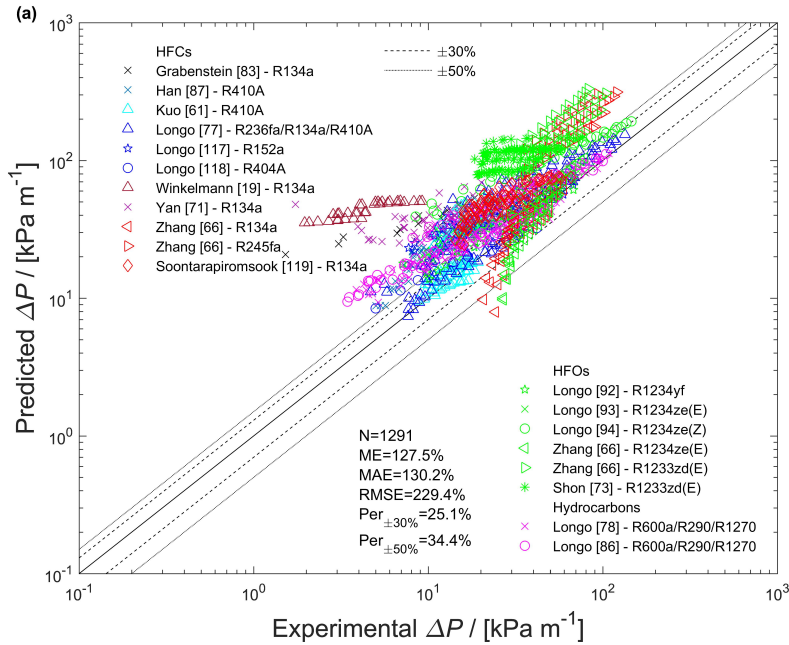
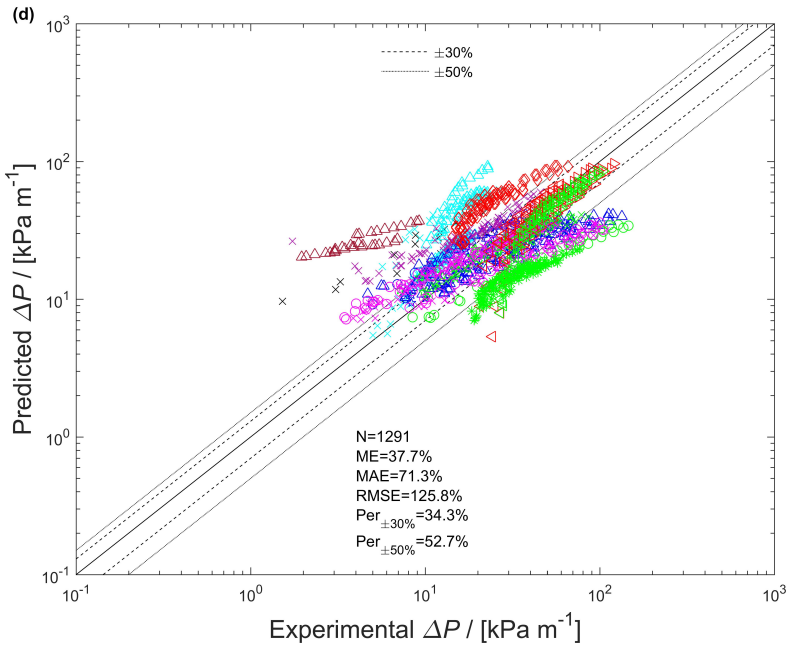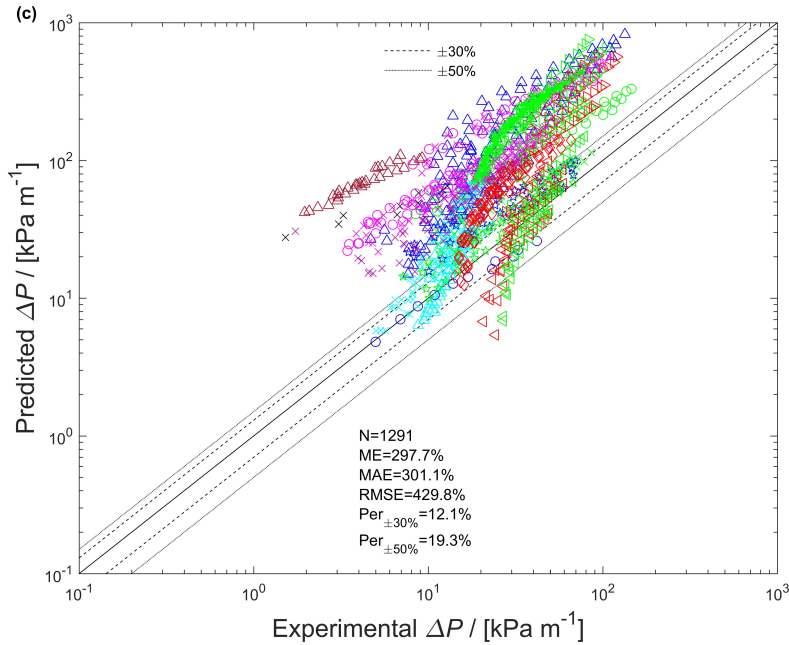## 3.6. A NEW FRICTIONAL PRESSURE DROP CORRELATION

The prediction of frictional pressure drop is poor compared with heat transfer. This Section develops a new frictional pressure drop correlation using multi-variable regression analysis. The experimental database is composed of HFCs, HCs and HFOs, which generally have small two-phase density ratio. In Figures 3.3(e) and 3.3(f), these experimental data are under-predicted by modified Lockhart-Martinelli models [19, 100]. Lockhart-Martinelli model is more suitable for fluids of large two-phase density ratio [57]. In Figures 3.3(a) and 3.3(d), the disagreement between the correlations and the experimental data shows overall over-prediction [53, 61]. The two-phase Fanning friction factor approach has the potential to accurately predict these experimental data.

The shear force is a function of mass flux, vapor quality, heat flux, condensation pressure, fluid properties and plate geometries [10]. These influencing factors are expressed using the non-dimensional numbers listed in Section 2.1: X_{tt}, Co, Re_{eq}, Re_{L}, Re_{LO}, Re_{G}, We_{homo}, We_{L}, Fr_{L}, J_{G}, Bd, Bo, P_{sat}/P_{cr} and β.

The two-phase Fanning friction factor is derived from the experimental database. As shown in Eq. 3.60, the power law is chosen as the fitting mode by implementing least square method. Θ stands for non-dimensional numbers, and k_i, m_i and n_i are determined. Re_{eq}, Bd, P_{sat}/P_{cr} and β are found to be dominant. The inclusion of other numbers does not further improve the predictive accuracy. The resulting correlation is given in Eq. 3.61, where β is expressed in radian.

$$f_{TP} = \prod_{i=1}^{n} \left(k_i \Theta_i^{m_i} + n_i \right) \tag{3.60}$$
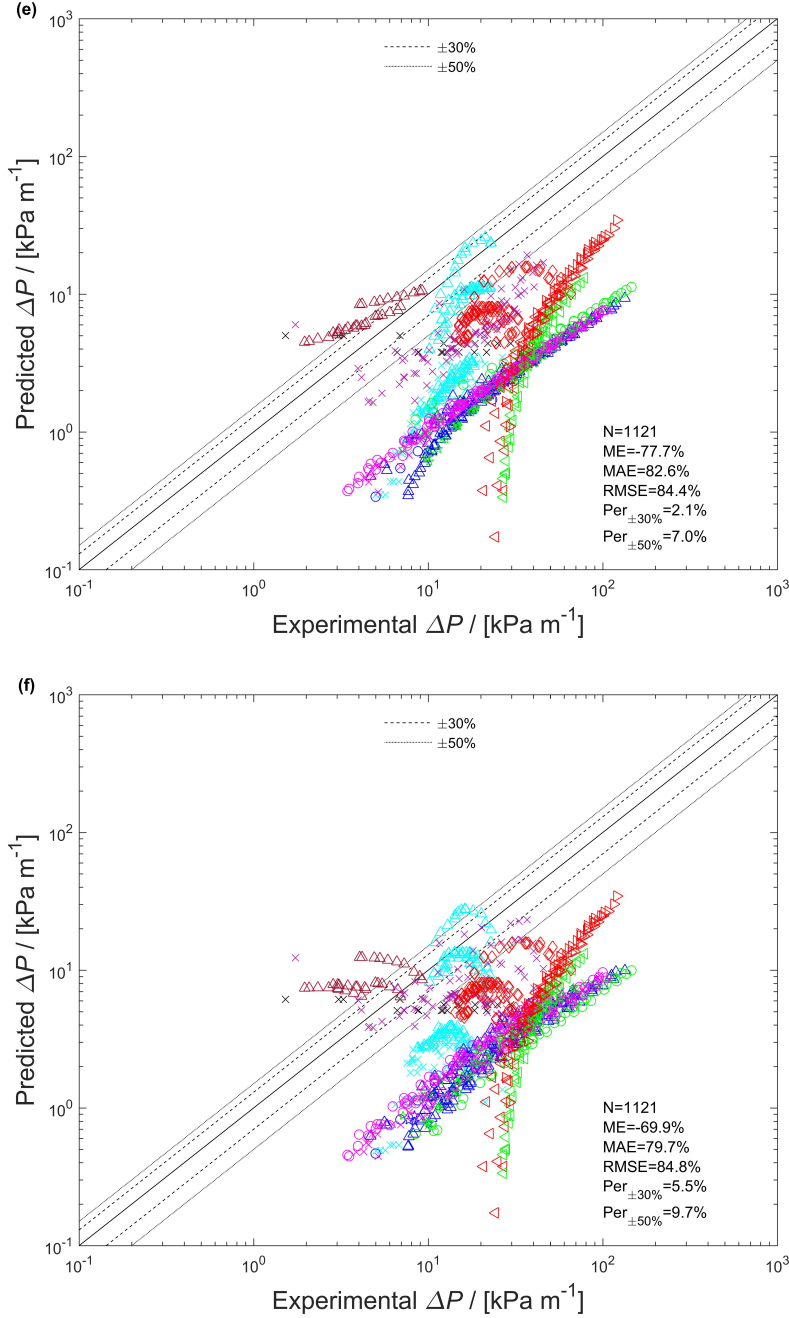
3

3

Figure 3.3: Comparison of frictional pressure drop correlations with the experimental data: (a) Kuo et al. [61], (b) Han et al. [87], (c) Hayes et al. [116], (d) Amalfi et al. [53], (e) Winkelmann [19], (f) Nilpueng and Wongwises [100]. Number of experimental data (N); Mean error (ME): $\frac{1}{n}\sum_1^n \frac{\Delta P_{pre}-\Delta P_{exp}}{\Delta P_{exp}}$; Mean absolute error (MAE): $\frac{1}{n}\sum_1^n \frac{|\Delta P_{pre}-\Delta P_{exp}|}{\Delta P_{exp}}$; Root mean squared error (RMSE): $\sqrt{\frac{1}{n}\sum_1^n \left(\frac{\Delta P_{pre}-\Delta P_{exp}}{\Delta P_{exp}}\right)^2}$; $Per_{\pm30\%}$: Percentage of experimental data within $\pm30\%$; $Per_{\pm50\%}$: Percentage of experimental data within $\pm50\%$.

$$f_{TP} = \left(4.207 - 2.673\beta^{-0.46}\right)\left(4200 - 5.41 Bd^{1.2}\right) Re_{eq}^{-0.95} \left(P_{sat}/P_{cr}\right)^{0.3} \qquad (3.61)$$

Figure 3.4 compares Eq. 3.61 with the experimental data. 87.5% of the data are predicted within ±50%, and the mean absolute error (MAE) is 31.2%. Since Eq. 3.61 is derived from the database, it is reasonable that the performance is much better than the other correlations shown in Figure 3.3. This correlation is suitable in the operating ranges covered by Table 3.1. Eq. 3.61 is developed assuming homogeneous flow, and shows satisfactory prediction. In fact, more than one flow pattern may prevail, and a mechanistic model can be built considering the transition of flow patterns.

Figure 3.5 validates the new correlation with experimental data that are not involved in the previous discussion. These experimental data were obtained in an oblong SPHE [128, 129]. Although the top and bottom of the oblong plates are semi-circular, the main heat transfer area is rectangular and can be compared with traditional PHEs. Frictional pressure drop increases with mass flux and vapor quality, and the prediction follows the trend closely. Though the frictional pressure drop of small mass fluxes are underestimated, most of these experimental data are predicted within ±30%. The MAE is 10.6% for R134a and 15.8% for R410A. Additionally, the frictional pressure drop is larger for lower condensation temperature or lower reduced pressure. In this case, the vapor density is smaller, and the resulting larger volume flux intensifies the shear force. The varying heat flux of the experimental data is not considered for the prediction, which has negligible influences. Nevertheless, the new correlation is not applicable for circular SPHEs, and under-predicts the experimental data significantly [114]. The circular plates change the flow passage area along the flow direction.

Figure 3.6 is a sensitivity analysis, and the frictional pressure drop increases nearly linearly with mass flux. According to Figure 3.6(a), R410A has the smallest frictional pressure drop. It is a high pressure refrigerant with the largest vapor density, which reduces the shear force. The frictional pressure drop of R601 is the largest. As will be shown in Table 6.1, R601 has large two-phase density ratio, and tends to be separated flow. The two-phase Fanning friction factor approach over-predicts the frictional pressure drop. The averaged density assuming homogeneous flow is not applicable. Eq. 3.61 is limited to fluids of small two-phase density ratio. Figure 3.6(b) shows the dependence on geometries. For smaller hydraulic diameter with narrower channel, the flow tends to be confined by the walls, and the corrugated structure promotes the disturbance. Larger chevron angles enhance the secondary flow and intensify the stirring [113, 130]. As a consequence, the frictional pressure drop is increased.
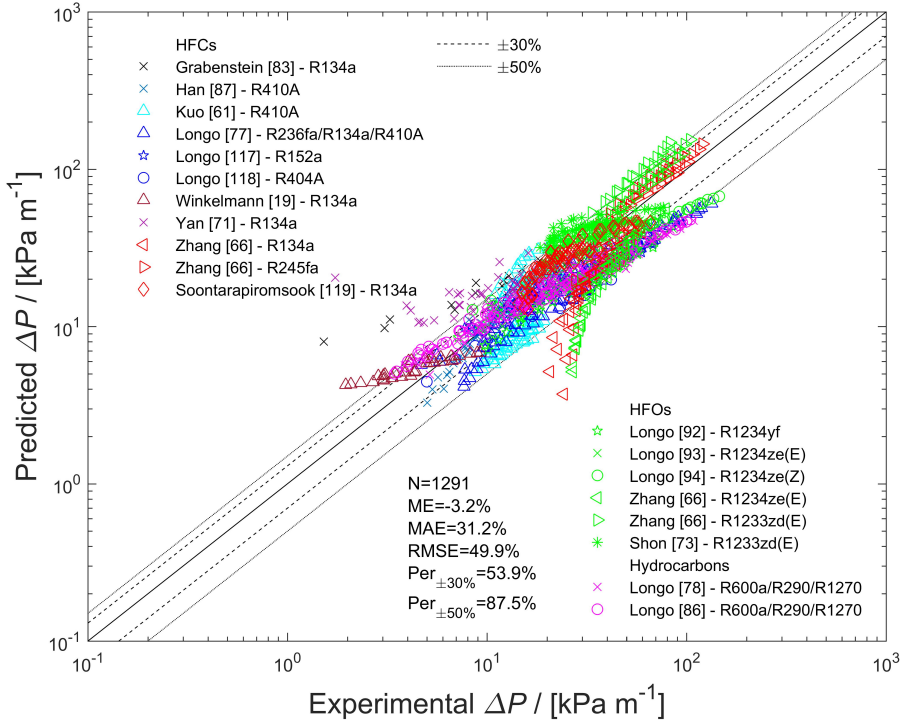
Figure 3.4: Comparison of the new frictional pressure drop correlation, Eq. 3.61, with the experimental data.

During condensation experiments, the overall pressure drop of PHEs, ΔP_{exp}, is measured directly. It is composed of frictional pressure drop, ΔP_{fri}, the pressure drop of inlet and outlet ports, $\Delta P_{\text{in,port}}$, $\Delta P_{\text{out,port}}$, deceleration pressure rise, ΔP_{de}, and elevation pressure rise, ΔP_{ele}. Eq. 3.62 calculates the frictional pressure drop as the flow passes the channels. The pressure drop of inlet and outlet ports is mostly obtained using empirical correlations. Although the port pressure drop accounts for a small portion of the overall value, these empirical correlations introduce uncertainties into the experimental frictional pressure drop, and should be validated depending on the port structures.

$$\Delta P_{\text{fri}} = \Delta P_{\text{exp}} - \Delta P_{\text{in,port}} - \Delta P_{\text{out,port}} + \Delta P_{\text{de}} + \Delta P_{\text{ele}} \qquad (3.62)$$
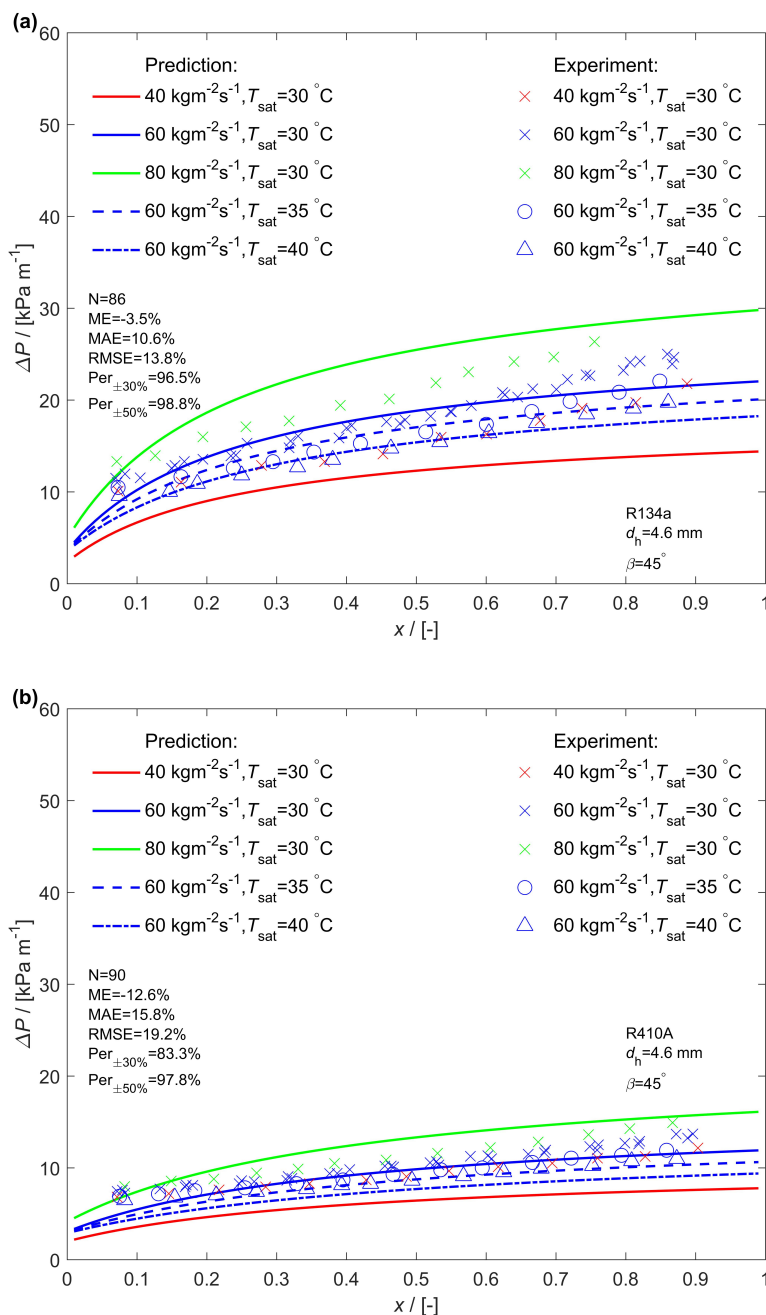
Figure 3.5: Validation of the new frictional pressure drop correlation, Eq. 3.61, with the experimental data of (a) Park and Kim [128], (b) Park et al. [129].
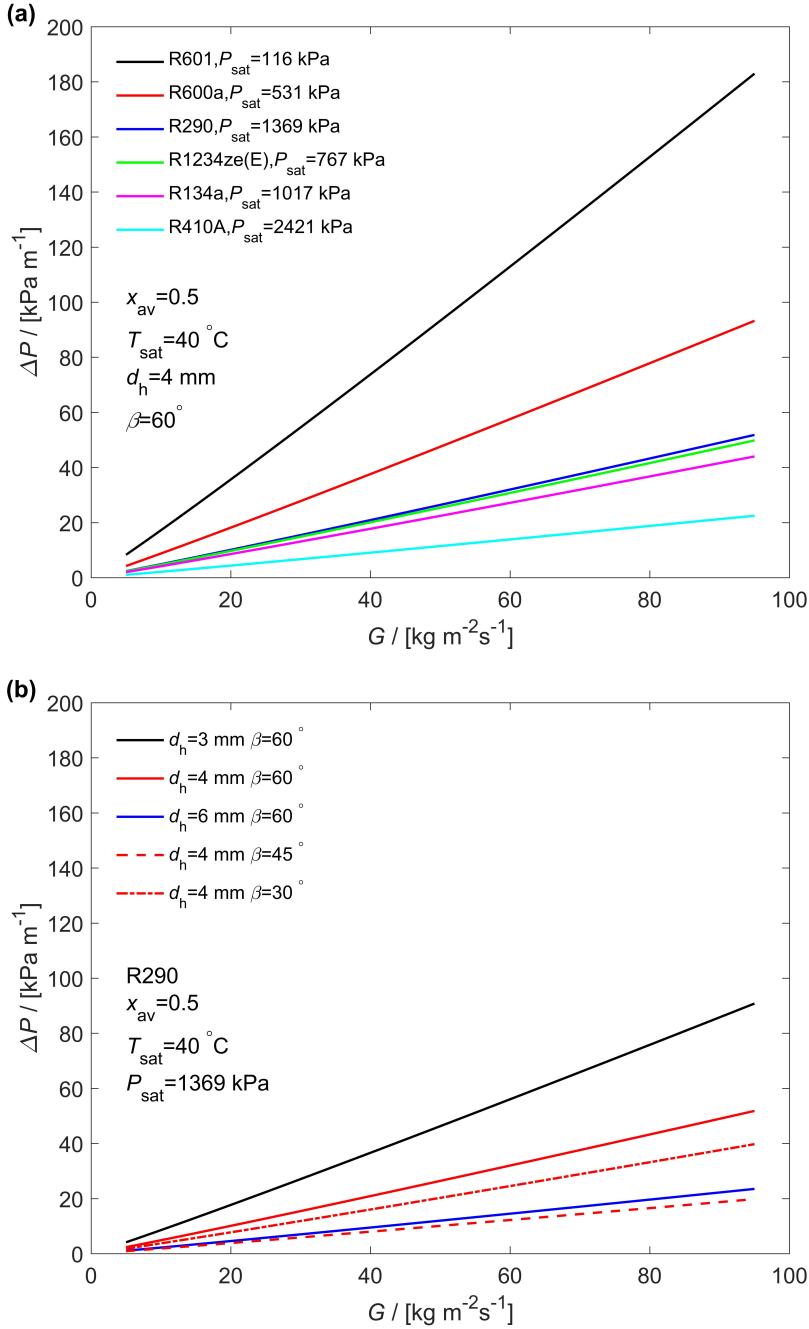
3

Figure 3.6: Sensitivity of frictional pressure drop with mass flux for (a) different refrigerants, (b) different hydraulic diameter and chevron angle.

3.7. CONCLUSIONS

In this Chapter, the predictive methods are investigated for heat transfer and frictional pressure drop during condensation in PHEs.

- An experimental database of condensation is built, which includes 2376 heat transfer data points and 1590 frictional pressure drop data points. The composition of the database is presented in terms of working fluids, chevron angles, hydraulic diameters, mass fluxes, saturated temperatures and reduced pressures.

- Heat transfer correlations are surveyed and are classified according to the basic forms. Eight heat transfer correlations are compared with the experimental database. The correlations of Longo et al. [60] and Kuo et al. [61] predict 93.0% and 88.4% of the data within ±50%, respectively.

- Frictional pressure drop correlations are also reviewed. Six correlations are assessed with the experimental database but show relatively poor performance. Thus a new correlation is developed, with 87.5% of the data predicted within ±50%. A cross validation shows good performance. A sensitivity analysis is provided for a wide range.

Suitable methods are presented to calculate the heat transfer and frictional pressure drop for HFCs, HCs and HFOs. NH_3 has distinct fluid properties and is not included in the database. The condensation of NH_3 is investigated in the following Chapters.

4

EXPERIMENTAL SETUP AND METHODS

In this Chapter, the experimental setup is described including the cycles and measurement instrumentations. The ranges and uncertainties of sensors are specified. The test section is a gasketed plate heat exchanger. A transparent plate is manufactured for visualization experiments. The methods of data reduction are explained. The secondary fluid is single-phase H_2O, whose HTCs and frictional pressure drop are obtained. The HTCs and frictional pressure drop of condensation are also calculated.
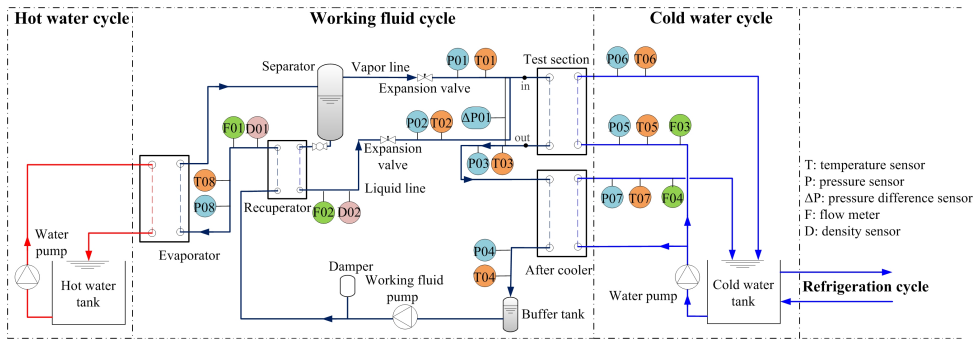
Figure 4.1: Diagram of the experimental setup including the working fluid cycle, cold water cycle and hot water cycle. The working fluid cycle is mainly composed of a evaporator, a separator, a recuperator, a test section, an after cooler, a buffer tank and a working fluid pump. The cold water feeds both the test section and after cooler, while the hot water feeds the evaporator.

4.1. EXPERIMENTAL SETUP

The experimental setup was originally built as an ocean thermal energy conversion system, and can operate as ORC or Kalina Cycle with NH_3 and NH_3/H_2O, respectively. The setup is composed of a working fluid cycle, a hot water cycle and a cold water cycle.

4.1.1. WORKING FLUID AND WATER CYCLES

Figure 4.1 shows the process flow diagram. NH_3 is heated by hot water in an evaporator, where it is partially evaporated. The two phases flow into a separator, after which the vapor flows through an expansion valve with the pressure being reduced. The liquid is subcooled in a recuperator and flows through an expansion valve. The two phases are controlled to be at the same pressure and mix up before entering the test section. The fluid is partially condensed in the test section by the cold water, and then is subcooled in an after cooler. Afterwards, it flows into a buffer tank. The liquid level in the buffer tank decreases for large mass flow rate, providing the upper limit of the mass flow rate. A variable speed diaphragm pump controls the flow rate of the NH_3. Diaphragm pumps are suitable for corrosive fluids like NH_3, and are able to cope with cavitation. To reduce the fluctuation of flow rate and operating pressure, a damper filled with nitrogen is installed at the outlet of the working fluid pump. The mass flow rate becomes unstable for small values, limiting the lowest mass flow rate. Next, NH_3 flows through the recuperator into the evaporator. Figure 4.2 (top) is the picture of the experimental setup. The experimental setup is enclosed by shields and is connected to a ventilation system.

Three brazed plate heat exchangers act as the evaporator, recuperator and

Figure 4.2: Pictures of the experimental setup (top), test section (bottom-left) and visualization section (bottom-right). In the top figure, the experimental setup consists of a GPHE (test section), three BPHEs (evaporator, recuperator, after cooler), two working fluid tanks (separator, buffer tank), two water tanks (cold water, hot water), a working fluid pump, four water pumps (cold water driven pump, cold water mixing pump, hot water driven pump, hot water mixing pump). In the bottom-left figure, the test section is shown before being wrapped with insulation materials. The inlet and outlet ports of NH_3 are connected with stainless steel tubes, while the inlet and outlet ports of H_2O are connected with PVC tubes. In the bottom-right figure, the visualization section is composed of a transparent end plate and a frame plate with three observation windows. It is illuminated by an LED-strip circumferentially.

after cooler. A sight glass is inserted into the separator to observe the liquid level. Two relieve valves are installed after the pump and before the separator. These valves open when the absolute pressure is above 1600 kPa. The setup is wrapped with a layer of insulation material of 20 mm, while the test section is insulated with two layers.

The cold water cycle feeds both the test section and after cooler in parallel. The cold water is pumped and separated to these two heat exchangers. The water flow is driven by a centrifugal pump. The inlets of the test section and after cooler have the same temperature and pressure, and share sensors. The flow rates of both lines are measured to determine the heat transfer rate. Another pump is installed to mix water in the tank, so the water has uniform temperature. The flow rate and temperature at the heat exchanger inlet are controlled by the water pump and a refrigeration cycle. During the experiments, the water side mass flow rate was close to the maximum attainable value by the driven pump to increase this HTC. A PID temperature controller is implemented to achieve the desired water temperature. The cold water cycle has a cooling capacity of about 6000 W at 8 °C. The cooling capacity is provided by a refrigeration cycle.

The hot water cycle is composed of a tank, an electrical heater, a centrifugal pump used to drive the water flow, a mixing pump and sensors. The heat transfer rate to the evaporator is determined by the water flow rate and temperature glide. The flow rate and temperature at the evaporator inlet are controlled by the water pump and heater. The heater has a maximum capacity of 6000 W.

4.1.2. Measurement instrumentation

Temperature and pressure are measured at several positions of the set up. For simplicity, Figure 4.1 only shows the sensors that are relevant for the discussion of this thesis. The temperature and pressure of NH_3 are measured at the following positions: the vapor and liquid inlets of the test section, as well as the outlets of the test section and after cooler. The NH_3 pressure drop within the test section is also measured. The overall and liquid mass flow rates of the working fluid are measured at the inlet of the evaporator and at the liquid line. The ratio of mass flow rates is used to check the vapor quality at the test section inlet. The temperature and pressure of the cold water are measured at the inlet and outlet of the test section and after cooler, as well as its volume flow rate. Density is measured by D01 at the same location as the overall NH_3 mass flow rate. When the setup is operated with NH_3/H_2O, the density is used to determine the bulk NH_3 concentration.

Table 4.1 lists the sensor features. The measurement system was originally described by Tao et al. [131], and was further modified to improve the accuracy and to extend the measurement range. Temperature is measured with four-wire

Table 4.1: Specification of the sensors.

Sensors	Type	Sensor uncertainty	Range
Temperature	PT-100	± 0.05 °C	2 /50 °C
NH_3 pressure	Absolute	$\pm 0.05\%$ FS	0/1000 kPa
NH_3 pressure	Gauge	$\pm 0.5\%$ FS	0/1000 kPa
Water pressure	Gauge	$\pm 0.5\%$ FS	0 /250 kPa
Differential pressure	SITRANS P DS	$\pm 0.3\%$ FS	1.6 /160 kPa
NH_3 overall flow	Coriolis	$\pm 0.2\%$ RD	0 /0.02 kgs^{-1}
NH_3 liquid flow	Coriolis	$\pm 0.2\%$ RD	0 /0.013 kgs^{-1}
Water flow	Turbine	$\pm 1\%$ FS ± 7.2 Lh^{-1a}	30 /3000 Lh^{-1}
NH_3 density	Anton Paar	± 0.1 kgm^{-3}	-

[a] These sensors have an uncertainty of $\pm 1\%$ FS in the full range. The measured value of F03 is kept almost constant at 432 Lh^{-1} during experiment. F03 is calibrated in this range with an uncertainty of ± 7.2 Lh^{-1}.

PT-100 of high precision. The uncertainty is ± 0.05 °C in the operating ranges. NH_3 pressure is measured by two types of sensors. P03 and P08 are absolute pressure sensors, and the uncertainty is $\pm 0.05\%$ FS. The other NH_3 pressure sensors are gauge pressure sensors and have an uncertainty of $\pm 0.5\%$ FS. The water pressure sensors are also gauge pressure sensors with $\pm 0.5\%$ FS uncertainty. The pressure drop of NH_3 within the test section is measured by a differential pressure sensor of $\pm 0.3\%$ FS uncertainty. The NH_3 mass flow rate is measured by Coriolis type mass flow meters of $\pm 0.2\%$ RD uncertainty. The water flow meters originally have an uncertainty of $\pm 1\%$ FS and considerably contribute to the uncertainty of condensation HTCs. The water flow rate was kept at the maximum value available by the driven pump and was almost constant. F03 is specially calibrated in the tested range and has an uncertainty of ± 7.2 Lh^{-1}. The uncertainty of the NH_3 density sensor is ± 0.1 kgm^{-3}.

Experimental data are acquired and recorded with LabVIEW. It also implements control and safety protection. A program is developed to analyze the measured data. In order to determine the steady state, the time derivatives of all the measured data are calculated. Both the slopes and amplitudes are assessed. Pressure and mass flow rate fluctuate sharply after the working fluid pump, and are stabilized by adjusting the damper. The steady state is kept for more than 10 minutes, and the time averaged values are used for data reduction.

Table 4.2: Geometrical parameters of the test section.

Plate number	L_p [mm]	W_p [mm]	A [m^2]	d_h [mm]	β [-]	ϕ [-]	d_g [mm]	d_p [mm]	Λ_{wave} [mm]
3	668	95	0.064*	2.99	63°	1.15	1.72	0.58	6.67

4.1.3. Test section: gasketed plate heat exchanger and transparent plate

The test section is a GPHE with the plate number adjustable. To avoid the flow maldistribution among channels, the GPHE consists of three plates forming two channels during the experiments. Only one plate is effective for heat transfer. Figure 4.2 (bottom-left) shows the test section before it is wrapped with insulation materials. NH$_3$ flows vertically downward in one channel, while cold water flows upward in the other channel. These three plates are pressed by frame plates from both sides. Figure 4.3 illustrates the plate of the GPHE, and Table 4.2 gives the geometrical parameters. It is actual heat transfer area instead of basic heat transfer area. Section 1.2 defines these parameters [10]. The GPHE is assembled from Alloy 316 plates and EPDM gaskets to be compatible with NH$_3$.

The plate has triangular inlet and outlet areas, where flow is distributed from the inlet port or into the outlet port. The plate surface is composed of sinusoidal corrugations, where the grooves can be considered as branching sub-channels in parallel. The grooves on one plate have an opposite direction with those on the adjacent plate. Fluid flows along the grooves, which is similar to inclined downward flow. Meanwhile, the fluid also passes across the grooves at the contact points of adjacent plates.

As shown in Figure 4.3, a transparent plate is fabricated to visualize the condensing flow. This plate has the same geometry as the metal plates except that the plate thickness is 25 mm. The corrugated surface is replicated so that the flow patterns during condensation are able to reappear. The visualization test section is composed of two metal plates and the transparent plate. The frame plate adjacent to the transparent plate has three observation windows. The visualization experiment is diabatic. The flow directions of NH$_3$ and cold water are the same as during the heat transfer experiments.

The transparent material is required to be machinable and compatible with NH$_3$. Section 2.3.2 summarized the transparent materials used to manufacture

---

* The actual heat transfer area is 0.064 m^2 instead of 0.640 m^2. In Table 3 of Tao, X., Dahlgren, E., Leichsenring, M., Infante Ferreira, C. A., 2020. NH$_3$ condensation in a plate heat exchanger: Experimental investigation on flow patterns, heat transfer and frictional pressure drop. Int. J. Heat Mass Transf. 151, 119374 [45], there is a typing error. It is correct in data reduction and other analysis. The exerimental results are not affected.
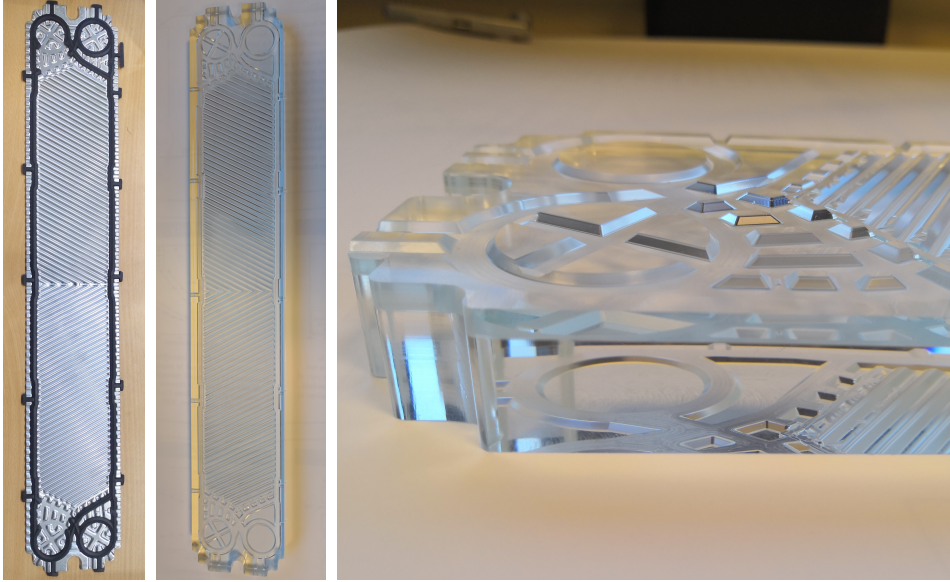
Figure 4.3: Pictures of the stainless steel plate and transparent plate. The stainless steel plate is composed of triangular inlet and outlet areas and rectangular fully developed area. The flow area is enclosed by a gasket. L_p=668 mm, W_p=95 mm, β=63°. The corrugated structure is mirrored to the transparent plate, which acts as the end plate during visualization experiments.

PHEs applicable for air/water [10], which are not compatible with NH_3. Kim et al. [133] and Nakamura et al. [134] 3D printed transparent plates of small sizes. Lee et al. [135] fabricated a transparent plate with polycarbonate. da Silva Lima et al. [136] and Arima et al. [137] used sight glass to fabricate smooth tubes and smooth plates for NH_3 visualization, but sight glass is not machinable. In order to test the compatibility, the samples of several polymers were immersed into liquid NH_3. Polystyrene (PS) has better compatibility compared with polymethylmethacrylaat (PMMA), polyvinylchloride (PVC), polycarbonate (PC) and terephthalate glycol (PETG). But PS may decay after long time operation. Leichsenring [138] and Leichsenring et al. [139] presented the details of material selection and strength analysis. The transparent plate is manufactured by glueing a layer of PS and a layer of PMMA. The PS plate contacts NH_3, which has a thickness of 5 mm and was machined. The PMMA plate improves the mechanical strength. It is 20 mm thick and is pressed by the frame plate. The visualization experiment lasted for 2 weeks. After then, the transparent plate started to decay so the experiment had to be stopped.

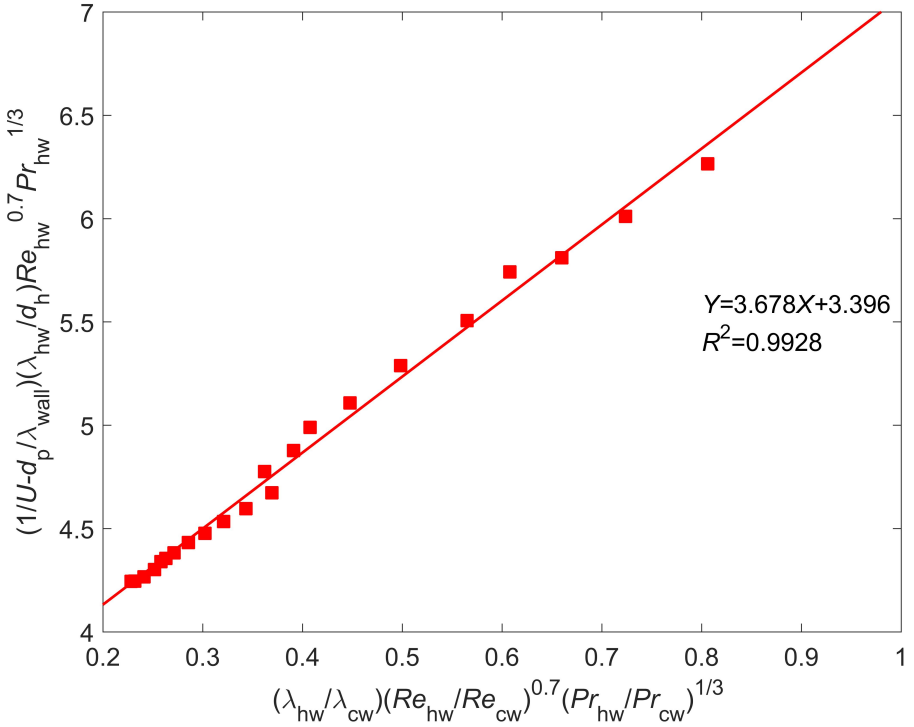Flow patterns were captured with a high speed camera from the front, with

4

Figure 4.4: Results of modified Wilson-plot method for H_2O-H_2O experiments, which determine a constant of Eq. 4.2 and calibrate H_2O HTC. The axes are chosen to reduce the experimental data so that the slope of the line is the reciprocal of Θ_1.

a frame rate of 3000 fps and a resolution of 1024×1024 pixels. The transparent plate was wrapped with an LED-strip on the sides circumferentially. The channel is well illuminated as shown in Figure 4.2 (bottom-right).

4.2. DATA REDUCTION

4.2.1. H_2O-H_2O EXPERIMENTS

H_2O-H_2O experiments were carried out to obtain the single-phase HTCs and Fanning friction factors. The working fluid cycle is designed for two-phase system. When the cycle is completely filled with H_2O, the fluctuations of flow rate and pressure are significant. Nitrogen is filled at the top of the separator. It is stationary and buffers fluctuations during operation. The single-phase HTCs of PHEs, α_w, are generally accepted to have the form of Eq. 4.1 [51]. Θ_1 and Θ_2 depend on the geometry of PHEs, and can be calculated by Wilson-plot method
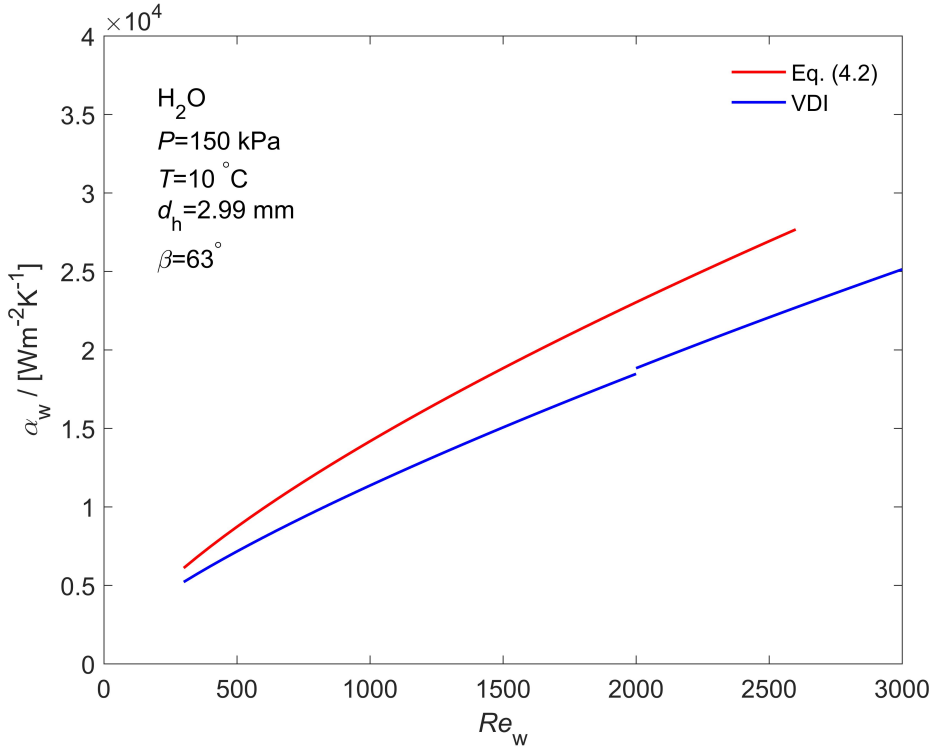
Figure 4.5: Comparison of Eq. 4.2 and VDI [20]. Eq. 4.2 is larger than VDI within 20%. Eq. 4.2 is derived from the data of the present experimental setup. The correlation from VDI is widely applicable.

[140]. During experiments, the mass flow rate of hot water was kept constant while the mass flow rate of cold water was varied. Θ_2 is determined to be 0.7 by best fitting. Figure 4.4 presents the results of Wilson-plot method obtained by curve fitting. U is the overall HTC, and $d_p/\lambda_{\text{wall}}$ is the wall thermal resistance. The resulting correlation is given in Eq. 4.2 and is compared with VDI in Figure 4.5. VDI provides the generally accepted single-phase correlation [20, 141]. Eq. 4.2 agrees with VDI, and the difference is smaller than 20%. Eq. 4.2 is more accurate in this specific condition.

$$Nu_{\text{w}} = \frac{\alpha_{\text{w}} d_{\text{h}}}{\lambda_{\text{w}}} = \Theta_1 Re_{\text{w}}^{\Theta_2} Pr_{\text{w}}^{1/3} \tag{4.1}$$

$$Nu_{\text{w}} = \frac{\alpha_{\text{w}} d_{\text{h}}}{\lambda_{\text{w}}} = 0.275 Re_{\text{w}}^{0.7} Pr_{\text{w}}^{1/3} \qquad 320 \leq Re_{\text{w}} \leq 2600 \tag{4.2}$$
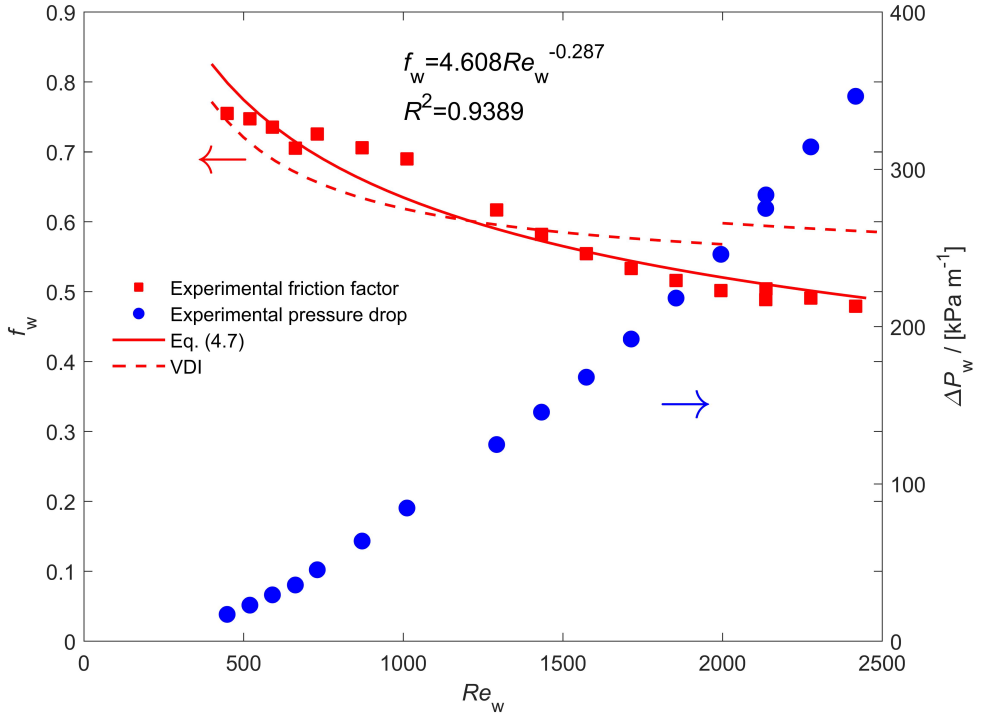
Figure 4.6: The correlation of single-phase Fanning friction factor and experimental data. The left axis is Fanning friction factor. Eq. 4.7 is compared with the correlation from VDI [20]. The agreement is good. The right axis is the experimental frictional pressure drop.

The frictional pressure drop of single-phase is also obtained. $\Delta P_{\text{exp,w}}$ is the measured pressure drop. Eqs. 4.3-4.5 calculate the water frictional pressure drop, $\Delta P_{\text{fri,w}}$, the pressure drops of inlet and outlet ports, $\Delta P_{\text{in,port,w}}$, $\Delta P_{\text{out,port,w}}$, and elevation pressure decrease, $\Delta P_{\text{ele,w}}$. In Eq. 4.4, $\Delta P_{\text{in,port,w}}$ and $\Delta P_{\text{out,port,w}}$ are calculated using the empirical correlation in Shah and Focke [142].

$$\Delta P_{\text{fri,w}} = \Delta P_{\text{exp,w}} - \Delta P_{\text{in,port,w}} - \Delta P_{\text{out,port,w}} - \Delta P_{\text{ele,w}} \qquad (4.3)$$

$$\Delta P_{\text{port,w}} = 1.5 G_{\text{w}}^2 / (2\rho_{\text{w}}) \qquad (4.4)$$

$$\Delta P_{\text{ele,w}} = \rho_{\text{w}} g L_{\text{p}} \qquad (4.5)$$

Eq. 4.6 defines the single-phase Fanning friction factor, f_{w}, which is correlated in Eq. 4.7, and the results are presented in Figure 4.6. Eq. 4.7 agrees with

the correlation of VDI [20], which is applicable in large ranges. VDI is used to develop condensation correlations in Chapter 6. The pressure drop experiments were conducted at the same operating conditions as heat transfer experiments, but the ranges of the pressure sensors were limited and the data at larger mass fluxes cannot be obtained. So Eq. 4.7 has a narrower range of Reynolds number compared with Eq. 4.2. The flow is expected to transit from laminar to turbulent flow with increasing mass fluxes. The transition in PHEs takes place at smaller Reynolds number than for tubes [113, 143]. In the tested range, Eq. 4.7 considers the flow as turbulent, and is only valid for the present measurement. Eq. 4.7 agrees with VDI in this range.

$$\Delta P_{\text{fri,w}} = 2 f_{\text{w}} \frac{G_{\text{w}}^2}{\rho_{\text{w}}} \frac{L_{\text{p}}}{d_{\text{h}}} \tag{4.6}$$

$$f_{\text{w}} = 4.608 Re_{\text{w}}^{-0.287} \qquad 400 \leq Re_{\text{w}} \leq 2500 \tag{4.7}$$

4.2.2. HTCS OF NH$_3$

In Eqs. 4.8-4.9, the inlet and outlet NH$_3$ enthalpies of the test section, $h_{\text{a,in}}$ and $h_{\text{a,out}}$, are determined from the energy balance of the after cooler and test section. The inlet and outlet vapor qualities are determined referring to Refprop 9.1 [39]. The averaged vapor quality is used to analyze the flow patterns, heat transfer and frictional pressure drop data. The inlet and outlet vapor qualities are also used to illustrate the flow patterns. The condensation HTC, α_{a}, is calculated using Eq. 4.10. The condensation temperature, T_{a}, changes slightly from the inlet to the outlet because of the frictional pressure drop.

$$h_{\text{a,out}} = h_{\text{a,04}} + \frac{\dot{Q}_{\text{after}}}{\dot{m}_{\text{a,01}}} = h_{\text{a,04}} + \frac{c_{p,\text{w}} \dot{m}_{\text{w,04}} \left(T_{\text{w,07}} - T_{\text{w,05}} \right)}{\dot{m}_{\text{a,01}}} \tag{4.8}$$

$$h_{\text{a,in}} = h_{\text{a,out}} + \frac{\dot{Q}_{\text{test}}}{\dot{m}_{\text{a,01}}} = h_{\text{a,out}} + \frac{c_{p,\text{w}} \dot{m}_{\text{w,03}} \left(T_{\text{w,06}} - T_{\text{w,05}} \right)}{\dot{m}_{\text{a,01}}} \tag{4.9}$$

$$\dot{Q}_{\text{test}} = c_{p,\text{w}} \dot{m}_{\text{w,03}} \left(T_{\text{w,06}} - T_{\text{w,05}} \right) = \dot{m}_{\text{a,01}} \left(h_{\text{a,in}} - h_{\text{a,out}} \right)$$
$$= UA \frac{\left(T_{\text{a,in}} - T_{\text{w,06}} \right) - \left(T_{\text{a,out}} - T_{\text{w,05}} \right)}{\ln \frac{T_{\text{a,in}} - T_{\text{w,06}}}{T_{\text{a,out}} - T_{\text{w,05}}}} = \frac{A}{\frac{1}{\alpha_{\text{a}}} + \frac{d_{\text{p}}}{\lambda_{\text{wall}}} + \frac{1}{\alpha_{\text{w}}}} \frac{\left(T_{\text{a,in}} - T_{\text{w,06}} \right) - \left(T_{\text{a,out}} - T_{\text{w,05}} \right)}{\ln \frac{T_{\text{a,in}} - T_{\text{w,06}}}{T_{\text{a,out}} - T_{\text{w,05}}}} \tag{4.10}$$

4.2.3. FRICTIONAL PRESSURE DROP

As shown in Eq. 4.11, the condensation frictional pressure drop, $\Delta P_{\text{fri,a}}$, is calculated by subtracting the other components from the measured pressure drop, $\Delta P_{\text{exp,a}}$, including: the mixing pressure drop, $\Delta P_{\text{mix,a}}$, pressure drop of inlet and

outlet ports, $\Delta P_{\text{in,port,a}}$, $\Delta P_{\text{out,port,a}}$, deceleration pressure rise, $\Delta P_{\text{de,a}}$, and elevation pressure rise, $\Delta P_{\text{ele,a}}$.

$$\Delta P_{\text{fri,a}} = \Delta P_{\text{exp,a}} - \Delta P_{\text{in,port,a}} - \Delta P_{\text{out,port,a}} - \Delta P_{\text{mix,a}} + \Delta P_{\text{de,a}} + \Delta P_{\text{ele,a}} \qquad (4.11)$$

In Eqs. 4.12-4.13, $\Delta P_{\text{in,port,a}}$ and $\Delta P_{\text{out,port,a}}$ are treated as sudden enlargement and sudden contraction of two-phase flow, respectively. G_{tube} is the mass flux in the connection tubes. A_{tube} and A_{port} are the flow areas of tubes and ports. v_{L} and v_{G} are the specific volume of liquid and vapor. x is the vapor quality. 0.591 is an empirical parameter and is determined by the ratio of A_{tube} to A_{port} [144].

$$\Delta P_{\text{in,port,a}} = G_{\text{tube}}^2 v_{\text{L}} \frac{A_{\text{tube}}}{A_{\text{port}}} \left(1 - \frac{A_{\text{tube}}}{A_{\text{port}}}\right) \left(1 + \frac{v_{\text{G}} - v_{\text{L}}}{v_{\text{L}}} x\right) \qquad (4.12)$$

$$\Delta P_{\text{out,port,a}} = 0.5 G_{\text{tube}}^2 v_{\text{L}} \left(\frac{1}{0.591} - 1\right)^2 \left(1 + \frac{v_{\text{G}} - v_{\text{L}}}{v_{\text{L}}} x\right) \qquad (4.13)$$

In Eqs. 4.14-4.15, $\Delta P_{\text{de,a}}$ and $\Delta P_{\text{ele,a}}$ are calculated using the homogeneous two-phase model, which considers the two-phase flow as a single fluid. G is the mass flux at the flow channel of the PHE. The averaged density, $\Delta P_{\text{ele,a}}$, is calculated at the averaged vapor quality as shown in Eq. 2.5 [144].

$$\Delta P_{\text{de,a}} = G^2 (v_{\text{G}} - v_{\text{L}})(x_{\text{in}} - x_{\text{out}}) \qquad (4.14)$$

$$\Delta P_{\text{ele,a}} = \rho_{\text{av}} g L_{\text{p}} \qquad (4.15)$$

At the inlet of the test section, liquid is sprayed into vapor through orifices. The pressure drop of flowing through orifices is composed of sharp-edged effects at the entrance and exit regions, as well as the frictional component through finite-thickness [145, 146]. This pressure drop is calculated in Eqs. 4.16-4.19. u_{ori} is the liquid velocity at the orifices. d_{ori} and d_{tube} are the diameters of the orifices and inlet tube. f_{com} is a combined friction factor, and includes sharp-edged term and frictional term in Eq. 4.17, respectively. $Re_{\text{L,ori}}$ is based on orifice diameter and velocity [145].

$$\Delta P_{\text{mix,a}} = 0.5 u_{\text{ori}}^2 \rho_{\text{L}} \left(1 - \left(\frac{d_{\text{ori}}}{d_{\text{tube}}}\right)^4\right) f_{\text{com}} \qquad (4.16)$$

$$f_{\text{com}} = \frac{25}{9} \left(1 + e^{-0.12 Re_{\text{L,ori}}^{0.5}} - 2.16 e^{-0.26 Re_{\text{L,ori}}^{0.5}} + 0.16 \left(\frac{1}{1 + Re_{\text{L,ori}}^{0.5}}\right)\right)^{-2}$$
$$+ \frac{4}{Re_{\text{L,ori}}} \frac{L_{\text{ori}}}{d_{\text{ori}}} \left(\frac{3.44}{\xi^{0.5}} + \frac{16 + 0.3125\xi^{-1} - 3.44\xi^{-0.5}}{1 + 2.12 \times 10^{-4}\xi^{-2}}\right) \qquad (4.17)$$

$$Re_{\mathrm{L,ori}} = \rho_{\mathrm{L}} u_{\mathrm{ori}} d_{\mathrm{ori}} / \mu_{\mathrm{L}} \tag{4.18}$$

$$\xi = L_{\mathrm{ori}} / \left(d_{\mathrm{ori}} Re_{\mathrm{L,ori}} \right) \tag{4.19}$$

4.3. CONCLUSIONS

The experimental setup is described in this Chapter. The measurement instrumentations are specified for the uncertainty analysis of experimental results. The methods are explained to calculate the HTCs and frictional pressure drop of single-phase and condensing flow. For one thing, the experimental data of single-phase are used to derive the predictive correlations suitable for the present experimental setup. For another, the data are used to validate the single-phase correlations in VDI [20], which are widely applicable and are used to develop the separated model of condensation in Chapter 6.

5

EXPERIMENTAL RESULTS AND DISCUSSION OF NH$_3$ CONDENSATION

In this Chapter, NH$_3$ condensation in a PHE is investigated by visualizing the flow patterns and measuring HTCs and frictional pressure drop. According to the visualization experiments, full film flow takes place at large mass fluxes and intermediate mass fluxes of low vapor qualities, while partial film flow happens at small mass fluxes and intermediate mass fluxes of high vapor qualities. The heat transfer and frictional pressure drop experiments cover various mass fluxes, vapor qualities and saturated pressure. Vapor qualities have significant influences on heat transfer and frictional pressure drop. In the tested ranges, the effect of mass fluxes is noticeable on frictional pressure drop, but is moderate on heat transfer. The impact of saturated pressure is small. The experimental data are compared with selected correlations, showing a poor agreement.

5.1. FLOW VISUALIZATION RESULTS

Visualization experiments of NH_3 were conducted at the condensation pressure of 690 kPa. The flow is maintained to be stable [147]. The flow patterns changed with vapor qualities and mass fluxes. Only film flow has been detected. Air/water experiments observed bubbly flow, slug flow, churn flow, film flow or the equivalent flow patterns [19, 83, 97–101]. Bubbly flow is known to be limited at large overall mass fluxes and low vapor qualities. The kinetic energy is strong enough to break up the bubbles, and the bubble breakup overcomes coalescence. The condensing NH_3 in the present study was below $100 \, \mathrm{kg m^{-2} s^{-1}}$. By contrast, bubbly flow of air/water happens above the overall mass flux of approximately 100 $\mathrm{kg m^{-2} s^{-1}}$ [83, 97–99, 101]. Buscher [101] did not observe slug flow or churn flow, which are characterized by the phenomenon that the whole channel width is occupied by gas or liquid periodically. In tubes, bubbles move faster with growing sizes, and coalesce more intensively. However, in the corrugated channels, the centrifugal forces weaken bubble acceleration and suppress two-phase separation. The slug or churn flow in other researches are mainly attributed to the gas-liquid injection [101].

The test section could not be insulated from the front, which results in some heat leak. According to uncertainty analysis, the heat leak has minor influences on vapor quality, but brings about significant errors to HTCs. Thus the condensation HTCs cannot be derived. The outlet vapor qualities are determined from the energy balance of the after cooler, and are not influenced by the heat leak. The inlet vapor qualities are based on the energy balance of the test section, and are affected by the heat leak. The effect is small since NH_3 has large latent heat. This has been checked making use of the overall and liquid flow meters, which are shown in Figure 4.1.

5.1.1. FLOW PATTERNS

The terms film flow and partial film flow are used in previous studies. To clarify the wetting characteristics, in this thesis, *full film flow* describes the flow pattern for which the wall is completely wetted, while *partial film flow* indicates part of the wall is dry. *Film flow* is the sum of full film flow and partial film flow.

Figure 5.1 shows the pictures of full film flow, which is similar to annular flow in tubes. The videos of full film flow are provided in the Appendix of the online version of Tao et al. [45]. Figure 5.2 illustrates the distribution of liquid and vapor. Continuous liquid film flows on the wall, while vapor core flows in the center of the groove. Because of the corrugated groove, the two-phase interface is rough even at low mass fluxes. Waves and ripples move at the interface. A basic wave has a small size. Different kinds of waves result from the interaction and combination of basic waves. The waves are dispersed with varying wavelengths and
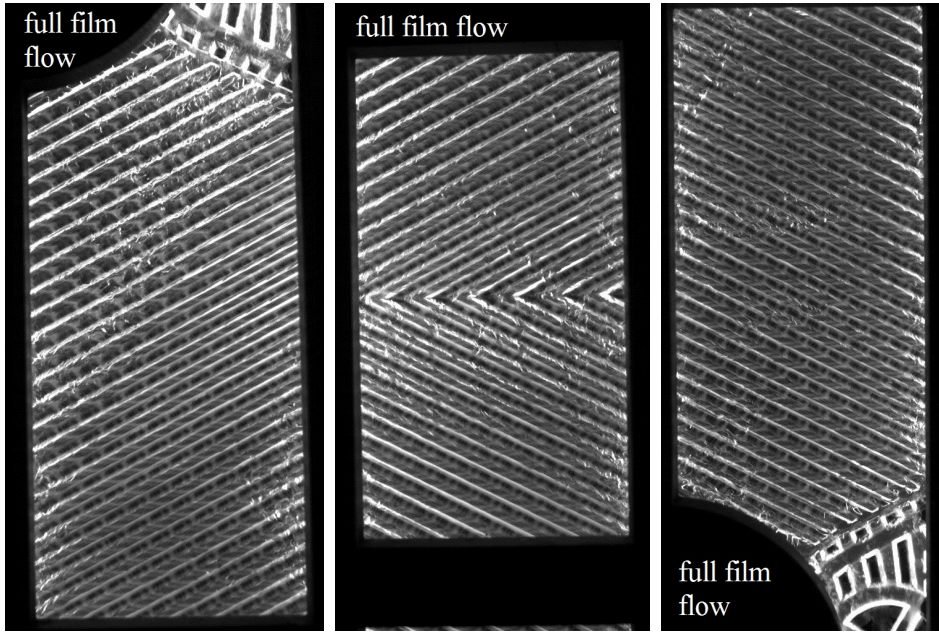
Figure 5.1: Full film flow with G=81 kgm^{-2}s^{-1} and x_{av}=0.30 at the top, middle and bottom windows. The top window is 170 mm(L)$\times$ 86 mm(W) (rectangle)+ 80 mm(L)$\times$ 86 mm(W) (triangle). The middle window is 157 mm(L)$\times$ 86 mm(W) (rectangle). The bottom window is 170 mm(L)$\times$ 86 mm(W) (rectangle)+ 80 mm(L)$\times$ 86 mm(W) (triangle). The corresponding videos are included in the Appendix of Tao et al. [45].

amplitudes, and grow larger with increasing mass fluxes. Various flow phenomena are observed, and are shown in Figure 5.2. For superposed waves, several waves interact with each other, making the flow more chaotic. Continuous waves have connected waves that flow at the same speed. These waves extend over adjacent grooves. Periodic waves flow in the same paths and have almost the same shapes. The rest waves are discrete and are independent of the other waves.

The waves gradually decrease in amplitude from the inlet to the outlet. In the inlet region, the liquid and vapor are distributed into adjacent grooves, and pass across grooves intensively. Additionally, the vapor quality decreases along the flow direction, which reduces the kinetic energy gradually. The vapor phase has larger velocity than the liquid phase, and tears liquid droplets off the film. The channel of the PHE is so narrow that droplets are easily deposited on the other side of the wall. Consequently, no stable entrained liquid droplets are formed in the vapor core.

Figure 5.3 shows partial film flow. It occurs when the liquid mass flux is re-
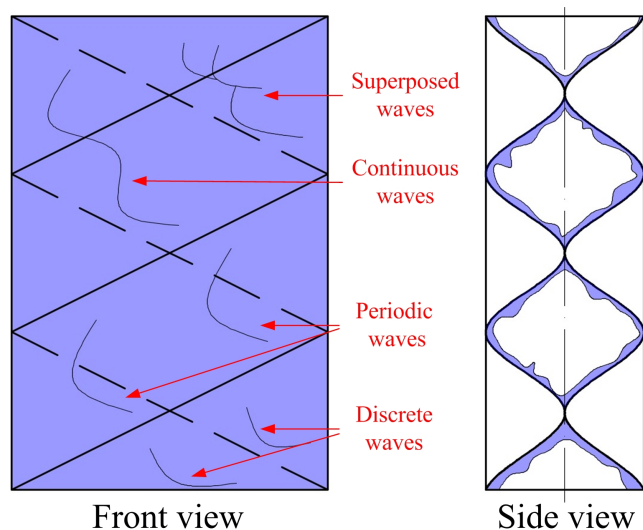
Figure 5.2: Schematic of full film flow. The wall is completely wetted by liquid. Indicating different kinds of waves. Superposed waves have several waves at the same location. Continuous waves are formed by neighbouring waves that are connected. Periodic waves repeat at the same path. Discrete waves are independent from the other waves.

duced. Less liquid results from higher vapor quality or smaller mass flux. The liquid is not enough to wet the entire wall, and parts of the wall become dry. NH_3 has large surface tension, whose influence becomes prominent in small diameter channels. Large contact angles reduce the wetting ability, break up the liquid film and change the flow pattern [148]. Large surface tension makes the liquid film discontinuous [149, 150]. Additionally, surface tension tends to stabilize the flow and suppress the waves [151]. The videos of partial film flow are provided in the Appendix of Tao et al. [45].

As shown in Figure 5.4, two types of dry zones coexist. In the first type, whole pieces of zones become dry, and the areas of these zones increase with decreasing liquid mass fluxes. In the inlet region next to the port, liquid and vapor are distributed into the parallel grooves. When the areas of these zones are small, dry zones are located close to one edge of the plate, and have triangular shapes. When these areas increase, the dry zones grow until covering most part of the plate. In the second type, dry spots are discretely distributed in the corrugated grooves. Under gravity force, these dry zones tend to appear at the top of the grooves. This flow is similar to stratified flow in inclined downward tubes. In both types, vapor condenses directly at the wall. These zones seem to be covered with a thin condensate layer, which makes it different from adiabatic flow. The layer is so thin that the observation can be subjective and needs further dis-
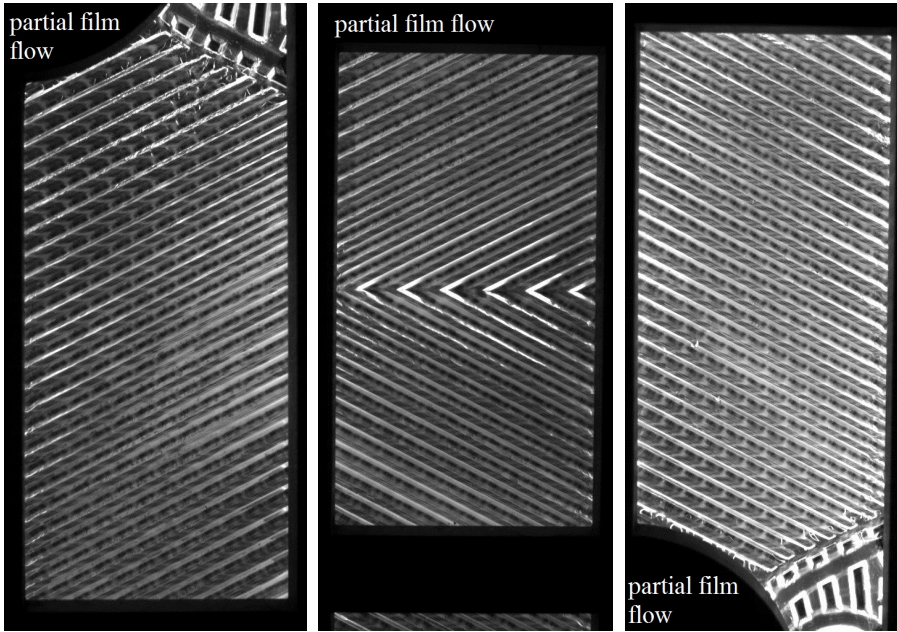
Figure 5.3: Partial film flow with G=43 kgm^{-2}s^{-1} and x_{av}=0.46 at the top, middle and bottom windows. The top window is 170 mm(L)$\times$ 86 mm(W) (rectangle)+ 80 mm(L)$\times$ 86 mm(W) (triangle). The middle window is 157 mm(L)$\times$ 86 mm(W) (rectangle). The bottom window is 170 mm(L)$\times$ 86 mm(W) (rectangle)+ 80 mm(L)$\times$ 86 mm(W) (triangle). The corresponding videos are included in the Appendix of Tao et al. [45].

cussion. Vapor condensates on the wall as long as the wall temperature is below the saturated temperature [90, 120]. During the present experiments, the inlet of the working fluid is in the two-phase region and is not superheated. The averaged wall temperature is lower than the saturated temperature for more than 1 K. Theoretically, condensation takes place once the vapor is in contact with the wall. Moreover, the occurrence of condensation can be proved from the opposite perspective. The dry zones become ineffective if condensation does not take place, and the heat transfer deteriorates because the effective area is reduced. However, the heat transfer is enhanced for partial film flow. This will be further discussed in Section 5.2.1.

The waves for partial film flow are weaker than for full film flow because of the smaller liquid mass flux. The liquid film of partial film flow is relatively thin. Thin film tends to be laminar, and the structure of two-phase interface is smoother. Deposition of entrained liquid droplets has been observed at the dry zones.
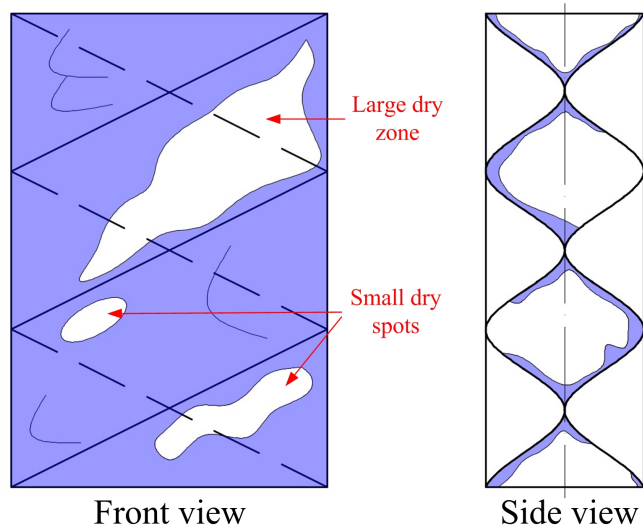
Figure 5.4: Schematic of partial film flow. The wall is completely wetted by liquid. Indicating different types of dry zones. Large dry zones tend to happen close to the inlet region. Dry spots have small areas and are discrete.

5.1.2. FLOW PATHS AND FLOW DISTRIBUTION

Section 2.4 describes flow paths, which were originally used for the flow direction of single phase flow. During two-phase flow, the liquid phase is traced by the movement of waves. Figure 5.5 schematically shows the flow paths of the liquid phase. Crossing flow goes from one side of the plate to the other side, and reflects at the edge of the plate, changing direction. Waves are more intensive close to the edge. Wavy longitudinal flow circles the contact points of two adjacent plates. The observed flow is a combination of both paths, and crossing flow is dominant. The liquid flows along grooves, and gradually goes across the grooves. The direction shifts downward. The combined flow paths make the flow turbulent at small mass fluxes, so PHEs have larger HTCs and frictional pressure drop than tubes.

Buscher [101] and Tribbe and Müller-Steinhagen [98] traced the flow paths of bubbles during bubbly flow. Crossing flow is dominant with small chevron angles (30°), while wavy longitudinal flow prevails with large chevron angles (60° and 75°). The chevron angle of the plates used in this study is 63°, and crossing flow dominates during film flow. Wavy longitudinal flow is expected if bubbly flow occurs. Apart from chevron angles, flow paths also depend on mass fluxes. Bubbly flow happens for large mass flux, while film flow obseved in this study has relatively small mass fluxes. Small mass fluxes are considered to promote crossing flow [113]. Additionally, the difference between homogeneous flow and
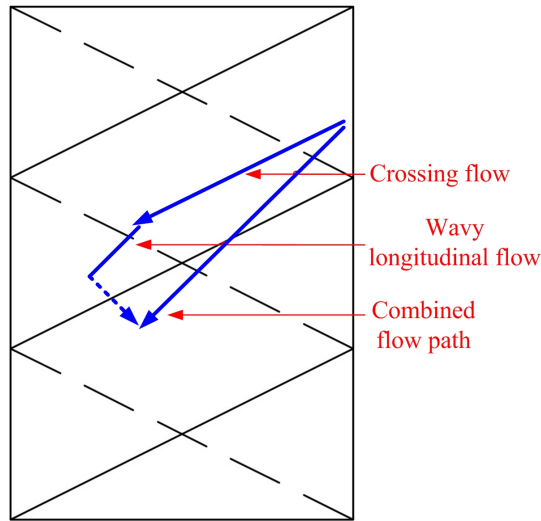
Figure 5.5: Representation of liquid flow paths. The observed flow path is a combination of crossing flow and wavy longitudinal flow, and crossing flow is dominant. The liquid flows along grooves, and gradually goes across the grooves.

separated flow plays a role. Bubbly flow tends to be homogeneous flow, and is similar to single phase flow. Film flow is separated flow, and shows distinct characteristics.

The flow distribution can be divided into three parts: inlet distributing region, fully developed region and outlet distributing region. The maldistribution of liquid and vapor is more severe at the inlet distributing region close to the inlet port. The liquid phase has larger momentum than vapor, and the flow splits among the grooves. Liquid preferentially flows into the front grooves directly connected to the inlet port, while vapor is distributed into all the grooves. At the fully developed region, the flow distribution becomes uniform in the downward direction. The flow reflects and recirculates at the edge, which improves the two-phase distribution. In the downward direction, the wave amplitudes decrease and the two-phase interface becomes smoother. Similar distribution was observed during the visualization of air/water flow without phase change [19]. At the outlet distributing region, the flow is gathered into the port. The test section has triangular inlet and outlet areas confined by the gasket, where the flow section area changes gradually and the fluid is well distributed.

5.1.3. FLOW PATTERN MAP
Figure 5.6 presents the flow pattern map plotted with the mass flux and vapor quality, which indicates the condensation process. The map includes the flow
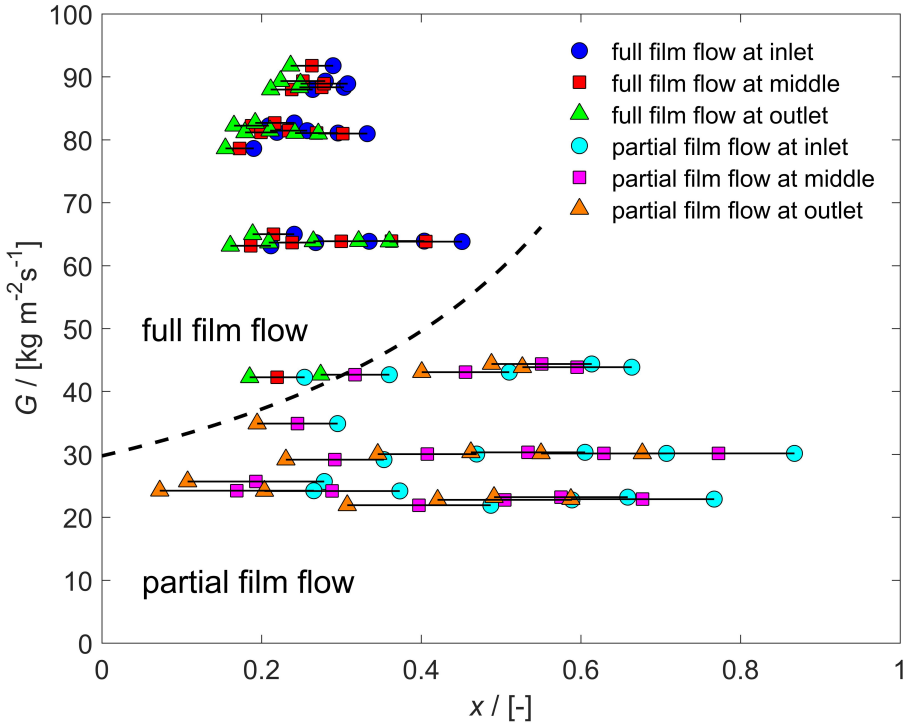
Figure 5.6: Flow pattern map of condensing flow in the PHE, with the vapor quality decreasing from the inlet to the outlet. The flow patterns at the inlet, middle and outlet windows of the same operating condition are connected by lines.

patterns at the inlet, middle and outlet of the test section, which were observed from the three windows. The data points are assigned to the inlet, averaged and outlet vapor qualities, respectively. These three flow patterns for each operating condition are connected by lines. The condensation is from the right end to the left end of the lines. The change of vapor qualities is small. At large and small mass fluxes, the flow patterns remain the same from the inlet to outlet, while the flow patterns change in the flow direction for intermediate mass fluxes.

Full film flow occurs at large mass fluxes or the combination of intermediate mass fluxes and low vapor qualities. On the contrary, partial film flow is at small mass fluxes or the combination of intermediate mass fluxes and high vapor qualities. Flow patterns depend on the liquid mass flux. A certain amount of liquid is required to completely wet the wall surfaces, otherwise the thin liquid film breaks up. The minimum wetting mass flux depends on the surface tension, liquid density and liquid viscosity. The liquid velocity distribution is not uni-

form especially for large contact angles [152, 153]. At intermediate mass fluxes of low vapor qualities, partial film flow changes into full film flow from the inlet to the outlet. These data points are considered to be in the transition region. The vapor quality decreases in the flow direction with increasing liquid mass fluxes. Moreover, the flow distribution among grooves becomes more uniform after reflection at the plate edges. This phenomenon illustrates the influence of the inlet distributing region on flow patterns. Partial film flow occurs at small mass fluxes. In the top window, dry zones are continuous and stretch. In the middle and bottom windows, liquid tends to be distributed among grooves uniformly. Dry spots are discrete in each groove.

5.2. HEAT TRANSFER COEFFICIENT

Condensation experiments of NH_3 are carried out. The sensitivity of HTCs and frictional pressure drop to vapor qualities, mass fluxes and saturated pressures is investigated. Because of the large latent heat, the change of the vapor qualities is small, and the following discussion is represented with the averaged vapor qualities. The measured HTCs and frictional pressure drop are considered to be quasi-local. During the experiments, some data points were repeated by increasing and decreasing the heating capacity, respectively. The repeatability is proved to be reliable.

5.2.1. EXPERIMENTAL HEAT TRANSFER COEFFICIENTS AND DISCUSSION

The condensation HTCs are large, and the corresponding heat transfer resistances are relatively small compared with the water side. In order to improve the measurement accuracy, the water side mass fluxes were kept large to reduce the corresponding heat transfer resistance. In the tested ranges, the ratio of heat transfer resistance between the condensation side to water side has an averaged value of 1.6. Additionally, the accurate measurement of the heat duty requires large rise of the cold water temperature, whose averaged value is 2.8 K during testing. HTCs larger than 30000 $Wm^{-2}K^{-1}$ are excluded because of their large uncertainty.

   Figure 5.7 illustrates the HTCs variation with averaged vapor qualities and mass fluxes. The saturated pressure is 690 kPa. It covers the averaged vapor qualities of 0.05-0.65 and mass fluxes of 21-78 $kgm^{-2}s^{-1}$. Limited by the cooling capacity of the setup, higher vapor quality cannot be obtained. HTCs increase sharply and almost linearly with vapor qualities. For 42 $kgm^{-2}s^{-1}$, the HTCs increase 2.5 times when the averaged vapor qualities rise from 0.2 to 0.65. A slight rise of the vapor quality increases the volume flux noticeably. The transition of flow patterns has been observed during the visualization experiments. With increasing vapor qualities, the vapor velocity increases and the film thickness de-
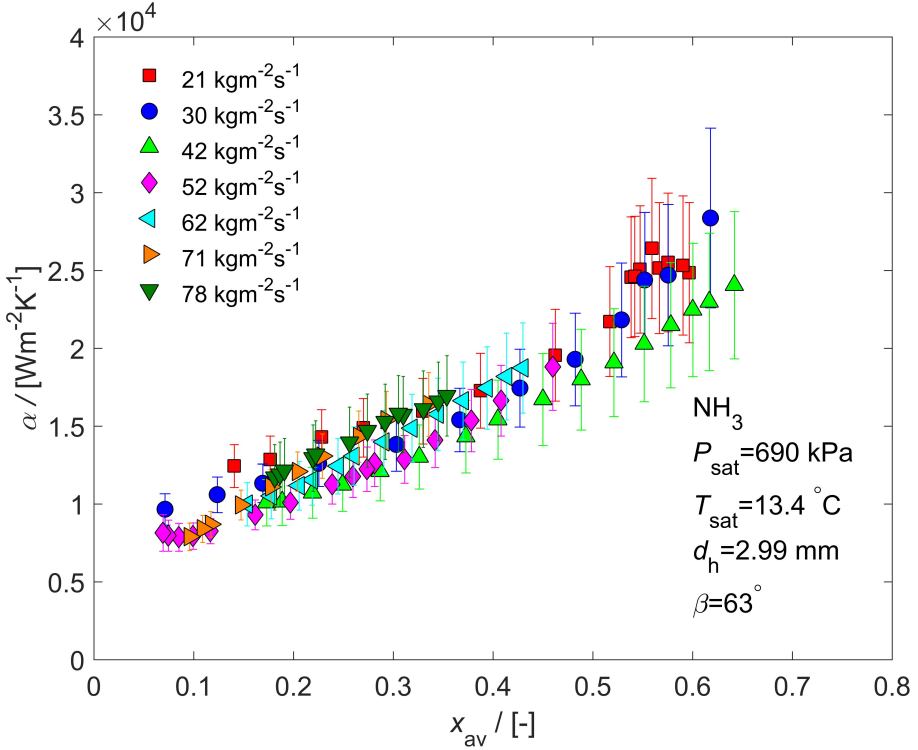
Figure 5.7: Condensation HTCs with varying averaged vapor quality at different mass fluxes. HTCs increase significantly with vapor qualities. HTCs decrease slightly with mass fluxes in the range of 21-42 kgm⁻²s⁻¹, and increase moderately from 42 to 78 kgm⁻²s⁻¹.

creases. Larger shear force disturbs the two-phase interface and enhances the heat transfer. Moreover, at high vapor qualities, the liquid film is locally extremely thin. The vapor condenses directly on the wall and the heat transfer resistance is small. Since NH_3 has a large two-phase density ratio, the sensitivity to vapor quality is stronger than for other refrigerants such as R134a and R410A [61, 71].

The influence of mass fluxes is not monotonic. HTCs decrease slightly with mass fluxes in the range of 21-42 $kgm^{-2}s^{-1}$, and increase moderately from 42 to 78 $kgm^{-2}s^{-1}$. It is attributed to the change of flow patterns. At small mass fluxes, a part of the wall surface is dry due to small amounts of liquid. The vapor velocity is low, and only limited shear force is exerted on the two-phase interface. Thus the liquid film is laminar. The condensation process is divided into two parts. Some vapor condenses directly on the wall, while other condenses on the two-phase interface where the wall is wetted. Gravity-controlled condensation dom-
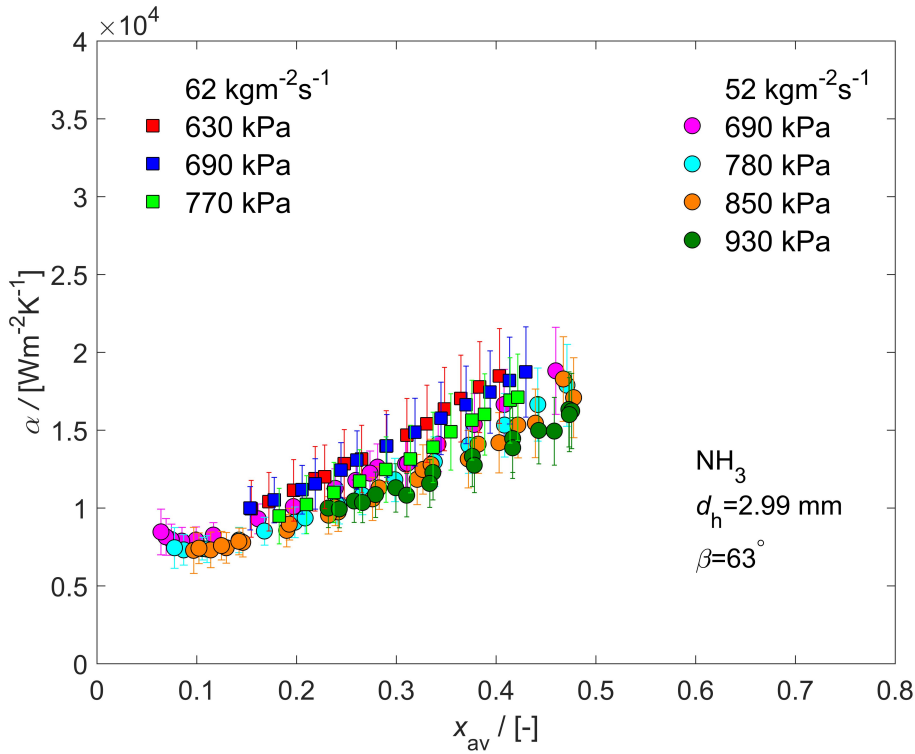
Figure 5.8: Condensation HTCs with varying averaged vapor quality at different condensation pressures. HTCs increase sharply with vapor qualities. Higher condensation pressures slightly reduce HTCs.

inates over convective condensation. For a certain vapor quality, the portion of wetted surface increases with mass fluxes because of more liquid. Consequently, the heat transfer resistance slightly increases. At large mass fluxes, the wall surface is completely wetted. Shear force is dominant, and convective condensation applies. For a certain vapor quality, the mass fluxes of both vapor and liquid increase. Higher vapor velocities intensify shear force and promote ripples on the two-phase interface. The liquid film becomes turbulent with increasing mass fluxes, while thicker liquid film increases the heat transfer resistance. As a consequence, HTCs increase moderately with mass fluxes at large values. In Figure 5.7, the averaged uncertainty of HTCs is ±14.4%. The measurement uncertainty is contributed by temperature sensors and flow meters. The temperature difference is smaller for higher HTCs, and the relative error becomes significant, which contributes prominently to the uncertainty propagation.

In Figure 5.8, the influence of saturated pressure is shown at two mass fluxes.
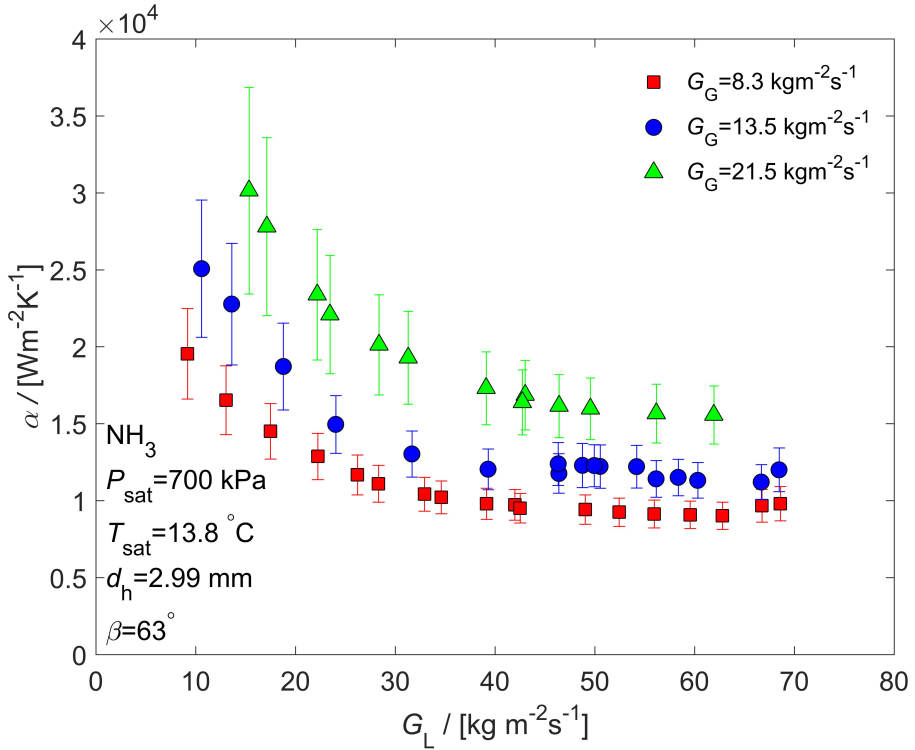
Figure 5.9: Condensation HTCs with varying liquid and vapor mass fluxes. HTCs decrease with increasing liquid mass fluxes at small values, and stay almost constant at larger values. Larger vapor mass fluxes increase the HTCs.

The trends at these mass fluxes are similar, and only the values at 52 $\text{kgm}^{-2}\text{s}^{-1}$ are discussed. HTCs decrease slightly with increasing saturated pressure, and become about 20% lower from 690 to 930 kPa. Higher saturated pressure has smaller two-phase density ratio, and the shear force at the interface is reduced. The thermal conductivity of liquid also decreases at higher pressure. Despite the minor effect of saturated pressure, the influence of vapor qualities is still significant. The averaged uncertainty of HTCs is ±14.1% according to the uncertainty analysis.

Figure 5.9 further presents the influence of liquid and vapor mass fluxes. The visualization experiments have indicated separated flow. For this reason, the two-phase mass fluxes are investigated separately.

The slope of HTCs for a certain vapor mass flux is divided into two parts. HTCs decrease noticeably with increasing liquid mass fluxes at small values, and stay almost constant at larger values. The liquid film is the main heat transfer

resistance during condensation. At small liquid mass fluxes, partial film flow applies, and a part of the wall surface is not wetted. Vapor condensates directly on the wall. The area of the dry zones decreases with increasing amount of liquid, and the HTC decreases significantly. At a certain value, the wall gets completely wetted. It becomes full film flow. Further increase of mass flux thickens the liquid film. Meanwhile, the liquid flow becomes more turbulent. These two effects counteract each other. Consequently, HTCs remain constant. The slope of HTCs changes at the liquid mass fluxes of around 40 kgm^{-2}s^{-1}. Partial film flow has larger HTCs than full film flow. This confirms that condensation takes place in the dry zones and indicates that all the heat transfer area is effective for partial film flow.

Larger vapor mass fluxes enhance the heat transfer. Higher vapor velocities intensify the two-phase shear and thin the liquid film. The enhancement is larger for partial film flow. Droplet entrainment is promoted by the higher vapor velocities and tends to increase the heat transfer.

5.2.2. Comparison with existing correlations

In Chapter 3, condensation heat transfer correlations in PHEs are summarized, and an extensive experimental database is developed [18]. Eight correlations have been assessed by comparing with the database. The correlations of Longo et al. [60] and Kuo et al. [61] show the best performance for the experimental data of HFCs, HCs and HFOs. Nevertheless, NH$_3$ is not included in the database.

Figure 5.10 compares these two correlations with the experimental data for three mass fluxes. Kuo et al. [61]'s correlation is a two-phase multiplier approach, which assumes annular flow [56]. The condensation heat transfer is similar to the convective heat transfer of liquid phase since all the heat is transferred through the liquid [56]. The vapor flow and heat flux enhance the heat transfer and are considered as a two-phase multiplier. According to this correlation, HTCs increase significantly with the vapor quality, agreeing with the trend of the experimental data.

The correlation of Longo et al. [60] is composed of convective condensation and gravity-controlled condensation. The convective correlation involves the equivalent Reynolds number, which treats the two-phase flow as a single equivalent fluid. The vapor flow is replaced with an additional liquid flow by keeping the same shear force at the two-phase interface. The conversion ratio depends on the two-phase density ratio [154]. In Figure 5.10, the sensitivity to the vapor quality is less noticeable than for the experimental data. Convective condensation is transformed into gravity-controlled condensation at low vapor qualities and small mass fluxes. The HTCs become insensitive to mass fluxes and vapor qualities.
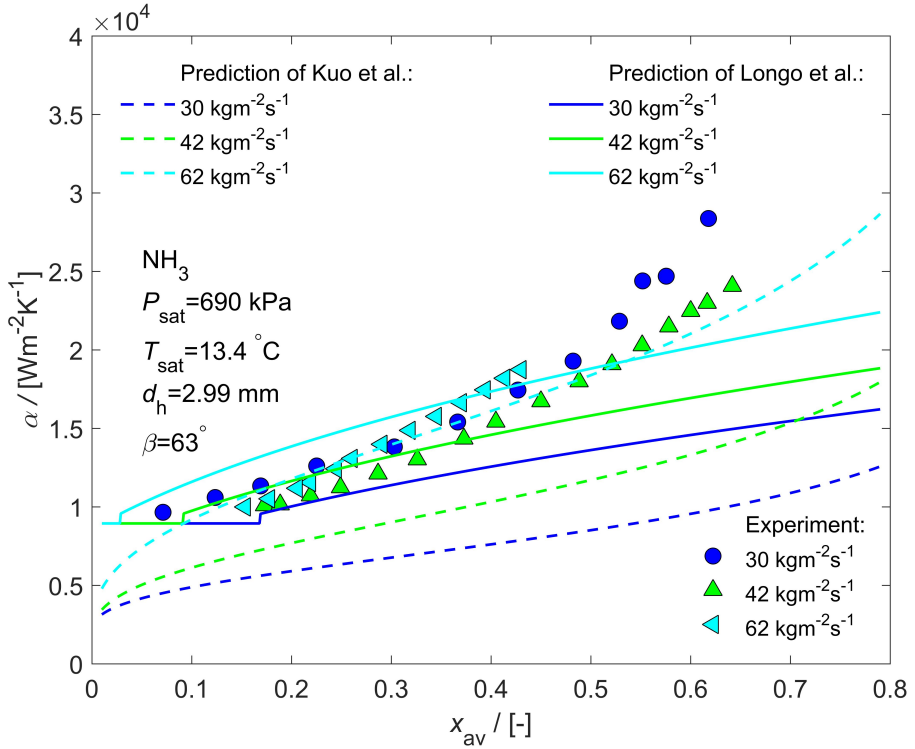
Figure 5.10: Condensation HTCs of NH_3 with varying averaged vapor quality and mass fluxes. Comparison of experimental and predicted data. The prediction is from Longo et al. [60] (solid lines) and Kuo et al. [61] (dashed lines).

Figure 5.11 presents the accuracy of the correlations. The correlation of Kuo et al. [61] predicts 75.7% of the experimental data within ±30%. The mean absolute error (MAE) is 21.3%. This correlation estimates correctly the significant sensitivity to vapor qualities and shows consistent trend with the experimental data. Nevertheless, predicted data of different mass fluxes are separated. This correlation is more accurate for intermediate and large mass fluxes, and dramatically under-predicts the data of small mass fluxes. Longo et al. [60]'s correlation predicts 72.4% of the data within ±30%. It over-predicts the experimental HTCs at low vapor qualities, and under-predicts the experimental HTCs at high vapor qualities. The predicted values of large and intermediate mass fluxes converge, but the under-prediction for small mass flux is noticeable. In short, the correlation of Kuo et al. [61] over-estimates the influence of mass fluxes, while Longo et al. [60]'s correlation cannot predict the sharp sensitivity to vapor qualities. A new correlation needs to be developed for NH_3 condensation [59].
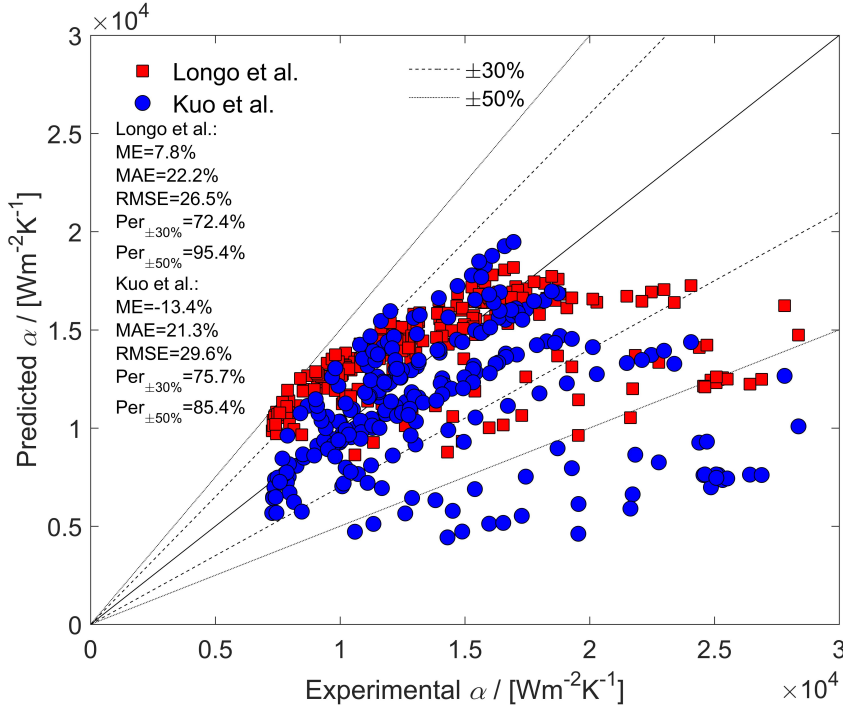
Figure 5.11: Comparison of NH$_3$ condensation HTCs with the correlations of Longo et al. [60] and Kuo et al. [61]. Mean error (ME): $\frac{1}{n}\sum_1^n \frac{\alpha_{\mathrm{pre}}-\alpha_{\mathrm{exp}}}{\alpha_{\mathrm{exp}}}$; Mean absolute error (MAE): $\frac{1}{n}\sum_1^n \frac{|\alpha_{\mathrm{pre}}-\alpha_{\mathrm{exp}}|}{\alpha_{\mathrm{exp}}}$; Root mean squared error (RMSE): $\sqrt{\frac{1}{n}\sum_1^n \left(\frac{\alpha_{\mathrm{pre}}-\alpha_{\mathrm{exp}}}{\alpha_{\mathrm{exp}}}\right)^2}$; $Per_{\pm 30\%}$: Percentage of experimental data within $\pm 30\%$; $Per_{\pm 50\%}$: Percentage of experimental data within $\pm 50\%$.

5.3. FRICTIONAL PRESSURE DROP

5.3.1. EXPERIMENTAL FRICTIONAL PRESSURE DROP AND DISCUSSION

Figure 5.12 shows the influence of averaged vapor qualities and mass fluxes on frictional pressure drop. At certain mass fluxes, frictional pressure drop increases almost linearly with vapor qualities. The increase is sharper at large mass fluxes. When the averaged vapor qualities have an increment of 0.1, the frictional pressure drop increases about 10 kPam^{-1} for 71 kgm^{-2}s^{-1} and increases 2 kPam^{-1} for 30 kgm^{-2}s^{-1}. The flow patterns have relatively small influences on frictional pressure drop compared with heat transfer [135]. Both full film flow and partial film flow are separated flows. Liquid and vapor flow separately and interact on the interface. The two-phase pressure drop is contributed by the following shear forces: between the vapor and wall, between the liquid and wall and at the two-phase interface. The volume flux and averaged velocity increase signifi-
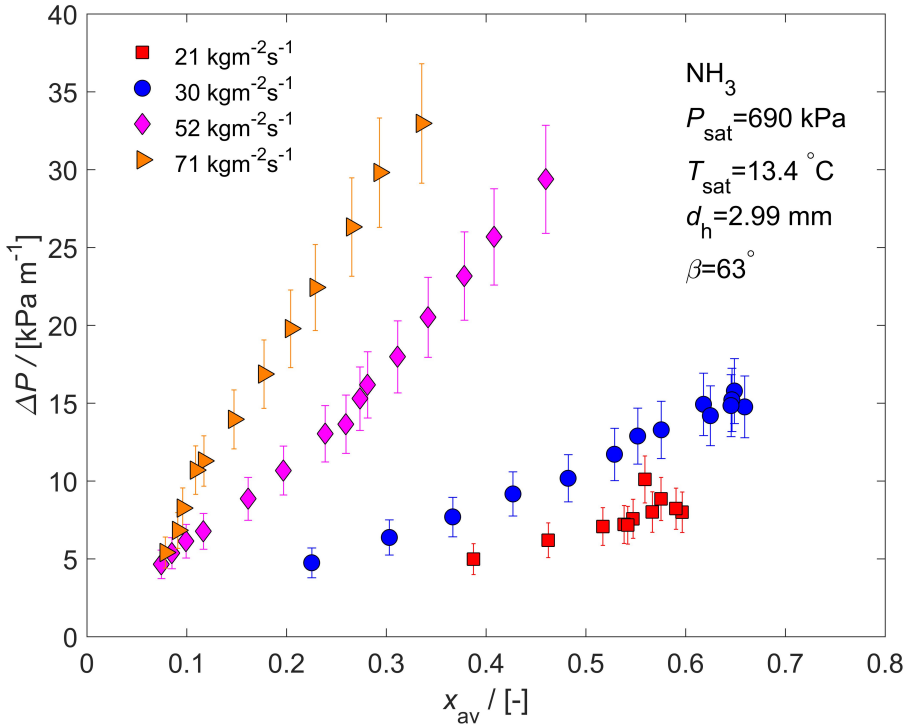
Figure 5.12: Frictional pressure drop with varying averaged vapor quality at different mass fluxes. Frictional pressure drop increase significantly with vapor qualities and mass fluxes.

cantly with vapor quality, and the shear forces are greatly enhanced.

Frictional pressure drop increases sharply with mass fluxes. Larger liquid mass fluxes thicken the film thickness and promote turbulence. Vapor phase has larger velocity than liquid and shaves the two-phase interface. Larger vapor mass fluxes intensify the shear forces and dissipate the momentum intensively. In Figure 5.12, the averaged uncertainty of frictional pressure drop is ±15.0%. As shown in Table 4.1, the differential pressure sensor has high accuracy. But the pressure drop fluctuates due to the operation of the working fluid pump. An extra uncertainty of ±10.0% is included. In order to ensure the accuracy, frictional pressure drop values lower than 3.5 kPam^{-1} are excluded.

Figure 5.13 shows the sensitivity to saturated pressures. The influence is negligible at low vapor qualities, and becomes noticeable at high vapor qualities. It is attributed to the change of vapor density. Higher saturated pressure has insignificant effects on liquid density, but increases vapor density remarkably. At high vapor qualities, higher saturated pressure decreases the averaged velocity
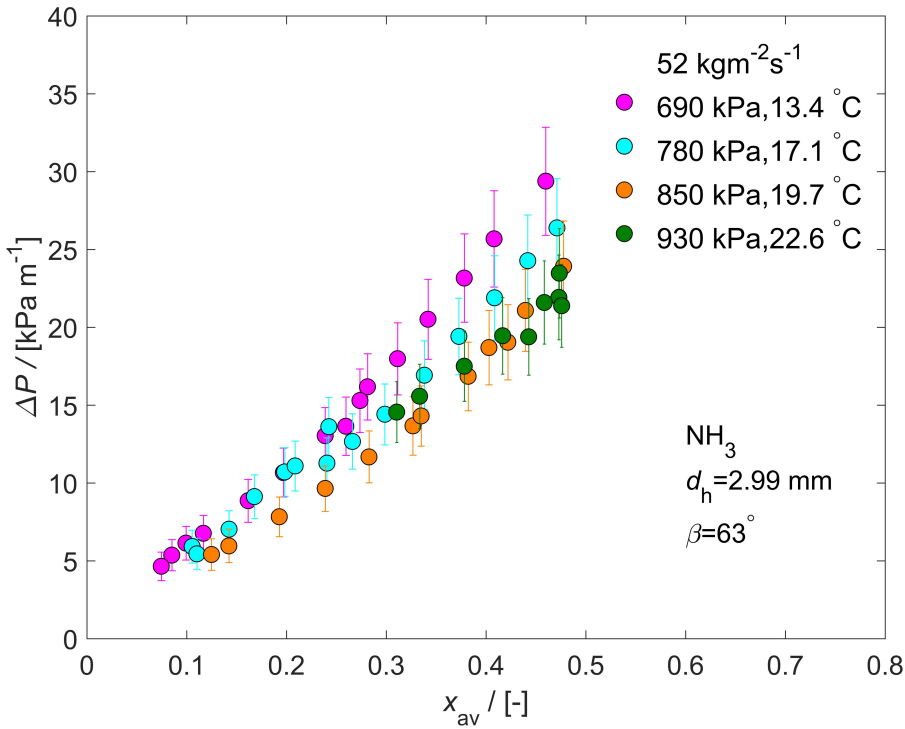
Figure 5.13: Frictional pressure drop with varying averaged vapor quality at different condensation pressure. Frictional pressure drop increases sharply with vapor qualities. Higher condensation pressures reduce frictional pressure drop.

because of the larger vapor density, and consequently reduces the momentum dissipation. Frictional pressure drop has an averaged uncertainty of ±14.2%.

Figure 5.14 shows the influence of liquid and vapor mass fluxes separately, and both phases contribute to the frictional pressure drop. At different vapor mass fluxes, the frictional pressure drop increases with liquid mass fluxes of similar trend. When the vapor mass flux increases from 13.5 to 21.5 $kgm^{-2}s^{-1}$, the frictional pressure drop more than doubles. In the same range of liquid mass fluxes, the frictional pressure drop increases about 1.2 times. This is in agreement with the phenomenon of separated flow. The vapor flow dominates the frictional pressure drop since the large velocity intensifies the momentum dissipation. For partial film flow, the trend lines with the variation of liquid mass fluxes are slightly steeper than those for full film flow. The frictional pressure drop is less affected by the transition from full film flow to partial film flow, while the transition has significant influences on heat transfer.
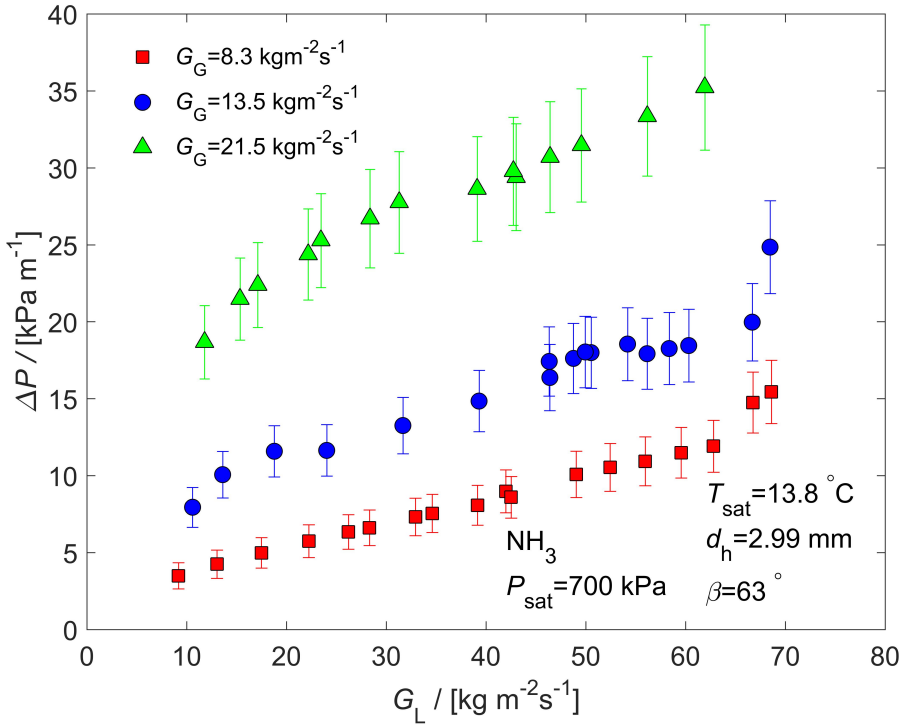
Figure 5.14: Frictional pressure drop with varying liquid and vapor mass fluxes. Frictional pressure drop increase with liquid mass fluxes and vapor mass fluxes.

5.3.2. COMPARISON WITH EXISTING CORRELATIONS

In Chapter 3, six frictional pressure drop correlations are assessed with an experimental database, including two-phase Fanning friction factor and Lockhart-Martinelli model [18]. The prediction of the correlations is poor, and a new correlation has been developed. In the previous researches of PHEs, Lockhart- Martinelli's model is mostly chosen for air/water flow [19, 98, 100]. The air/water system is characterized by a large two-phase density ratio, and separated flow patterns such as full film flow and partial film flow cover large ranges [10]. The database is mostly composed of HFCs, HCs and HFOs, whose two-phase density ratio is relatively small [18]. Nino et al. [155] and Adams et al. [156] suggested the homogeneous void fraction for fluids of small liquid-vapor density ratio and separated void fraction for large density ratio. The new correlation assumes homogeneous flow and calculates the two-phase Fanning friction factor. When applied for NH$_3$, this correlation significantly over-predicts the experimental data [11]. The two-phase slip ratio of NH$_3$ is much larger than 1. The homogeneous

void fraction over estimates the averaged velocity and thus the shear force. Jassim et al. [127] proposed to calculate the averaged density using the separated void fraction model.

The visualization experiments indicate that the NH_3 flow is separated [45]. To the best of the authors' knowledge, no void fraction model is specially developed for PHEs, and related researches can be referred to. In micro-channels, Nino et al. [155] and Adams et al. [156] tested the void fraction of five refrigerants representing a large range of two-phase densities. The homogeneous void fraction is suggested for refrigerants whose two-phase density ratio is small. A separated void fraction model is proposed for refrigerants of large density ratio. Yashar et al. [157] developed a separated void fraction model for smooth and micro-fin tubes, which was validated by a large number of experimental data and showed good performance [127].

da Silva Lima et al. [136] recommended the drift flux model of Rouhani and Axelsson [158] to calculate the void fraction of NH_3 during evaporation. According to Wojtan et al. [159] and El Hajal et al. [107], the void fraction model of Rouhani and Axelsson [158] is suggested for evaporation, and the log mean of this model and the homogeneous model is recommended for condensation. Additionally, Keinath and Garimella [160] measured the void fraction in micro-channels at large mass fluxes, and proposed a drift flux model. The void fraction was not sensitive to flow patterns in the tested range. Jassim et al. [127] analyzed the frictional pressure drop of two-phase flow in PHEs. It was argued that the homogeneous void fraction model over-predicted the averaged density corresponding to experimental data.

Figure 5.15 compares the void fraction models of Nino et al. [155] and Yashar et al. [157]. The homogeneous model and Zivi's [161] model are taken as reference. The homogeneous model is the upper limit. Zivi [161] derived the void fraction model from entropy generation minimization, and claimed that his model provides the lower limit. These two reference models are theoretical and are not sensitive to mass fluxes. Void fractions increase sharply with vapor qualities at low values, especially in the range of 0-0.2. The over-prediction of the homogeneous model is significant in this range. At higher vapor qualities, the prediction of Nino et al. [155] model is significantly lower than Zivi's [161] model. According to the definition, all the void fraction models become 0 when the flow is pure liquid, and approach 1 when it is pure vapor. When the vapor quality is increased to 1, the void fraction of Nino et al. [155] is slightly lower than 1 for small mass fluxes. The void fraction of Yashar et al. [157] is generally consistent with Zivi's [161], with the values larger at low vapor qualities and smaller at high vapor qualities. Additionally, the models of Nino et al. [155] and Yashar et al. [157] increase slightly with mass fluxes.

Figure 5.15: Comparison of Nino et al. [155] void fraction and Yashar et al. [157] void fraction for varying mass fluxes. The homogeneous model is the upper limit, while Zivi [161] provides the lower limit.

Figure 5.16 shows the void fraction models of Rouhani and Axelsson [158] and El Hajal et al. [107]. Rouhani and Axelsson's [158] model was originally developed for flow boiling. This model is sensitive to mass fluxes and includes the influence of surface tension. The predicted values are lower than Zivi's [161] model at high vapor qualities. Since Rouhani and Axelsson's [158] model is less suitable for high pressure, El Hajal et al. [107] calculated the log mean of this model and homogeneous model for condensation. The predicted values of El Hajal et al. [107] are between the homogeneous model and Zivi's [161] model at low vapor qualities, and approach Zivi's [161] model from intermediate to high vapor qualities.

The averaged density is calculated according to Eq. 2.6 using the models of Zivi [161] and Rouhani and Axelsson [158]. The results are presented in Figure 5.17. Zivi [161] proposed a theoretical model and claimed to provide the lower limit of void fraction. Rouhani and Axelsson's [158] model is suitable for low pres-
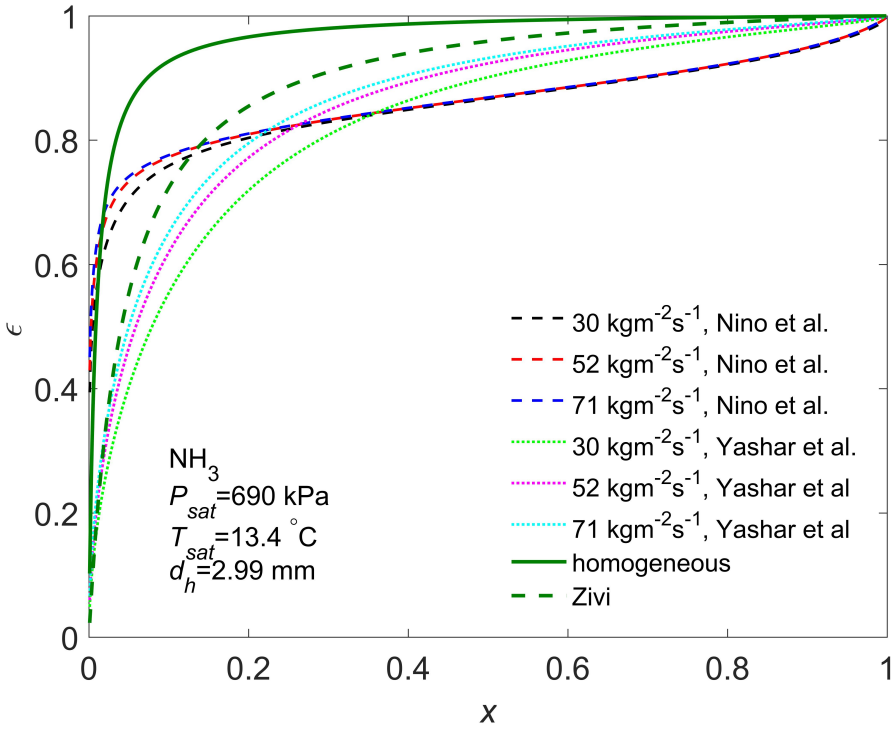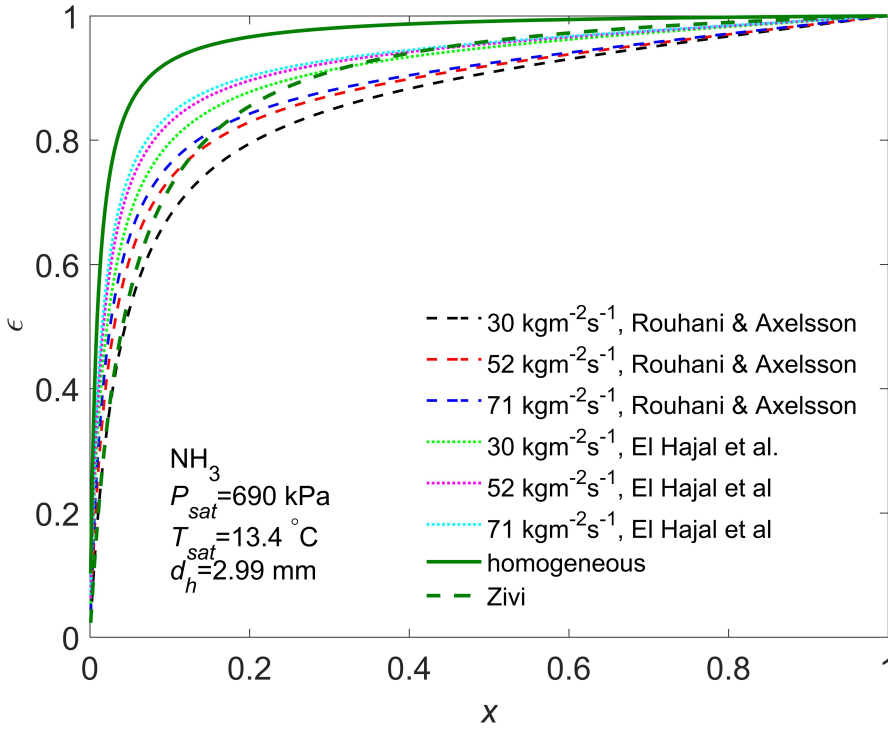
Figure 5.16: Comparison of Rouhani and Axelsson [158] void fraction and El Hajal et al. [107] void fraction for varying mass fluxes. The homogeneous model is the upper limit, while Zivi [161] provides the lower limit.

sure, which corresponds to the experimental data of this thesis.

According to Figure 5.17, both prediction methods show larger values than the experimental data. The possible reason is that the estimated void fraction is larger than the actual values in PHEs. At low vapor qualities, the prediction based on Zivi [161] void fraction has deviations larger than three times. The slope of the lines based on Rouhani and Axelsson's [158] void fraction becomes flat at intermediate vapor qualities. The flow passage of PHEs is approximately rectangular, and the ratio of width to length is small. The channel has a corrugated structure and is interrupted by the contact points of adjacent plates. The void fraction is different from what applies for smooth channels. Liquid is likely to be held at the corner of the flow passages and at the contact points, which reduces the liquid velocity and increases the slip ratio. The void fraction consequently decreases. Figure 5.18 shows the void fraction calculated by Wilson et al.'s [162] model, which indicates the geometry influence by comparing round
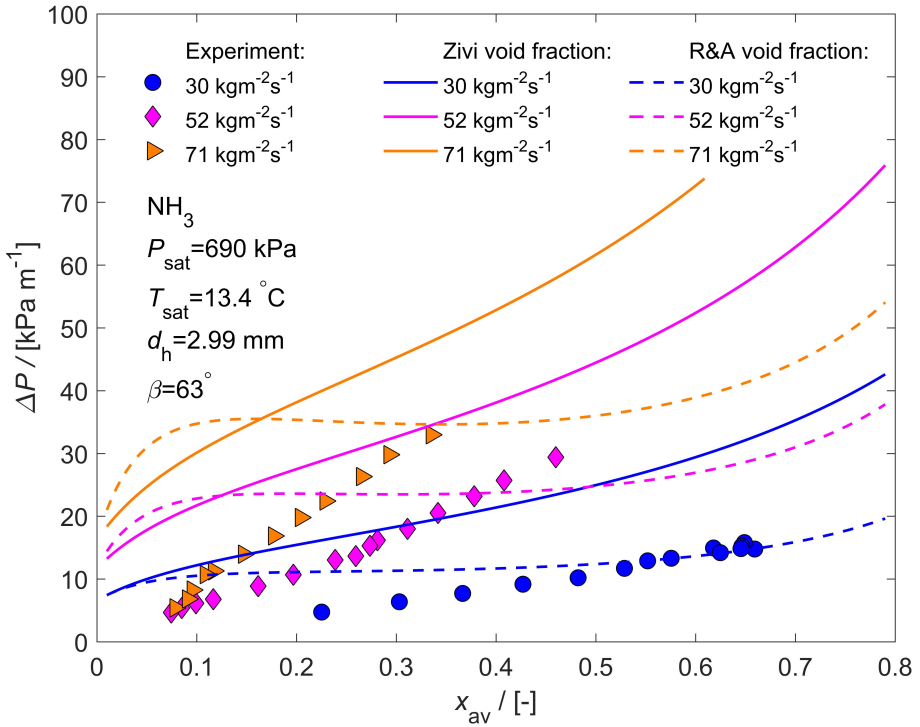
Figure 5.17: Frictional pressure drop of NH₃ with varying averaged vapor quality and mass fluxes. Comparison of experimental and predicted data. The prediction is from Tao and Infante Ferreira (2019) and is based on the void fraction of Zivi [161] (solid lines) and Rouhani and Axelsson [158] (R&A) (dashed lines).

tubes and oval tubes with and without microfins. The void fraction in oval tubes is lower than in round tubes. The oval tubes are flatter for smaller heights and have lower void fraction. Microfin tubes have generally lower void fraction than smooth tubes. The void fraction of smooth-round tubes is close to Zivi [161] model, while the micro-fins and oval structures reduce the void fraction. Moreover, in Figure 5.17, the experimental data increase sharply with vapor qualities, which is a characteristic of separated flow.

Although the calculation proposed in Chapter 3 has been derived from an extensive experimental database, the application is limited to the working fluids covered by the database (HFCs, HCs and HFOs), which are characterized by small two-phase density ratio and tend to stream in homogeneous flow [18]. Triplett et al. [163] concluded that the homogeneous model predicted correctly the frictional pressure drop of bubbly and slug flow, but significantly over-estimated the
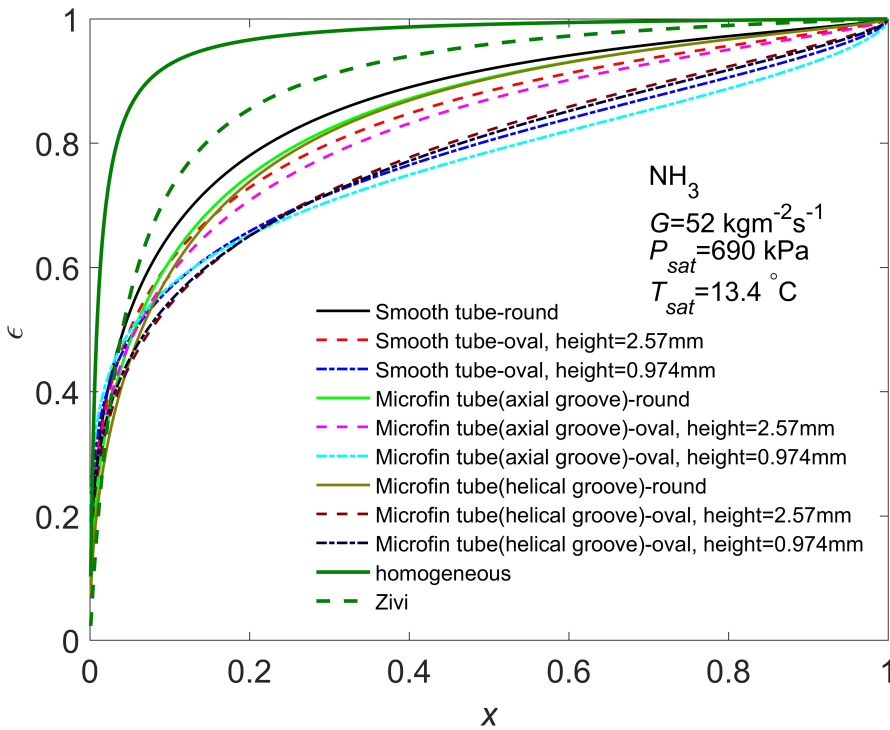
Figure 5.18: Influence of geometrical structure on void fraction. Round tubes and oval tubes with and without microfins are compared. The oval tubes with 0.974 mm height are flatter than those with 2.57 mm (adapted from Wilson et al., [162]).

data of annular flow. The flow of NH_3 is separated. The frictional pressure drop needs to be analyzed making use of a different approach [59].

5.4. CONCLUSIONS

In this Chapter, NH_3 condensation in PHEs is experimentally investigated. The experimental results are compared with selected correlations.

- In the tested ranges, the flow patterns are full film flow and partial film flow. The transition mainly depends on the wetting characteristics. Full film flow occurs at large liquid mass fluxes, while partial film flow takes place at small liquid mass fluxes. The inlet distribution also plays a role. The liquid is unevenly distributed among grooves close to the inlet, and becomes uniform along the flow direction.

- HTCs increase significantly with vapor qualities. HTCs decrease with mass

fluxes from 21 to 42 kgm^{-2}s^{-1}, and then increase with mass fluxes in 42-78 kgm^{-2}s^{-1}. The transition is at the overall mass flux of 42 kgm^{-2}s^{-1}. HTCs decrease slightly with increased saturated pressures. Heat transfer is enhanced for partial film flow since vapor condenses directly on the dry zones. In Chapter 3, the heat transfer correlations of Longo et al. [60] and Kuo et al. [61] are recommended for HFCs, HCs and HFOs, but under-predict the data of NH$_3$.

• Frictional pressure drop increases sharply with vapor qualities and mass fluxes. Larger two-phase mass fluxes enhance the shear forces at the interface and at the wall. Frictional pressure drop slightly decreases with increasing saturated pressures. In Chapter 3, a correlation of two-phase Fanning friction factor is proposed for frictional pressure drop of HFCs, HCs and HFOs, which over-predicts the data of NH$_3$.

The HTCs and frictional pressure drop show the characteristics of separated flow. The flow patterns result from the fluid properties of NH$_3$ and form the basis of predictive models for NH$_3$ condensation in PHEs, which is discussed in Chapter 6.

6

FLOW PATTERN BASED MODELS OF NH$_3$ CONDENSATION

In this Chapter, the theories of condensation in tubes are reviewed including heat transfer and frictional pressure drop. These theories are referred to develop the predictive models for PHEs. The heat transfer model is based on flow patterns and identifies the transition of condensation mechanisms. The transition criterion reveals the wetting characteristics. A modified Lockhart-Martinelli model is proposed to predict the frictional pressure drop, which characterizes separated flow.

6.1. PREVIOUS PHYSICALLY BASED MODELLING OF CONDENSA- TION

During condensation in tubes, the theory of heat transfer and frictional pressure drop has been established to describe the physical process of two-phase flow. The theoretical researches on PHEs are limited, and the geometric influence is not thoroughly understood. This Section reviews the previous studies that are used as the starting points to develop the predictive models.

6.1.1. HEAT TRANSFER MODELS BASED ON FLOW PATTERNS

During the condensation in horizontal tubes, flow pattern based heat transfer models have been recognized to be accurate and widely applicable. Annular flow is modelled as fully convective condensation. Stratified flow is considered to combine gravity-controlled condensation at the top of the tube and convective condensation at the bottom, and gravity-controlled condensation is mostly dominant. Slug and churn flows fall into these two regimes and are not analyzed separately. Bubbly flow only takes place at large mass fluxes, which go beyond the general operating ranges of condensation [68, 106, 107, 126]. Some papers used different terms, but the physical interpretation is similar [164].

Dobson and Chato [106] experimentally analyzed the reliance of HTCs on flow patterns. The flow patterns are classified into gravity-controlled flow and shear-controlled flow. In gravity-controlled regime, HTCs are sensitive to temperature driving force but are almost independent of mass fluxes. The HTCs of shear-controlled flow are characterized by the significant influences of mass fluxes and vapor qualities. These authors proposed mechanistic models for these two condensation regimes.

Thome et al. [126] developed heat transfer models on the basis of a flow pattern map [107]. The liquid film thickness is assumed to be uniform for annular flow. The film thickness is calculated using a void fraction model [158]. Convective condensation takes place for annular flow. For stratified flow, the film is considered as a part of the annular ring located at the bottom, where convective condensation prevails. The wall is unwetted at the top, where the Nusselt theory is applied. The portions of the two condensation mechanisms are determined by stratified angles. To predict NH$_3$ in-tube (8 mm diameter) condensation, Park and Hrnjak [42] kept the flow pattern map and condensation mechanisms of El Hajal et al. [107] and Thome et al. [126], but modified the heat transfer correlations.

Cavallini et al. [68] divided the condensation mechanisms according to the dependence on temperature driving force. Temperature driving force independent regime is equivalent to convective condensation, while temperature driv-

ing force dependent regime is similar to gravity-controlled condensation. The non-dimensional gas velocity, J_G, is calculated in Eq. 2.20. When J_G is larger than the transition value, convective condensation applies. At smaller values of J_G, the HTC combines convective condensation and Nusselt correlations. Fronk and Garimella [37, 69] developed a heat transfer model for NH_3 condensation in small diameter tubes (0.98, 1.44 and 2.16 mm). They also used J_G as the transition criterion. For annular flow, the heat transfer is enhanced by the interfacial roughness arising from two-phase momentum difference. The correlations of Cavallini et al. [68] were recommended for non-annular flow.

The above models have been proposed for horizontal flow. Shah [164] specified the influence of flow directions. During horizontal flow, condensation mechanisms were divided into convective condensation and gravity-controlled condensation. Fully gravity-controlled condensation only happens for vertical and inclined flow. The difference between gravity-controlled condensation and fully gravity-controlled condensation is the convection effect. For gravity-controlled condensation, convection still contributes to heat transfer. The convection attenuates during fully gravity-controlled condensation. Instead of analyzing flow patterns, Shah [164] developed the heat transfer models by fitting a large number of experimental data.

Figure 6.1 shows several transition lines. Dobson and Chato [106] used Soliman's modified Froude number to distinguish stratified flow from annular flow [165]. The transition generally happens at higher vapor quality for small mass fluxes. El Hajal et al. [107] differentiated stratified flow and annular or intermittent flow using the void fraction and stratified angle. Stratified flow includes fully-stratified flow and stratified-wavy flow, whose difference results from the occurrence of waves at the two-phase interface. These two sub-flow patterns are considered the same in terms of condensation mechanisms. Cavallini et al. [68] classified the condensation mechanisms by referring to J_G. The variation of HTCs is gradual during transition. According to Shah [164], vertical and inclined flows have smaller transition mass fluxes than horizontal flow. Fully gravity-controlled condensation only happens at small mass fluxes and high vapor qualities for vertical and inclined flow, where little condensate accumulates at the bottom of the tubes and convection is negligible.

6.1.2. FRICTIONAL PRESSURE DROP MODELS BASED ON FLOW PATTERNS

Two-phase flow is divided into homogeneous flow and separated flow. The homogeneous model assumes the two-phase velocities are the same, and the flow is considered as an equivalent fluid. Bubbly flow and mist flow are generally categorized as homogeneous flow. According to the separated flow model, vapor velocity is larger than liquid mainly because of the density ratio. Separated flow
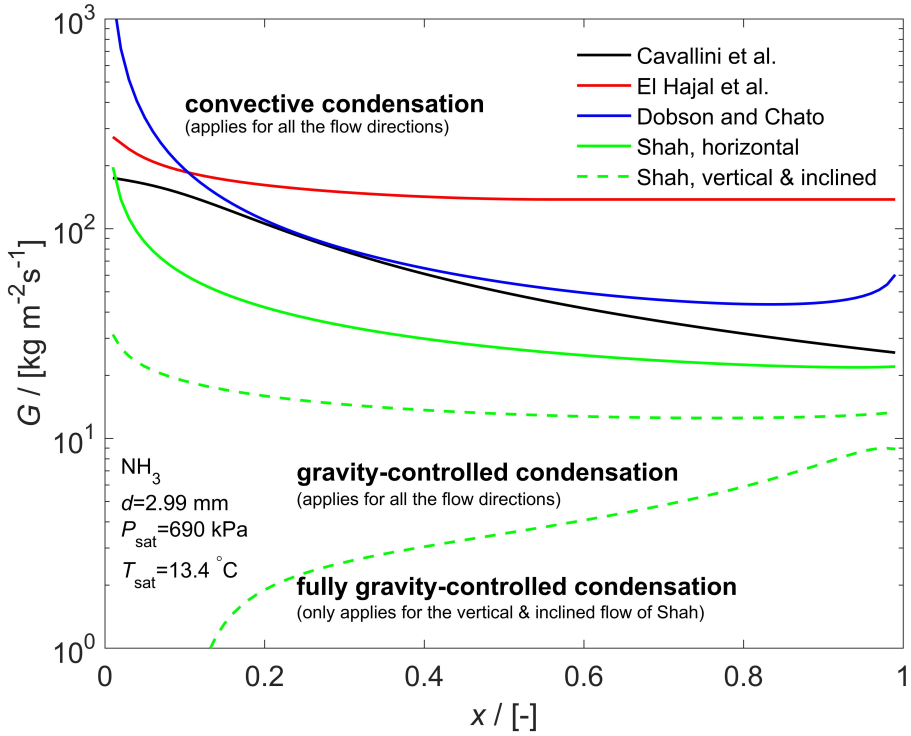
Figure 6.1: Transition of condensation mechanisms. The criteria of Cavallini et al. [68], El Hajal et al. [107] and Dobson and Chato [106] were developed for horizontal tubes. Shah [164] included horizontal, vertical and inclined tubes.

includes stratified flow and annular flow.

The separated flow model calculates the two-phase frictional pressure drop by summing the liquid pressure drop, vapor pressure drop and the pressure drop at the interface. Lockhart and Martinelli [57] analyzed separated flow by assuming the static pressure drops of liquid and vapor are the same. This assumption applies to space unchanged flow patterns and excludes intermittent flow. Chisholm [58] developed the theoretical basis of this model and specified the interfacial shear force. According to the theoretical assumption, the liquid and vapor streams have the same flow mechanisms for two-phase flow as single-phase flow. Homogeneous flow is a special case of this model with zero slip and uniform density. In this case, the experimental data are generally over-predicted.

Friedel [166] claimed that the frictional pressure drop depends on the flow direction because the slip at the two-phase interface is different. Under gravity, liquid moves faster vertically downward, resulting in larger void fraction or

smaller slip ratio. One correlation was proposed for horizontal and vertically upward flow, while another one was developed for vertically downward flow. Additionally, surface tension affects the frictional pressure drop by acting on the two-phase interface.

Müller-Steinhagen and Heck [167] analyzed the sensitivity of frictional pressure drop with vapor qualities, and observed a peak value for $x \approx 0.85$. At higher vapor qualities, the frictional pressure drop decreases as a smaller amount of liquid reduces the interfacial shear force. A correlation was developed and was compared with others. This correlation satisfactorily predicted the experimental database which is mainly composed of air/water and steam/water. The homogeneous correlations were only applicable for low vapor qualities, while Lockhart-Martinelli [57] model generally over-predicted the experimental data.

During NH_3 condensation in a tube (8 mm diameter), Park and Hrnjak [42] recommended the models of Friedel [166] and Müller-Steinhagen and Heck [167] for the experimental frictional pressure drops in the range above $1\,kPam^{-1}$, which were predicted to be intermittent or annular flow. For values below $1\,kPam^{-1}$, the homogeneous model had better performance. Under these conditions stratified flow was expected to occur. Stratified flow is separated flow, but the two-phase velocity difference is small because of the small mass fluxes. Fronk and Garimella [168] measured the frictional pressure drop during NH_3 condensation inside a small diameter tube (1.44 mm). The experimental data were under-predicted by the Friedel [166] model for about 30%. The deviation is mainly attributed to the large surface tension of NH_3.

Figure 6.2 compares the separated flow models. The trends of these models are similar. With increasing vapor qualities, the two-phase pressure drop increases at low and intermediate values, and then decreases when approaching pure vapor. The maximum two-phase pressure drop is between $x = 0.8$ and $x = 0.9$. The changes of the liquid and vapor pressure drop are monotonic. Vapor pressure drop is much larger than liquid pressure drop because the two-phase densities and viscosities of NH_3 differ dramatically. The interfacial pressure drop is larger at intermediate vapor qualities when both phases play roles.

6.2. DEVELOPMENT OF A HEAT TRANSFER MODEL

In this Section, a heat transfer correlation is firstly developed for convective condensation. The transition criterion of condensation mechanisms is established depending on the wetting characteristics. A heat transfer correlation for combined condensation is also developed, and is composed of convective condensation and gravity-controlled condensation.
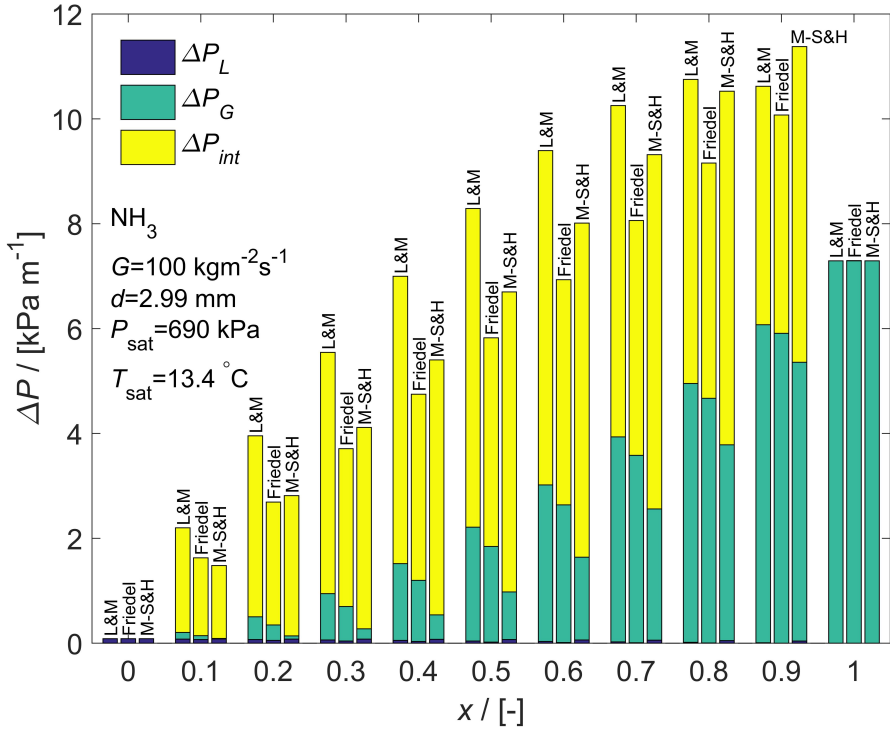
Figure 6.2: Comparison of models by dividing the two-phase pressure drop into the liquid pressure drop, vapor pressure drop and the pressure drop at the interface. The separated models are Lockhart and Martinelli [57] model (L&M) [58], Friedel [166] model and Müller-Steinhagen and Heck [167] model (M-S&H). The single-phase correlation is from Kast et al. [62].

6.2.1. CONVECTIVE CONDENSATION

During NH$_3$ condensation in a PHE, the flow patterns are full film flow and partial film flow below 100 kgm^{-2}s^{-1} [45]. For full film flow, the wall surface is completely wetted by the liquid. Full film flow is equivalent to annular flow in tubes, but the liquid cannot develop a regular ring around the plate surface due to the corrugated flow passages. The interaction between the vapor in the core and the liquid around it gives rise to convective condensation.

All the heat is transferred through the liquid film, where the heat transfer process is similar to single-phase flow. Vapor phase shaves the two-phase interface and enhances the heat transfer. The two-phase multiplier approach was originally developed for annular flow in tubes and is applicable for the full film flow in PHEs [56]. The two-phase multiplier depends on the vapor flow and two-phase fluid properties. It generally has the form of Eq. 6.1. α_{cc} is the HTC of convective

condensation. α_L is the liquid HTC and only identifies the liquid mass flux. It is calculated using the liquid Reynolds number, Re_L. In Eq. 6.2, the liquid only HTC, α_{LO}, assumes all the fluid is liquid and is determined according to VDI [20]. $f_{D,LO}$ is the Darcy friction factor and is calculated in Eqs. 6.4-6.6 [20, 141]. This equation is derived from a large range of geometrical parameters and agrees well with the H_2O HTCs presented in Section 4.2.1 [45, 132]. Eq. 6.3 shows the difference between α_L and α_{LO}. $f_{D,L}/f_{D,LO}$ is approximately 1 especially for large chevron angles. Eqs. 2.11-2.12 calculate Re_{LO} and Re_L.

$$\alpha_{cc} = \alpha_L F(x, \rho_L/\rho_G, G) \tag{6.1}$$

$$\alpha_{LO} = 0.122(f_{D,LO}\sin 2\beta)^{0.374} Re_{LO}^{0.748} Pr_L^{0.333} \left(\frac{\mu}{\mu_{wall}}\right)^{0.167} \frac{\lambda_L}{d_h} \tag{6.2}$$

$$\begin{aligned}\alpha_L &= 0.122(f_{D,L}\sin 2\beta)^{0.374} Re_L^{0.748} Pr_L^{0.333} \left(\frac{\mu}{\mu_{wall}}\right)^{0.167} \frac{\lambda_L}{d_h} \\ &= \alpha_{LO}\left(\frac{f_{D,L}}{f_{D,LO}}\right)^{0.374}(1-x)^{0.748} \approx \alpha_{LO}(1-x)^{0.748}\end{aligned} \tag{6.3}$$

$$f_{D,LT1} = \begin{cases} 64Re^{-1}, & Re < 2000 \\ (1.8\log_{10}(Re) - 1.5)^{-2}, & Re \geq 2000 \end{cases} \tag{6.4}$$

$$f_{D,LT2} = \begin{cases} 3.8(597Re^{-1} + 3.85), & Re < 2000 \\ 3.8(39Re^{-0.289}), & Re \geq 2000 \end{cases} \tag{6.5}$$

$$f_D = \left(\frac{\cos\beta}{(0.18\tan\beta + 0.36\sin\beta + f_{D,LT1}/\cos\beta)^{0.5}} + \frac{1-\cos\beta}{f_{D,LT2}^{0.5}}\right)^{-2} \tag{6.6}$$

In order to confine the experimental data to fully developed convective condensation, only data with $G_L > 40 \text{ kgm}^{-2}\text{s}^{-1}$ are included to develop the correlation. Eq. 6.7 is obtained by multi-variable regression analysis. The first term of the two-phase multiplier interprets the enhancement contributed by the vapor flow. It approaches 0 when x is 0, indicating that the enhancement vanishes as the fluid becomes liquid only. In Eq. 2.3, Co is the convection number and represents the slip velocity at the two-phase interface. As the reduced pressure increases, the two-phase properties become alike and the density ratio is close to 1, suppressing the slip at the interface. In Eq. 2.18, the liquid Froude number, Fr_L, is the ratio of inertia to gravity, and indicates the dominance of momentum effect or stratifying effect for separated flow [169]. The second term in the bracket of Eq. 6.7 specifies the difference between α_{LO} and α_L. α_{cc} becomes α_{LO} when the flow is single-phase liquid.
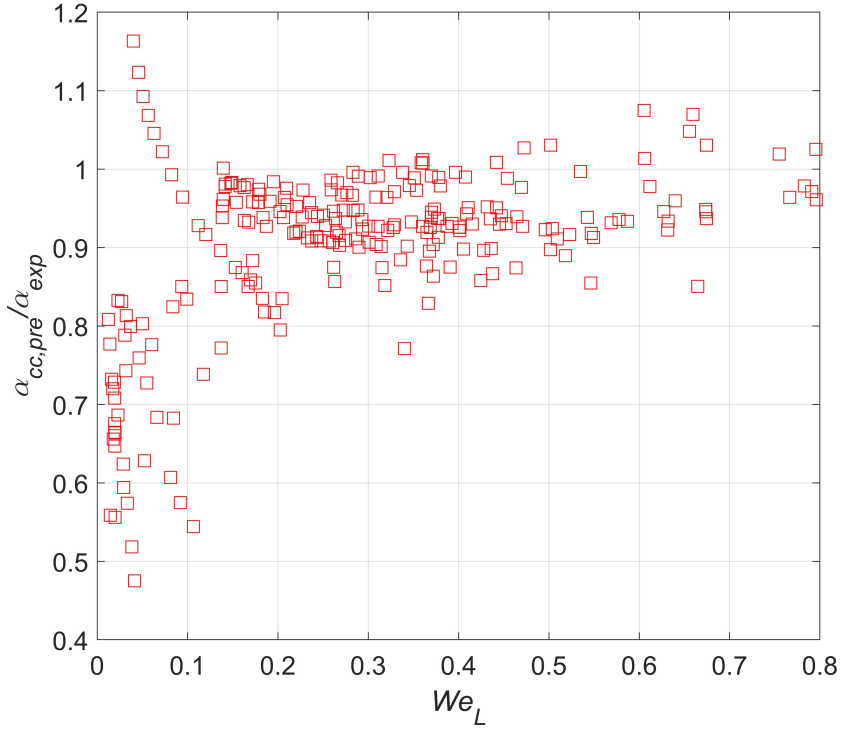
Figure 6.3: Applicability of the correlation of convective condensation (Eq. 6.7) in terms of We_L. Eq. 6.7 is applicable for large We_L, and is inapplicable for small We_L. The transition criterion is $We_L = 0.12$.

$$\alpha_{cc} = \alpha_{LO} \left(\underbrace{0.17 Co^{-1.12} Fr_L^{-0.2}}_{\text{vapor flow enhancement}} + \underbrace{(1-x)^{0.748}}_{\text{difference between } \alpha_{LO} \text{ and } \alpha_L} \right) \tag{6.7}$$

The previous analysis is restricted to the data with $G_L > 40$ kgm^{-2}s^{-1}. Convective condensation extends to lower liquid mass fluxes. In small diameter channels, the magnitude of surface tension becomes prominent relative to gravity and shear force. Larger surface tension promotes the change from annular flow to wavy flow in tubes [170]. The surface tension affects the wetting characteristics and condensation mechanisms, while the inertial force tends to distribute the liquid film around the wall surface. In Eq. 2.15, the liquid Weber number, We_L, is the ratio of liquid inertia to surface tension. We_L is used to distinguish the condensation mechanisms. Eq. 6.7 is used to predict all the experimental data, and the comparison is presented in Figure 6.3. When $We_L > 0.12$, the experi-
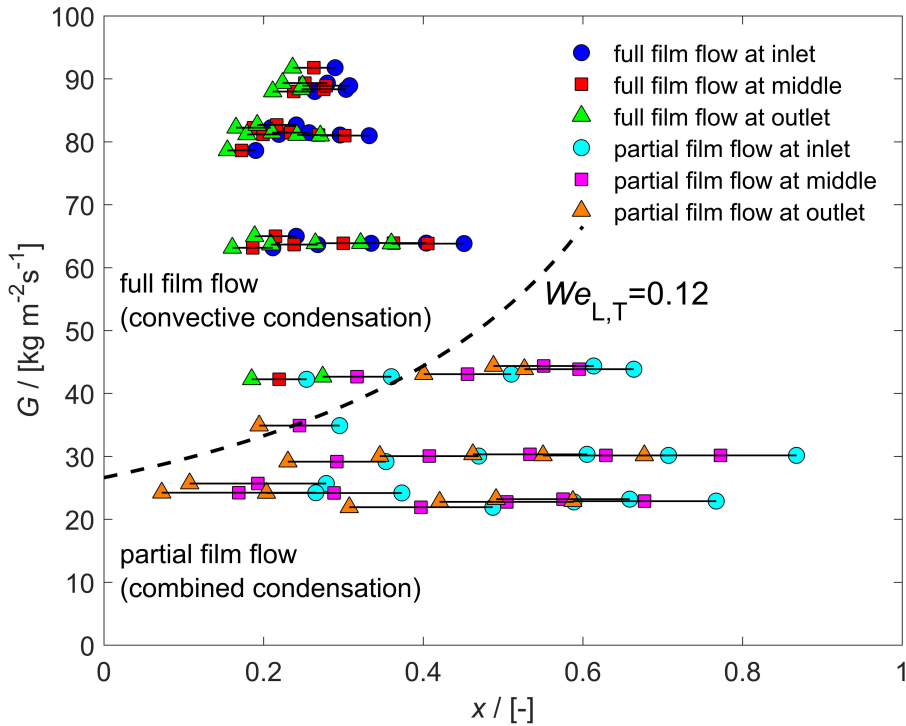
Figure 6.4: Comparison of the flow pattern map with the criterion of condensation mechanisms ($We_L = 0.12$). Full film flow takes place for $We_L > 0.12$. Partial film flow happens for $We_L < 0.12$. The transition line of condensation mechanisms agrees with the change of flow patterns.

mental data are well predicted, and the deviation is within ±20%. As $We_L < 0.12$, the experimental data are under predicted. Another condensation mechanism is involved, which enhances the heat transfer. The value of $We_L = 0.12$ is the transition criterion of condensation mechanisms.

The transition line is presented in Figure 6.4, which agrees well with the change of flow patterns. As compared with Figure 6.1, the transition mass flux is smaller than that in horizontal tubes, but is close to the value for vertical and inclined tubes. The flow direction affects the transition of condensation mechanisms because of the interaction between gravity and shear force. For fully gravity-controlled condensation, the condensate film formed on the wall flows almost vertically downward. By contrast, interfacial shear force dominates for convective condensation. The condensate film is less affected by gravity and flows along the main flow direction. The transition depends on the relative magnitudes of gravity and shear force. The flow in the corrugated groove of PHEs is similar

to inclined downward flow in tubes [45]. The gravity is divided into the directions parallel to the groove and perpendicular to the groove [171]. Gravity supplements the shear force and has reduced stratifying effect. Consequently, convective condensation is promoted for inclined downward flow.

The transition happens at higher vapor quality for large mass fluxes. This trend of the transition line is different from Figure 6.1. The criterion of PHEs is based on the wetting characteristics, while the criteria of tubes are mainly derived from J_G. The possible reason is the difference in channel geometries. The velocity distribution is not uniform within the flow section. The velocity is larger at the center and becomes smaller close to the wall. The vapor has a larger velocity than the liquid. The vapor with large inertia pushes the liquid radially. In circular tubes, the force is nearly uniform in circumferential direction, and liquid tends to reside on the wall uniformly. Larger vapor mass fluxes enhance the inertia effect so as to overcome the stratifying effect. PHEs have irregular flow section, and the ratio of width to length is small. The liquid is pushed by the vapor in all directions. The corrugated surface breaks up the liquid film and distributes the broken droplets randomly. Consequently, a certain amount of liquid is required to completely wet the wall and to promote convective condensation. Larger liquid mass fluxes also enhance the waviness of the film flow and change the flow patterns.

In PHEs, the transition mass fluxes of other refrigerants are smaller than for NH$_3$. According to Longo et al. [60], the transition mass fluxes are about 20 kgm^{-2}s^{-1} for HFCs and HFOs (R134a, R410A, R236fa, R1234yf, R1234ze(E)), and are around 15 kgm^{-2}s^{-1} for HCs (R600a, R290, R1270). Mancin et al. [80] stated that the transition values are around 20 kgm^{-2}s^{-1} for R410A and R407C. Thonon and Bontemps [82] identified the transition mass fluxes as 5-13 kgm^{-2}s^{-1} for R601, R600 and R290. These experiments were conducted at small mass fluxes, and the HTCs of gravity-controlled condensation are larger than convective condensation. Zhang et al. [66] concluded that the transition mass fluxes are about 20 kgm^{-2}s^{-1} for R134a and R1234ze(E). Sarraf et al. [27] reported condensation of R601 in the range of 9-30 kgm^{-2}s^{-1}. Gradual transition happens at 10-20 kgm^{-2}s^{-1} and relies on the vapor qualities. The difference can be attributed to the surface tension. NH$_3$ has larger surface tension and reduces the wettability. The mass flux needs to be larger for complete wetting. Consequently, gravity-controlled condensation extends to larger mass fluxes.

6.2.2. Combined condensation

During the visualization experiments of NH$_3$ condensation in a PHE [45], the flow direction of the fluid is observed to be a combination of crossing flow and wavy longitudinal flow. The flow in grooves is inclined downward. As the liquid

mass fluxes decrease, a part of the wall surface is not wetted. The flow pattern becomes partial film flow, and some vapor is in contact with the wall directly. Partial film flow is similar to stratified flow in tubes. The condensation deviates from convective condensation and shows similarity to gravity-controlled condensation. Convective condensation occurs in the wetted area. In the dry zones, the condensation is similar to the Nusselt's theory except for the influence of shear force. The vapor phase exerts shear force on the thin condensate film and enhances the heat transfer [172]. In Eq. 6.8, the heat transfer correlation combines convective condensation, α_{cc}, with gravity-controlled condensation, α_{gc}. Θ is the fraction of convective condensation. Because the overall heat transfer area is only composed of these two mechanisms, the fraction of gravity-controlled condensation can be determined as $1-\Theta$.

$$\alpha_{\mathrm{c}} = \Theta\alpha_{\mathrm{cc}} + (1-\Theta)\alpha_{\mathrm{gc}} \tag{6.8}$$

The flow pattern changes gradually from full film flow to partial film flow, and the HTC of convective condensation is identified to be the same as given by Eq. 6.7. Θ needs to be determined before calculating the gravity-controlled condensation. During the condensation in horizontal tubes, for stratified flow, Dobson and Chato [106] and Thome et al. [126] estimated the fraction of gravity-controlled condensation by using the wetted angle. Cavallini et al. [68] used J_{G} to quantify the fraction of gravity-controlled condensation. In PHEs, the wetted angle is difficult to measure. As shown in Eq. 6.9, Θ is determined to be the ratio of liquid Weber number to the transition liquid Weber number. The fraction of the wetted area increases with the liquid mass flux [173], and Eq. 6.8 approaches convective condensation.

$$\Theta = We_{\mathrm{L}}/We_{\mathrm{L,T}} \tag{6.9}$$

In Eq. 6.10, the Nusselt correlation is kept as the starting point [79]. The original Nusselt correlation is based on several assumptions. The deviations from the assumptions have minor influences, or the resulting overprediction and underprediction partly offset each other. Consequently, the correlation is applicable in wide ranges of conditions [174]. Nevertheless, most of the complicating factors in the confined channels enhance heat transfer, and thus the influences need to be identified. The film thickness reduces when the vapor shaves the interface. The vapor flow accelerates the condensate film and generates waves, contributing to film convection [174–177]. It is recommended to modify original Nusselt correlation by identifying vapor flow and shear force [106, 178]. In Eq. 6.10, Pr_{L} and Co are used. Pr_{L} indicates the relative importance of convection and conduction. Co is included to quantify the enhancement contributed by two-phase
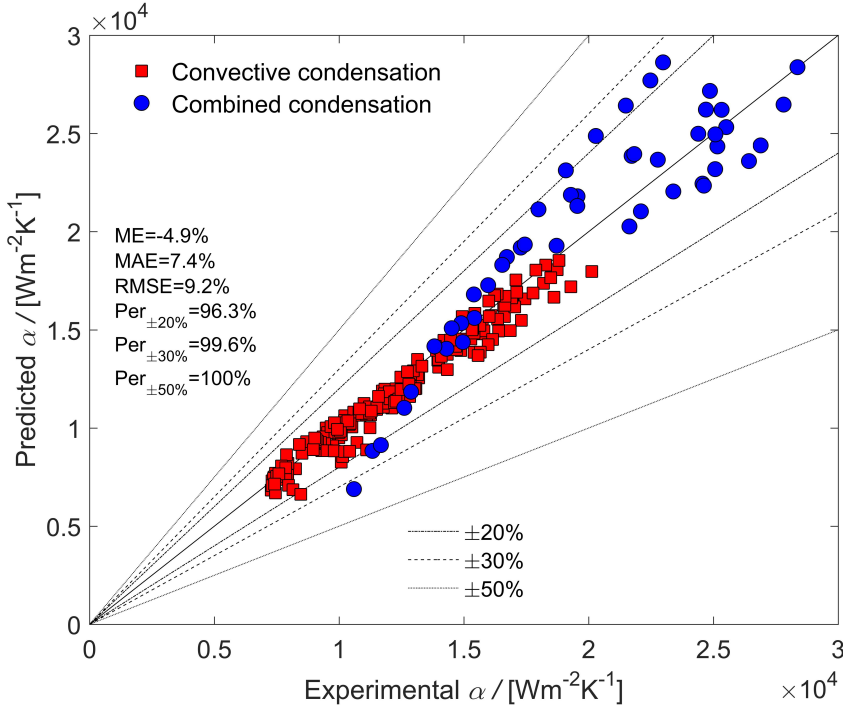
Figure 6.5: Comparison of NH₃ condensation HTCs with the proposed model. Mean error (ME): $\frac{1}{n}\sum_1^n \frac{\alpha_{\mathrm{pre}}-\alpha_{\mathrm{exp}}}{\alpha_{\mathrm{exp}}}$; Mean absolute error (MAE): $\frac{1}{n}\sum_1^n \frac{|\alpha_{\mathrm{pre}}-\alpha_{\mathrm{exp}}|}{\alpha_{\mathrm{exp}}}$; Root mean squared error (RMSE): $\sqrt{\frac{1}{n}\sum_1^n \left(\frac{\alpha_{\mathrm{pre}}-\alpha_{\mathrm{exp}}}{\alpha_{\mathrm{exp}}}\right)^2}$; $Per_{\pm 20\%}$: Percentage of experimental data within ±20%; $Per_{\pm 30\%}$: Percentage of experimental data within ±30%; $Per_{\pm 50\%}$: Percentage of experimental data within ±50%.

slip, and the constants are obtained by fitting the data.

$$\alpha_{\mathrm{gc}} = 0.36 Co^{-0.28} \left(\frac{g\rho_{\mathrm{L}}(\rho_{\mathrm{L}} - \rho_{\mathrm{G}})\Delta h_{\mathrm{LG}}\lambda_{\mathrm{L}}^3}{\mu_{\mathrm{L}}\Delta T d_{\mathrm{h}}} \right)^{0.25} Pr_{\mathrm{L}}^{0.333} \tag{6.10}$$

The original Nusselt correlation is derived for free flow on a vertical plate, and the characteristic length is the plate length. When extended to confined channels such as tubes [68, 106, 126, 164], the Nusselt correlation uses the tube diameter, which better characterizes the flow channels. In PHEs, the flow is interrupted by the corrugation, and the liquid film cannot be fully developed in the plate length. The hydraulic diameter characterizes the flow channels where the liquid film is developed locally.

Table 6.1: Two-phase fluid properties of typical refrigerants at T_{sat}=20 °C[a]

	P_{sat} [kPa]	$P_{\text{sat}}/P_{\text{cr}}$ [-]	ρ_G [kgm^{-3}]	ρ_L [kgm^{-3}]	μ_G [μPas]	μ_L [μPas]	Δh_{LG} [kJkg^{-1}]	σ [mNm^{-1}]	λ_L [Wm^{-1}K^{-1}]	Pr_L [-]
NH$_3$	857	0.075	6.70	610	9.69	134	1186	21.7	0.481	1.32
R601	57	0.017	1.72	626	6.61	230	370	16.0	0.114	4.64
R600a	302	0.083	7.91	557	7.36	159	334	10.6	0.091	4.20
R600	208	0.055	5.31	579	7.21	167	367	12.5	0.107	3.78
R290	836	0.197	18.08	500	8.01	102	344	7.6	0.096	2.84
R134a	572	0.141	27.78	1225	11.49	207	182	8.7	0.083	3.50
R410A	1447	0.295	56.80	1083	13.33	126	194	6.0	0.092	2.27
R1234ze(E)	427	0.118	22.61	1179	11.92	203	171	9.6	0.076	3.66
Air/water	857[b]	-	10.22	999	18.32	1001	-	72.8[c]	0.598	7.00

[a] The fluid properties are calculated using Refprop 9.1 [39]

[b] This is not the saturated pressure, but the pressure used to determine the fluid properties of mixture

[c] The surface tension of mixture is calculated using Vargaftik et al. [109]

6.2.3. ASSESSMENT OF HEAT TRANSFER MODEL

Figure 6.5 compares the proposed heat transfer model with the experimental data from Chapter 5 [45]. 96.3% of the experimental data are predicted within ±20%. The MAE is 7.4%. The data are composed of convective condensation and combined condensation. This model predicts accurately the noticeable sensitivity to vapor qualities and moderate sensitivity to mass fluxes.

In Chapter 3, an extensive experimental database is developed for condensation in PHEs [18]. The database is composed of HFCs, HCs and HFOs, which mostly have much smaller two-phase density ratio than NH$_3$. Table 6.1 gives the fluid properties of typical refrigerants and air/water mixture. R601, R600a and R600 also have large two-phase density ratio, and are used to validate the proposed heat transfer correlations.

Sarraf et al. [27] measured the local HTCs during R601 condensation in a PHE, and the experimental data are presented in Figure 6.6(a). HTCs increase sharply with vapor qualities, and are less sensitive to mass fluxes. Larger mass fluxes slightly reduce the HTCs at low vapor qualities, and have greater influences at high vapor qualities. The model predicts well the trends of vapor qualities. Because of the large two-phase density ratio, a slight rise of the vapor qualities greatly intensifies the shear force and enhances the heat transfer. According to the proposed model, the shear force is weak at low vapor qualities. Larger mass fluxes promote full film flow. Larger wetted areas reinforce the liquid film, which serves as heat transfer resistance. The scatter is larger at high vapor qualities. The model is derived from data limited to low and intermediate vapor qualities. Moreover, the measurement at high vapor qualities has large uncertainties.

(a)

(b)
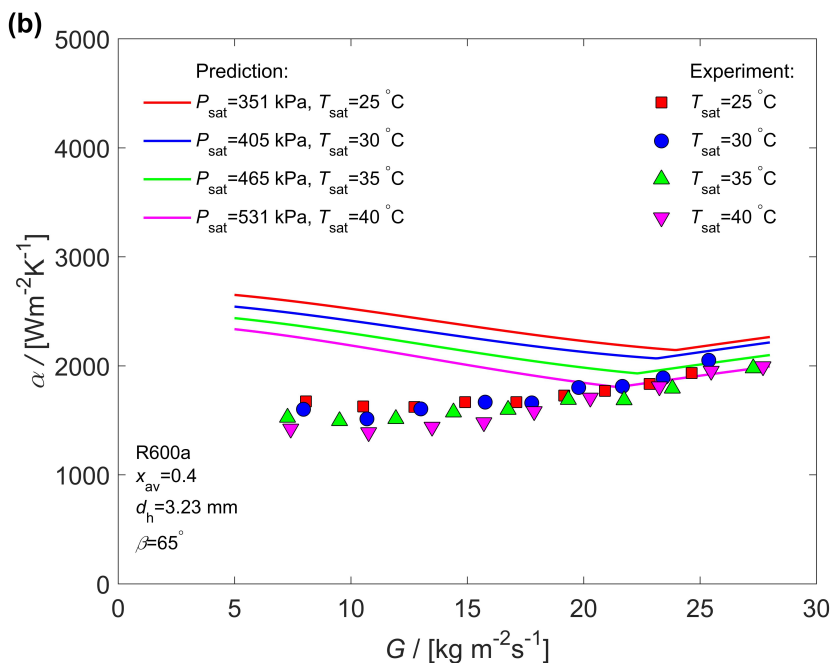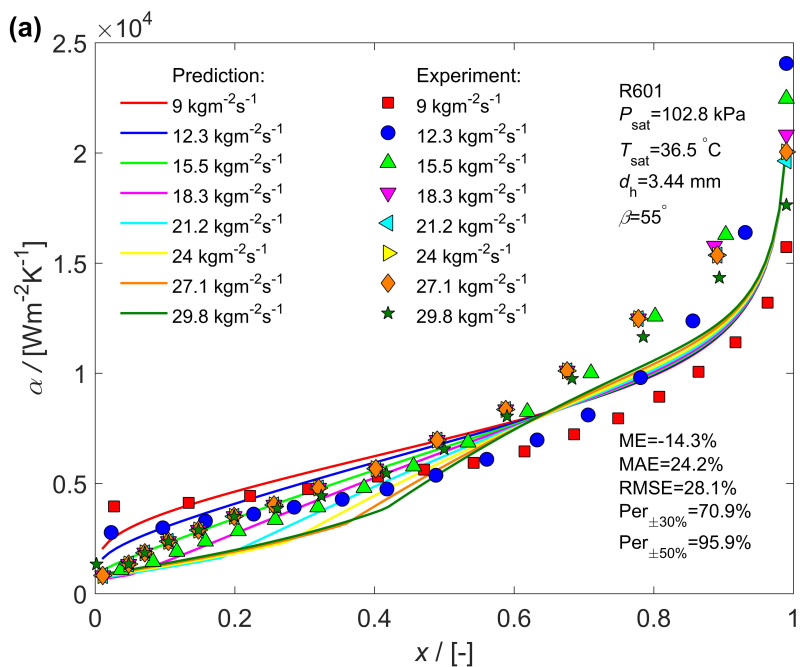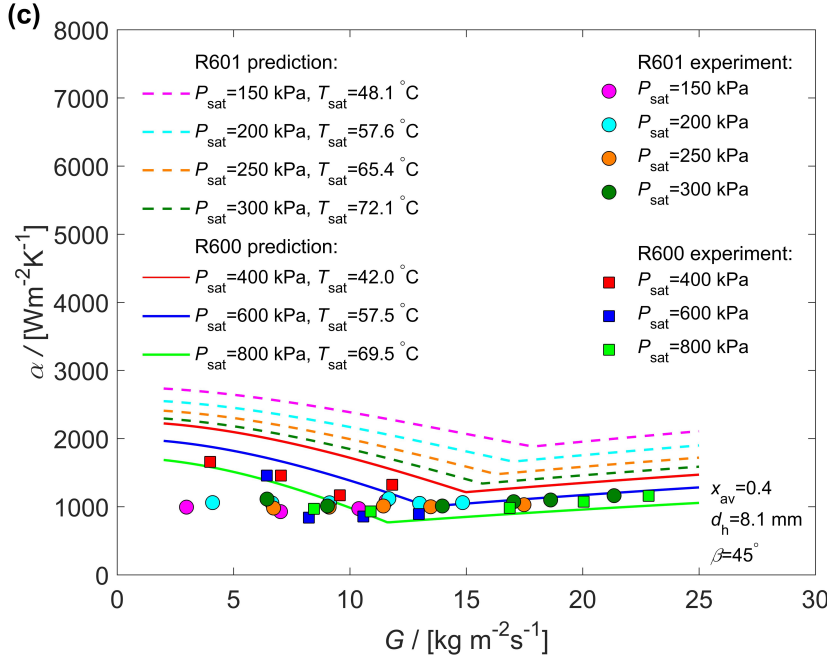
Figure 6.6: Validation of the new heat transfer model, Eqs. 6.7-6.10, with the experimental data of (a) Sarraf et al. [27], (b) Longo [78], (c) Thonon and Bontemps [82]. The prediction is accurate for the vapor qualities of 0-0.8 and the mass fluxes of 20-80 kgm^{-2}s^{-1}.

Larger HTCs reduce the temperature difference and enlarge the relative uncertainty for given sensor accuracy. Fortunately, because of the small heat transfer resistance, the heat transfer areas corresponding to high vapor qualities account for a small portion of PHEs, which brings about limited design uncertainty.

Longo [78] and Thonon and Bontemps [82] measured the overall HTCs during the complete condensation of R600a, R600 and R601. Figures 6.6(b) and 6.6(c) compare the experimental data with prediction. The averaged vapor quality is the integrated mean value of the whole condenser. Shah [56] argued that the averaged vapor quality is closer to 0.4 than 0.5. Larger mass fluxes have minor influences on HTCs, which is the compensating effect of larger shear force and thicker liquid film. The model is more accurate at large mass fluxes, but overpredicts the experimental data at small mass fluxes.

In summary, the model can be extended from NH_3 to other refrigerants of large two-phase density ratio. The model is applicable to the vapor qualities of 0-0.8 and the mass fluxes of 20-80 kgm^{-2}s^{-1}. Application to higher vapor qualities

and smaller mass fluxes should be with concern. The foremost PHE geometries are hydraulic diameters and chevron angles, which generally span the range of 3-8 mm and 25°-70°, respectively [18]. The heat transfer model is a two-phase multiplier approach. The involved single-phase correlation identifies geometric parameters [20]. The model is expected to apply to most commercial chevron PHEs with standard geometries. The influence of saturated pressure is mainly attributed to vapor density, liquid thermal conductivity and latent heat. The model is suitable for low reduced pressure.

Figure 6.7 shows a sensitivity analysis according to the proposed heat transfer model, indicating a sharp increase with vapor qualities. In Figure 6.7(a), the condensation mechanism is combined condensation at 20 kgm^{-2}s^{-1} since the wall cannot be completely wetted. At larger mass fluxes, convective condensation applies at low vapor qualities and changes into combined condensation with increasing vapor qualities. Combined condensation takes place when parts of the wall become dry. The transition vapor quality is higher for larger mass fluxes. When the condensation mechanism remains the same, HTCs increase with mass fluxes. It applies for both combined condensation at high vapor qualities and convective condensation at low vapor qualities. For lower vapor qualities, the HTCs at 20 kgm^{-2}s^{-1} are larger because the earlier transition to combined condensation. Figure 6.7(b) shows the influence of saturated pressures. The HTCs are slightly larger for lower condensation pressures. The larger two-phase density ratio and viscosity difference intensify the shear force. Additionally, the thermal conductivity of liquid is larger for low pressures. The condensation mechanism changes close to the vapor quality of 0.4. Lower saturated pressures slightly reduce the transition vapor quality.

6.3. DEVELOPMENT OF FRICTIONAL PRESSURE DROP MODEL

The frictional pressure drop is less affected by the transition of condensation mechanisms. Thus a unified model is developed in this Section. The original Lockhart-Martinelli model is firstly presented, and then is modified to identify the influence of surface tension and the contribution of the vapor pressure drop.

6.3.1. SEPARATED FLOW MODEL

Both full film flow and partial film flow are separated two-phase flows. The vapor phase has larger velocity than the liquid phase. The two-phase frictional pressure drop is the sum of the liquid pressure drop, vapor pressure drop and interface pressure drop. Lockhart-Martinelli model is selected as the starting point to predict the frictional pressure drop.

The original Lockhart-Martinelli model was developed for tubes and has the form of Eqs. 6.11-6.15 [57, 58]. X is the ratio of the liquid to vapor pressure drops.
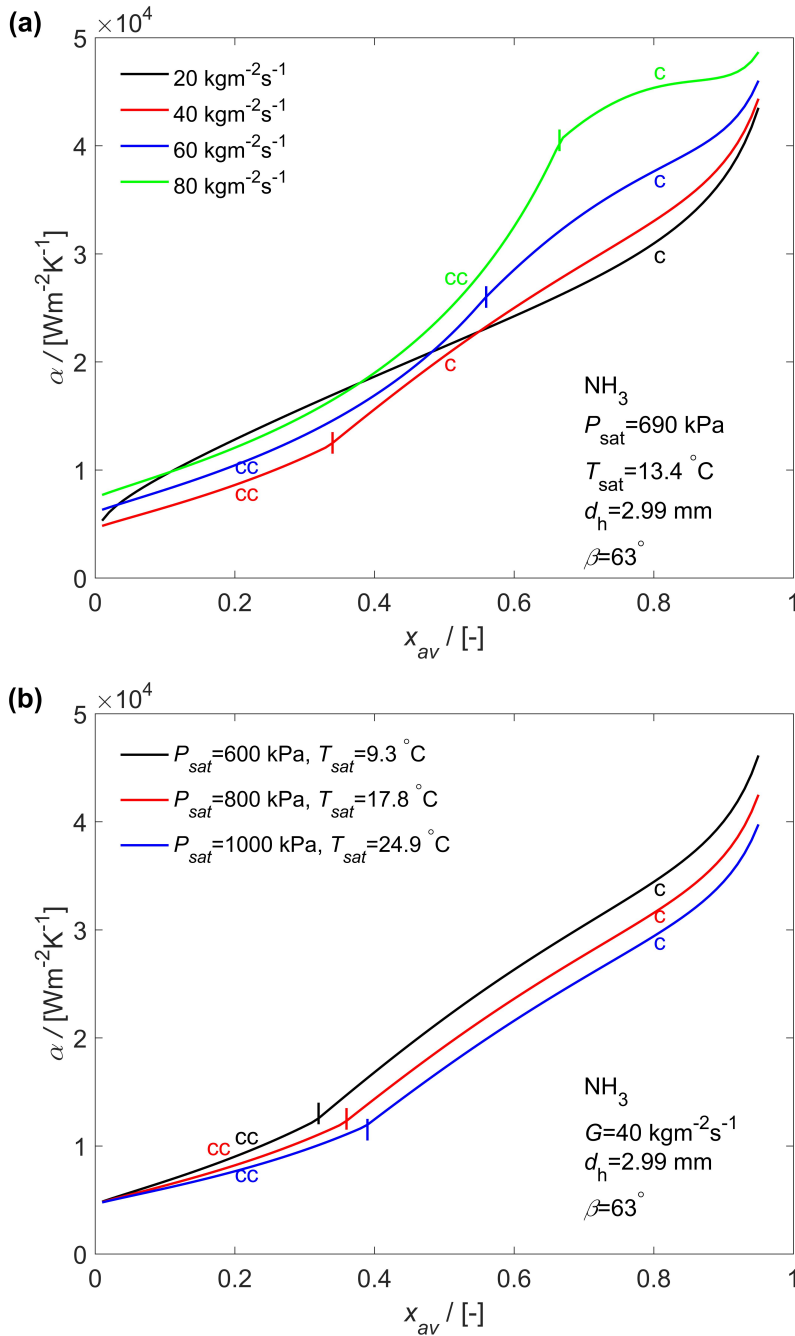
Figure 6.7: Sensitivity of the HTCs to vapor qualities for (a) different mass fluxes, (b) different condensation pressures. cc: convective condensation, c: combined condensation.

X determines the contributions of liquid and vapor pressure drops. The value of X depends on whether the liquid and vapor are laminar or turbulent. Eqs. 2.1-2.2 apply to turbulent-turbulent flow and laminar-laminar flow based on the single-phase pressure drop correlations in tubes [62]. X is a function of vapor qualities and two-phase fluid properties. The ratios of densities and viscosities determine the two-phase slip at the interface. Eq. 6.11 can be converted into Eq. 6.16 by substituting Eqs. 6.12-6.13.

$$\phi_L^2 = 1 + \frac{C}{X} + \frac{1}{X^2} \tag{6.11}$$

$$X^2 = \frac{\Delta P_L}{\Delta P_G} = \frac{f_{D,L}}{f_{D,G}} \left(\frac{1-x}{x}\right)^2 \frac{\rho_G}{\rho_L} \tag{6.12}$$

$$\phi_L^2 = \frac{\Delta P_{TP}}{\Delta P_L} \tag{6.13}$$

$$\Delta P_L = 2 f_L \frac{G_L^2}{\rho_L} \frac{L_p}{d_h} = 2 f_L \frac{G^2 (1-x)^2}{\rho_L} \frac{L_p}{d_h} \tag{6.14}$$

$$\Delta P_G = 2 f_G \frac{G_G^2}{\rho_G} \frac{L_p}{d_h} = 2 f_G \frac{G^2 x^2}{\rho_G} \frac{L_p}{d_h} \tag{6.15}$$

$$\Delta P_{TP} = \underbrace{\Delta P_L}_{\text{liquid pressure drop}} + \underbrace{C \sqrt{\Delta P_L \Delta P_G}}_{\text{interface pressure drop}} + \underbrace{\Delta P_G}_{\text{vapor pressure drop}} \tag{6.16}$$

In PHEs, the ratio of f_D cannot be easily represented by vapor quality and fluid properties like for tubes in Eqs. 2.1-2.2. As shown in Eqs. 6.4-6.6, $f_{D,L}$ and $f_{D,G}$ are calculated based on single-phase flow correlations. It is recommended to calculate X according to Eq. 6.13 or calculate ΔP_{TP} directly using Eq. 6.16. The interface pressure drop is proportional to the geometric mean of the liquid and vapor pressure drops. The two-phase frictional pressure drop approaches the liquid or vapor pressure drop when x is 0 or 1, respectively. The interface pressure drop vanishes as the fluid becomes single phase.

During two-phase flow, the Lockhart-Martinelli model assumes that the vapor flow mechanism stays the same as for single-phase flow [58]. As shown in Figure 6.2, the vapor pressure drop is predicted to be larger than the prediction of other models. Müller-Steinhagen and Heck [167] proposed the model introduced in Eq. 6.17, where ΔP_{LO} and ΔP_{GO} are the liquid only and vapor only pressure drops, respectively. This model is limited by the liquid and vapor pressure drops when the fluid becomes single phase. In order to be compared with

Lockhart-Martinelli model, it is converted into Eq. 6.18. For fluids with large two-phase density ratio, the vapor pressure drop contributes primarily to the overall pressure drop. The Lockhart-Martinelli model involves the vapor pressure drop directly, while the model of Müller-Steinhagen and Heck reduces the contribution by multiplying with $(f_{D,GO}/f_{D,G})x$. In PHEs, the single-phase frictional pressure drop identifies the influence of corrugated flow passages and has large values because of the geometry induced momentum dissipation [20]. The direct inclusion of vapor pressure drop over-predicts the two-phase pressure drop. The proposed model is presented in Eqs. 6.19-6.20. The contribution of the vapor pressure drop is modified and is proportional to the vapor quality.

$$\Delta P_{TP} = (1-x)^{1/3}\Delta P_{LO} + 2x(1-x)^{1/3}(\Delta P_{GO} - \Delta P_{LO}) + x^3 \Delta P_{GO} \qquad (6.17)$$

$$\Delta P_{TP} = \underbrace{\frac{f_{D,LO}}{f_{D,L}}(1-x)^{-5/3}\Delta P_L}_{\text{liquid pressure drop}} + \underbrace{2x(1-x)^{1/3}(\Delta P_{GO} - \Delta P_{LO})}_{\text{interface pressure drop}} + \underbrace{\frac{f_{D,GO}}{f_{D,G}}x\Delta P_G}_{\text{vapor pressure drop}}$$
$$(6.18)$$

The original Lockhart-Martinelli model was reported to over-predict the frictional pressure drop when the surface tension becomes dominant [41, 179]. Larger surface tension reduces the wetted area and flow resistance contributed by the large viscosity of the liquid phase [40]. Surface tension tends to smooth the two-phase interface and reduce the pressure drop [41]. The friction at the two-phase interface depends on flow patterns, and the Lockhart-Martinelli model should be modified accordingly [180]. Lower values of C are recommended when surface tension dominates at small diameter channels. In Eqs. 6.19-6.20, C is selected to be 2. Eq. 6.20 is obtained by substituting Eqs. 6.12-6.13 into Eq. 6.19. The single-phase pressure drop is calculated using the friction factor obtained from Eqs. 6.4-6.6. The two-phase frictional pressure drop is limited by single-phase pressure drop when the flow becomes liquid or vapor.

$$\phi_L^2 = 1 + \frac{2}{X} + \frac{x}{X^2} \qquad (6.19)$$

$$\Delta P_{TP} = \underbrace{\Delta P_L}_{\text{liquid pressure drop}} + \underbrace{2\sqrt{\Delta P_L \Delta P_G}}_{\text{interface pressure drop}} + \underbrace{x\Delta P_G}_{\text{vapor pressure drop}} \qquad (6.20)$$

6.3.2. Assessment of frictional pressure drop model
In Figure 6.8, the proposed frictional pressure drop model predicts 73.8% of the experimental data within ±20%. The MAE is 14.6%. The data are divided into
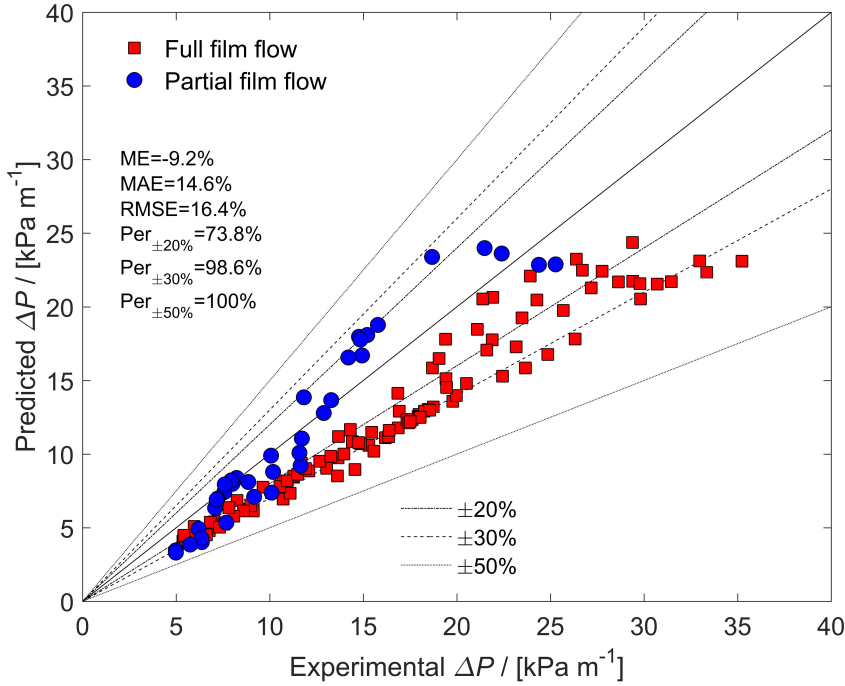
Figure 6.8: Comparison of NH$_3$ frictional pressure drop with the present model. Mean error (ME): $\frac{1}{n}\sum_1^n \frac{\Delta P_{\text{pre}} - \Delta P_{\text{exp}}}{\Delta P_{\text{exp}}}$; Mean absolute error (MAE): $\frac{1}{n}\sum_1^n \frac{|\Delta P_{\text{pre}} - \Delta P_{\text{exp}}|}{\Delta P_{\text{exp}}}$; Root mean squared error (RMSE): $\sqrt{\frac{1}{n}\sum_1^n \left(\frac{\Delta P_{\text{pre}} - \Delta P_{\text{exp}}}{\Delta P_{\text{exp}}}\right)^2}$; $Per_{\pm 20\%}$: Percentage of experimental data within $\pm 20\%$; $Per_{\pm 30\%}$: Percentage of experimental data within $\pm 30\%$; $Per_{\pm 50\%}$: Percentage of experimental data within $\pm 50\%$.

full film flow and partial film flow according to $We_{\text{L,T}} = 0.12$, which correspond to convective condensation and combined condensation, respectively. The experimental data of partial film flow are slightly over-predicted. For partial film flow, parts of the wall are sheared by the vapor instead of liquid, and the overall flow resistance is reduced. Moreover, the shear force at the two-phase interface is reduced since the interface shrinks and the vapor contacts the wall directly.

In Table 6.1, the two-phase fluid properties of air/water are similar to those of NH$_3$ with large density ratio and surface tension. The flow characteristics are expected to be similar. According to the experimental results of Tribbe and Müller-Steinhagen [105] and Winkelmann [19], the frictional pressure drop increases linearly with the vapor quality, which is the mass flow ratio of air to water. No maximum value exists at the region of high vapor qualities as shown in Figure 6.2. The two-phase pressure drop is the sum of three components. In tubes with

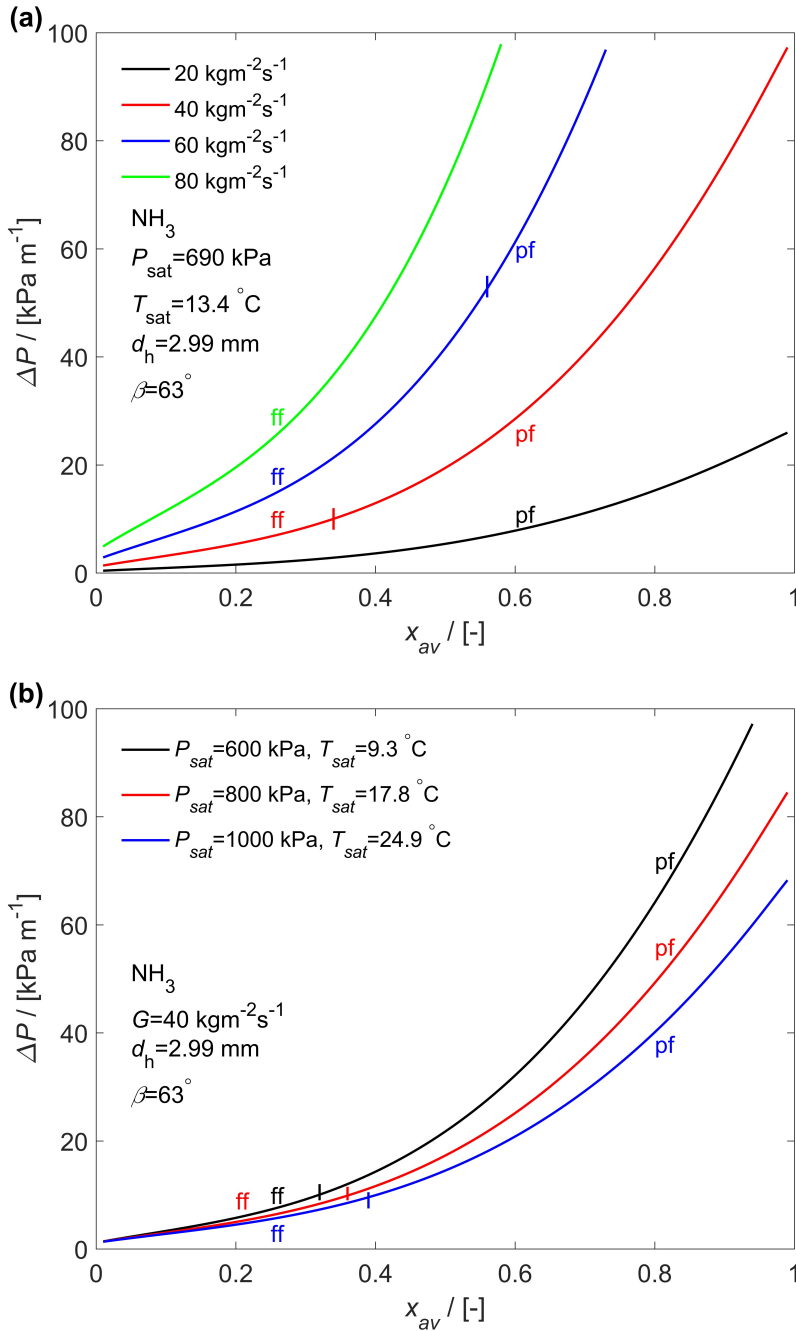Figure 6.9: Sensitivity of the frictional pressure drop with vapor qualities for (a) different mass fluxes, (b) different condensation pressure. ff: full film flow, pf: partial film flow.

smooth surface, the liquid and vapor pressure drops are limited, while the inter-face pressure drop is noticeable because of the sags and crests. The maximum pressure drop results from the shear force at the two-phase interface. The cor-rugated channels of PHEs significantly intensify the single-phase pressure drop [20]. Bumpy two-phase interface is unlikely to further aggravate the momentum dissipation superposed to the wall friction. The interface pressure drop becomes secondary. Thus the two-phase pressure drop is proportional to vapor qualities. These data cannot be used to validate the proposed model because the operating conditions are not reported [19, 105].

The model is limited to two-phase NH$_3$ flow. It is expected to cover the vapor qualities of 0-1 and the mass fluxes of 20-80 kgm^{-2}s^{-1}. Experimental data at high vapor qualities are not obtained. But the model approaches vapor only pressure drop with increasing vapor qualities, which agrees with physical interpretation. Similar to the proposed heat transfer model, the pressure drop model appears to be applicable to most commercial chevron PHEs and low reduced pressure. The sensitivity to geometric parameters is included in the single-phase correlations [20].

Figure 6.9 presents the sensitivity of frictional pressure drop calculated from the proposed model. The frictional pressure drop increases dramatically with vapor qualities as the vapor phase occupies a larger portion of the flow section. In Figure 6.9(a), larger mass fluxes increase the frictional pressure drop significantly and contribute to a later transition of flow patterns in terms of vapor qualities. As shown in Figure 6.9(b), the saturated pressure has a minor influence at low vapor qualities where the frictional pressure drop is mainly contributed by the liquid phase. Higher saturated pressure has larger vapor density and reduces the volume flux significantly at high vapor qualities. Thus the slip and shear force between phases decrease.

6.4. CONCLUSIONS

In this Chapter, the wetting characteristics and interfacial properties of two-phase flow patterns are analyzed for NH$_3$ condensation in PHEs. Based on the analysis, heat transfer and frictional pressure drop models are derived from the experi-mental data presented in Chapter 5.

- The heat transfer model is presented in Eqs. 6.7-6.10. It distinguishes convective condensation and combined condensation. Convective con-densation happens for full film flow, and a two-phase multiplier correla-tion has been developed. Combined condensation takes place for partial film flow. The heat transfer is composed of convective condensation and gravity-controlled condensation. The HTCs of gravity-controlled conden-

sation deviate from Nusselt's theory because of the two-phase shear force and liquid convection. The transition criterion of condensation mechanisms is $We_{L,T} = 0.12$. A cross validation shows that the model is applicable for other refrigerants of similar fluid properties to NH_3.

- A unified model of separated flow is developed for frictional pressure drop, which is shown in Eqs. 6.19-6.20. The Lockhart-Martinelli model is modified to identify the reduction of vapor pressure drop and the influence of surface tension on the interface pressure drop.

6

7

CONCLUSIONS AND RECOMMENDATIONS

Condensation within PHEs is investigated in this thesis experimentally and theoretically. NH$_3$ condensation is experimentally investigated, resulting in heat transfer and frictional pressure drop correlations based on flow patterns. This work mainly focuses on the analysis of NH$_3$ condensation in PHEs. The two-phase vertically downward flow of other working fluids is analyzed by collecting experimental data from literature, including the flow patterns of air/water, as well as the HTCs and frictional pressure drop of HFCs, HCs and HFOs. Different predictive methods are selected for NH$_3$ and other working fluids. Future work is recommended. The condensing flow is a function of fluid proprtties such as two-phase density ratio and surface tension. To predict the flow characteristics of various fluids in PHEs with unified suites, a void fraction model needs to be developed, and the liquid film characteristics need to be described. The condensation of zeotropic mixtures involves both heat and mass transfer. The prediction of HTCs involves the quantification of mass transfer resistance.

7.1. CONCLUSION

7.1.1. FLOW PATTERNS

Four main flow patterns occur in air/water flows within PHEs: bubbly flow, slug flow, churn flow and film flow. An integrated map describes the transition of flow patterns, whose coordinates are Re_L and $J_G/\Lambda^{0.5}$. The flow is film flow when gas phase is dominant, while bubbly flow happens when liquid dominates. When both phases have large mass fluxes, the flow becomes slug or churn. Churn is more chaotic than slug and takes place at larger mass fluxes. Film flow is separated flow and covers a large range of vapor qualities above 0.5.

During the visualization experiments of NH_3 condensation, only film flow has been observed including full film flow and partial film flow. The wall is completely wetted for full film flow, while parts of the wall are dry for partial film flow. The tested ranges are the common operating conditions of NH_3 condensation. The transition mainly depends on the wetting characteristics and is predicted by the criterion of $We_{L,T} = 0.12$. Full film flow takes place at large liquid mass fluxes, while partial film flow happens at small liquid mass fluxes.

7.1.2. HEAT TRANSFER

An experimental database for condensation in PHEs has been built including HFCs, HCs and HFOs. This database covers a wide range of chevron angles, hydraulic diameters, mass fluxes, saturated temperatures and reduced pressures. The database is composed of heat transfer data and frictional pressure drop data. Heat transfer correlations are summarized and compared with the database. The correlations of Longo et al. [60] and Kuo et al. [61] accurately predict this database. However, these correlations are not applicable for NH_3 because of the distinct fluid properties such as two-phase density ratio, latent heat and thermal conductivity.

According to the experimental results of NH_3 condensation in PHEs, HTCs increase significantly with vapor qualities, change moderately with mass fluxes, and decrease slightly with higher saturated pressures. Heat transfer is enhanced during partial film flow because of the wetting characteristics. When parts of the wall are dry, vapor condenses directly on the wall surface. The HTCs correspond to the characteristics of separated flow.

A heat transfer model is developed for NH_3 in Eqs. 6.7-6.10, which identifies condensation mechanisms. Convective condensation corresponds to full film flow, and a two-phase multiplier correlation has been developed. The two-phase multiplier correlation is applicable for separated flow. The multiplier is a function of vapor qualities and two-phase densities. Combined condensation happens for partial film flow, and includes convective condensation and gravity-controlled condensation. The gravity-controlled condensation is predicted with

a modified Nusselt's correlation. The modification accounts for the shear force at the two-phase interface and convection of the condensate film. The same transition criterion of flow patterns applies to condensation mechanisms, namely, $We_{L,T} = 0.12$. Convective condensation prevails for larger We_L, where all the heat is transferred through the condensate film. For smaller We_L, gravity-controlled condensation takes place at dry zones. This model is applicable for NH_3 and other refrigerants of large two-phase density ratio, covering the vapor qualities of 0-0.8, the mass fluxes of 20-80 $kgm^{-2}s^{-1}$ and low reduced pressures. The influence of PHE geometries is also involved.

7.1.3. FRICTIONAL PRESSURE DROP

In Eq. 3.61, a new correlation of frictional pressure drop is derived from the experimental database of condensation in PHEs. This correlation is developed for HFCs, HCs and HFOs, and applies for various chevron angles, hydraulic diameters, mass fluxes, saturated temperatures and reduced pressures. This correlation has the form of two-phase Fanning friction factors and assumes homogeneous flow. The assumption is reasonable for fluids of small two-phase density ratio, but is not suitable for NH_3. In general, correlations of two-phase Fanning friction factor over-predict the experimental data of seperated flow, while Lockhart-Martinelli models under-predict the experimental data of homogeneous flow [18, 59].

The experimental frictional pressure drop of NH_3 increases sharply with vapor qualities and mass fluxes, and decreases slightly with higher saturated pressures. Frictional pressure drop is not sensitive to the transition from full film flow to partial film flow since both flow patterns are separated flow.

As shown in Eqs. 6.19-6.20, a modified Lockhart-Martinelli model is proposed for NH_3 condensation in PHEs. The overall pressure drop is mainly contributed by the vapor phase and the interaction at the two-phase interface. The vapor pressure drop contribution is predicted to be less than that when the vapor flows alone. Since PHEs have corrugated channels, the interface pressure drop is estimated to be relatively small compared with the vapor pressure drop. This model is limited to two-phase NH_3 flow because of the large two-phase density ratio and surface tension, which are distinct from those of other fluids. It is applicable for the vapor qualities of 0-1, the mass fluxes of 20-80 $kgm^{-2}s^{-1}$ and low reduced pressures. This model is expected to apply for most commercial chevron PHEs with limited range of geometrical parameters.

7.2. RECOMMENDATIONS

PHEs are replacing conventional tube-in-tube and shell-and-tube heat exchangers in multiple applications [181–185]. In laboratories, PHEs are widely used

since the compact structure fits the confined installation spaces and simplifies the supporting structures. It is easy to enlarge the heat transfer area when the design has large uncertainties. The accurate design of PHEs is essential in industries to fully exploit the advantage such as heat transfer superiority and reduction of working fluid charges. Knowledge of the thermal-hydraulic mechanisms instructs the researches in how to enhance heat transfer for PHEs [186]. Apart from the investigation in this thesis, several research challenges need to be addressed.

1. The condensation mechanisms rely on flow patterns. Based on the visualization results, the physical interpretation of the transition criterion for NH_3 condensation is discussed in this thesis. The transition criteria of HFCs, HCs and HFOs are expected to be different because of the smaller two-phase density ratios and surface tension, whose flow patterns have not been reported in literature. The transition criterion is a function of vapor qualities. During the condensation of NH_3 in PHEs, lower vapor qualities promote convective condensation since all the wall surface is wetted and the heat is transferred through a liquid film. This feature is different from that in tubes. The wetting characteristics of corrugated surfaces need to be quantitatively analysed including the influence of contact angles [152, 153, 173].

2. The comprehensive description of two-phase condensation processes includes the prediction of heat transfer, frictional pressure drop and void fraction. Depending on flow patterns, the entrained liquid fraction, turbulence model and local liquid film thickness also play roles [187]. Void fraction forms the foundation of the mechanistic models for two-phase heat transfer. The distinction between homogeneous flow and separated flow determines the basic forms of heat transfer and frictional pressure drop correlations. Moreover, the liquid film thickness is quantified making use of the void fraction. Void fraction is a function of channel geometries and fluid properties. Void fraction models are indispensable to develop universal predictive methods for various fluids. Additionally, turbulence models are needed to describe the interfacial characteristics, to quantify the heat transfer enhancement and to determine the interface pressure drop.

3. The condensation of zeotropic mixtures exhibits large temperature glide during the phase change. In PHEs, the heat and mass transfer characteristics depend on the flow patterns [188]. High concentration NH_3/H_2O is a suitable working fluid for Kalina cycles used for the recovery of low grade heat. The modelling approaches of zeotropic condensation are classified

into conservation equation models, non-equilibrium models, equilibrium models and empirical models. Non-equilibrium and equilibrium models are promising considering their applicability and computational complexity [25]. The fundamental assumption of non-equilibrium models is the thermodynamic equilibrium of vapor/liquid at the interface. The heat and mass transfer resistances of the vapor are assumed to be restricted to a thin film [189]. Equilibrium models simplify the computation under the assumption that equilibrium applies to overall vapor/liquid bulk. The mass transfer is considered by adding a heat transfer resistance to the phase change of vapor, but the mass transfer resistance is not calculated directly. According to the experimental results of NH_3/H_2O, the vapor mass transfer resistance plays an important role in the heat transfer performance [188]. The modelling of the mass transfer resistance is coupled with the transition from full film flow to partial film flow.

4. This work is limited to partial condensation excluding superheating and subcooling. During the condensation from superheated vapor to subcooled liquid, thermal non-equilibrium is non-negligible between the two-phase region and single-phase region [121]. To design PHEs applied in energy conversion plants, distributed numerical models are useful tools on condition that validated heat transfer and frictional pressure drop correlations are selected. Numerical models can be integrated into the design of plants to locate the pinch point temperature difference and to improve the heat transfer performance [190, 191].

7

BIBLIOGRAPHY

BIBLIOGRAPHY

[1] D. M. Van de Bor, C. A. Infante Ferreira, and A. A. Kiss, *Low grade waste heat recovery using heat pumps and power cycles,* Energy **89**, 864–873 (2015).

[2] A. B. Little and S. Garimella, *Comparative assessment of alternative cycles for waste heat recovery and upgrade,* Energy **36**, 4492–4504 (2011).

[3] Q. Shi, J. Zhu, M. Hertogh, and Z. Sheng, *Incentive mechanism of prefabrication in mega projects with reputational concerns,* Sustainability **10**, 1260 (2018).

[4] H. Öhman, *Implementation and evaluation of a low temperature waste heat recovery power cycle using NH_3 in an Organic Rankine Cycle,* Energy **48**, 227–232 (2012).

[5] H. Mergner and K. Schaber, *Performance analysis of an evaporation process of plate heat exchangers installed in a Kalina power plant,* Energy **145**, 105–115 (2018).

[6] B. F. Tchanche, G. Lambrinos, A. Frangoudakis, and G. Papadakis, *Low-grade heat conversion into power using organic rankine cycles–a review of various applications,* Renewable and Sustainable Energy Reviews **15**, 3963–3979 (2011).

[7] X. Zhang, M. He, and Y. Zhang, *A review of research on the kalina cycle,* Renewable and Sustainable Energy Reviews **16**, 5309–5318 (2012).

[8] B. M. Fronk and K. R. Zada, *Application of microchannel condensers for small scale kalina waste heat recovery systems,* (American Society of Mechanical Engineers Digital Collection, 2015).

[9] J. Kirkenier, *Techno-economic optimization of Organic Rankine Cycles using working fluid mixtures for 10 to 25 MW OTEC power plants,* MSc Thesis, TU Delft (2014).

[10] X. Tao, M. P. Nuijten, and C. A. Infante Ferreira, *Two-phase vertical downward flow in plate heat exchangers: Flow patterns and condensation mechanisms,* International Journal of Refrigeration **85**, 489–510 (2018).

[11] X. Tao, J. A. Kirkenier, and C. A. Infante Ferreira, *Condensation of NH_3 within a plate heat exchanger of small diameter channel,* in *the 6th ASME International Conference on Micro/Nanoscale Heat and Mass Transfer. Dalian, China,* paper 3920 (2019).

[12] L. Wang, B. Sundén, and R. M. Manglik, *Plate heat exchangers: design, applications and performance,* Vol. 11 (Wit Press, 2007).

[13] J. Chen, K. Zhu, X. Luo, Y. Chen, and Z. Yang, *Application of liquid-separation condensation to plate heat exchanger: Comparative studies,* Applied Thermal Engineering **157**, 113739 (2019).

[14] O. J. Kwon, J. H. Jung, and Y. T. Kang, *Development of experimental Nusselt number and friction factor correlations for condensation of R-1233zd(E) in plate heat exchangers,* International Journal of Heat and Mass Transfer **158**, 120008 (2020).

[15] X. Zhu and F. Haglind, *Computational fluid dynamics modeling of liquid–gas flow patterns and hydraulics in the cross-corrugated channel of a plate heat exchanger,* International Journal of Multiphase Flow **122**, 103163 (2020).

[16] M. Wang, L. He, and C. A. Infante Ferreira, *Ammonia absorption in ionic liquids-based mixtures in plate heat exchangers studied by a semi-empirical heat and mass transfer framework,* International Journal of Heat and Mass Transfer **134**, 1302–1317 (2019).

[17] M. Wang and C. A. Infante Ferreira, *Absorption heat pump cycles with NH_3 – ionic liquid working pairs,* Applied Energy **204**, 819–830 (2017).

[18] X. Tao and C. A. Infante Ferreira, *Heat transfer and frictional pressure drop during condensation in plate heat exchangers: Assessment of correlations and a new method,* International Journal of Heat and Mass Transfer **135**, 996–1012 (2019).

[19] D. Winkelmann, *Condensation of pure refrigerants and their zeotropic mixtures in plate heat exchangers,* PhD Thesis, TU Berlin (2010).

[20] H. Martin, *Pressure drop and heat transfer in plate heat exchangers.* (Springer, Dusseldorf, 2010) Chap. VDI Heat Atlas, 2nd Edition, pp. 1516–1521.

[21] R. L. Amalfi, F. Vakili-Farahani, and J. R. Thome, *Flow boiling and frictional pressure gradients in plate heat exchangers. part 1: Review and experimental database,* International Journal of Refrigeration **61**, 166–184 (2016).

[22] A. Muley and R. M. Manglik, *Experimental study of turbulent flow heat transfer and pressure drop in a plate heat exchanger with chevron plates,* Journal of Heat Transfer **121**, 110–117 (1999).

[23] H. M. Metwally and R. M. Manglik, *Enhanced heat transfer due to curvature-induced lateral vortices in laminar flows in sinusoidal corrugated-plate channels,* International Journal of Heat and Mass Transfer **47**, 2283–2292 (2004).

[24] P. R. Bobbili, B. Sunden, and S. K. Das, *Thermal analysis of plate condensers in presence of flow maldistribution,* International Journal of Heat and Mass Transfer **49**, 4966–4977 (2006).

[25] B. M. Fronk and S. Garimella, *In-tube condensation of zeotropic fluid mixtures: A review,* International Journal of Refrigeration **36**, 534–561 (2013).

[26] R. L. Amalfi, J. R. Thome, V. Solotych, and J. Kim, *High resolution local heat transfer and pressure drop infrared measurements of two-phase flow of R245fa within a compact plate heat exchanger,* International Journal of Heat and Mass Transfer **103**, 791–806 (2016).

[27] K. Sarraf, S. Launay, G. El Achkar, and L. Tadrist, *Local vs global heat transfer and flow analysis of hydrocarbon complete condensation in plate heat exchanger based on infrared thermography,* International Journal of Heat and Mass Transfer **90**, 878–893 (2015).

[28] R. Mancini, B. Zühlsdorf, V. Aute, W. B. Markussen, and B. Elmegaard, *Performance of heat pumps using pure and mixed refrigerants with maldistribution effects in plate heat exchanger evaporators,* International Journal of Refrigeration **104**, 390–403 (2019).

[29] C. W. Jung, S. S. An, and Y. T. Kang, *Thermal performance estimation of ammonia-water plate bubble absorbers for compression/absorption hybrid heat pump application,* Energy **75**, 371–378 (2014).

[30] J. Cerezo, R. Best, M. Bourouis, and A. Coronas, *Comparison of numerical and experimental performance criteria of an ammonia–water bubble absorber using plate heat exchangers,* International Journal of Heat and Mass Transfer **53**, 3379–3386 (2010).

[31] J. Cerezo, M. Bourouis, M. Vallès, A. Coronas, and R. Best, *Experimental study of an ammonia–water bubble absorber using a plate heat exchanger for absorption refrigeration machines,* Applied Thermal Engineering **29**, 1005–1011 (2009).

[32] H. Lee, Y. Hwang, R. Radermacher, and H.-H. Chun, *Experimental investigation of novel heat exchanger for low temperature lift heat pump,* Energy **51**, 468–474 (2013).

[33] J. Fernández-Seara, F. J. Uhía, and R. Diz, *Experimental analysis of ammonia condensation on smooth and integral-fin titanium tubes,* International Journal of Refrigeration **32**, 1140–1148 (2009).

[34] J. Fernández-Seara and F. J. Uhía, *Heat transfer and friction characteristics of spirally corrugated tubes for outer ammonia condensation,* International Journal of Refrigeration **35**, 2022–2032 (2012).

[35] H. B. Komandiwirya, P. S. Hrnjak, and T. A. Newell, *An experimental investigation of pressure drop and heat transfer in an in-tube condensation system of ammonia with and without miscible oil in smooth and enhanced tubes,* Report (Air Conditioning and Refrigeration Center. College of Engineering. University of Illinois at Urbana-Champaign., 2005).

[36] P. Hrnjak and A. D. Litch, *Microchannel heat exchangers for charge minimization in air-cooled ammonia condensers and chillers,* International Journal of Refrigeration **31**, 658–668 (2008).

[37] B. M. Fronk and S. Garimella, *Condensation of ammonia and high-temperature-glide ammonia/water zeotropic mixtures in minichannels–part i: Measurements,* International Journal of Heat and Mass Transfer **101**, 1343–1356 (2016).

[38] L. Chen, Y. S. Tian, and T. G. Karayiannis, *The effect of tube diameter on vertical two-phase flow regimes in small tubes,* International Journal of Heat and Mass Transfer **49**, 4220–4230 (2006).

[39] E. W. Lemmon, M. L. Huber, and M. O. McLinden, *NIST Standard Reference Database 23: Reference Fluid Thermodynamic and Transport Properties-REFPROP, Version 9.1, National Institute of Standards and Technology, Standard Reference Data Program, Gaithersburg,* See http://www.nist.gov/srd/nist23.cfm (2013).

[40] Y. Chen, K.-S. Yang, Y.-J. Chang, and C.-C. Wang, *Two-phase pressure drop of air–water and R-410A in small horizontal tubes,* International Journal of Multiphase Flow **27**, 1293–1299 (2001).

[41] E. Ungar and J. Cornwell, *Two-phase pressure drop of ammonia in small diameter horizontal tubes,* in *AIAA 17th Aerospace Ground Testing Conference* (1992).

[42] C. Y. Park and P. Hrnjak, *NH₃ in-tube condensation heat transfer and pressure drop in a smooth tube,* International Journal of Refrigeration **31**, 643–651 (2008).

[43] H. Kumar, *The design of plate heat exchangers for refrigerants,* in *Proceedings Institute of Refrigeration. London, the UK* (1992) pp. 50–55.

[44] C. B. Panchal and T. J. Rabas, *Thermal performance of advanced heat exchangers for ammonia refrigeration systems,* Heat Transfer Engineering **14**, 42–57 (1993).

[45] X. Tao, E. Dahlgren, M. Leichsenring, and C. A. Infante Ferreira, *NH₃ condensation in a plate heat exchanger: Experimental investigation on flow patterns, heat transfer and frictional pressure drop,* International Journal of Heat and Mass Transfer **151**, 119374 (2020).

[46] M. S. Khan, T. S. Khan, M.-C. Chyu, and Z. H. Ayub, *Experimental investigation of evaporation heat transfer and pressure drop of ammonia in a 30 chevron plate heat exchanger,* International Journal of Refrigeration **35**, 1757–1765 (2012).

[47] T. S. Khan, M. S. Khan, M.-C. Chyu, and Z. H. Ayub, *Experimental investigation of evaporation heat transfer and pressure drop of ammonia in a 60 chevron plate heat exchanger,* International Journal of Refrigeration **35**, 336–348 (2012).

[48] F. Táboas, M. Vallès, M. Bourouis, and A. Coronas, *Flow boiling heat transfer of ammonia/water mixture in a plate heat exchanger,* International Journal of Refrigeration **33**, 695–705 (2010).

[49] F. Taboas, M. Valles, M. Bourouis, and A. Coronas, *Assessment of boiling heat transfer and pressure drop correlations of ammonia/water mixture in a plate heat exchanger,* International Journal of Refrigeration **35**, 633–644 (2012).

[50] B. Thonon, R. Vidil, and C. Marvillet, *Recent research and developments in plate heat exchangers,* Journal of Enhanced Heat Transfer **2** (1995).

[51] J. R. García-Cascales, F. Vera-García, J. M. Corberán-Salvador, and J. Gonzálvez-Maciá, *Assessment of boiling and condensation heat transfer correlations in the modelling of plate heat exchangers,* International Journal of Refrigeration **30**, 1029–1041 (2007).

[52] W. W. Akers, H. A. Deans, and O. K. Crosser, *Condensing heat transfer within horizontal tubes,* Chemical Engineering Progress **54**, 89–90 (1958).

[53] R. L. Amalfi, F. Vakili-Farahani, and J. R. Thome, *Flow boiling and frictional pressure gradients in plate heat exchangers. part 2: Comparison of literature methods to database and new prediction methods,* International Journal of Refrigeration **61**, 185–203 (2016).

[54] F. Vakili-Farahani, R. L. Amalfi, and J. R. Thome, *Two-phase heat transfer and pressure drop within plate heat exchangers,* in *Encyclopedia of Two-Phase Heat Transfer and Flow II: Special Topics and Applications* (World Scientific, 2016) pp. 145–215.

[55] R. Eldeeb, V. Aute, and R. Radermacher, *A survey of correlations for heat transfer and pressure drop for evaporation and condensation in plate heat exchangers,* International Journal of Refrigeration **65**, 12–26 (2016).

[56] M. M. Shah, *A general correlation for heat transfer during film condensation inside pipes,* International Journal of Heat and Mass Transfer **22**, 547–556 (1979).

[57] R. W. Lockhart and R. C. Martinelli, *Proposed correlation of data for isothermal two-phase, two-component flow in pipes,* Chemical Engineering Progress **45**, 39–48 (1949).

[58] D. Chisholm, *A theoretical basis for the Lockhart-Martinelli correlation for two-phase flow,* International Journal of Heat and Mass Transfer **10**, 1767–1778 (1967).

[59] X. Tao and C. A. Infante Ferreira, *NH_3 condensation in a plate heat exchanger: Flow pattern based models of heat transfer and frictional pressure drop,* International Journal of Heat and Mass Transfer **154**, 119774 (2020).

[60] G. A. Longo, G. Righetti, and C. Zilio, *A new computational procedure for refrigerant condensation inside herringbone-type brazed plate heat exchangers,* International Journal of Heat and Mass Transfer **82**, 530–536 (2015).

[61] W. S. Kuo, Y. M. Lie, Y. Y. Hsieh, and T. F. Lin, *Condensation heat transfer and pressure drop of refrigerant R-410A flow in a vertical plate heat exchanger,* International Journal of Heat and Mass Transfer **48**, 5205–5220 (2005).

[62] W. Kast, E. S. Gaddis, K. Wirth, and J. Stichlmair, *Pressure drop in single phase flow,* (Springer, Dusseldorf, 2010) Chap. VDI Heat Atlas, 2nd Edition, pp. 1055–1115.

[63] M. M. Shah, *A new correlation for heat transfer during boiling flow through pipes,* ASHRAE Transaction **82**, 66–86 (1976).

[64] T. Oshinowo and M. E. Charles, *Vertical two-phase flow part i. flow pattern correlations,* The Canadian Journal of Chemical Engineering **52**, 25–35 (1974).

[65] A. Jokar, M. H. Hosni, and S. J. Eckels, *Dimensional analysis on the evaporation and condensation of refrigerant R-134a in minichannel plate heat exchangers,* Applied Thermal Engineering **26**, 2287–2300 (2006).

[66] J. Zhang, M. R. Kærn, T. Ommen, B. Elmegaard, and F. Haglind, *Condensation heat transfer and pressure drop characteristics of R134a, R1234ze (E), R245fa and R1233zd (E) in a plate heat exchanger,* International Journal of Heat and Mass Transfer **128**, 136–149 (2019).

[67] A. E. Bergles, J. G. Collier, J. M. Delhaye, G. F. Hewitt, and F. Mayinger, *Two-phase flow and heat transfer in the power and process industries* (Hemisphere New York, 1981).

[68] A. Cavallini, D. D. Col, L. Doretti, M. Matkovic, L. Rossetto, C. Zilio, and G. Censi, *Condensation in horizontal smooth tubes: a new heat transfer model for heat exchanger design,* Heat Transfer Engineering **27**, 31–38 (2006).

[69] B. M. Fronk and S. Garimella, *Condensation of ammonia and high-temperature-glide zeotropic ammonia/water mixtures in minichannels–part ii: Heat transfer models,* International Journal of Heat and Mass Transfer **101**, 1357–1373 (2016).

[70] S. C. Palmer, W. V. Payne, and P. A. Domanski, *Evaporation and condensation heat transfer performance of flammable refrigerants in a brazed plate heat exchanger,* Report (NIST, See https://citeseerx.ist.psu.edu/viewdoc/download?doi=10.1.1.460.3234&rep =rep1&type=pdf, 2000).

[71] Y.-Y. Yan, H.-C. Lio, and T.-F. Lin, *Condensation heat transfer and pressure drop of refrigerant R-134a in a plate heat exchanger,* International Journal of Heat and Mass Transfer **42**, 993–1006 (1999).

[72] Z. Y. Shi, J. P. Chen, V. Grabenstein, and S. Kabelac, *Experimental investigation on condensation heat transfer and pressure drop of R134a in a plate heat exchanger,* Heat and Mass Transfer **46**, 1177–1185 (2010).

[73] B. H. Shon, C. W. Jung, O. J. Kwon, C. K. Choi, and Y. T. Kang, *Characteristics on condensation heat transfer and pressure drop for a low GWP refrigerant in brazed plate heat exchanger,* International Journal of Heat and Mass Transfer **122**, 1272–1282 (2018).

[74] Z.-Z. Wang and Z.-N. Zhao, *Analysis of performance of steam condensation heat transfer and pressure drop in plate condensers,* Heat Transfer Engineering **14**, 32–41 (1993).

[75] N. Hayes, A. Jokar, and Z. H. Ayub, *Study of carbon dioxide condensation in chevron plate exchangers; heat transfer analysis,* International Journal of Heat and Mass Transfer **54**, 1121–1131 (2011).

[76] S. Mancin, D. Del Col, and L. Rossetto, *R32 partial condensation inside a brazed plate heat exchanger,* International Journal of Refrigeration **36**, 601–611 (2013).

[77] G. A. Longo, *Heat transfer and pressure drop during HFC refrigerant saturated vapour condensation inside a brazed plate heat exchanger,* International Journal of Heat and Mass Transfer **53**, 1079–1087 (2010).

[78] G. A. Longo, *Heat transfer and pressure drop during hydrocarbon refrigerant condensation inside a brazed plate heat exchanger,* International Journal of Refrigeration **33**, 944–953 (2010).

[79] W. Nusselt, *The condensation of steam on cooled surfaces,* Z. Ver. Dtsch. Ing **60**, 541–546 (1916).

[80] S. Mancin, D. Del Col, and L. Rossetto, *Condensation of superheated vapour of R410A and R407C inside plate heat exchangers: experimental results and simulation procedure,* International Journal of Refrigeration **35**, 2003–2013 (2012).

[81] S. Mancin, D. Del Col, and L. Rossetto, *Partial condensation of R407C and R410A refrigerants inside a plate heat exchanger,* Experimental Thermal and Fluid Science **36**, 149–157 (2012).

[82] B. Thonon and A. Bontemps, *Condensation of pure and mixture of hydrocarbons in a compact heat exchanger: experiments and modelling,* Heat Transfer Engineering **23**, 3–17 (2002).

[83] V. Grabenstein and S. Kabelac, *Experimental and theoretical analysis of the local condensation heat transfer in a plate heat exchanger,* (IOP Publishing, 2012) p. 012169.

[84] G. A. Longo, *Refrigerant R134a condensation heat transfer and pressure drop inside a small brazed plate heat exchanger,* International Journal of Refrigeration **31**, 780–789 (2008).

[85] G. A. Longo, *R410A condensation inside a commercial brazed plate heat exchanger,* Experimental Thermal and Fluid Science **33**, 284–291 (2009).

[86] G. A. Longo, *The effect of vapour super-heating on hydrocarbon refrigerant condensation inside a brazed plate heat exchanger,* Experimental Thermal and Fluid Science **35**, 978–985 (2011).

[87] D.-H. Han, K.-J. Lee, and Y.-H. Kim, *The characteristics of condensation in brazed plate heat exchangers with different chevron angles,* Journal-Korean Physical Society **43**, 66–73 (2003).

[88] A. Jokar, S. J. Eckels, M. H. Honsi, and T. P. Gielda, *Condensation heat transfer and pressure drop of brazed plate heat exchangers using refrigerant R-134a,* Journal of Enhanced Heat Transfer **11**, 161–182 (2004).

[89] E. M. Djordjević, S. Kabelac, and S. P. Šerbanović, *Heat transfer coefficient and pressure drop during refrigerant R-134a condensation in a plate heat exchanger,* Chemical Papers **62**, 78–85 (2008).

[90] P. Hrnjak and C. Kondou, *Refrigerant side heat transfer in condensers with round tubes,* in *Proceedings of the 4th IIR Conference on Thermophysical Properties and Transfer Processes of Refrigerants, Delft, The Netherlands,* paper TP-087 (2013).

[91] K. Sarraf, S. Launay, and L. Tadrist, *Analysis of enhanced vapor desuperheating during condensation inside a plate heat exchanger,* International Journal of Thermal Sciences **105**, 96–108 (2016).

[92] G. A. Longo and C. Zilio, *Condensation of the low GWP refrigerant HFC1234yf inside a brazed plate heat exchanger,* International Journal of Refrigeration **36**, 612–621 (2013).

[93] G. A. Longo, C. Zilio, G. Righetti, and J. S. Brown, *Condensation of the low GWP refrigerant HFO1234ze (E) inside a brazed plate heat exchanger,* International Journal of Refrigeration **38**, 250–259 (2014).

[94] G. A. Longo, C. Zilio, G. Righetti, and J. S. Brown, *Experimental assessment of the low GWP refrigerant HFO-1234ze (Z) for high temperature heat pumps,* Experimental Thermal and Fluid Science **57**, 293–300 (2014).

[95] S. Jin and P. Hrnjak, *Effect of end plates on heat transfer of plate heat exchanger,* International Journal of Heat and Mass Transfer **108**, 740–748 (2017).

[96] R. Würfel and N. Ostrowski, *Experimental investigations of heat transfer and pressure drop during the condensation process within plate heat exchangers of the herringbone-type,* International Journal of Thermal Sciences **43**, 59–68 (2004).

[97] V. Grabenstein, A.-E. Polzin, and S. Kabelac, *Experimental investigation of the flow pattern, pressure drop and void fraction of two-phase flow in the corrugated gap of a plate heat exchanger,* International Journal of Multiphase Flow **91**, 155–169 (2017).

[98] C. Tribbe and H. M. Müller-Steinhagen, *Gas/liquid flow in plate-and-frame heat exchangers-part ii: two-phase multiplier and flow pattern analysis,* Heat Transfer Engineering **22**, 12–21 (2001).

[99] P. Vlasogiannis, G. Karagiannis, P. Argyropoulos, and V. Bontozoglou, *Air–water two-phase flow and heat transfer in a plate heat exchanger,* International Journal of Multiphase Flow **28**, 757–772 (2002).

[100] K. Nilpueng and S. Wongwises, *Two-phase gas–liquid flow characteristics inside a plate heat exchanger,* Experimental Thermal and Fluid Science **34**, 1217–1229 (2010).

[101] S. Buscher, *Visualization and modelling of flow pattern transitions in a cross-corrugated plate heat exchanger channel with uniform two-phase distribution,* International Journal of Heat and Mass Transfer **144**, 118643 (2019).

[102] T. Fukano and A. Kariyasaki, *Characteristics of gas-liquid two-phase flow in a capillary tube,* Nuclear Engineering and Design **141**, 59–68 (1993).

[103] H. B. Mehta and J. Banerjee, *An investigation of flow orientation on air–water two-phase flow in circular minichannel,* Heat and Mass Transfer **50**, 1353–1364 (2014).

[104] C. Jiang and B. Bai, *Flow patterns and pressure drop of downward two-phase flow in a capsule-type plate heat exchanger,* Experimental Thermal and Fluid Science **103**, 347–354 (2019).

[105] C. Tribbe and H. M. Müller-Steinhagen, *Gas/liquid flow in plate-and-frame heat exchangers-part i: Pressure drop measurements,* Heat Transfer Engineering **22**, 5–11 (2001).

[106] M. K. Dobson and J. C. Chato, *Condensation in smooth horizontal tubes,* ASME Journal of Heat Transfer **120**, 193–213 (1998).

[107] J. El Hajal, J. R. Thome, and A. Cavallini, *Condensation in horizontal tubes, part 1: two-phase flow pattern map,* International Journal of Heat and Mass Transfer **46**, 3349–3363 (2003).

[108] P. L. Spedding, G. S. Woods, R. S. Raghunathan, and J. K. Watterson, *Vertical two-phase flow: Part i: Flow regimes,* Chemical Engineering Research and Design **76**, 612–619 (1998).

[109] N. B. Vargaftik, B. N. Volkov, and L. D. Voljak, *International tables of the surface tension of water,* Journal of Physical and Chemical Reference Data **12**, 817–820 (1983).

[110] D. Barnea, Y. Luninski, and Y. Taitel, *Flow pattern in horizontal and vertical two phase flow in small diameter pipes,* The Canadian Journal of Chemical Engineering **61**, 617–620 (1983).

[111] W. W. Focke and P. G. Knibbe, *Flow visualization in parallel-plate ducts with corrugated walls,* Journal of Fluid Mechanics **165**, 73–77 (1986).

[112] D. Dović, B. Palm, and S. Švaić, *Generalized correlations for predicting heat transfer and pressure drop in plate heat exchanger channels of arbitrary geometry,* International Journal of Heat and Mass Transfer **52**, 4553–4563 (2009).

[113] K. Sarraf, S. Launay, and L. Tadrist, *Complex 3D-flow analysis and corrugation angle effect in plate heat exchangers,* International Journal of Thermal Sciences **94**, 126–138 (2015).

[114] J. Lim, K. S. Song, D. Kim, D. Lee, and Y. Kim, *Condensation heat transfer characteristics of R245fa in a shell and plate heat exchanger for high-temperature heat pumps,* International Journal of Heat and Mass Transfer **127**, 730–739 (2018).

[115] S. Kabelac and S. W. Freund, *Local two-phase flow heat transfer in plate heat exchangers,* in *ASME/JSME Thermal Engineering Heat Transfer Summer Conference* (American Society of Mechanical Engineers, 2007) pp. 469–477.

[116] N. Hayes, A. Jokar, and Z. H. Ayub, *Study of carbon dioxide condensation in chevron plate exchangers; pressure drop analysis,* International Journal of Heat and Mass Transfer **55**, 2916–2925 (2012).

[117] G. A. Longo, C. Zilio, and G. Righetti, *Condensation of the low GWP refrigerant HFC152a inside a brazed plate heat exchanger,* Experimental Thermal and Fluid Science **68**, 509–515 (2015).

[118] G. A. Longo, S. Mancin, G. Righetti, and C. Zilio, *HFC404A condensation inside a small brazed plate heat exchanger: Comparison with the low GWP substitutes propane and propylene,* International Journal of Refrigeration **81**, 41–49 (2017).

[119] J. Soontarapiromsook, O. Mahian, A. S. Dalkilic, and S. Wongwises, *Effect of surface roughness on the condensation of R-134a in vertical chevron gasketed plate heat exchangers,* Experimental Thermal and Fluid Science (2018).

[120] C. Kondou and P. Hrnjak, *Condensation from superheated vapor flow of R744 and R410A at subcritical pressures in a horizontal smooth tube,* International Journal of Heat and Mass Transfer **55**, 2779–2791 (2012).

[121] J. Xiao and P. Hrnjak, *Heat transfer and pressure drop of condensation from superheated vapor to subcooled liquid,* International Journal of Heat and Mass Transfer **103**, 1327–1334 (2016).

[122] J. Xiao and P. Hrnjak, *A new flow regime map and void fraction model based on the flow characterization of condensation,* International Journal of Heat and Mass Transfer **108**, 443–452 (2017).

[123] R. L. Webb, *Convective condensation of superheated vapor,* Journal of Heat Transfer **120**, 418–421 (1998).

[124] L. Silver, *Gas cooling with aqueous condensation,* Transactions of the Institution of Chemical Engineers **25**, 30–42 (1947).

[125] K. J. Bell and M. A. Ghaly, *An approximate generalized design method for multicomponent/partial condenser,* in *AIChE symposium series,* Vol. 69 (1973) pp. 72–79.

[126] J. R. Thome, J. El Hajal, and A. Cavallini, *Condensation in horizontal tubes, part 2: new heat transfer model based on flow regimes,* International Journal of Heat and Mass Transfer **46**, 3365–3387 (2003).

[127] E. W. Jassim, T. A. Newell, and J. C. Chato, *Refrigerant pressure drop in chevron and bumpy style flat plate heat exchangers,* Experimental Thermal and Fluid Science **30**, 213–222 (2006).

[128] J.-H. Park and Y.-S. Kim, *Condensation heat transfer and pressure drop of R-134a in the oblong shell and plate heat exchanger,* International Journal of Air-Conditioning and Refrigeration **12**, 158–167 (2004).

[129] J. H. Park, Y. C. H. Kwon, and Y. S. Kim, *Experimental study on R-410A condensation heat transfer and pressure drop characteristics in oblong shell and plate heat exchanger,* in *International Refrigeration and Air Conditioning Conference. Purdue, America* (2004).

[130] H. B. Luan, J. P. Kuang, Z. Cao, Z. Wu, W. Q. Tao, and B. Sundén, *CFD analysis of two types of welded plate heat exchangers,* Numerical Heat Transfer, Part A: Applications **71**, 250–269 (2017).

[131] X. Tao, E. Dahlgren, and C. A. Infante Ferreira, *Local NH_3 condensation in a plate heat exchanger,* in *13th IIR Gustav Lorentzen Conference On Natural Refrigerants. Valencia, Spain,* paper 1160 (2018).

[132] X. Tao, E. Dahlgren, and C. A. Infante Ferreira, *Condensation heat transfer and pressure drop of NH_3 and NH_3/H_2O within a plate heat exchanger,* in *25th IIR International Congress of Refrigeration. Montreal, Canada,* paper 727 (2019).

[133] H. J. Kim, L. Liebenberg, and A. M. Jacobi, *Flow visualization of R-245fa boiling in a brazed plate heat exchanger (BPHE) near the micro-macroscale transition,* in *International Refrigeration and Air Conditioning Conference. Purdue, America* (2018).

[134] M. Nakamura, Y. Kawabata, T. Yasunaga, and Y. Ikegami, *The visualization of phase change phenomena in herringbone type plate heat exchanger using 3D-printer,* in *The 27th International Symposium on Transport Phenomena. Honolulu, America* (2016).

[135] D. Lee, D. Kim, S. Yun, and Y. Kim, *Two-phase flow patterns and pressure drop of a low GWP refrigerant R-1234ze (E) in a plate heat exchanger under adiabatic conditions,* International Journal of Heat and Mass Transfer **145**, 118816 (2019).

[136] R. J. da Silva Lima, J. M. Quibén, C. Kuhn, T. Boyman, and J. R. Thome, *Ammonia two-phase flow in a horizontal smooth tube: flow pattern observations, diabatic and adiabatic frictional pressure drops and assessment of*

prediction methods, International Journal of Heat and Mass Transfer **52**, 2273–2288 (2009).

[137] H. Arima, J. H. Kim, A. Okamoto, and Y. Ikegami, *Local boiling heat transfer characteristics of ammonia in a vertical plate evaporator,* International Journal of Refrigeration **33**, 359–370 (2010).

[138] M. Leichsenring, *Flow visualization of downward condensing ammonia in a gasketed plate heat exchanger,* Master's thesis, TU Delft, See http://resolver.tudelft.nl/uuid:1f9c5c33-b909-464f-820a-5f57d02bbd40 (2019).

[139] M. Leichsenring, X. Tao, C. A. Infante Ferreira, and J. A. Kirkenier, *Flow visualization of ammonia inside a gasketed plate heat exchanger condenser,* in *25th IIR International Congress of Refrigeration. Montreal, Canada,* paper 746 (2019).

[140] J. Fernandez-Seara, F. J. Uhía, J. Sieres, and A. Campo, *A general review of the Wilson plot method and its modifications to determine convection coefficients in heat exchange devices,* Applied Thermal Engineering **27**, 2745–2757 (2007).

[141] H. Martin, *A theoretical approach to predict the performance of chevrontype plate heat exchangers,* Chemical Engineering and Processing: Process Intensification **35**, 301–310 (1996).

[142] R. K. Shah and W. W. Focke, *Plate heat exchangers and their design theory,* Heat Transfer Equipment Design **227**, 254 (1988).

[143] W. W. Focke, J. Zachariades, and I. Olivier, *The effect of the corrugation inclination angle on the thermohydraulic performance of plate heat exchangers,* International Journal of Heat and Mass Transfer **28**, 1469–1479 (1985).

[144] J. G. Collier and J. R. Thome, *Convective boiling and condensation* (Clarendon Press, 1994).

[145] T. A. Jankowski, E. N. Schmierer, F. C. Prenger, and S. P. Ashworth, *A series pressure drop representation for flow through orifice tubes,* Journal of Fluids Engineering **130**, 051204 (2008).

[146] A. Ushida, T. Hasegawa, and T. Narumi, *Anomalous phenomena in pressure drops of water flows through micro-orifices,* Microfluidics and Nanofluidics **17**, 863–870 (2014).

[147] D. Liu, Z. Gan, A. de Waele, X. Tao, and Y. Yao, *Temperature and mass-flow behavior of a He-4 Joule-Thomson cryocooler,* International Journal of Heat and Mass Transfer **109**, 1094–1099 (2017).

[148] A. M. Barajas and R. L. Panton, *The effects of contact angle on two-phase flow in capillary tubes,* International Journal of Multiphase Flow **19**, 337–346 (1993).

[149] C. Zhang, C. Shen, and Y. Chen, *Experimental study on flow condensation of mixture in a hydrophobic microchannel,* International Journal of Heat and Mass Transfer **104**, 1135–1144 (2017).

[150] J. Wang, J. Yan, S. Hu, and J. Liu, *Marangoni condensation heat transfer of water–ethanol mixtures on a vertical surface with temperature gradients,* International Journal of Heat and Mass Transfer **52**, 2324–2334 (2009).

[151] L. Galbiati and P. Andreini, *The transition between stratified and annular regimes for horizontal two-phase flow in small diameter tubes,* International Communications in Heat and Mass Transfer **19**, 185–190 (1992).

[152] D. E. Hartley and W. Murgatroyd, *Criteria for the break-up of thin liquid layers flowing isothermally over solid surfaces,* International Journal of Heat and Mass Transfer **7**, 1003–1015 (1964).

[153] M. S. El-Genk and H. H. Saber, *Minimum thickness of a flowing down liquid film on a vertical surface,* International Journal of Heat and Mass Transfer **44**, 2809–2825 (2001).

[154] K. W. Moser, R. L. Webb, and B. Na, *A new equivalent Reynolds number model for condensation in smooth tubes,* Journal of Heat Transfer **120**, 410–417 (1998).

[155] V. G. Nino, P. S. Hrnjak, and T. A. Newell, *Characterization of two-phase flow in microchannels*, Report (Air Conditioning and Refrigeration Center. College of Engineering. University of Illinois at Urbana-Champaign., 2002).

[156] D. C. Adams, P. S. Hrnjak, and T. A. Newell, *Pressure drop and void fraction in microchannels using carbon dioxide, ammonia, and R245fa as refrigerants*, Report (Air Conditioning and Refrigeration Center. College of Engineering. University of Illinois at Urbana-Champaign., 2003).

[157] D. A. Yashar, M. J. Wilson, H. R. Kopke, D. M. Graham, J. C. Chato, and T. A. Newell, *An investigation of refrigerant void fraction in horizontal, microfin tubes,* HVAC&R Research **7**, 67–82 (2001).

[158] S. Z. Rouhani and E. Axelsson, *Calculation of void volume fraction in the subcooled and quality boiling regions,* International Journal of Heat and Mass Transfer **13**, 383–393 (1970).

[159] L. Wojtan, T. Ursenbacher, and J. R. Thome, *Investigation of flow boiling in horizontal tubes: Part i—a new diabatic two-phase flow pattern map,* International Journal of Heat and Mass Transfer **48**, 2955–2969 (2005).

[160] B. Keinath and S. Garimella, *Measurement and modeling of void fraction in high-pressure condensing flows through microchannels,* Heat Transfer Engineering **37**, 1172–1180 (2016).

[161] S. M. Zivi, *Estimation of steady-state steam void-fraction by means of the principle of minimum entropy production,* Journal of Heat Transfer **86**, 247–251 (1964).

[162] M. J. Wilson, J. C. Chato, T. A. Newell, and A. G. Kireta, *A study of refrigerant pressure drop and void fraction in flattened copper tubes,* in *International Refrigeration and Air Conditioning Conference. Purdue, America* (2000).

[163] K. A. Triplett, S. M. Ghiaasiaan, S. I. Abdel-Khalik, A. LeMouel, and B. N. McCord, *Gas–liquid two-phase flow in microchannels part ii: void fraction and pressure drop,* International Journal of Multiphase Flow **25**, 395–410 (1999).

[164] M. M. Shah, *An improved and extended general correlation for heat transfer during condensation in plain tubes,* HVAC&R Research **15**, 889–913 (2009).

[165] H. M. Soliman, *On the annular-to-wavy flow pattern transition during condensation inside horizontal tubes,* The Canadian Journal of Chemical Engineering **60**, 475–481 (1982).

[166] L. Friedel, *Improved friction pressure drop correlations for horizontal and vertical two-phase flow,* in *The European Two-Phase Flow Group Meeting. Ispra, Italy* (1979).

[167] H. Müller-Steinhagen and K. Heck, *A simple friction pressure drop correlation for two-phase flow in pipes,* Chemical Engineering and Processing: Process Intensification **20**, 297–308 (1986).

[168] B. M. Fronk and S. Garimella, *Heat transfer and pressure drop during condensation of ammonia in microchannels,* in *the 3rd ASME International Conference on Micro/Nanoscale Heat and Mass Transfer* (American Society of Mechanical Engineers, 2012) pp. 399–409.

[169] A. L. Souza, J. C. Chato, J. M. S. Jabardo, J. P. Wattelet, J. S. Panek, B. R. Christoffersen, and N. Rhines, *Pressure drop during two-phase flow of refrigerants in horizontal smooth tubes*, Report (Air Conditioning and Refrigeration Center. College of Engineering. University of Illinois at Urbana-Champaign., 1992).

[170] J. Hart, P. J. Hamersma, and J. M. H. Fortuin, *Correlations predicting frictional pressure drop and liquid holdup during horizontal gas-liquid pipe flow with a small liquid holdup,* International Journal of Multiphase Flow **15**, 947–964 (1989).

[171] B.-X. Wang and X.-Z. Du, *Study on laminar film-wise condensation for vapor flow in an inclined small/mini-diameter tube,* International Journal of Heat and Mass Transfer **43**, 1859–1868 (2000).

[172] M. K. Dobson, *Heat transfer and flow regimes during condensation in horizontal tubes*, Report (Air Conditioning and Refrigeration Center. College of Engineering. University of Illinois at Urbana-Champaign., 1994).

[173] T. Ahn, J. Moon, B. Bae, J. Jeong, B. Bae, and B. Yun, *An empirical model of the wetted wall fraction in separated flows of horizontal and inclined pipes,* Chemical Engineering Science **178**, 260–272 (2018).

[174] J. W. Rose, *Fundamentals of condensation heat transfer: laminar film condensation,* JSME International Journal. Ser. 2, Fluids engineering, heat transfer, power, combustion, thermophysical properties **31**, 357–375 (1988).

[175] E. M. Sparrow and J. L. Gregg, *A boundary-layer treatment of laminar-film condensation,* Journal of Heat Transfer **81**, 13–18 (1959).

[176] M. M. Chen, *An analytical study of laminar film condensation: part 1—flat plates,* Journal of Heat Transfer **83**, 48–54 (1961).

[177] J. C. Y. Koh, E. M. Sparrow, and J. P. Hartnett, *The two phase boundary layer in laminar film condensation,* International Journal of Heat and Mass Transfer **2**, 69–82 (1961).

[178] H. Jaster and P. G. Kosky, *Condensation heat transfer in a mixed flow regime,* International Journal of Heat and Mass Transfer **19**, 95–99 (1976).

[179] H. J. Lee and S. Y. Lee, *Pressure drop correlations for two-phase flow within horizontal rectangular channels with small heights,* International Journal of Multiphase Flow **27**, 783–796 (2001).

[180] Y. S. Muzychka and M. M. Awad, *Asymptotic generalizations of the Lock-hart–Martinelli method for two phase flows,* Journal of Fluids Engineering **132**, 031302 (2010).

[181] H. Lee, Y. Hwang, R. Radermacher, and H.-H. Chun, *Thermal and hydraulic performance of sinusoidal corrugated plate heat exchanger for low temperature lift heat pump,* International Journal of Refrigeration **36**, 689–700 (2013).

[182] H. Lee, S. Li, Y. Hwang, R. Radermacher, and H.-H. Chun, *Experimental investigations on flow boiling heat transfer in plate heat exchanger at low mass flux condition,* Applied Thermal Engineering **61**, 408–415 (2013).

[183] V. Solotych, D. Lee, J. Kim, R. L. Amalfi, and J. R. Thome, *Boiling heat transfer and two-phase pressure drops within compact plate heat exchangers: Experiments and flow visualizations,* International Journal of Heat and Mass Transfer **94**, 239–253 (2016).

[184] J. Zhang, A. Desideri, M. R. Kærn, T. S. Ommen, J. Wronski, and F. Haglind, *Flow boiling heat transfer and pressure drop characteristics of R134a, R1234yf and R1234ze in a plate heat exchanger for organic Rankine cycle units,* International Journal of Heat and Mass Transfer **108**, 1787–1801 (2017).

[185] D. Triché, S. Bonnot, M. Perier-Muzet, F. Boudéhenn, H. Demasles, and N. Caney, *Experimental and numerical study of a falling film absorber in an ammonia-water absorption chiller,* International Journal of Heat and Mass Transfer **111**, 374–385 (2017).

[186] J. Zhang, X. Zhu, M. E. Mondejar, and F. Haglind, *A review of heat transfer enhancement techniques in plate heat exchangers,* Renewable and Sustainable Energy Reviews **101**, 305–328 (2019).

[187] J. R. Thome and A. Cioncolini, *Unified modeling suite for two-phase flow, convective boiling, and condensation in macro-and microchannels,* Heat Transfer Engineering **37**, 1148–1157 (2016).

[188] X. Tao and C. A. Infante Ferreira, *Absorption of high concentration NH_3/H_2O in a plate heat exchanger,* in *International Sorption Heat Pump Conference. Berlin, Germany,* Accepted (2021).

[189] J. Sieres and J. Fernández-Seara, *Modeling of simultaneous heat and mass transfer processes in ammonia–water absorption systems from general correlations,* Heat and Mass Transfer **44**, 113–123 (2007).

[190] X. Tao, D. L. Liu, L. Y. Wang, J. Shen, and Z. H. Gan, *A cryogenic heat exchanger with bypass and throttling and its thermodynamic analysis,* (IOP Publishing, 2015) p. 012167.

[191] H. Qiao, V. Aute, H. Lee, K. Saleh, and R. Radermacher, *A new model for plate heat exchangers with generalized flow configurations and phase change,* International Journal of Refrigeration **36**, 622–632 (2013).

CURRICULUM VITÆ

Xuan TAO (陶轩)

01-03-1991   Born in Ningshan, Shannxi province, China.

2009-2013   Bachelor of Science in Energy, Power System & Automation
Xi'an Jiaotong University
Xi'an, China
Thesis: The performance analysis and numerical simulation
of cryogenic heat exchanger using wire mesh surface

2013-2016   Master of Science in Power Engineering & Engineering Thermophysics
Zhejiang University
Hangzhou, China
Thesis: Numerical and Open Cycle Experimental Investigation on a Precooled J-T Cryocooler at Liquid Helium Temperature including the Last Stage Heat Exchanger

2016-now   PhD. Mechanical Engineering
Delft University of Technology
Delft, The Netherlands
Thesis: NH_3 condensation within plate heat exchangers: Flow patterns, heat transfer and frictional pressure drop

LIST OF PUBLICATIONS

JOURNAL PAPERS

1. **Xuan Tao***, Carlos A. Infante Ferreira. *NH_3 condensation in a plate heat exchanger: Flow patten based models of heat transfer and frictional pressure drop*, International Journal of Heat and Mass Transfer **154**, 119774, (2020). (Chapter 6)

2. **Xuan Tao***, Elias Dahlgren, Maaike Leichsenring. Carlos A. Infante Ferreira. *NH_3 condensation in a plate heat exchanger: Experimental investigation on flow patterns, heat transfer and frictional pressure drop*, International Journal of Heat and Mass Transfer **151**, 119374, (2020). (Chapters 4&5)

3. **Xuan Tao***, Carlos A. Infante Ferreira. *Heat transfer and frictional pressure drop during condensation in plate heat exchangers: Assessment of correlations and a new method*, International Journal of Heat and Mass Transfer **135**, 996-1012, (2019). (Chapters 2&3)

4. **Xuan Tao**, Menno P.Nuijten, Carlos A. Infante Ferreira*. *Two-phase vertical downward flow in plate heat exchangers: Flow patterns and condensation mechanisms*, International Journal of Refrigeration **85**, 489-510, (2018). (Chapters 1&2)

CONFERENCE PAPERS

1. **Xuan Tao***, Carlos A. Infante Ferreira. *Absorption of high concentration NH_3/H_2O in a plate heat exchanger*, In Proceedings of the International Sorption Heat Pump Conference 2021, Paper No.49, Berlin, Germany, (2021). (not included in this thesis)

2. **Xuan Tao***, Elias Dahlgren, Carlos A. Infante Ferreira. *Condensation heat transfer and pressure drop of NH_3 and NH_3/H_2O within a plate heat exchanger*, In Proceedings of the 25th IIR International Congress of Refrigeration (ICR2019), Paper No.727, Montreal, Canada, (2019). (Chapter 4)

3. Maaike Leichsenring, **Xuan Tao***, Joost Kirkenier, Carlos A. Infante Ferreira. *Flow visualization of ammonia inside a Gasketed Plate Heat Exchanger condenser*, In Proceedings of the 25th IIR International Congress of Refrigeration (ICR2019), Paper No.746, Montreal, Canada, (2019). (not included in this thesis)

4. **Xuan Tao***, Joost Kirkenier, Carlos A. Infante Ferreira. *Condensation of NH_3 within a Plate Heat Exchanger of Small Diameter Channel*, In Proceedings of the 6th ASME International Conference on Micro/Nanoscale Heat and Mass Transfer, Paper No.3920, Dalian, China, (2019). (Chapter 1)

5. **Xuan Tao***, Elias Dahlgren, Carlos A. Infante Ferreira. *Local NH_3 Condensation in a Plate Heat Exchanger*, In Proceedings of the 13th IIR Gustav Lorentzen Conference (GL2018), Paper No.1160, Valencia, Spain, (2018). (Chapter 4)

6. **Xuan Tao***, Elias Dahlgren, Carlos A. Infante Ferreira. *Local measurement of NH_3/H_2O absorption in a plate heat exchanger*, In Proceedings of the 6th International Conference on Cryogenics and Refrigeration (ICCR2018), Paper No.015, Shanghai, China, (2018). (not included in this thesis)

ACKNOWLEDGEMENTS

Applying for a PhD in the Netherlands is a life-changing decision. At a disappointment moment, my courage and confidence dropped. I slowed down but had no excuse to stop. I never questioned my decision, and always believed that the solution is to proceed no matter how slow the progress is. I am proud at the end of the journey and learn to live with regret. The journey becomes unforgettable, although not easy, because of many guides and companions.

My supervisor, Dr. Carlos Infante Ferreira, has supported me continuously during these four years. In order to finish a paper, we discussed on the last day before the Christmas holiday and on the first working day of new year. We came to the DEMO together to discuss the manufacturing details of the transparent plate. You have been patient with my faults, so I am comfortable to admit mistakes and to learn from lessons. As the regional editor of IJR, you perform work actively and give timely feedback. Your office is open to students. When I am required to take more responsibility decades later, I will always remember your dedication and conscientiousness.

Prof. Thijs Vlugt build an effective and productive team. Being a member of the group of Engineering Thermodynamics, I benefited from the discussions and ideas during the group meetings. He has an in-depth understanding of what makes scientific writing. His comments helped me to improve my thesis. Prof. Bendiks Jan Boersma and Prof. Wiebren de Jong kindly approved to be my committee members. I have attended several PhD defence challenged by them and been inspired by these insightful discussions.

Prof. Felix Ziegler commented my work during his visit to Delft. I learned from his requirement of academic standard and examine my work accordingly. Prof. Pega Hrnjak gave me constructive suggestions during several conferences. His passion makes the research on two-phase flow lively stories. Prof. Yong Tae Kang encouraged me when I just started my PhD and was nervous. Prof. Ruzhu Wang leads a productive research group whose members are active internationally. Prof. Xianting Li takes every oral presentation and question seriously. The researches of Prof. Alberto Coronas motivate me to extend my work from NH_3 to NH_3/H_2O. When preparing my GO/NO GO exam, I spent one month on NH_3/H_2O absorption models. The paper of Prof. José Fernández Seara is my entry point to non-equilibrium model. Prof. Yunho Hwang explores magnetic cooling and novel heat exchangers, bringing new ideas to refrigeration.

Dr. Kumar Patchigolla and Ms. Maisie Cooper-Carlyle arrange for my new position in Cranfield university, so my pressure is reduced when finishing my PhD. Prof. John Thome organized workshops on two-phase flow and shared the flow visualization results online (VIR2AL). I was inspired when visiting his laboratory. Dr. Henk Polinder offered me the opportunity to promote my research in Ocean Energy Platform as a part of Delft Energy Initiative. Prof. Christian Poelma and Dr. Wim-Paul Breugem hosted several lectures of multiphase flow, which are attractive for me.

Experimental work is full of uncertainties. I am fortunate with the collaboration with my colleagues of previous Bluerise BV and now Allseas BV. Joost is enthusiastic for OTEC and shared his knowledge about the experimental setup. He also helped with my Dutch summary. Bram offered solid technical support especially in terms of LabView and Python. Berend Jan is motivated to exploit the potential of ocean energy. I enjoyed working with master students. Elias was hard-working and eager to learn more. Maaike was excited about the project and excellently coordinated the activities about the visualization experiments. Christopher was able to absorb large amounts of information and made clear plans.

The discussions with Meng and Vilborg were fruitful. We helped each other during experimental work and shared ideas about heat and mass transfer. Our conference trips were full of information and joy. Meng has an effective way to relieve pressure. Long came from the university I almost attended (SJTU), and has creatively developed his academic career around sorption. Liang shows potential as a young researcher.

The technical support from PE DEMO team is indispensable. Jaap and Michel facilitated the operation of the laboratory and risk managements. My life was saved when an NH_3 tank leaked. The first-hand help comes from Daniel, Martijn, Gerard and Bas. The strict processing takes more time at the beginning but avoids rework afterwards. At the end of my PhD, I realized I contribute significantly to the noise in the lab. This might be the reason for my being kicked out. The help from the secretaries reduces my pressure in daily work. They are Linda, Eveline, Leslie, Helma and Rob. Mascha from 3ME GS gave me the first and last courses of time management.

I always appreciate my education in Xi'an Jiaotong University and Zhejiang University. In XJTU, I started to undertake tasks independently and to find answers by myself when given questions. Actions are more powerful than words in teaching. Prof. Jianlin Yu provided me the initial research training. Prof. Yu Hou instructed me to view problems integrally. Dr. Weifeng Wu encouraged me to exceed the basic requirement of courses and offered helpful discussion. Dr. Huibao Luan is devoted to the commercialization of plate heat exchangers and gave me

valuable advices. ZJU has an international environment and has widened my horizon. Prof. Zhihua Gan taught me the way to integrate into a team and to promote lab work. Rather than avoiding mistakes, it is more important to do right things. Prof. Limin Qiu showed how to make research work understandable and popular. Prof. Xiaobin Zhang answered my questions about numerical methods. Cryoboat group was a happy family and has prepared me for the challenge abroad.

My friends in Delft make my life colorful and joyful. We explored the journey in different ways and were brought together by trust. The only thing to fear is fear itself. The first thing to break through is mental breakthrough. To face the difficulty directly is a big step. If Jiefang worked on energy technology, her experimental skills would be as good as cooking skills, which would result in excellent publications. The badminton matches against Jie were the moments I could forget a lot and was pushed to be aggressive. Alice and Chunyan are more than excellent chefs and hosts. I can hardly deny their comments on my weight. Beien and Tianyuan guided me around the Netherlands, who are energetic when crossing grassland and finding fantastic restaurants. Zhe Hou introduced me to the ZJU Alumni Association where I met Zhe Li and other friends. We climbed the highest mountain of Zuid Holland whose altitude is 37 m.

Xiuxiu and Cong gave me patience when I was in a difficult moment. We also spent new year's eve together on dumplings and board games. Qianqian chose to be considerate when other choices might save efforts. When being impressed by a merit, I can learn it by myself.

Xiaodong and Rong are helpful neighbors, and are the persons I met in the period of coronavirus. Liangyuan and Shilong helped me to move NH_3 tanks, which look like bombs. Xu represents the highest level of Chinese football in PE. I am glade to meet my PE colleagues: Otto, Brian, Mahinder, Hakan, Luis, Sergio, Haoyu, Mengmeng, Teng, Reza, Seyed, Mariette, Sebastian, Noura, Mate and Hirad. Remco carefully translated my Dutch summary. I hope to translate Chinese for him one day. Fatma was optimistic when our train was delayed for three hours.

Wenjie reminded me to slow down and to reflect. Sincerity and frankness make the complex a bit easier. Dongli took me back to the colorful life in Hangzhou. Hui and I hanged out in West Lake but failed to make it in Kinderdijk. Mengjian gave birth to a baby when I was producing my thesis. Bin does not need to explain which Jiaotong University he is from since he has both.

The devotion and patience of my family stays with me all the time. It is not easy to have a son being farther and farther away. Sometimes I am disappointed when my concern was replied with silence. At a certain point, I realized the significance of the growth environment you created, which is relaxed and enlight-

ened, being the root of my courage and confidence.

Finally, I cannot make the title *NH_3 and NH_3/H_2O condensation within plate heat exchangers.* It is in my mind. What behind this mountain are other mountains instead of plains. I have been confident in my persistence and concentration. What if the challenge is to explore the unknown and change? I will be armed with my harvest in Delft (Challenge the Future).

Xuan Tao
Delft, The Netherland